Inkjet Printing Conductive Materials on Textiles

A thesis submitted to the University of Manchester for
the degree of Doctor of Philosophy
in the Faculty of Science and Engineering

2021

Zixin Wang

School of Natural Sciences

Department of Materials

List of Contents

Word count: 36595

List of Tables

List of Figures

Abstract

Inkjet printing functional materials on textiles has attracted considerable attention from researchers and industries due to its promising prospects on wearable applications. Inkjet printing is cost saving and provides customisation ability of printing electronic patterns. Textile substrate is flexible, stretchable, comfort to wear and breathable. The advantages from both the printing technique and the substrate material can be displayed when the deposition of the ink in textiles is well studied. Thus, this thesis investigates fundamental interaction of conductive silver ink on textiles, and the effects of printing parameters and textile properties on the printing quality and electrical performance of the products.

The complexity of textile substrates leads to three scales of ink textile interaction mechanisms, which are fibres, yarns, and fabrics. Those mechanisms were compared with existing liquid textile interaction theories, and it was found that ink/fibre and ink/yarn interactions correspond with existing theories. Capillarity confines the transport of the ink, low fibre surface energy leads to increased spreading length, small fibre spacing promotes ink columns formation on fibres but limits the ink spreading in yarns. It was also found that the inkjet printed ink transports predominantly within the warp or weft yarns of the fabric and there is little transport of ink between the yarns. Nevertheless, various yarns woven into fabric structures with different densities can result in distinct ink transporting behaviours.

X-Ray tomographic reconstruction reveals that the distribution of Ag after inkjet printing and sintering a nanoparticle conducting ink on a woven polyester textile substrate is strongly controlled by the fibre surface properties and fabric architecture. Reduced drop spacing, increased printing layers and textile hydrophobicity through Scotchgard treatment increased the volume and connectivity of inkjet printed silver ink deposition. In the meantime, the sintering per layer technique further increased the volume and connectivity of inkjet printed silver ink on textiles through enhanced ink penetration mechanism perpendicular to the fibre tows. Electrical conductivity is strongly influenced by the fibre architecture in each yarn direction and, in this case, higher fibre density in warp yarns leads to higher electrical conductance values. Conductance within a yarn is shown to depend on Ag concentration via a percolation mechanism and this is confirmed by a simple model relating the volume of the largest interconnected Ag object present to the measured conductance.

To improve the printing quality and electrical performance of electronic textiles through altering fabric structures without additional surface treatment, six types of polyester woven structures were compared. It was found that the increased overall capillarity in the fabric could enhance the conductive ink connectivity in textiles and thus improve the electrical performance of electronic textiles, however, on the other hand, creating unwanted ink bleeding on textiles and reducing printing quality of inkjet printed electronic textiles.

Declaration

No portion of the work referred to in the thesis has been submitted in support of an application for another degree or qualification of this or any other university or other institute of learning. Partial content in Chapter 5 has been published in journal paper ACS Applied Materials & Interfaces, 2020 Oct 7; 12(40):45516-45524. DOI: 10.1021/acsami.0c11535.

Copyright Statement

i. The author of this thesis (including any appendices and/or schedules to this thesis) owns certain copyright or related rights in it (the "Copyright") and s/he has given the University of Manchester certain rights to use such Copyright, including for administrative purposes.

ii. Copies of this thesis, either in full or in extracts and whether in hard or electronic copy, may be made only in accordance with the Copyright, Designs and Patents Act 1988 (as amended) and regulations issued under it or, where appropriate, in accordance with licensing agreements which the University has from time to time. This page must form part of any such copies made.

iii. The ownership of certain Copyright, patents, designs, trademarks and other intellectual property (the "Intellectual Property") and any reproductions of copyright works in the thesis, for example graphs and tables ("Reproductions"), which may be described in this thesis, may not be owned by the author and may be owned by third parties. Such Intellectual Property and Reproductions cannot and must not be made available for use without the prior written permission of the owner(s) of the relevant Intellectual Property and/or Reproductions.

iv. Further information on the conditions under which disclosure, publication and commercialisation of this thesis, the Copyright and any Intellectual Property and/or Reproductions described in it may take place is available in the University IP Policy (see http://documents.manchester.ac.uk/DocuInfo.aspx?DocID=24420), in any relevant Thesis restriction declarations deposited in the University Library, the University Library's regulations (see http://www.library.manchester.ac.uk/about/regulations/) and in the University's policy on Presentation of Theses.

Acknowledgement

There are many people that I would like to acknowledge during the journey of my PhD study. First of all, I would like to express my sincere gratitude to my supervisor Professor Brian Derby for giving me the opportunity to explore this interesting research area. I really appreciate his visionary guidance, comprehensive support and encouragement, which helped and motivated me all along during my studies. I would also like to thank him for the time and feedback provided for this project and this thesis, through which I gained countless knowledge and experience.

It is my pleasure to thank Professor Ian A. Kinloch and Dr David Lewis for their advice on my annual reports and viva. I would also like to thank Dr Rachel Saunders, Dr Tristan Lowe, Mr Andy Wallwork, Mr David Kenyon, Mrs Hannah Rampley, Dr Celina Jones, Dr Teruo Hashimoto, Dr Julia Behnsen, Dr Patrick Hill, Miss Jasmine Fernley and Dr Chloe Loveless from department of materials, for their technical support and contribution on this project. Some of them also gave me valuable suggestions for my research and my life, which I really appreciate.

I also appreciate my colleagues Dr Hui Ding, Dr Hu Zhao, Dr Chongguang Liu, Dr Jinxin Yang, Dr Joseph Neilson, Dr Mike Avery, Dr Pei He, Dr Fei Zheng and Dr Kirstie Ryan for their sincere advice on my research. They also made my PhD life interesting and colourful, I really enjoyed working with them.

Special thanks to EPSRC for funding the Henry Mosely X-ray Imaging Facility used in this project, and the Manchester Centre for Digital Fabrication where most of the experiments were conducted for this project.

Finally, I would like to give thanks to my family who funded my PhD and for their support and care. I appreciate all my friends for their encouragement and time spending with me to support my work-life balance. The last but the most, to Roke Cepeda-Arroita, my dear boyfriend, for his unconditional love and support all the time.

Preface

Degrees

- 2016-2017, The University of Manchester
  Masters by Research in Nanostructured Materials
- 2013-2016, The University of Manchester
  BSc in Textile Science and Technology with Industrial Experience

Research Experience and Contributions

- 2017-present, The University of Manchester

  Inkjet printing conductive materials on textiles

  i) Wang, Z., Lowe, T., & Derby, B. (2020). Fluid/Fiber Interactions and the Conductivity of Inkjet Printed Ag on Textile Substrates. ACS Applied Materials & Interfaces, 12 (40), 45516-45524.
  ii) Print for fabrication 2020, online, oral presentation.
  iii) Materials Research Society conference 2019, Boston, poster presentation (Best poster award nominee).
  iv) IoM3 Young Person's Lecture competition 2019, Manchester heat, oral presentation (2nd prize).
  v) Materials Research Society conference 2018, Boston, oral presentation.

- 2016-2017, The University of Manchester

  The Effect of Particle Size and Functionalisation on Electro-thermo-mechanical Properties of Graphene-enhanced Epoxy and Carbon Fibre Epoxy Nanocomposites

  i) Wang, Z., Gresil, M., Soutis, C. (2021). Fracture Toughness of Hybrid Carbon Fibre/Epoxy Enhanced by Graphene and Carbon Nanotubes. Applied Composite Materials, 1573-4897.
  ii) Gresil, M., Wang, Z., et al. (2017). Thermal mapping of graphene polymer-based composites. Scientific report, 7, 5536.
  iii) Poutrel, QA., Wang, Z., et al. (2016). Effect of pre and post-dispersion on electro-thermo-mechanical properties of a graphene enhanced epoxy. Applied Composite Materials, 24, 313–336.
- 2018, Diamond light source

  i) Barui, S., Ding, H., Wang, Z., et al. (2020). Probing Ink-Powder Interactions During 3D Binderjet Printing Using Time Resolved X-Ray Imaging. ACS Applied Materials & Interfaces, 12 (30), 34254–34264.

Chapter 1 Introduction

1.1 Background

Inkjet printing conductive materials on textiles has attracted considerable attentions from researchers and industries for a wide range of wearable applications, such as communicating, sensing and energy harvesting.[1–3] Inkjet printing technique is low cost and versatile comparing to other techniques, and textile substrate is ideal for wearables due to its flexible, stretchable, and breathable properties.[4–6] Inkjet printing on textiles has been widely used in the fashion industry with coloration pigments. [7] However, the commercialisation journey of inkjet printed electronic textiles is still challenging due to the difficulty of achieving continuous conductive patterns and high printing resolution on textile substrate, due to the uneven surface and porosity of textiles.[8,9]

Unlike inkjet printing conductive paths on solid surface, there are two competing fluid processes after drop impact: the flow of fluid along the surface and the infiltration of the liquid into the pores via capillary interaction. [10] Due to the complex structure of textiles which is made from fibre, yarn to fabric scales, it is extremely difficult to predict and control the flow of the conductive ink to form continuous and homogeneous conductive paths. [11] To predict fluid flowing process in textiles, researchers have studied the interaction of liquids with textiles of relevance to engineering problems in textiles or polymer composite industries. [12] However, existing models can only provide some understanding of the factors that influence the structures formed after inkjet printing on textiles.

The study of printing conductive inks on textiles is relatively recent and only started in the 21st century. In current studies of improving the inkjet printed conductive textiles, main approaches include developing inkjet printable conductive inks and altering textile surface properties.[13–15] A wide range of printable functional inks have been developed, yet the interaction between the ink and the textile remains as the biggest challenge to reach optimal conductive performance without sacrificing intrinsic advantages of textiles. Moreover, the durability and washability of the conductive paths on textiles require efforts of researching to achieve the possibility of commercialising inkjet printed conductive textiles.

1.2 Motivation and Outline of the Thesis

In the research field of inkjet printing electronic textiles, there is a clear need of finding a breakthrough point through understanding the fundamentals. The aim of this project is to study the fundamental mechanisms of inkjet printed conductive ink interaction with porous textile structures, through which to evaluate the fit of the existing liquid textile models and to explore the parameters that could be used to control the printing quality. 3d structures are visualised through X-ray tomography of silver conductive ink on fabrics to understand the contribution of printed structures to conductivity. In the meantime, the effect of textile surface treatment, inkjet printing settings and sintering techniques are investigated to improve the performance of electronic textiles.

A summary of each chapter is as follows.

Chapter 1 provides a concise background, motivation, and outline of the thesis.

Chapter 2 gives a thorough literature review of topics related to this project. Starting from a brief introduction of wearable technology to the complex textile structures and surface properties and the existing studies on liquid textile interactions from fibre, yarn and fabric scales, followed by the principle and development of inkjet printing technology. Then the use of inkjet printing on conductive electronic textiles is studied, providing the current development and applications of electronic textiles, printable conductive inks and remaining challenges and frontier work.

Chapter 3 lists the detailed information of the conductive ink and textile substrates, inkjet printing and sintering methods and characterisation techniques used in this project.

Chapter 4 describes the fundamentals of silver ink deposition on as received and hydrophobic treated polyester textile substrates. Using contact angle values of silver ink on textile as a centre point expanding and evaluating the applicability of existing models for liquid interaction with fibres, yarns, and fabrics. The theories applied on individual textile scales are at variance, and the textile surface energy and the drop and textile geometries play the most important roles determining the ink deposition on textiles. It is found that low textile surface energy leads to increased ink spreading and penetration, and smaller pore size/fibre size creates ink columns between fibres and larger pore size/ fibre size leads to ink penetration. When pores are filled with inks, greater average pore spacing leads to faster and longer ink spreading in yarns, however, opposite finding is observed in ink/fabric interaction.

Chapter 5 applies X-ray tomography technique to visualise and quantify the silver ink objects distribution in textiles in a 3d view. The effect of changing textile surface hydrophobicity, inkjet printing drop spacing and layer, and sintering techniques on Ag distribution on textiles are clearly shown in 3d images. The connectivity and concentration of silver objects are found to be the key factors to improve the electrical conductance of electronic textiles. A simple model is developed to predict the conductance of specimens through X-ray tomography images and ohm’s law. Additionally, the anisotropic behaviour between warp and weft fabric directions demonstrates the inappropriate used of a ‘sheet resistance’ in measuring conductive textiles.

Chapter 6 collects the findings of different behaviours on fabric warp and weft directions as observed from previous chapters and examined six types of polyester fabric structures, in order to evaluate the hypothesis of improving the printing quality and electrical performance of inkjet printed electronic textiles through altering fabric structures. It is a promising approach to improve the performance of e-textiles without compromising the intrinsic advantages of textiles. It is found that increased total capillarity in textiles through reduced effective pore size, and tighter and thicker packed fabrics improve the printing quality. However, the relative electrical conductance which depends on the silver objects connectivity reduces as the ink transportation is prohibited.

Chapter 7 summarises this thesis and gives an outline for possible future work.

Chapter 2 Literature Review

2.1 Wearable Technology

Wearable technology has attracted considerable attention due to its numerous potential applications for health and environmental monitoring [16,17], energy storage and harvesting [18] and entertainment [19]. The modern definition of wearable technology includes devices that can collect physiological and environmental information in a real-time manner in a portable and wearable approach [20]. To achieve this, wearable monitoring systems must integrate sensors, signal conditioning circuitry, information storage or transmission devices, power supplies and interconnecting conductors all on an appropriate flexible or stretchable substrate [21].

The development of wearable technology can be described through significant milestones in the past century, as shown in some examples in Figure 2.1. From the design of the ‘Walkie-Talkie’ in 1937, to the ‘Stereophonic Television Head Mounted Display’ and the first wearable computer hidden in the shoe [22] in the 1960s, and the invention of the ‘Calculator Watch’ and ‘Camera-to-tactile vest for blinds’ in the 1970s [23]. In the beginning of the 90s, the ‘Active Badge’ was invented as the first portable indoor location tracker, and the development personal digital assistant became popular until it morphed into smartphones [24]. In the 21st century, some well-known products came into the market, such as the Levi’s industrial clothing division (ICD) jacket, Fitbit, Google Glass, Apple Watch and so on [25,26]. In recent years, there has been extensive development of wearable technology, with more focus on the design and manufacture of electronics directly on flexible fabric substrates, instead of assembling separate rigid components that are subsequently attached to the substrates. The topics include but are not limited to the specific design of flexible electronic components, the design and selection of substrates, and developing new manufacturing techniques. Some but not all of this prior work has been described as flexible electronics.

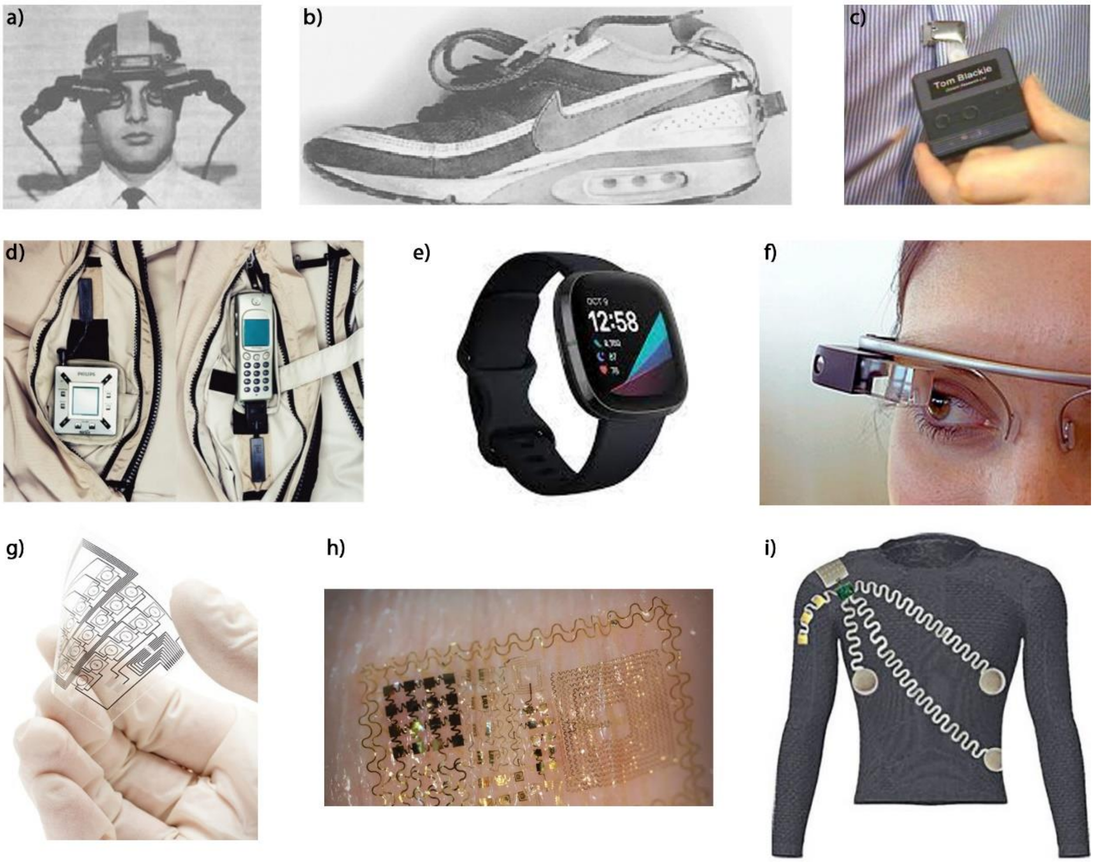

Figure 2.1 Wearable technology inventions including: a) the world’s first head-mounted display [27], b) the first wearable computer in shoe [28], c) the active badge location system [29]; commercial products such as: d) Levi’s industrial clothing division jacket, e) Fitbit f) Google Glass; prototypes of: printed flexible electronics on plastic films g) [30], skins h) [31], and textiles i) [32].

Flexible electronics include functional components e.g. transistors, sensors, solar cells, light emitting diodes, batteries and supercapacitors, resistors, conductors and interconnects; their assembly into devices and systems such as: displays, self-powered devices, communication devices, and radio frequency identification devices. The particular design of the devices depends on the applications of the wearables but generally require multilayer structures, some examples are listed in Figure 2.2. The materials applied in the systems can be classified into conducting, semi-conducting and dielectric materials [5,33,34]. Conducting materials exist in most of wearable devices as interconnectors between different components; semi-conducting materials play important roles in some electronic components such as field effect transistors, LEDs, solar cells and so on; dielectric materials are electrical insulating, which are used in electronics that require high capacitance such as transistors and capacitors [4]. A significant challenge for the use of these structures on textile substrates is the development of appropriate fabrication technologies.

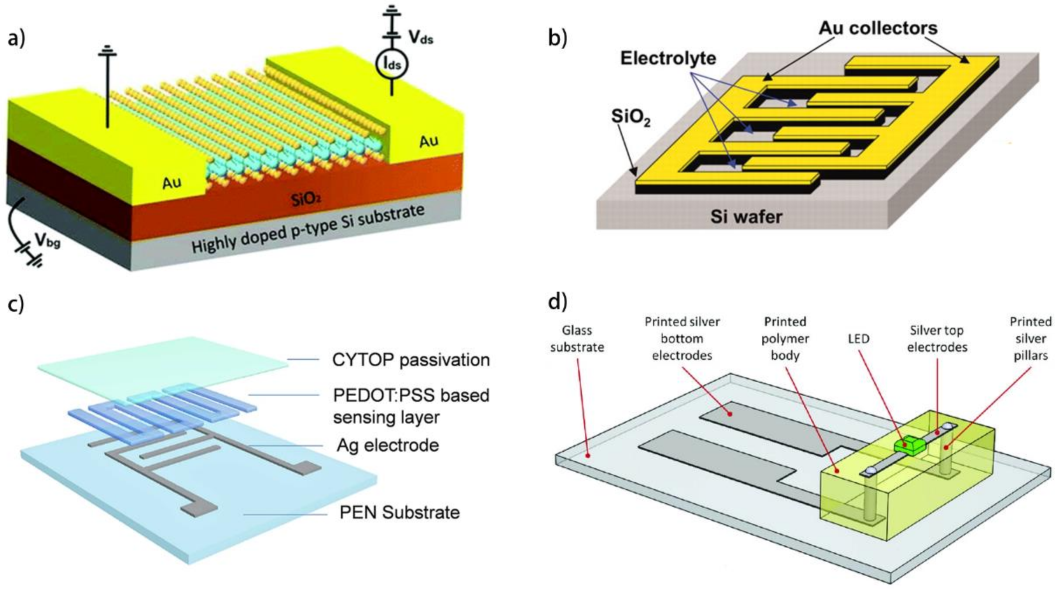

Figure 2.2 Schematics of inkjet printed a) MoS2 FET [35], b) micro-supercapacitor [36], c) temperature sensor structure [37], and d) LED interconnectors [38], all showing the use of conductive materials in the system.

Flexible substrates are essential to provide wearability for those devices. There have been many studies of applying functional materials to polymer film flexible substrates [4]. Polydimenthylsiloxane (PDMS), Polyethylene naphthalate (PEN), polyimide (PI) and polyethylene terephthalate (PET), Poly(vinyl alcohol) (PVA) and Ecoflex are commonly used flexible substrates [39]. However, all these substrates cannot easily accommodate more than a single curvature as they flex, reducing comfort if used in clothing. In contrast, textile substrates provide a platform that can provide both strength and flexibility, and is potentially more comfortable to wear, as well as being more stretchable, breathable, washable and environment-friendly than polymer films [6]. With the variability of textile structures and the great number of components in a wearable system, research into wearable technology includes, but is not limited to, developing functional filaments [40–43], printing and coating functional materials on fabrics [44–47], and fabricating fully integrated textile systems [48–51].

Current technologies used for developing electronic textiles can be broadly grouped into two classes: embroidering functional threads into fabrics and coating functional materials on the surface of textiles. Metal threads are simpler in concept but can break easily during manufacturing and use, which influences comfort. A number of different coating methods that have been used, these include: printing, electroless plating, evaporation deposition, sputtering functional materials on substrates [9]. However, many of these methods have limitations, which may reduce their applicability with textile substrates. The high cost of the reducing agent may limit the application of electroless plating and the reducing environment will be incompatible with some textile fibres [52]. Coatings deposited by evaporation often show low values of adhesion [53]. Sputtering is limited by its poor patterning capability [9]. Printing technologies, however, show promise due to their reasonable capital equipment costs and simple manufacturing methods that have been previously developed for decorative patterning of fabrics. Inkjet printing is a contactless printing technique that avoids using a plate or a screen mesh like lithographic or screen printing. Thus, it allows rapid design changes with a relatively low cost machine set-up and reduced material waste [5451,3,4,55–57].

Inkjet printed textile electronics has significant potential to advance the development of wearable technology with current research on the formulation of functional inks and the deposition of the desired patterns [8,39,58,59]. However, challenges must be overcome to achieve continuity of printed patterns due to the roughness and porosity of textile substrates, in contrast to the smooth dense surfaces of conventional polymeric flexible substrates. In addition, most of the fabrics can withstand only a limited range of temperature, which limits the processing routes available, Finally, it is desired that the printed fabrics should retain characteristics similar to the unprinted fabrics, such as the flexibility, stretchability, breathability and washability of textiles.

The aim of this project is to study these challenges in inkjet printing conductive materials on textiles and to better understand the mechanisms that control the behaviour of printed electrical conductors. Thus, the fundamentals of liquid textile interactions relevant to ink deposition and the inkjet printing technology used to achieve this will be reviewed in this chapter, and the recent developments in this research field will be explored and discussed.

2.2 Liquid Textile Interaction

2.2.1 Textile Materials

Textiles represent materials consisting of fibres, yarns, and fabrics. These terms are related. Yarns are formed by the assembly, through spinning, of many, approximately parallel, individual fibres. Different textile structures or fabrics are formed through different manufacturing processes using yarns or individual fibres. In general, there are four main textile structures classified as: woven, knitted, braided and non-woven fabrics [60]. Non-woven fabrics are made from bonded staple or long fibres, and the other three types of fabrics are made from yarns (otherwise known as tows or threads)[61]. Woven fabrics are produced using a loom on which one set of fibres are arranged, under tension, as a series of parallel yarns, these are the warp fibres. During the weaving process, the weft yarns are passed above and below the warp yarns, in a repeated and controlled manner, to produce a sheet of fabric. The process leads to the warp yarns retaining an approximately in-plane orientation with the weft yarns, showing a pronounced undulation as they pass over and under the warp yarns. [12,62,63] Knitted fabrics can be made either manually or mechanically. They can be categorised into two basic styles: warp knit, and weft knit. Warp knit contains the meandering yarns following paths on the warp direction (wales) and weft knit contains the yarns following paths on the weft direction (courses) [64]. As for braided fabrics, they are made of interlacing three or more yarns or fabric stripes in diagonal formation, forming flat or tubular fabrics [65].

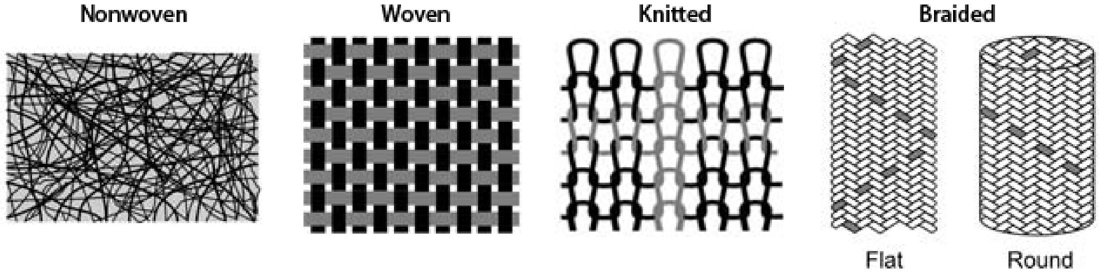

Figure 2.3 Fabric structures: nonwoven, woven, knitted and braided structures, adapted from ref. [66]

Each type of fabric (Figure 2.3) has its own application range. Non-woven fabrics are recognised for their low-cost and soft surface, woven fabrics show good stability and strength, knitted fabrics show superiority in their stretchability, and braided fabrics display high impact resistance. Non-woven textiles can be made at the highest production rate and this is leading to a growing market share for applications in the sectors of personal care, health care, clothing, household, automotive, geotextiles, constructure, and filtration [67]. Weaving is one of the longest established and most commonly used technique for textile manufacture is dominant in application areas of garments and technical textiles [68]. Knitting offers more comfort and better fitting, which is the most demanding technique in apparels [69]. Braided fabrics are often found in the use of technical applications in the field of sporting goods, medicine, aerospace and transport. Additionally, each type of fabric can produce a variety of structures through different fibre and yarn composition and orientation methods, to meet the specific requirements of an application [70].

There are a variety of yarns used to manufacture fabrics, which can be made from fibres spun together or an individual (mono) filament. Depending on the fibres used or the spinning process, different yarn structures are possible, with examples shown in Figure 2.4. The spinning process imparts a slight twist such that, when loaded in tension, frictional stresses between individual fibres transmit tension loads relatively uniformly across the bundle of fibres. This allows load bearing yarn lengths much greater than the individual lengths of the constituent fibres. This twist can be clockwise (Z-twist) or counter clockwise (S-twist) [71].

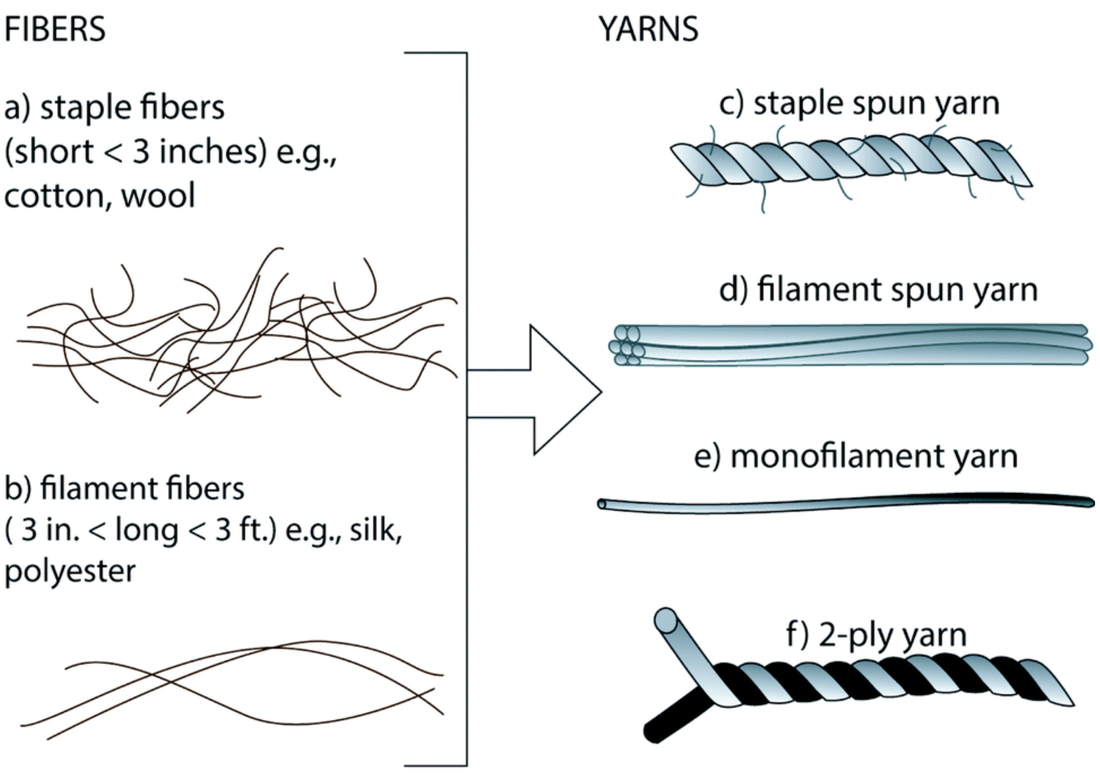

Figure 2.4 Different yarn structures (c-d) formed with staple (a) and filament (b) fibres, adapted from ref [72].

Yarns are made of fibres, and in general, staple fibre spun yarns made with cotton or wool present easier pilling and lower strength compared with the filament yarns [73]. Continuous filament yarns can create smoother and stronger fabrics. The scanning electron microscopic (SEM) images (Figure 2.5) of cotton and polyester fabrics and fibres illustrate the hairiness of staple cotton fibres made fabrics, and the irregular cotton fibre surface which could increase the difficulty of depositing smooth functional materials on textile substrates [74].

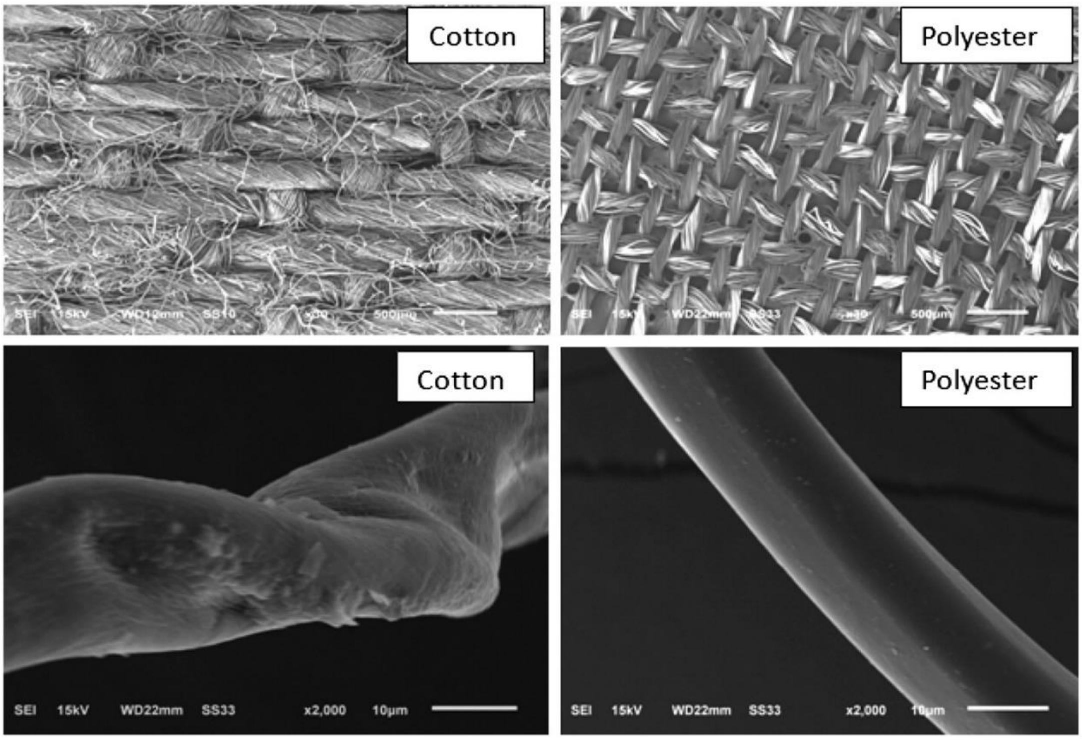

Figure 2.5 SEM images of cotton and polyester fabrics (top) under 30 × magnification and single strand structure (bottom) under 2000 × magnification, adapted from ref [74].

In addition to structural differences, fibres can be classified into natural fibres and man-made fibres; examples of fibre types and their classification are shown in Figure 2.6. Cotton fibres with a diameter range of 11-22 μm are mostly used in the clothing industry. Cotton fabrics are breathable and provide easy transport of moisture away from the body, the air trapped within the fabric can provide thermal insulation, and the fibres are soft and hypoallergenic. However, natural fibres are expensive when compared to synthetic fibres and can wear more easily. Polyester is the most used synthetic fibre in the fashion industry, with a greater usage than cotton. Although the breathability of polyester is lower than cotton, it is less expensive and stronger, in addition its hydrophobicity allows faster drying of moisture. Commonly used polyester fibres have a circular and smooth shape, with a diameter range of 12-25 μm [75].

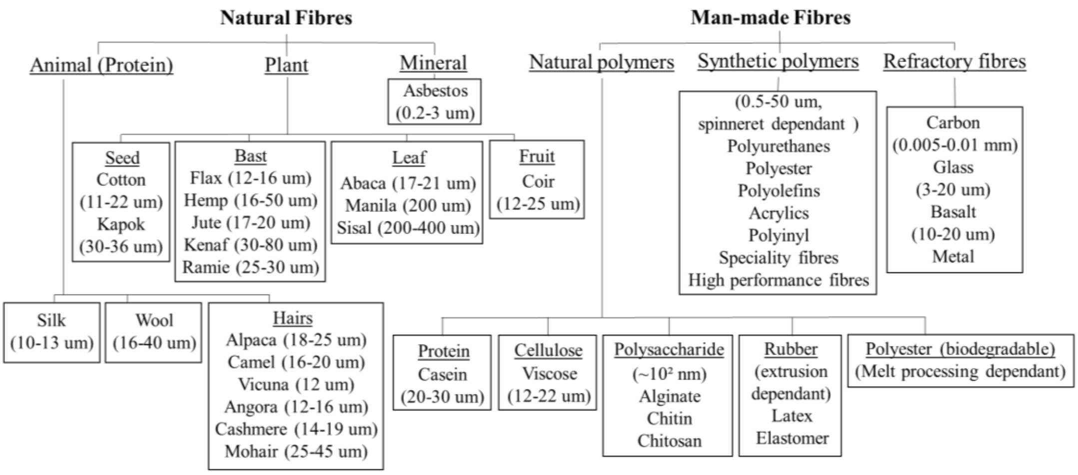

Figure 2.6 Different types of fibres and their diameters.

The difference in hygroscopicity between cotton and polyester fibres is mainly due to their different chemical compositions. Cotton is a cellulose with a polysaccharide polymer structure, which is comprised of a long chain of glucose molecules with hydroxyl groups on the outer edges, as shown schematically in Figure 2.7 (a) [76]. These hydroxyl groups interact strongly with dipolar water molecules so as to be hydrophilic. Polyester fibre is melt spun from polymers that contain the ester functional group in the main chain. There are a variety of polyesters with different main chain composition. Polyethylene terephthalate (PET) and poly-1, 4-cyclohexylene-dimethylene terephthalate (PCDT) are the two main types of polyesters used in the textile industries, in which PET is commonly used for clothing and PCDT is used for heavy consumer products such as furniture coverings. The chemical structure of PET is shown in Figure 2.7 (b), and it is hydrophobic due to the polarity of the ester group not being sufficient to attract water molecules to form hydrogen bonds.

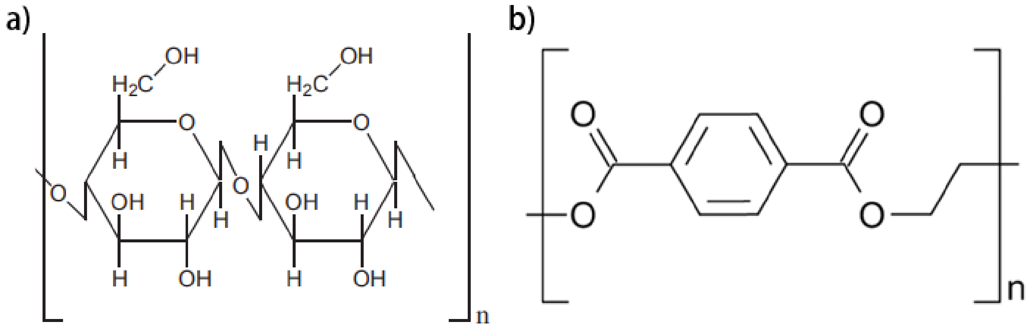

Figure 2.7 a) Chemical structure of cellulose cotton fibre [76]; b) Chemical structure of polyester (PET) fibres [77].

The choice of fibre, yarn and fabric in a particular application is based on the end-use requirement of the fabric [78,79]. In the field of electronic textiles, the required connected conductive paths are easier to be achieved in woven or knitted structures. Examples of prior research publications related to electronic textiles are listed in Table 2.1 showing their choices of textiles and applications. Knitted fabrics are more flexible and stretchable than woven fabrics, which could be useful for sensor application on measuring deformation or power generation. However, the flexibility of the yarn movement in the knitted structures could also induce instability in the electronic circuits, which is not ideal if stable interconnections are required in the design [80]. Additionally, the yarn structures play an important role in electronic textiles since material transport is governed by the capillary forces in the yarn tows. Monofilament yarns could potentially provide smoother materials deposition, yet the detailed deposition of functional materials in different yarn structures has not yet been reported. In terms of the fibre choices, there are many research papers about the application of functional materials on cotton fabrics, due to easier functionalisation of cotton fabrics with their hydroxyl groups. However, the higher hygroscopicity in cotton yarns could potentially lead to further damage to functional materials that require a dry environment.

Table 2.1 Different fabric choices for the application of electronic textiles.

Methods	Materials	Application	Fabric structure	Fabric material	Ref
Screen printing	Silver	ECG, EMG	Woven	Polyester/cotton/lyca blend	81
Electroless deposition	Nickel	Solar battery	Woven	Polyester	82
Immersion	MnO_2-Zn Silver	Stretchable battery	Knitted	Nylon	83
Inkjet printing	Reactive silver ink	Interconnector	Knitted	Polyethylene terephthalate	2
Inkjet printing	Graphene/h-BN	Field effect transistor	Woven	Polyester	3
Chemical deposition	Multi-layers	triboelectric nanogenerator	Woven	Spandex	84
Electroless plating	Silane, Silver	Conductive tracks	Woven	Cotton	85
Inkjet printing	rGO	ECG	Woven	Cotton	1

*ECG: electrocardiogram; EMG: electromyography; h-BN: hexagonal boron nitride; rGO: reduced graphene oxide.

2.2.2 Wetting and Wicking on Textile Substrates

Liquid/textile interactions play an important role in many fields within the textile industries. These include: the wetting and wicking properties for high absorbency medical and sanitary products, ensuring comfort in clothing, colouration of fabrics through dyeing for aesthetic purposes, functional surface treatment for hydrophobic and oleophobic fabrics, and the infiltration of resin during the manufacture of textile composites.[10,86–89] The interaction is also the main mechanism requiring studying for printed electronic textiles. Wetting and wicking are the two main and most important mechanisms during liquid and fibrous materials interaction. Wetting is generally defined as the spreading of a liquid on the outer surface of a textile fabric and wicking is capillary driven infiltration into the fabric after wetting and initial spreading of the liquid across the surface. On solid surfaces, wetting is the only considered mechanism, while with porous substrates, such as textiles, the wetting and wicking processes are complicated and inseparable.

Previous works have studied the differences between liquid spreading on porous and nonporous substrates; and investigated the effect of the porosity and the pore size. Denesuk et al. [90] studied the spreading kinetics of incomplete wetting on porous substrates, which highlights the competition between liquid spreading and infiltration, as shown in Figure 2.8. This assumed a rapid impact-driven spreading process defining an initial contact area, before a capillary-driven mechanism leads to infiltration by wicking. However, Holman et al. proposed that the time scales of infiltration and spreading are similar, and that the spreading of the liquid can be interrupted by infiltration. It was observed in experiments that the spreading phase ends rapidly and is followed by the sorption phase with capillary force domination, and slower infiltration leads to greater spreading. [91]

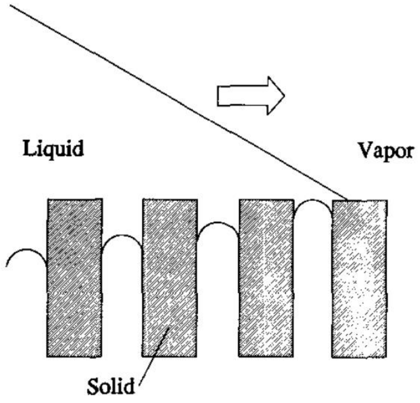

Figure 2.8 Drop spreading and absorption on a cylindrical porous substrate in a slow advancing spreading process [90].

The morphological evolution of wetting and wicking on a porous surface, including the maximum spreading diameter, has been studied and computationally simulated [92,93,94]. For better understanding of the absorption behaviour in porous substrates, X-ray imaging system [95], neutron radiography [96] or nuclear magnetic resonance [97,98] have proposed as suitable techniques for studying fluid flows during spreading and sorption. However, the spatial resolution of the imaging methods needs further improvement to resolve features at the micron scale. In this section, wetting and wicking mechanisms will be introduced individually, and the models used to explain both phenomena in textile substrates will be discussed.

2.2.2.1 Wetting

For an ideal solid surface, the equilibrium contact angle (θ_C) is typically used to illustrate the drop wetting extent on the surface. It is defined as the tangent angle at the contact between the liquid/vapour interface and the solid surface where equilibrium occurs through a balance of forces [99], as shown in Figure 2.9 and defined by Young's Equation (2.1) [100]. A low contact angle represents a strong interaction between the solid and the liquid phase, and vice versa. A hydrophilic surface usually refers to a high wettable surface with contact angle considerably less than 90°, and a hydrophobic surface generally indicates a low wettable surface with contact angle greater than 90°, and perfect wetting is achieved when $\theta_C = 0^0$.

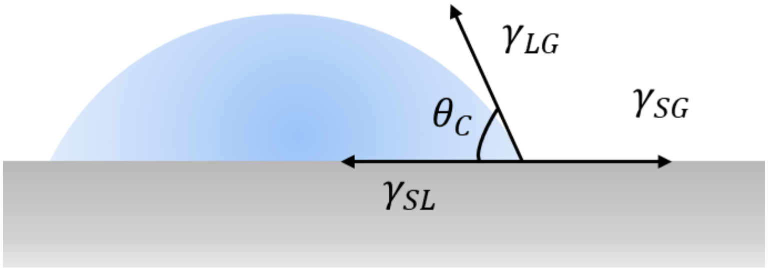

Figure 2.9 Schematic of the equilibrium contact angle (θ_C) of a liquid drop on a solid surface, showing the force balance with the surface tensions of the liquid/vapour (γ_{LG}), solid/vapour (γ_{SG}) and liquid/solid (γ_{SL}) interfaces.

$$\gamma_{SG} - \gamma_{SL} - \gamma_{LG} \cos \theta_C = 0 \qquad (2.1)$$

The wettability of a liquid on an ideal solid surface depends on the difference between work of adhesion (the energy per unit area required to separate the contacting liquid and the solid) and work of cohesion of the liquid (energy per unit area required to separate a liquid column into two liquid surfaces). A spreading coefficient S, defined in Young-Dupre Equation (2.2), is used to distinguish a complete or a partial liquid and surface wetting occasion. When $S > 0$, complete wetting occurs, and when $S < 0$, partial wetting occurs, as shown in Figure 2.10 [12].

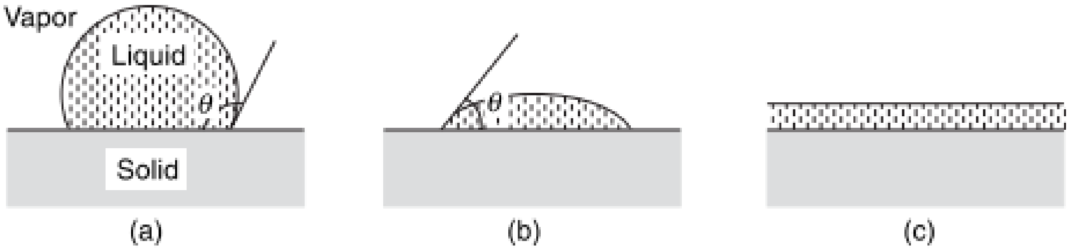

Figure 2.10 Liquid droplet on solid surface in the status of (a) hydrophobic partial wetting (b) hydrophilic partial wetting and (c) complete wetting, ref [12].

$$S = \gamma_{SG} - (\gamma_{SL} + \gamma_{LG}) = \gamma_{LG}(\cos\theta_C - 1) \tag{2.2}$$

For rough surfaces, such as textile surfaces in the absence of infiltration, the wetting is characterised by a contact angle hysteresis. Contact angle hysteresis is defined as the difference between the advancing contact angle and the receding contact angle. The advancing contact angle is the maximum steady angle, and the receding contact angle is the minimum steady angle of the liquid on the surface. These definitions are used to characterise the dynamic movement of liquids on surfaces. When the surface is rough, the drop of liquid deforms as the surface is tilted to different angles, and to maintain the same contact area between the drop and the surface, a higher contact angle is adopted at the 'downhill' side of the liquid drop while a lower contact angle is adopted at the 'uphill' side of the drop as shown in Figure 2.11. Thus, the extent of wetting will depend on whether the liquid is in the status of advancing or receding on the surface [101].

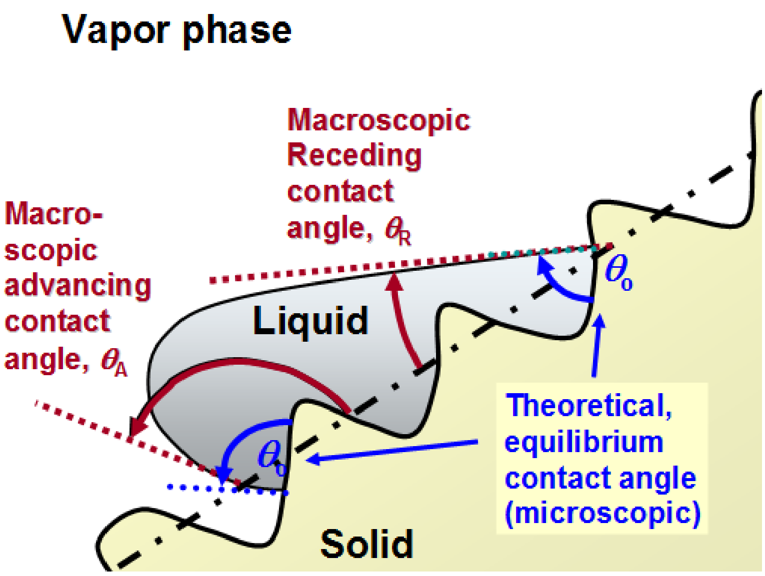

Figure 2.11 Schematic illustration of the advancing and receding contact angles on rough surface, adapted from ref [102].

Wenzel and Cassie-Baxter models are often used to characterise the relationship between the surface roughness and wettability, as shown in Figure 2.12. The Wenzel model[103] (Figure 2.12 a) considers the homogeneous wetted area of a rough surface to be larger than that of a plane flat surface by a factor r and this modifies the balance of Young's equation such that the effective or apparent contact angle, θ^*, is defined:

$$\cos(\theta^*) = r\cos(\theta_C) \tag{2.3}$$

where the surface roughness at the contact line (r) is quantified as the ratio of the actual surface to the projected solid surface area, and θ_C represents the Young's equilibrium contact angle of liquid on the ideal surface.

If the equilibrium contact angle is large and there is significant surface roughness, the liquid may not penetrate fully into the lowest points of the surface and the Cassie-Baxter model[104] is used, which considers a heterogeneous surface with a fraction of air trapped underneath the droplet (Figure 2.12 b) [105]. In this case the apparent contact angle is defined:

$$\cos(\theta^*) = \sigma_1\cos(\theta_C) - \sigma_2 \tag{2.4a}$$

$$\cos(\theta^*) = \sigma_1(\cos(\theta_C) + 1) - 1 \tag{2.4b}$$

Here, the trapped air fractional area is σ_2, which equals to $1 - \sigma_1$, where σ_1 represents the fractional surface area of the solid. When the apparent contact angle is considerably greater than 90°, there is little contact between the liquid drop and the tips of the surface roughness and the drop can easily move across the surface. This is known as the lotus leaf effect or a superhydrophobic surface. [106] Note that these models are only applicable for droplet sizes which are significantly larger than the scale of the roughness or surface pores in the structure.

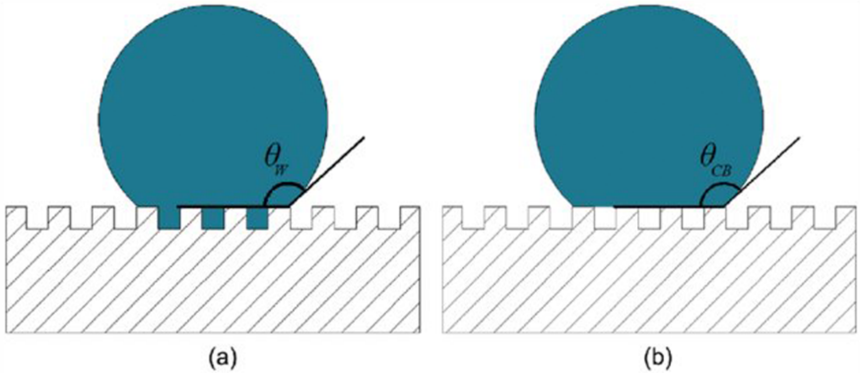

Figure 2.12 Wenzel model (a) and Cassie-Baxter model (b) [107].

Surface and liquid/solid interfacial energies are the major parameters that control the wetting between a fluid and a substrate [108]. The surface properties of textiles can be easily modified through a variety of surface coating and functionalising methods. Hydrophilic treatment contributes to the wetting ability of textiles, which is especially profitable for synthetic textiles that lack polarity in their chemical groups [108]. On the other hand, hydrophobic treatment have been widely applied for manufacturing waterproof garments to generate a repellent fluid interaction with textile surfaces [109].

Methods for hydrophilic treatment include polymer chain scission at the ester linkage, co-polymerisation to graft hydrophilic monomers and plasma treatment to introduce water compatible functional groups, such as -COOH, -OH and $-NH_2$ on the fibre surface [108]. The polymer chain scission of the polyester fabric produces hydrophilic chemical groups, which however reduces the mechanical strength of the fabric. Copolymerisation method of hydrophilic monomers is time consuming and expensive. Plasma treatment is one of the most environmentally friendly method that also maintain the properties of textiles [110].

For hydrophobic treatments, coating and laminating hydrophobic polymers such as synthetic rubbers, polyolefins, polyvinyl chloride, acrylic derivatives and polyurethanes [111] can achieve waterproof textiles with reduced breathability. Breathable-waterproof textiles can be achieved though applying a hydrophilic outer layer, eg. Polyvinyl alcohol (PVA), with water vapour diffusion ability or a microporous outer layer, eg. Polytetrafuoroethylene (PTFE) film or polyurethane.

To manufacture water repellent textiles that water drops can be easily removed from the fabric surface, surfactants are used to reduce the surface energy to provide hydrophobicity [112]. Fluoro-surfactant finishing (γ = 10-20 mN m^{-1}) on textiles leads to both water (γ = 73 mN m^{-1}) and oil (γ = 20-35 mN m^{-1}) repellence through reduced surface energy of the substrates, which provides performance superior to other conventional surfactants. Fluorine atoms are closely packed with carbon atoms forming strong carbon-fluorine bonds and a hydrophobic perfluorinated tail. The polar hydrophilic head is attracted towards the hydrophilic hydroxyl (-OH) groups from cotton as shown in Figure 2.13 [113]. It was found that surface energy decreases with increased the number of C-F bonds up to a critical chain length of $n = 9$ [114]. Additionally, the weak van der Waals forces leads to poor adhesion between the surfactant and the substrate. Thus chemical attachment such as fluorinated acrylates are used to react with -OH groups on cotton [115]. Nanoparticles can also impart the hydrophobicity of textiles or even superhydrophobicity as studied in Nano-Tex, where 10-100 nanometre ‘whiskers’ are attached to the cotton fabric [116]. However, fluorocarbon surfactants are not environment-friendly. Other hydrophobic alkyl acrylates and maleic anhydride copolymers have been developed to replace fluorocarbon surfactants [117]. Sivaramakrishnan et al. [112] summarised a list of available surfactants for textiles, and many of them are used during the pre-treatment of fabrics such as sizing, scouring, softening and dyeing. In addition to wet-processing surface treatments, plasma-based treatments through physical etching or chemical vapour deposition (CVD), cleaning or grafting save the use of chemicals.

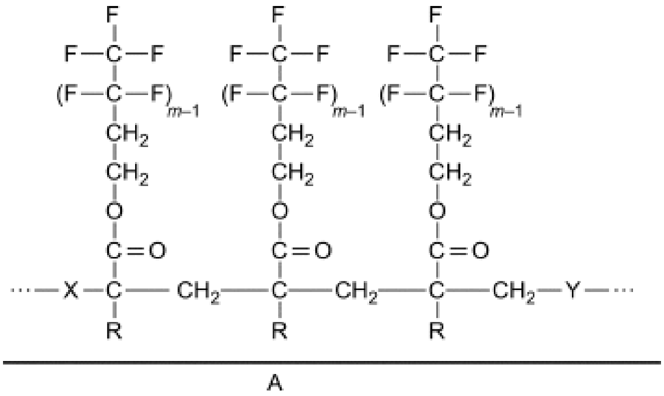

Figure 2.13 Fluorocarbon surface treatment on A fibre surface, where X and Y refer to comonomers such as stearyl acrylates, R = H or CH_3 (polyacrylic or polymethacrylic acid esters) [113].

It is not only the chemical composition of the fibres that influences the surface properties of textiles, the textile structure and roughness of the fibre surfaces also alters their wettability as illustrated by the Wenzel and Cassie-Baxter models. For example, Shim et al.[118] discovered that a liquid can completely wet fabrics made of hydrophobic polyester fibres in a woven structure. Additionally, it was found that hydrophilic woven fabrics with higher roughness increases the wettability of textiles [119,120]. Superhydrophobic surface treatment on textiles is mainly from biomimetic principles as the Lotus leaf effect[121], which are manifestations of the Cassie-Baxter model. Sol-gel methods can be used to produce hydrophobic porous nanoparticle thin films to be coated on textile substrates that leads to super-hydrophobicity [122]. Plasma etching can also be used to change the surface morphology and roughness so as to modify surface wetting [123].

In the field of printing on textiles, surface treatment is an essential step to control the wetting of functional materials on textiles. The wetting ability directly relates to the printing pattern quality, the functionality, and the adhesion of the products. For example, poly(ethylene terephthalate) fabrics with low surface-free energy lead to poor wettability, thus the printed patterns have poor colour yield performance and can easily bleed away. [124] Hydrophilic cotton fabrics can also be treated with oxygen plasma to enable better colour strength through increased hydrophilicity and roughness of the fabric surface. [125]

2.2.2.2 Wicking

Wicking occurs when the liquid wets a substrate that contains a fine scale porosity, for example the spaced between fibres within a fabric. Capillary forces are able to drive the liquid into these spaces. The resulting work of penetration comes from the different interfacial energies between the solid/vapour energy of the fibre surface and the solid/liquid energy between the liquid and the solid fibre, compared to the cohesion forces within the liquid. [11] It is a dynamic process with the fluid responding to a pressure difference across the fluid interface until reaching hydrostatic equilibrium. The Young-Laplace equation derived by Thomas Young and Pierre-Simon Laplace is used to quantify the pressure difference as shown in Equation (2.5) [100,126]. The pressure difference (ΔP) is related to the shape of the surface of the fluid, defined byR_1 and R_2, which are the principal radii of curvature of the surface and the surface tension (γ_{lv}), with

$$\Delta P = \gamma_{lv}\left(\frac{1}{R_1} + \frac{1}{R_2}\right) \tag{2.5}$$

For example, when the liquid is in a sufficiently narrow tube with a circular cross section as shown in Figure 2.14, the radii of the curved interfaces R_1 and R_2 equal to R, and R equals to the tube cross section radius a divided by $cos\theta$, and the capillary pressure can be written as shown in Equation (2.6).

$$\Delta P = \frac{2\gamma_{lv} cos\theta}{a} \tag{2.6}$$

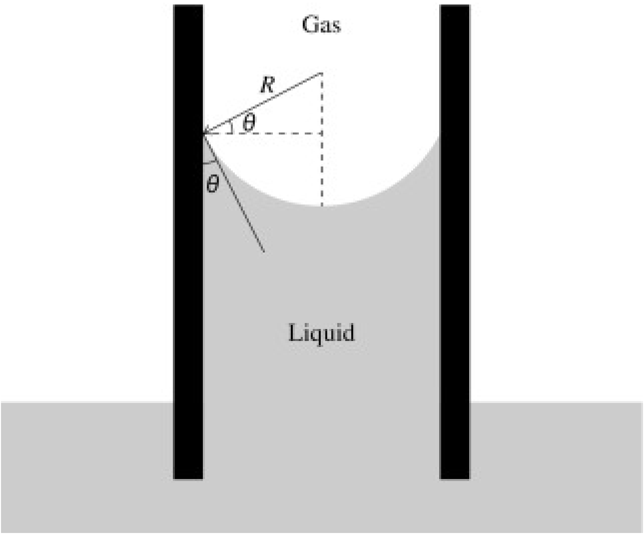

Figure 2.14 Capillary rise of a liquid in a hydrophilic tube with the radius of curvature R and the contact angle θ. [127]

When liquid transport occurs in yarns or fabrics, the phenomenon is known as wicking and is driven by these capillary forces generated by the pore structure. There are two different important pore length scales within a fabric, governed by the inter-tow spacing (yarn) and intra-tow spacing (fibre) which leads to different pore shapes and sizes within the fabric [128,129] Inter-tow spacing is governed by the yarn density and thickness, intra-tow spacing is related to the fibre thickness and density within the tow as well as the twist level [130]. The pores will also change due to swelling, heating or deformation when the fluids are transported in textiles and the fibres respond to the capillary forces [12]. There are also two different directions of wicking in textiles, which are trans planar and in planar wicking (Figure 2.15). Trans planar wicking ability in daily wear textiles plays an important role in sweating away the liquid from the skin, and in planar wicking can facilitate the evaporation of liquid from the fabric. [131] Moreover, the wicking can occur from a limited amount of liquid such as a droplet or from an infinite reservoir such as a pool of liquid. [132]

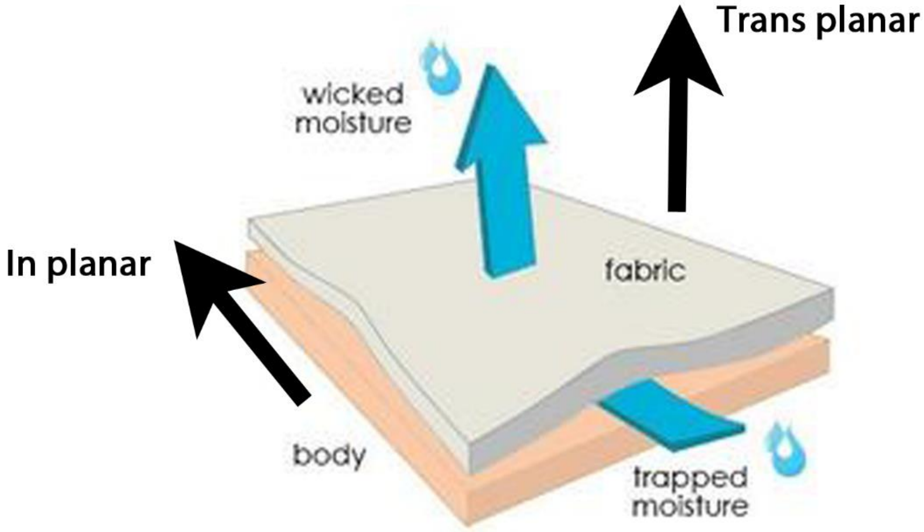

Figure 2.15 Trans planar and in planar fabric wicking for moisture transportation. [133]

As a consequence of the wide range of applications of textiles and the complexity of textile structures, theoretical analyses relevant for each phenomenon have often been developed without considering applications and equivalent modelling in related application fields. Here we consider the role of these interactions for inkjet printing ink on textiles, it is essential to consider each aspect of the liquid textile interaction mechanisms for a comprehensive understanding of the printing process. Wetting and wicking of ink on textiles are fundamentally two dynamic processes, thus, the spreading and penetration rates and heights are the two main field of interests of liquid and textile interaction. However, due to different length scales of fibre, yarn and fabrics which leads to different pore scales, as well as different liquid drop sizes, the analysis of the interaction mechanism is complicated [12]. There have been a large number of theoretical and experimental research studies reported in this field and a comprehensive review is given in this section.

2.2.3 Models of Interaction

2.2.3.1 Liquid/Fibre Interactions

The simplest liquid/solid interaction to consider within a textile architecture is that of a single liquid drop with an isolated cylindrical fibre. Liquid single fibre interactions are appropriate when small volume droplets land on fibre surfaces and the droplet radius is similar to the fibre radius. It is important to understand that the curvature of the fibre surface leads to important differences between the modelling of liquid/fibre interactions and liquid/ideal flat surface interactions. For example, the critical value of the spreading parameter used to define complete wetting on an ideal solid surface was found to be higher than zero for fibres. Brochard[134] introduced the critical value S_c, above which a liquid sheath structure of a droplet on a cylindrical fibre would form, with

$$S_c = \frac{3}{2}\boldsymbol{\gamma}_{\boldsymbol{LG}}\left(\frac{a}{b}\right)^{2/3} \tag{2.7}$$

where $\boldsymbol{\gamma}_{\boldsymbol{LG}}$ refers to the liquid/air surface tension, a is the molecular size and b is the radius of the cylinder.

When $S < S_c$, partial wetting occurs and considering an individual fibre as a cylinder and assume that the gravitational force can be ignored, three different interaction morphologies between droplets and fibres can be observed as shown in Figure 2.16 [135–137]. A barrel shape (Figure 2.16 i) was seen when the droplet volume is large or the contact angle is small, when a smaller drop is used or the contact angle value increases there is a transition to a clam-shell shape (Figure 2.16 ii). Finally, if there is more than one fibre present, a drop may bridge between two fibres (Figure 2.16 iii). The contact angle, defined by the Young's equation, quantifies the wetting behaviour of a liquid drop on a planar solid surface. The different geometry of fibres means that this approach is not possible and different approaches have been used to predict the equilibrium drop shape during interactions with a fibre.

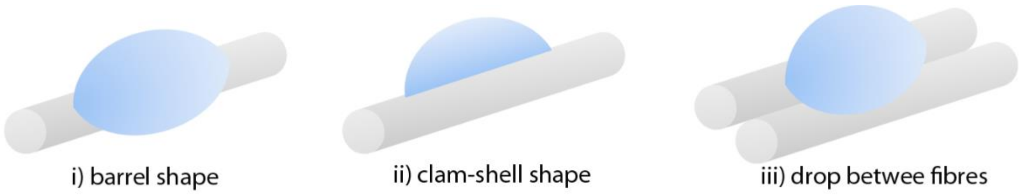

Figure 2.16 Three types of liquid droplet impact on an ideal cylindrical fibre [12].

Yamaki and Katayama [138] assumed that an equilibrium drop covering a fibre must have a constant Laplace pressure within the fluid and used a second order differential equation to define the barrel-shaped drop surface, assuming $\Delta P/\gamma_{lv}$ to be constant, giving.

$$\frac{d^2y}{dx^2} = -\frac{\Delta P}{\gamma_{lv}}\left[1+\left(\frac{dy}{dx}\right)^2\right]^{\frac{3}{2}} + \left[1+\left(\frac{dy}{dx}\right)^2\right]/y \tag{2.8}$$

This equation was solved numerically with the y_0, $[dy/dx]_{x=x_0}$ and x_0 at point C selected as the boundary conditions, where $y_0 = d/2$ (fibre radius), $[dy/dx]_{x=x_0} = tan\theta$, as shown in Figure 2.17 (a). Therefore, the drop spreading length l and drop deposition radius k can be obtained with a known contact angle θ, and conversely, the contact angle value can be obtained from measuring the drop shape on the fibre (Figure 2.17 (b)).

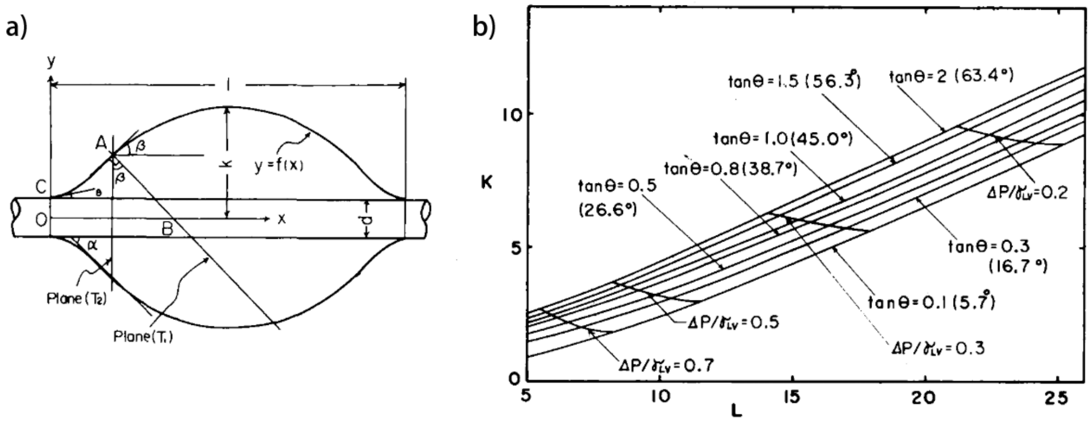

Figure 2.17 (a) Cross section of a barrel shape drop on fibre and its parameters, and b) the calculated nominated spreading length L as a function of droplet height K based on different contact angle and $\Delta P/\gamma_{lv}$ values, ref [138].

Later on, Carroll[139] introduced Legendre's standard incomplete elliptic integrals of the first and second kind based on Yamaki and Katayams's theory, where analytical expressions were derived based on the drop geometry and the calculation of droplet volume and surface area was extended. Then, Carroll and McHale [140,141] considered the droplet rolling up process from the barrel shape to the clam-shell shape and defined the critical inflection angle and drop thickness to fibre diameter values for the transition of conformation (Figure 2.18), in which McHale applied Finite element calculations (Surface Evolver) to determine the clam-shell shaped droplets based on the principle of minimising the surface free energy of the droplet conformation[135,136]. In Figure 2.18, x_f stands for the fibre radius and x_2 is the maximum drop radius, it is observed that fibre contact angle reduces with reduced drop radius or increased fibre radius, which means that smaller droplets contain higher wettability.[142] On the other hand, if the same volume of droplets is deposited, fibre surface with smaller contact angle values leads to higher wettability. Nevertheless, if small radius droplets land on thick fibres with a large surface contact angle, a transition from a barrel to a clam-shell morphology occurs[143].

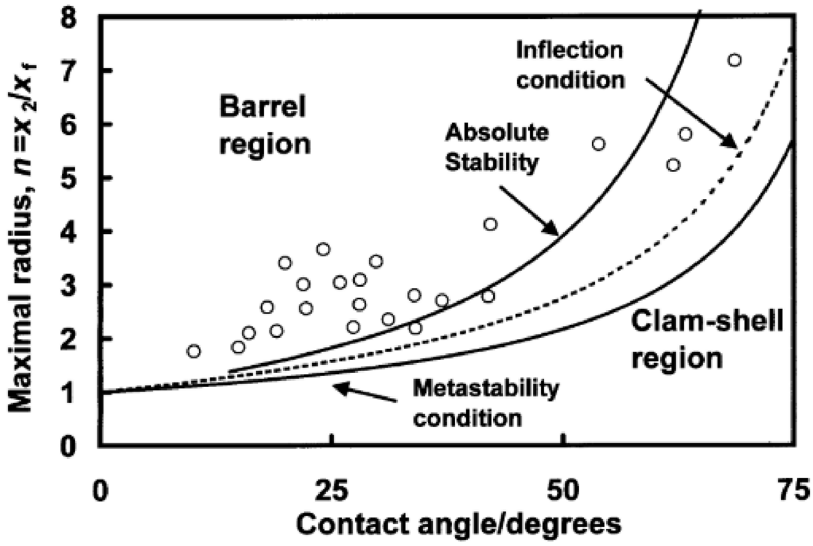

Figure 2.18 Regions of barrel shape and clam-shell shape depending on the contact angle values and the maximum drop radius, with the lines presenting the calculated regions and empty circle dots represents the experimental values, ref[135].

In reality, a fibre in a fabric is not an ideal isolated cylinder as described. Many hundreds of fibres may be present in close proximity and in partial contact with their neighbours within a yarn. Thus, a single drop is likely to interact with many fibres in close proximity. The shape of droplets landing between fibres has been studied first by Princen[144–146] and it was found that two types of liquid columns can form depending on the pore spacing between the fibres and the diameter of the fibres (Figure 2.19). This was further studied by Bedarkar et al. [137] through finite element analysis and experimentally by Duprat [147] and Protiere [148]. Detailed experiments were conducted studying the transition from a drop shape to a column by changing the fibre separation distance and the liquid volume, As the pore spacing/fibre diameter decreases, the drop evolves from a bridge between the fibres to a spread column. Moreover, it was found that on increasing the drop volume on parallel fibres, the droplet morphology transitioned from columns to bridges to barrel-shaped droplets. [149] Two critical common ratios of pore spacing/fibre diameter of √2 and 0.57 were found in many literatures, above √2 a drop forms, and when pore spacing/fibre is below 0.57, column shape occurs. The range in between (0.57-√2) leads to non-uniqueness of the drop shape, in which Protiere [148] reported the uncertainty rises when the ratio of drop volume to fibre radius increases reaching the value of $V/r^3 > 700$ (V stands is the drop volume, r is the fibre radius).

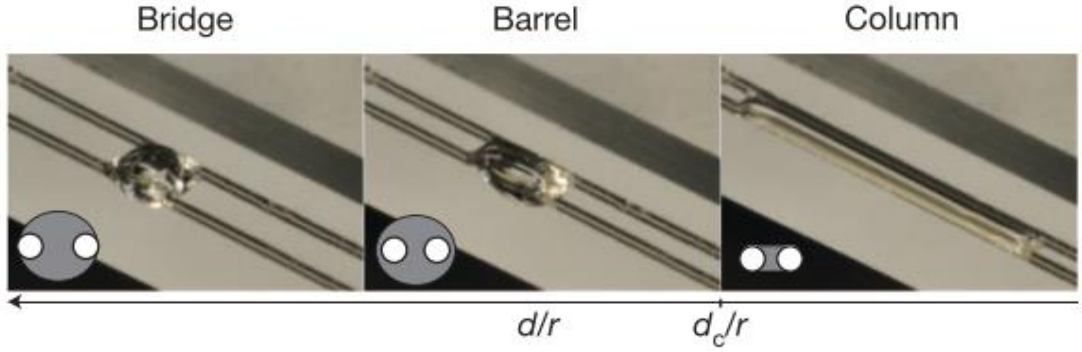

Figure 2.19 Drop formation of column, barrel and bridge when silicone oil of volume 2μl landing between two parallel fibres, ref [144] (in the figure 2d represents the pore spacing and r is the fibre radius).

It is clear that the contact angle can be determined from the drop shape when the droplet forms an axisymmetric barrel on a single fibre. However, in the cases when the droplet interacts in an asymmetric way, the droplet interacts with more than one fibre, and when elastic fibres deform under capillary forces, the drop shape becomes difficult to analyse and extract a contact angle. Liquid/fibre wetting plays an important role in defining the intrinsic surface properties of textiles, not only theoretical methods as mentioned above were used to measure the intrinsic fibre contact angle, but also experimental methods such as optical microscopy, environmental scanning electron microscopy and the Wilhelmy balance method were applied to measure the intrinsic contact angle of droplet on fibres. The microscope methods are based on direct imaging analysis, whereas the Wilhelmy balance method as shown in Figure 2.20, is based on a local force balance, represented by the Wilhelmy equation, where d represents the fibre diameter[150].

$$\cos\theta = \frac{F_{capillary}}{\pi d \gamma_{LG}} \qquad (2.9)$$

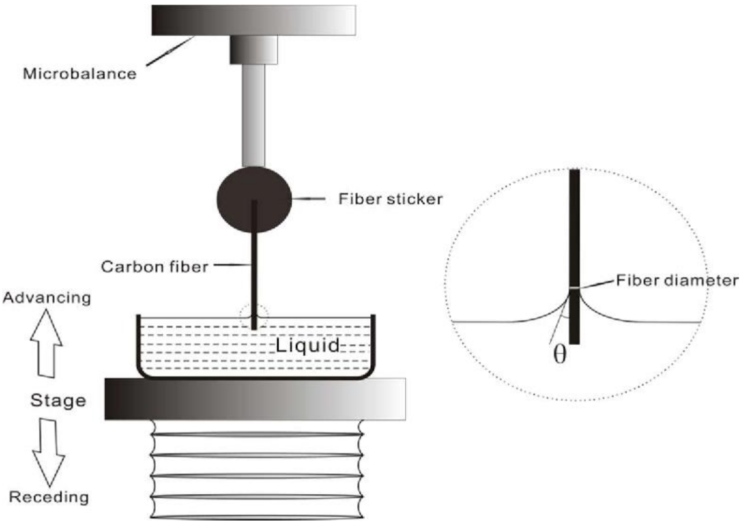

Figure 2.20 Schematic drawing of the use of a tensiometer to measure a single fibre contact angle using the Wilhelmy method, adapted from ref [150].

2.2.3.2 Liquid/Yarn Interaction

After a drop impacts on the surface of a fabric, both spreading and infiltration processes may occur. For small volume droplets, spreading on a single fibre, as discussed above may occur leading to no infiltration. However, for larger volume droplets or multiple coalesced droplets, interaction with more than one fibre will occur and infiltration is likely to happen. Drop volume, pore size, substrate wettability, fluid surface tension and viscosity could lead to different competition between these two processes. It is found that low substrate wettability leads to a Cassie state for a drop on a substrate, and droplets penetrates easier on hydrophilic surface with large pore sizes. [91] Additionally, increased fluid surface tension can assist the infiltration process. [151,152]

However, most studies of the dynamic process of liquid spreading and infiltration on porous substrates have focussed on a porous powder bed or consider liquid penetration solely along the direction of the fibre tows. The dynamic impact process of liquid droplets interacting perpendicular to the fibres which are bundled into yarns has not seen fundamental study. Instead, the dynamic process of liquid droplets imbibed in yarns has been widely studied as a wicking process, which is driven by capillary forces created by the pores between the fibres, as shown in Figure 2.21. To understand the ink-yarn interaction, two governing laws, the Washburn equation[153] and Darcy's law[154] can be used, providing a dynamic prediction of both liquid spreading and penetration in multiple filaments, considering the influence of the spacing between filaments and the fibre surface energy.

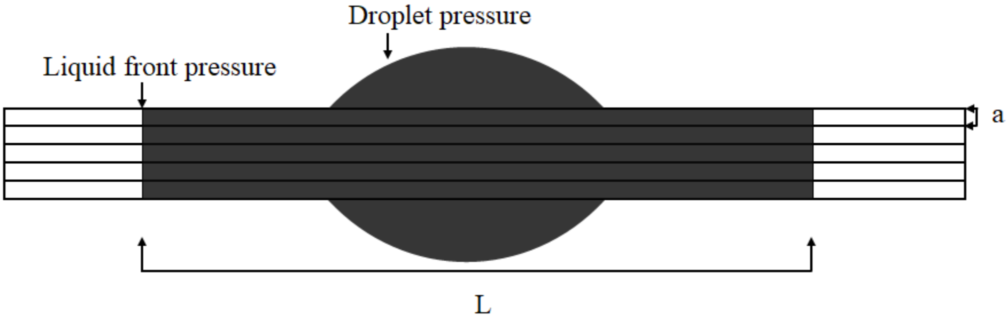

Figure 2.21 Schematic of liquid droplet wicking in yarn, adapted from ref [155].

Lucas-Washburn's equation considers the liquid absorption rate in porous materials due to the capillary pressure, as shown in equation (2.10). It predicts the drop penetration depth with time ($\frac{L^2}{t}$) as a function of ink surface tension (γ_{lv}), viscosity (μ), pore radius (r) and the contact angle ($cos(\theta)$). However, it is based on the Hagen-Poiseuille equation (2.11) [156] and Young-Laplace equation (2.12**)** [100] modelling incompressible, Newtonian and laminar flow in parallel cylindrical capillary tubes, which does not represent the actual internal architecture of many porous bodies [157]. Washburn equations have been used to study the liquid/yarn interaction, modifications to the equations have been introduced to provide more accurate predictions [66,141,147,155,158].

$$\frac{L^2}{t} = \frac{\gamma_{lv} r cos(\theta)}{2\mu} \tag{2.10}$$

$$Volumetric\ flow\ rate\ Q = \frac{dV}{dt} = \frac{\pi r^2 dl}{dt} = \frac{\pi r^4 \Delta P}{8\mu l} \tag{2.11}$$

$$\Delta P = \frac{2\gamma_{lv} cos\theta}{r} \tag{2.12}$$

Darcy's law, shown in equation (2.13), which is typically used to model the flow of liquids such as water flowing through porous geological media e.g. sand, illustrates the relationship between the flow velocity and the pressure drop. It describes the flow flux (q), which is the flow volume per time (Q) per area (A) and relates to the flow velocity (v) and porosity (φ), as a function of the permeability of the medium (κ), cross-sectional area of flow (A), and total pressure drop (ΔP), liquid viscosity (μ) and length of pressure drop (L). It has been used to model capillary flow in a variety of porous substrates [159,160].

$$q = \frac{Q}{A} = v\varphi = \frac{dl}{dt}\varphi = \frac{\kappa \Delta P}{\mu L} \qquad (2.13)$$

When the Laplace pressure is calculated for parallel cylindrical capillary tubes as shown in equation (2.12), Darcy's law can be integrated as in equation (2.14), where φ represents the porosity of the medium[161,162].

$$\boldsymbol{\frac{L^2}{t} = \frac{4k\gamma_{lv}\cos\theta}{\mu r \varphi}} \qquad (2.14)$$

Kozeny and Carman proposed the hydraulic radius theory to predict the permeability of a porous medium for use in Darcy's law [163], [164,165], [166]. K is an empirical constant related to fibre geometry, which introduces difficulties to evaluate the permeability of the yarn k (Equation (2.15)). [167–171] where $\emptyset$ represents the sphericity of the particles in the packed bed (Equation (2.16)).

$$k = \emptyset^2 \frac{\varphi^3 D^2}{K(1-\varphi)^2} \qquad (2.15)$$

$$\emptyset = \frac{\pi^{\frac{1}{3}}(6V)^{2/3}}{A} \qquad (2.16)$$

To allow for specific textile properties, such as the swelling effect, changes in the size of the fibre tows changes, modifications to the Kozeny Carman equation and Darcy' law have been investigated [161,172]. However, Darcy's law only considers saturated flow, whereas several studies have found that unsaturated flow phenomena often occur in liquids flowing in porous substrates [98,173].

Both these governing laws have been used to study liquid yarn interactions and both predict a faster liquid infiltration rate with increased pore spacing and liquid surface tension, and decreased contact angle values and liquid viscosity. More recently, a few studies of the equilibrium spreading length (the spreading length when the system reaches the stable state) of a liquid in yarn have been reported finding smaller spreading lengths in yarns with a highly packed fibre density, however, this behaviour varies when gravity is considered (Jurin's law) and when the packing geometry changes. [133,174–176,177]. Gravity is considered since the most common experimental setup for liquid wicking in yarns is observing the vertical wicking height and rate in yarns. In twisted yarns, high twist level generally reduces the wicking performance.[133] In twistless yarns, different shaped fibres as shown in Figure 2.22 were found leading different maximum liquid height, in which non-circular fibres with decreased pore spacing increases, due to the higher specific surface area of the fibres resulting in higher capillary pressure [174].

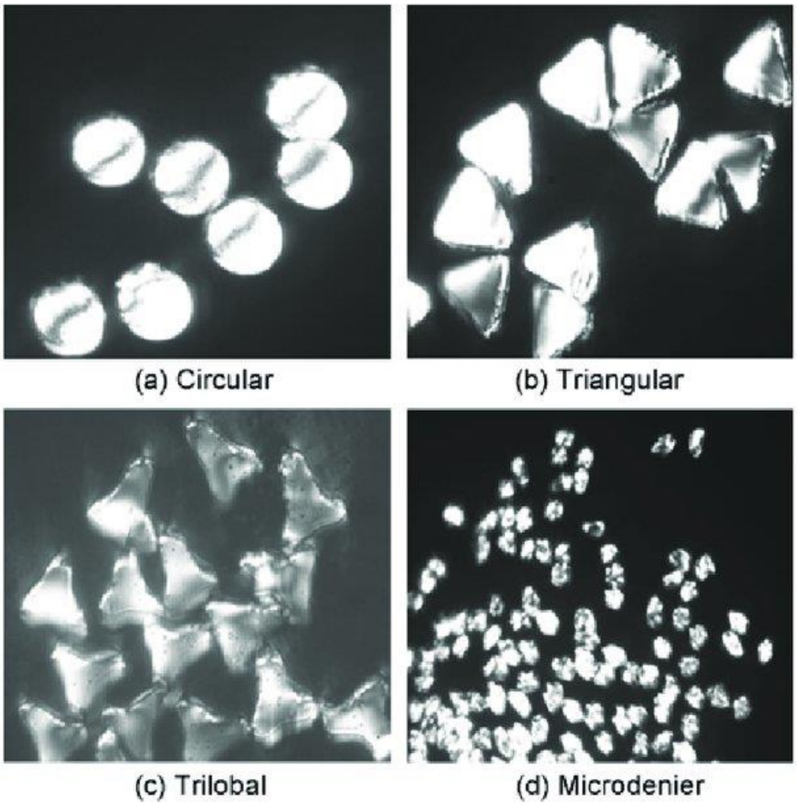

Figure 2.22 Cross sections of different polyester fibres, ref [178].

Despite these limitations, most experiments of liquid wicking in yarns were found to obey both the Washburn and Darcy's law [152], even though much effort has been dedicated to modifying these equations to match the theories with experimental values.

2.2.3.3 Liquid/Fabric Interaction

Prior studies of liquid transport in fabrics have mainly addressed fabric thermal and comfort control for personal wear, or the flow of resin in fibre assemblies for composites manufacturing [179]. However, when yarns are woven or knitted into fabrics, the porous structure becomes complicated considering the yarn density, size, and structures. Additionally, as a planar structure, both in-plane and through-plane liquid wicking mechanisms in fabrics are considered depending on their applications.

Common testing approaches for in-plane and through-plane wicking process are shown in Figure 2.23.

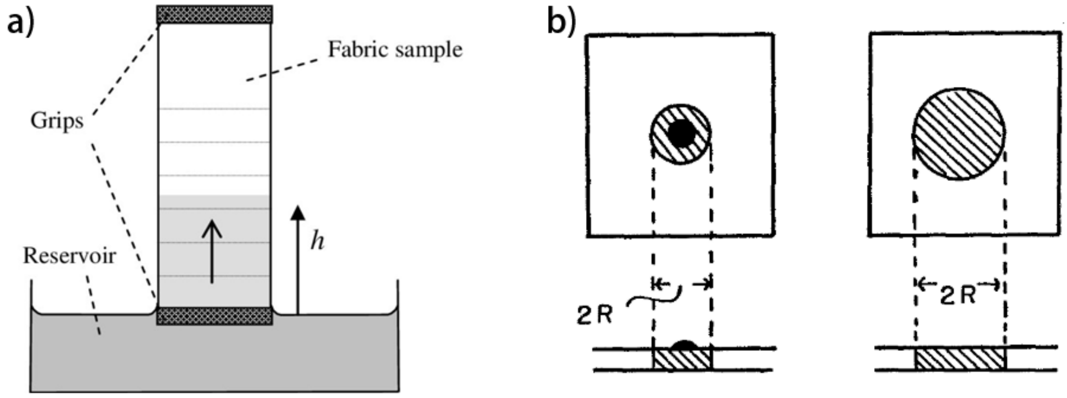

Figure 2.23 (a) Vertical wicking test set-up, ref [180] and (b) two stages in horizontal drop spreading, ref [181].

A typical in-planar wicking experiment with the weight gain as a function of time is shown in Figure 2.24. As soon as the fabric touches the liquid, weight gain increases immediately from wicking driven by the capillary forces that overcome the inertial, gravitational and viscous forces, until reaching the critical point (maximum absorption capacity). Evaporation could happen along the process and induces unsteady performance (Phase I) until the absorption capacity reaches the critical point and the steady wicking-evaporating stage (Phase II) occurs. Current models of fluid penetration into fabrics are based on a homogeneous porous medium approach using either the Washburn equation or Darcy's law. [10] For the in-plane wicking process, Yu and Lee [168] proposed a simplified one-dimensional analytical model to relate the permeability to the actual architectures of fibres, which showed good agreement with experiments. In addition, the fractal character of textiles was introduced, and the permeability modelled using this theory was also found through fitting the experimental results [182–184].

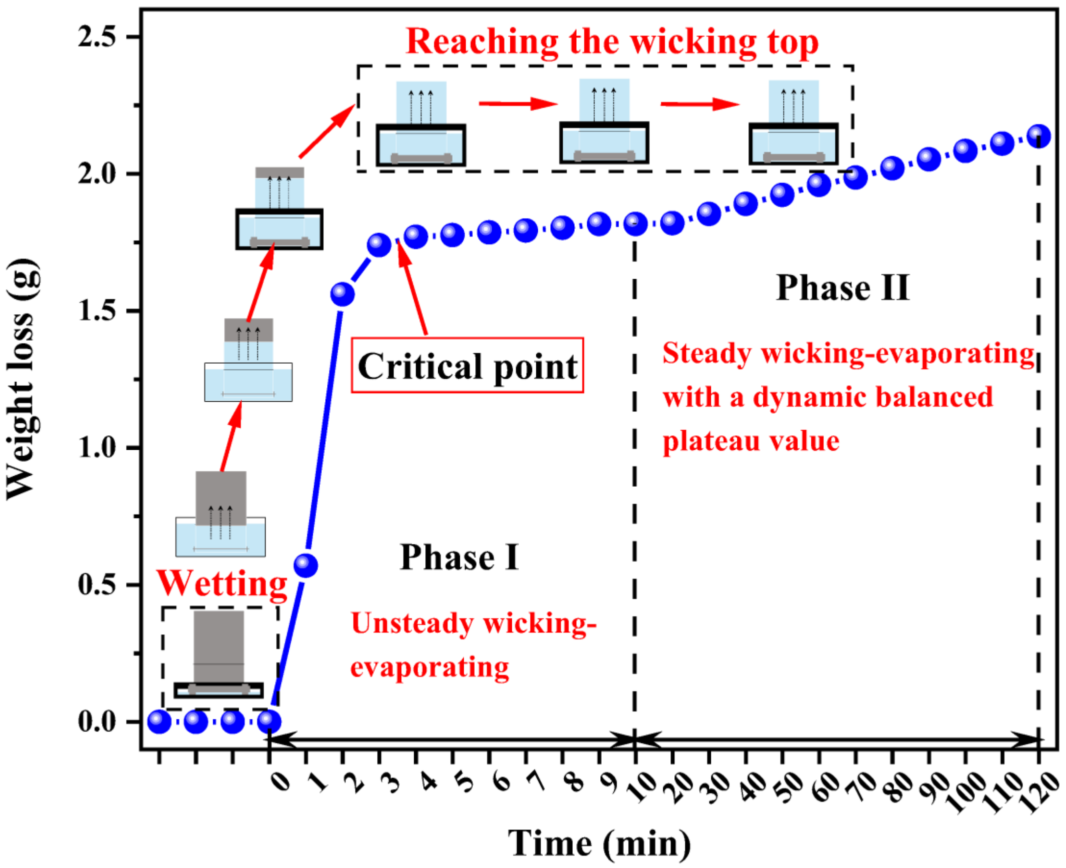

Figure 2.24. Typical curve of the wicking–evaporating process in woven fabrics within two phases, ref [174].

The through-plane liquid wicking process in fabrics plays an important role in printing on textiles. Theoretically, Gillespie[181] related the fabric thickness to Darcy's law to predict the radius of the spreading liquid, and Kissa[132] and Kawase[132] adapted the equation further to determine the liquid spreading area rate. Practically, researchers have studied the effect of the pore size and size distribution in the fabric on the fluid transport behaviour. It was found that smaller and interconnected pores lead to longer and faster liquid transport during fabric sorption, however, the capacity of liquid intake depends on the overall porosity of the fabrics. [11,185–187] It was also observed that in knitted fabrics, faster wicking occurs in coarse yarns [11], while thinner yarns with an overall more open fabric structure lead to an increased liquid transport rate in woven fabrics.[188] Different woven structures have been studied and it was found that interlacing points between yarns can decrease the liquid transfer in the fabric wicking process.[189]

Most of the above studies are based on the study of relatively large quantity of liquid depositing on fabrics. There have been a few studies on the effect of inkjet printed liquid drops on fabrics. In 2006, Park et al. discussed the effect of printing direction, weave structure and the surface finishing of textiles on printed image quality. Better image quality was found when printed along the warp yarn direction, and an acrylic resin finish and alcohol-based ink with a fast solvent evaporating rate contributed to better printed image quality [190]. In 2010, another detailed analysis was reported by Mhetre et al. showing inkjet printed lines on different fabric substrates (Figure 2.25), and it was observed that cotton fabrics gave the least average sideways wicking length, yet the print was still irregular and inhomogeneous. On polyester fabrics, the printing quality alters with the direction of the yarns. [191]

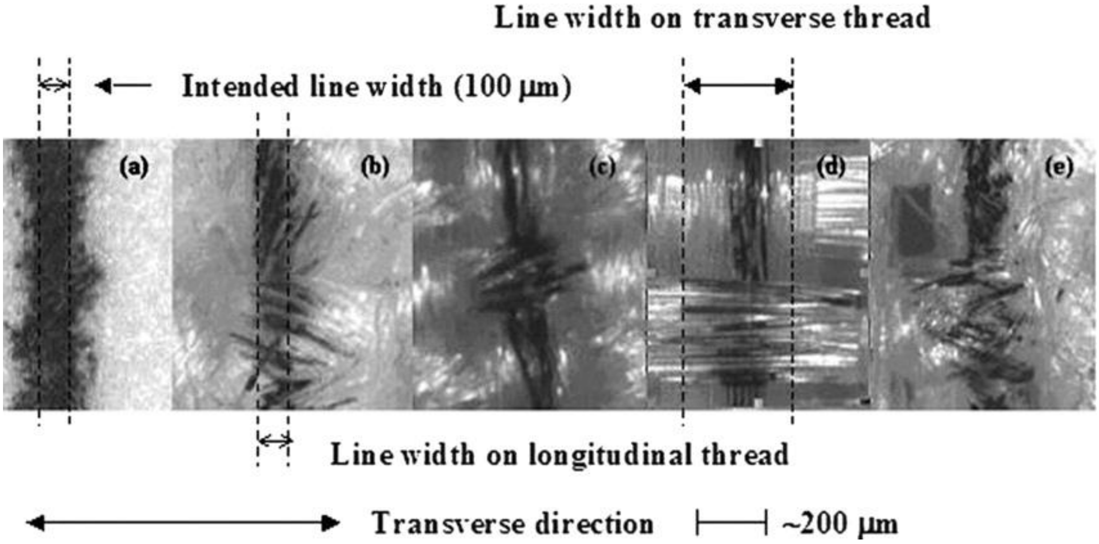

Figure 2.25 Microscopic images of lines on (a) paper, (b) cotton, (c) PET 88 fabric, (d) PET tape fabric, and (e) sized PET fabric.

In general, the research for the optimum capillary size for the optimum wicking performance of liquid in fabrics remains an open-ended topic [186,192,193]. Real textile structures show inhomogeneous pore distributions with larger scale pores from the arrangement of the yarn in the weave and minor micron-scale porosity from the fibre spacing within the yarn. The complexity and the variability of fabric structures requires further understanding of the liquid interaction within it, and this project will focus on the interaction mechanisms of inkjet printed ink droplets on woven textile structures.

2.3 Inkjet Printing Technology

Printed materials are closely related to our daily life, from graphical newspapers or packaging to functional materials with industrial applications ranging over electronics, textile, ceramics, and biomedical engineering [5,9,194–197]. The printing process creates a pattern on a substrate, and the techniques used have evolved and expanded from the earliest woodblock printing to methods such as lithography, gravure, screen printing, flexography, and inkjet printing [198]. Of these, inkjet printing is a relatively new technique, and provides contactless printing with an enhanced customisation ability without the need of physically changing masks or screens. This can simplify the production process and provides cost-saving through reduced materials wastage [195,199].

The development of the inkjet printer can be traced back to the nineteenth century when Lord William Kelvin proposed the "Siphon Recorder" with the use of electrostatic force to steer ink droplets [200]. Lord Rayleigh analysed the instability of liquid jets and the mechanism for the formation of drops through minimising their surface area.[201] The technology was then extensively developed since the 1950s, first for the plotting of experimental charts before the development of the continuous inkjet (CIJ) printers to drop-on-demand (DOD) printers for product marking and text printing, with continuing improvement on printing quality and productivity[202,203]. Nowadays, inkjet printing has become one of the most versatile printing techniques, and it is studied in this project since it meets promise as a manufacturing tool for printing large area electronics on a range of flexible substrates such as displays, sensors, energy storage devices and interconnectors. Many challenges still remain to be overcome and include, but are not limited to: ink formulation, droplet generation, nozzle clogging, interaction between ink droplets and substrates[194,195,199] and the performance of printed electronics [5,33].

2.3.1 Drop Generation

There are two distinct mechanisms of drop generation used in inkjet printing. These are generally described as: continuous inkjet printing (CIJ), which generates drops around 100 μm in diameter, and drop-on-demand printing (DOD), which produces smaller drops typically in the range 20-50 μm) [204]. With CIJ, the ink is forced at high pressure through a small nozzle, where the Rayleigh instability[201] breaks the stream of ink into small droplets (normally promoted through a synchronising vibration) providing a high rate of droplet ejection (20,000-60,000 droplets/s) with drop velocities > 10 ms^{-1}. The drops are electrically charged at generation and their trajectory controlled by applied electrical or magnetic fields. Normally deflected droplets land on the substrates in a desired location, while undeflected drops land in a gutter to be recycled.

With DOD individual droplets are ejected on demand in response to mechanical or thermal actuation, with drop location controlled by mechanically moving the printer nozzle or substrate as required (Figure 2.26 (a)). This eliminates the complexity of drop charging and deflection hardware as well as the inherent unreliability of the ink recirculation systems. However, DOD operates at a lower droplet production rate (1,000 - 20,000 droplets/s/nozzle) than CIJ and produces drops with a lower velocity < 10 ms^{-1}. To eject the droplet, DOD mechanically excites a small volume of fluid in a small reservoir immediately behind the printer nozzle. This generates a pressure wave that ejects the drop when it reaches the free surface of the ink in the nozzle. The pressure wave can be generated by piezoelectric, electrostatic (Figure 2.26 (b) and acoustic actuation, or by thermal excitation (Figure 2.26 (c) where a small volume of ink is rapidly heated to form a vapour bubble that subsequently collapses. Thermal inkjet is simpler and cheaper to fabricate, while the range of ink is limited by the vaporisation conditions required, indeed most commercial desk-top inkjet printers use thermal actuation. For industrial scale printing and most applications in printed electronics, piezoelectric DOD is preferred because it is compatible with a wider range of inks and it is relatively easy to control the drop size and the velocity [194,195,204–206].

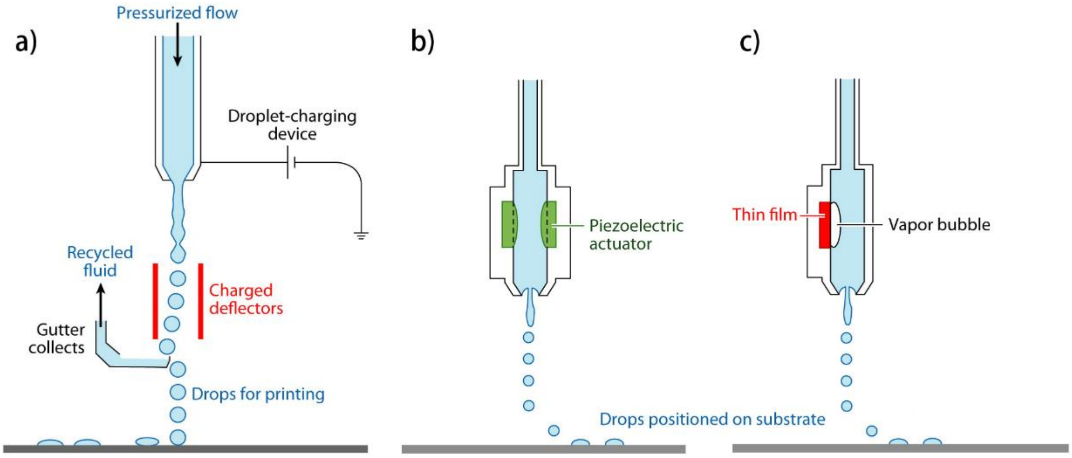

Figure 2.26 Schematic diagram showing the principle of CIJ (a) and DOD inkjet printing system with piezoelectric actuation (b) and thermal actuation (c), adapted from ref [194].

When ink travels from the nozzle to the substrate during DOD printing, a characteristic drop morphology of a leading drop with an extended fluid tail is formed (Figure 2.27) [194]. The elongated tail is often not stable and through the Rayleigh-Plateau instability the tail may break up into a train of drops [207]. They often catch up with the leading droplet; otherwise, satellite droplets would form and can influence the printing quality. Air currents from the environment also affects the droplet trajectory, thus the distance between the ink ejection to the substrate is normally minimised [194].

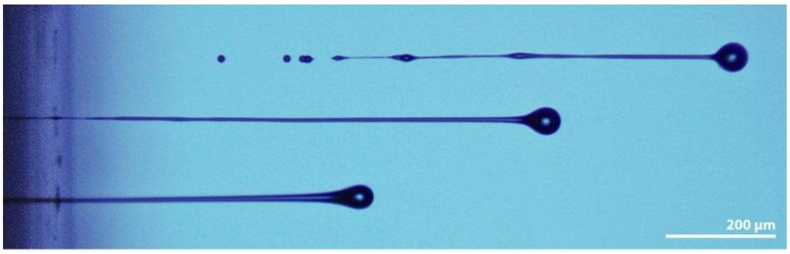

Figure 2.27 Drop generation process in a DOD printer: from an ejected liquid column with a leading drop (bottom), to an elongated thin liquid tail (middle), to the formation of tail droplets (top) [204].

2.3.2 Printable Inks

In addition to the printer settings, the ink physical properties play a significant role in controlling droplet generation. Printable inks require the formation of stable individual droplets, and this can be evaluated through the following dimensionless numbers that relate appropriate properties: balance between inertial and viscous forces - Reynolds number (*Re*) [208], balance between inertial and capillary forces - Weber number (*We*) [209] and balance between capillary and viscous forces - Ohnesorge number (*Oh*) [210] with:

$$Re = \frac{\nu\rho\alpha}{\eta}, \tag{2.17}$$

$$We = \frac{\nu^2\rho\alpha}{\gamma}, \tag{2.18}$$

$$Oh = \frac{\sqrt{We}}{Re} = \frac{\eta}{\sqrt{\gamma\rho\alpha}}, \tag{2.19}$$

where ν, α, ρ, η and γ refer to the velocity, drop diameter, density, viscosity and surface tension of the ink respectively. A minimum fluid velocity for drop ejection is required to overcome the energy to form the area of a drop which leads to $We > 4$ for printing [211]. The parameter $Z = 1/Oh$, was identified by Fromm [212] as being a characteristic for the drop forming process and it has been proposed that this needs to be in a range of 1 to 10 to allow stable droplet formation range [212], as shown in Figure 2.28. The lower bound to *Z* indicates the viscous limit for ink ejection, and the high *Z* threshold indicates a transition to a large number of satellite drops [194]. It has also been suggested that a drop impact splashing threshold occurs at $We^{½}/Re^{¼} > 50$ [213]. However, the above fluid property limits only apply to Newtonian fluids; thus other factors such as their viscoelastic properties need to be considered when printing non-linear polymer solutions or dispersion of particles [214,215].

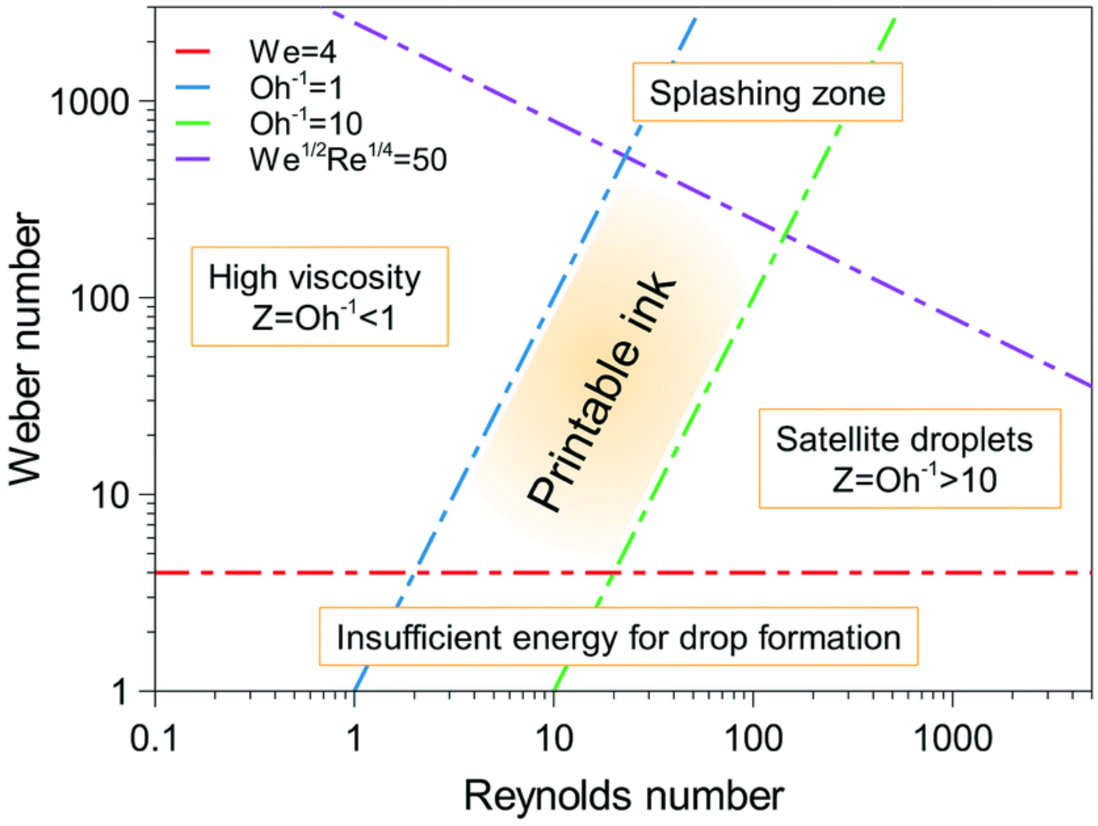

Figure 2.28 DOD inkjet printing regions, defined by the Reynolds and Weber numbers, adapted from ref [216].

2.3.3 Drop Impact and Surface Interaction

The ink drops with a given velocity impact on the substrate during printing. The physical processes that control the interaction are inertial forces, capillary forces and gravitational forces [194]. In inkjet printing, the density of fluids is around 1000 kg m^{-3}, the surface energy is below 0.1 J m^{-2}, and the drop diameter is < 100 μm, thus the Bond number (measuring the importance of the gravitational force compared to the surface tension force) is $\ll$ 1, which indicates that gravitational forces can be neglected when compared with the capillary forces [194]. The initial ink drop interaction with the substrate can be either impact-driven (inertial force domination) or capillary-driven (capillary force domination) [217], until the equilibrium contact angle is reached [218]. The sequence of these processes is shown schematically in Figure 2.29 [194]. Splashing, receding, rebounding, spreading and deposition are the possible outcomes beforehand [219].

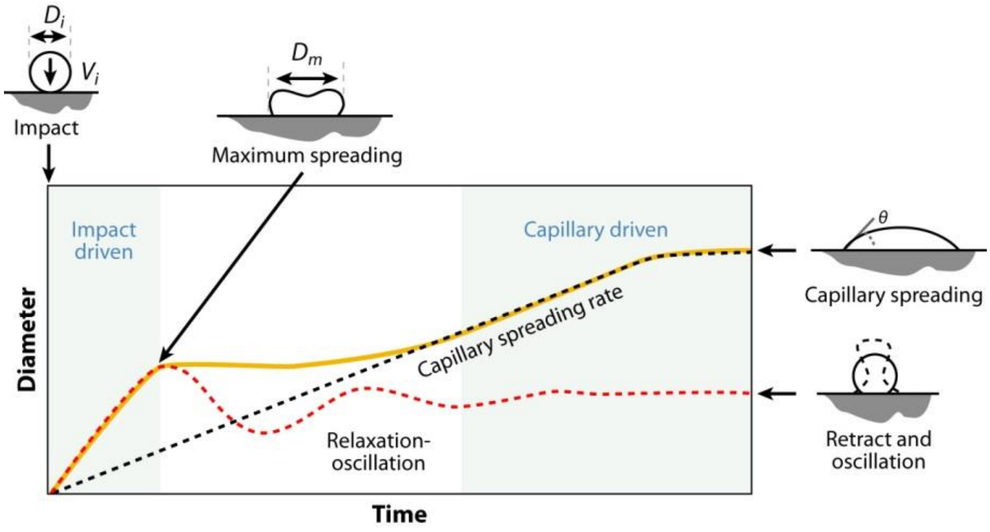

Figure 2.29 Droplet impact events on a substrate, D_i and V_i refer to the initial drop diameter and velocity, and D_m is the maximum spreading diameter. Provided by Dr. H.K. Hsiao, institute of Manufacturing, University of Cambridge [194].

The interaction is dependent on the properties of the ink and the surface. A drop reaching the substrate with increased kinetic energy leads to slightly faster spreading, yet the same spreading ratios were obtained [99]. The surface tension of the ink showed no effect on spreading and relaxation phases, but the speed of expansion and the final spreading factor were changed; the effect of viscosity showed opposite behaviours [99,220]. However, it was also found that a lower surface tension leads to greater spreading and weaker recoil, while higher viscosity slows down both spreading and the recoil process [221]. The Weber number which indicates the ratio between the inertial force and the surface tension force can be used to determine drop behaviour is the impact driven (high Weber number) or capillary driven (low Weber number)[217]. It was also found that DOD printing leads to a relatively inviscous drop with impact driven behaviour in the initial stage [217], as shown in Figure 2.30. In which case, the contact diameter of the deposited drop (d_{con}) for inkjet printed drops can be calculated through Equation (2.20), where the shape of the spread drop is assumed as a segment of a sphere. d_{con} is shown to be proportional to the diameter of drop in flight (d_0) and inversely related to the equilibrium contact angle (θ_C). In general, the surface tension of a droplet during spreading is not fully stable, and the effects from the substrate wettability and roughness need to be considered. There have been many have numerical and experimental studies of these effects on spreading, yet no simple conclusion could be made due to the large number of variables involved [222,223].

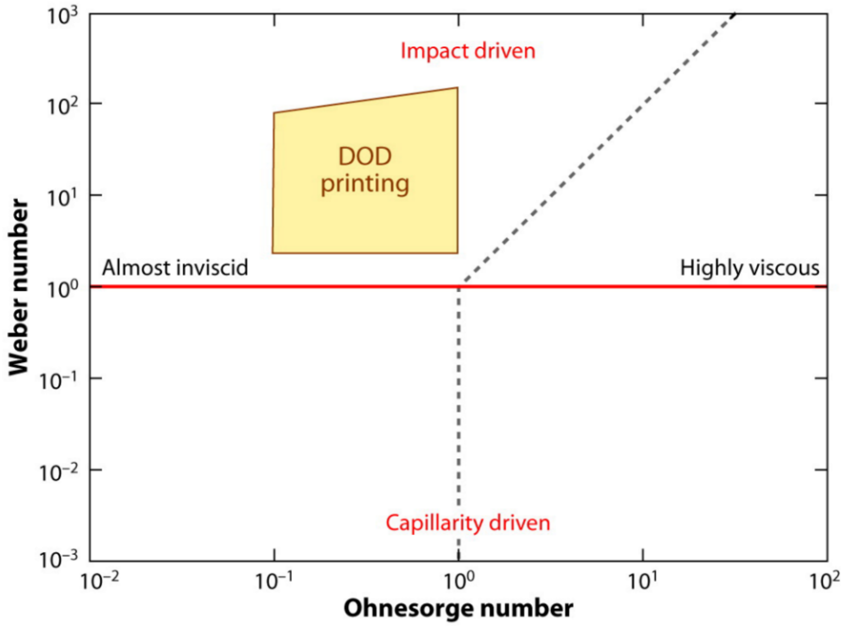

Figure 2.30 Driving force for initial drop spreading after impact defined by Oh and We numbers, with DOD inkjet printing condition highlighted, adapted from ref [194]**.**

$$d_{con} = d_0 \sqrt[3]{\frac{8}{\tan\frac{\theta_C}{2}\left(3+\tan^2\frac{\theta_C}{2}\right)}} \tag{2.20}$$

When more than one inkjet printed droplet lands on the substrate, liquid beads can form through the overlap and coalescence of adjacent droplets. However, to form stable lines, greater hysteresis in the contact angle (difference in advancing and receding contact angles) with a low value of the receding contact angle is essential. Moreover, to avoid bulging instability in lines, sufficient droplet spacing and traverse speed are necessary [224–230]. Figure 2.31 shows results from a study of Soltman and Subramaian [224] with four liquid bead morphologies forming under different conditions of drop spacing and printing traverse speed, with only Figure (c) achieving a parallel-sided bead.

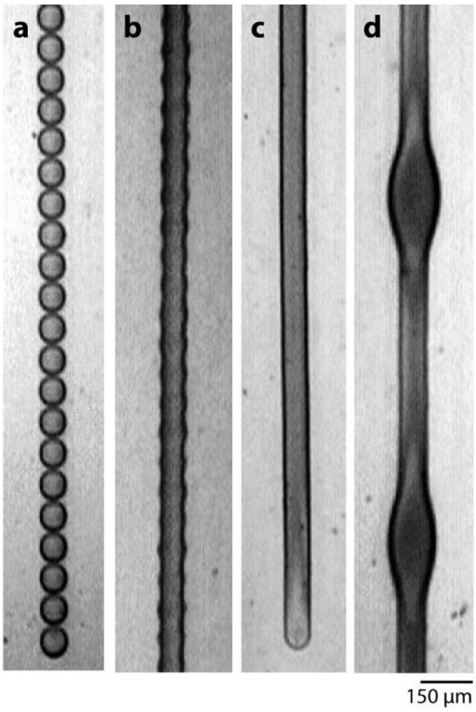

Figure 2.31 (a) excessive drop spacing for drop coalescence, (b) initial drop coalescence to form periodically irregular liquid bead, (c) sufficient drop coalescence to form stable and parallel-sided bead, (d) building instability in bead due to small drop spacing, ref [224].

2.3.4 Drop Solidification

During the drying process, the shape of the printed drops may change and result in non-uniform ink deposition. Under certain conditions the particles in the dispersion flow towards the pinned edge or contact line, resulting in the coffee ring effect[231]. This occurs if the contact line is pinned and is a consequence of the need to replenish the thinner regions of the drop with fluid to maintain the pinned contact line. Marangoni flows, caused by the change in surface tension during ink drying, can reduce the coffee stain effect [224,232,233], as shown in Figure 2.32.

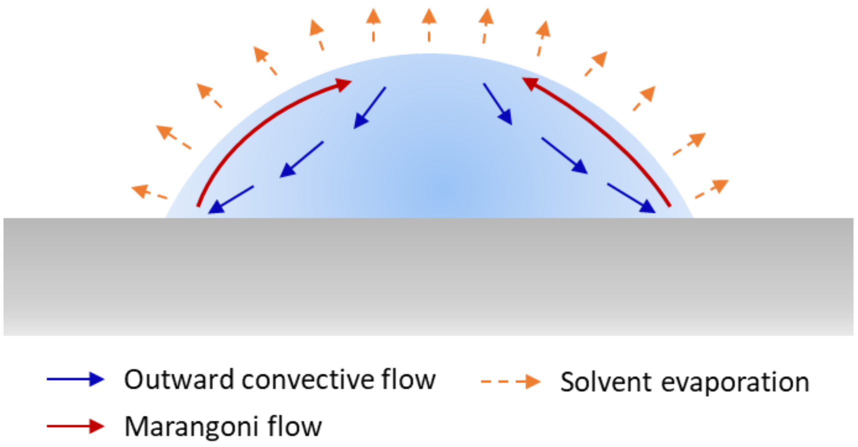

Figure 2.32 Droplet drying process involving solvent evaporation (yellow arrow), outward convective flow (blue arrow) and Marangoni effect (red arrow).

On porous substrates, drop spreading, fluid absorption and evaporation must all be considered during the drying process, which can lead to different deposition behaviours. As shown in Figure 2.33, Dou and Derby [234] found that when the pores are smaller than a critical size, evaporation occurs as on a solid surface. With increasing pore sizes, reduced evaporation leads to reduced Marangoni flow and the coffee ring effect occurs. When the pore size is increased larger than a critical point, penetration dominates without filtration, and the coffee ring effect is eliminated. Pack et al. [235] studied the drying of single-solvent colloidal drops at the picolitre scale on nanoporous substrates. with the particle size in the solvent larger than the pore size. The relative time scales of the particle moving to the contact line (t_p) and the evaporation time of the residual drop (t_{EI}) determines whether a coffee-ring forms (when $t_p/t_{EI} < 1$).

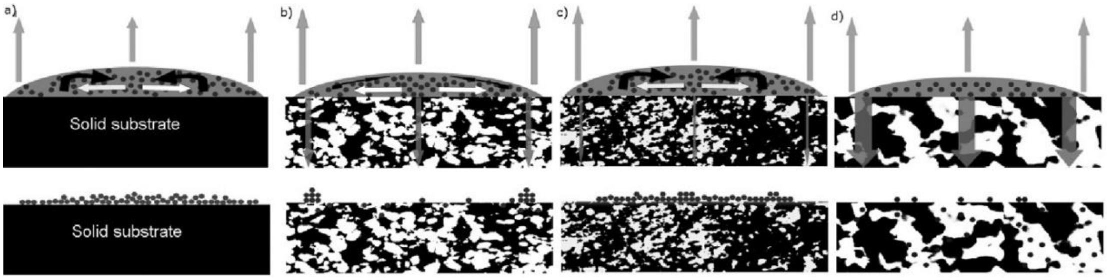

Figure 2.33 Conductive ink evaporation process with the effect of different pore sizes [234].

It is clear that drop impact, absorption and evaporation may have similar time scales on porous substrates. Ink properties, pore sizes and distributions are the important parameters effecting the drop deposition behaviour. There has been a large amount of studies in this field, however many simplifying assumptions are used in these studies and experimental techniques for observing the interior structures of fluids in porous substrates require higher resolutions.

From considering the above studies on inkjet printing technology, the low viscosity inks required and the complicated drop impact and sorption processes make it difficult to fully analyse the process of inkjet printing on textiles. The low viscosity inks are easily wicked and can spread some distance from the drop location in the fabric, reducing the printing quality Also, the uneven and porous textile surface can vary the deposition and evaporation process of inkjet printed textiles. Inkjet printing on textile substrates has been widely used in the fashion industry with colouration pigments [236]. The pre-treatment of textiles and the development of inks have been studied as solutions to achieve optimal printing quality on textiles. [7,54,237] However, a very limited amount of research has been conducted to understand the fundamental interaction of inkjet printed inks with textiles.

2.4 Inkjet Printing Conductive Electronic Textiles

2.4.1 Background

The advantages of inkjet printing such as its high printing resolution, allowing rapid response for changing designs, and relatively low cost for machine set up makes it an outstanding candidate for prototyping and manufacturing printed electronics. With the success of inkjet printing pigment inks on textiles, and the unique wearable properties of textiles, inkjet printing electronic textiles have attracted an enormous amount of attention for the wearable technology field from researchers and industries. [6,8,9,39]

However, it is well-known that there are difficulties in achieving continuous patterns on textile substrates with this method. This is mainly due to the high porosity level and uneven structure of the textile surfaces, which leads to different dynamics in the spreading, absorption and drying of ink in comparison with existing theoretical models developed for printing on solid polymeric films [8]. Additionally it is not clear that existing inks are fully optimised for use with textile surfaces because the ink properties (e.g. rheology and surface tension) are defined by the requirements of inkjet printing without consideration of their properties on a given substrate [238].

The study of printing functional inks on textiles is relatively recent and significant research only started in the 21st century. Researchers have studied a wide range of textile substrates and have applied a variety of textile treatments to study the behaviour of printed conductive inks [1,239]. In the meantime, a number of functional materials have been successfully formulated into printable inks to manufacture active, passive and electromechanics printable wearable electronics [1,4,59,240]. Current research progress will be considered and reviewed in this section, and will focus on the use of conducting materials, which not only play an essential role in different electronic systems, but also provide connections between the components.

Table 2.2 Recent research on inkjet printed conductive textiles.

Materials	Application	Electrical Performance	Comments	Ref
Silver NP ink	Antenna	1 *10^6 S/m	15µm, 2 layers, PU interface layer	13
Silver NP ink	Tracking device	1.85*10^6 S/m	Interface layer, 6 layers	241
Silver NP ink	Interconnector	2.9 Ω/sq	CNF coating, 3 layers	15
Reactive silver ink	Capacitors, heating actuators, antennas, transmission lines	0.016 Ω/sq	8 layers	242
Reactive silver ink	Interconnector	0.09 Ω/sq	15 layers, insitu	2
Reactive silver ink	Interconnector	2.3 Ω/sq	10µm, 4 layers, 50 ºC	14
rGO	ECG	2.14*10^3 Ω/sq	Pre-treatment, 6 layers	1
PEDOT:PSS	Interconnector	3185.7 Ω/sq	10 layers	243

*NP: nanoparticles; PU: polyurethane; rGO: reduced graphene oxide; ECG: electrocardiogram.

With the rapid development of wearable devices, it is surprising that there are only a limited number of journal papers with a focus on inkjet printing conductive inks on textiles**.** Table 2.2 lists some of recent development of this research topic with a range of applications. The electrical performance in above papers is comparable with other reports in the literature for conductive devices on flexible substrates, yet it is obvious that multiple printed layers have been applied in all the papers in the table, highlighting the deficiency of the low concentration inkjet printing inks and the effect of deposition on rough textile substrates on the electrical performance of conductive textiles. Apart from printing multi layers of ink on textiles, the use of interface layers or pre-treatment of textiles shows enhancement of the electrical properties of conductive textiles. Additionally, Stempien et al.[244] compared the electrical performance of inkjet printed reactive silver ink on different fabric substrates, and the lowest sheet resistance value was found in plain woven polyester fabrics.

Interestingly, electrical performance of conductive textiles is characterised in different units: electrical conductivity (S/m) and sheet resistance (Ω/sq). Electrical conductivity is the reciprocal of the resistivity, and the resistivity equals to the sheet resistance times the film thickness. Nevertheless, the measurement of sheet resistance requires samples in uniform thickness, which is not appropriate for use with textiles as the conducting material can be absorbed into the fabric architecture and is not present as a sheet on a flat substrate. Furthermore, conductive inks play an important role in the electrical performance of textiles, and the details of printable conductive inks will be discussed in the following section.

2.4.2 Printable Conductive Inks

Polymer-, carbon- and metal-based inks are commonly used to form conductive patterns, where metal-based inks show the highest electrical conductivity while polymer and carbon-based inks present better mechanical properties [212]. Moreover, hybridisation of conducting inks, which combines the advantages of different ink types, has been found attractive. For example, Song et al. printed Ag/graphene oxide hybrids and observed a greatly enhanced electrical conductivity from the Ag nanoparticles coupled with good mechanical properties contributed by the graphene oxide [240].

The polymer poly-(3,4-ethylenedioxythiophene) (PEDOT) that contains dioxyalkylene bridging groups shows high conductivity. However, due to its low solubility, it is often doped with polystyrene sulfonate (PSS) to obtain a stable dispersion in water for improved printability but with reduced conductivity [245]. Adding solvents such as dimethyl sulfoxide (DMSO) and tetramethylene sulfone (TMS) have been found to be an effective method for increasing the conductivity of PEDOT/PSS through weakening the interactions between the PEDOT and PSS chains [246].

Carbon-based conductive materials such as carbon black, carbon nanotubes and graphene exhibit high conductivity, good mechanical properties and chemical stability. The challenge for their use in conducting ink applications lies in their poor dispersion in many common solvents primarily on account of their hydrophobic character. This can be resolved through adding surfactants or other stabilising chemicals, although their conductivity can be reduced [4]. Thus, high-temperature post-deposition treatment of these inks is normally required to achieve optimal electrical conductivity. Solvent exchange methods can be used to replace high boiling point solvents with those more compatible with printing [247]. Alternatively, hydrophilic graphene oxide (GO) containing functional groups can be used form stable dispersions in many common solvents, e.g. water [248]. To improve the conductivity and stability of GO, reduced GO has been used in inks and applied on textiles [249, 250, 251, 252]. However, the remaining unreduced oxygen functional groups on reduced GO limit its conductivity [253,254,255].

Metal-based conductive inks present the best conductivity compared with the previous mentioned materials. Silver (Ag) is commonly used in electronics printing owing to its chemical stability and low resistance to oxidation during manufacture and service. However, metal nanoparticles are likely capped with protecting non-conducting polymeric agents introduced to avoid agglomeration during processing. Thus, as with carbon based inks, thermal annealing is normally required to achieve high conductivity by removing the capping agent and promoting interparticle sintering, and this may limit its applicability to certain substrates [4]. Therefore, different methods have been explored to reduce the temperature required to promote conductivity after printing. For instance, low-temperature post-processing methods that involve high intensity ultra-violet (UV) illumination [256], microwave [257] and plasma sintering [258], or adopting reactive inks [45,259]. Additionally, using a hot plate simultaneously heating up the substrate while printing facilitated higher electrical conductivity at lower sintering temperature [242,260]. Chemical sintering agents such as HCl were found to increase the contact probability between silver nanoparticles through oppositely charged polyelectrolytes, and it eliminates the monolayer densely protected surface and enhances the conductivity [261,262].

The use of a silver precursor ink has been suggested to solve nozzle clogging issues associated with nanoparticle inks [263]. After thermal post-treatments, the organic silver complex decomposes to form silver thin films. One type relies on thermal decomposing silver carboxylate [264 265], and the other relies on thermal activation of reducing agents [266]. These methods have been commercialised for manufacturing silver fabrics for electronics and antimicrobial applications [267,268], as well as introduced for patterned sensor inkjet printing by Calvert et al. [269–271]. Another invention referred to the reactive ink from Walker and Lewis [58] that exhibits high conductivity after annealing at 90 ºC. It is a modified Tollens' process involving silver acetate, formic acid and ammonia. The synthesis methods are shown in Scheme 2.1, and as ink dries, silver cations are reduced by the formate anions and acetic acid as shown in Scheme 2.2.

$$2\ AgCH_3CO_2 + 2\ NH_4OH \xrightarrow{H_2O} Ag_2O + 2\ NH_4CH_3CO_2 + H_2O$$

$$Ag_2O + 4\ NH_3 + 2\ NH_4CH_3CO_2 + H_2O \xrightarrow{NH_3\ /\ H_2O} 2\ Ag(NH_3)_2CH_3CO_2 + 2\ NH_4OH$$

Scheme 2.1 Reactive process of the silver complex formation.

$$2\ Ag(NH_3)_2CH_3CO_2 + NH_4HCO_2 \xrightarrow{\triangle} 2\ Ag + 5\ NH_3 + 2\ CH_3CO_2H + CO_2 + H_2O$$

Scheme 2.2 Degradation mechanism: bulk silver formed and the other products are evaporated.

However, the low viscosity (2 mPa·s) and high surface tension (>60 $mN.m^{-1}$) of the reactive ink makes it difficult to use for inkjet printing. A modified process with alkylamine ligands was introduced to solve the problem [272]. Kim et al. achieved a sheet resistance of 0.09 $\Omega\ sq^{-1}$ with 15 number of printing passes through reactive silver ink inkjet printing on knitted structures. [2]

Additionally, high stretchability is expected in conductive textiles, acrylic rubber as a binder combined with Ag flakes formed ink was reported to be flexible, stretchable and waterproof [273]. Similarly, Matsuhisa et al. recorded stable conductivity using a silver flake ink when the substrate is stretched to 215% strain, with addition of a fluorine rubber and a fluorine surfactant [274]. Ecoflex® silicone rubber was developed likewise [275]. The bridging effect from Ag nanowires can also contributes to the ink elasticity [276].

2.4.3 Durability of Inkjet Printed Patterns on Textiles

Apart from improving the performance of conductive ink, the main challenge to the application of inkjet printed conductive electronic textiles is to achieve continuous conductive and durable printing tracks. The high porosity and uneven surface of textile materials [53,162,277,278] leads to discontinuous and anisotropic conductive paths[279–284]. The low viscosity of inkjet printable inks [285,286] promote an ink bleeding or wicking effect and reduced conductivity. Additionally, the weak adhesion between the inks and the textile substrates reduces the durability and washability of the products.[8,33,34] In principle, all these issues are related to the interaction between the ink and the textiles, and a number of recent studies are reviewed in this section.

One of the most direct methods to overcome above challenges is to apply functional surface treatments to the textiles. A flexible interface layer that acts as a solid pore-free layer can reduce or eliminate ink bleeding and lead to continuous conductive patterns. Polyurethane (PU), silicone and acrylic polymers have been applied as dense surface layers. PU showed superior extensibility, silicone led to excellent bendability, while acrylic coating material presented limited stability and durability [287]. Interface layers such as polydimethylsiloxane, polyimide, poly(vinyl alcohol) reduce the fabric surface roughness and improve inkjet-printed fabric performance [3]. A polyvinyl butyral coated polyester fabric was reported to provide a desired level of hydrophobicity and reduce the roughness of the fabric, which can improve the continuity of printed patterns and the electrical conductivity [288]. Those polymer layers can also be applied as protective coatings to protect the electronics and to improve the adhesion and durability [1,3,4,59,242,288,289]. However, the intrinsic breathability of textiles is reduced or eliminated by these impermeable surface layers.

This type of surface treatment is similar to that developed for use with pigment inks for textile colour printing. In pigment inks, the pigment particle is typically about 1 μm in diameter. Pigment particles are generally found to adhere poorly to textile fibres, and a binder is essential to provide adhesion between the pigments and the textile substrate [290]. Thus inks are formulated with polymeric binders, water or other solvents, co-solvents for solubility and compatibility, surfactants for nozzle and substrate wetting and jetting reliability, and humectants to control drying [291].

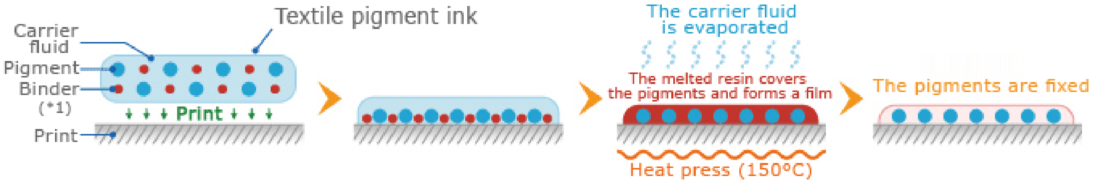

Figure 2.34 Pigment ink fixation process on textiles, ref [292].

Most binders are in the form of water insoluble droplets, and they coalesce during drying to form a film a few microns thick, in which pigment particles are embedded to stay on the fibre surface [290], as shown in Figure 2.34. The well-known binders include styrene acrylic emulsions, vinyl acrylic emulsions, pure acrylic emulsions, polyurethane emulsions/dispersions and plastisols. Binders used for conductive materials coating have also been studied [293,294]. They can be either self-crosslinked or requiring a co-monomer as the crosslinking agent such as N-methylol acrylamide. Yet, this crosslinking agent is not environmentally-friendly with the emission of formaldehyde. In addition, the electrical conductivity and breathability could be reduced when the polymer film network forms, and inkjet printability (low viscosity) need to be considered.

Thus, core-shell latex binders comprising styrene and butyl acrylate was introduced, which allows more functionality to the binder such as elasticity and mechanical stability [295]. In Akerfeldt et al.'s work [296], a commercial textile coating polyurethane-based binder, which contains self-crosslinking acrylates, was used to improve the adhesion between a PEDOT:PSS ink and a woven polyester fabric to enhance the conductivity. Topp et al. [297] investigated metallic pigments for antimicrobial application on textiles, using an acrylate-based binder. It was also found that pre-treating the fabric with a cationic reagent or ultraviolet treatment with ozone improves the fastness of pigment printing [298]. This is due to the negative charged surface of the water dispersible pigment particles and the introduction of oxide groups to the fibres by the UV/ozone treatment [290]. Unconventional textile polymeric binders have been developed to meet the requirements of low ink viscosity for inkjet printing. These involve ink medium soluble but water insoluble random and block copolymers or dispersants [7]. As for the breathability of the pigment ink, the solvent used to dissolve the binder plays an important role, plastisol-based pigment inks show increased stiffness and reduced breathability, whereas water-based pigment inks lead to more breathable fabrics.

To further improve the conductive performance of conductive textiles, without compromising the intrinsic textile properties, other types of binding mechanism apart from mechanical bonding (polymer network interlocking) have been studied, such as electrostatic force, diffusion, and surface reaction. Electrostatic forces are only present when charged particles are interacting a polar medium. It is found that positively formed polyaniline and polypyrrole may cause electrostatic attraction forces with a negatively charged polyacrylonitrile (PAN) fabric. Polyaniline can further be used with Ag nanoparticle (AgNP) ink to improve the adhesion [261]. Diffusive force occurs when materials are mobile or soluble, which are not likely to happen between conductive ink and textile. As for surface reaction, it includes surface wettability and chemical bonding.[299]

There are many articles that emphasise the importance of enhancing the hydrophilicity of textile substrates, such as through UV-ozone plasma treatment, to obtain better wetting of the ink, which aims to ensure the adhesion between the ink and the substrate through particles penetration [300]. Cotton fabrics were modified with β-cyclodextrin via esterification of its hydroxyl groups with citric acid, by simply dipping and padding. The modified cotton fabric contains hydroxyls, where the ink is blocked by the cohesive force. Moreover, β-cyclodextrin can form inclusion complex to keep the ink inside the cavity [301]. However, increasing the wettability of the ink with adhesives leads to ink bleeding and the pattern printing quality is reduced.

In chemical bonding, the bonding strength ranks ionic > covalent > dipole-dipole > hydrogen bonding > van der Waals force. The promising strategies of introducing chemical bonding between the textile substrates and conductive pigment ink have been reported with increasing attention on antibacterial textiles, and a summary is shown in Figure 2.35. These polymers generally contain two functional groups, one of which forming coordination bonds with nanoparticles such as amine and thiol, and the other form covalent bonds with the textiles such as siloxane and carboxylic acid. [302] Carboxymethyl chitosan has been reported to improve the adhesion of Ag on hydroxyl cellulous fabrics with the functional amine group.[303,304] With the assistance of thiol group on L-cysteine, only 10-15% silver loss was observed after more than 90 times laundry cycles.[305–308] However, among all these studies, chitosan was found to be applied in a small number of literatures of with improved performance on conductive textiles.[305,308,309]

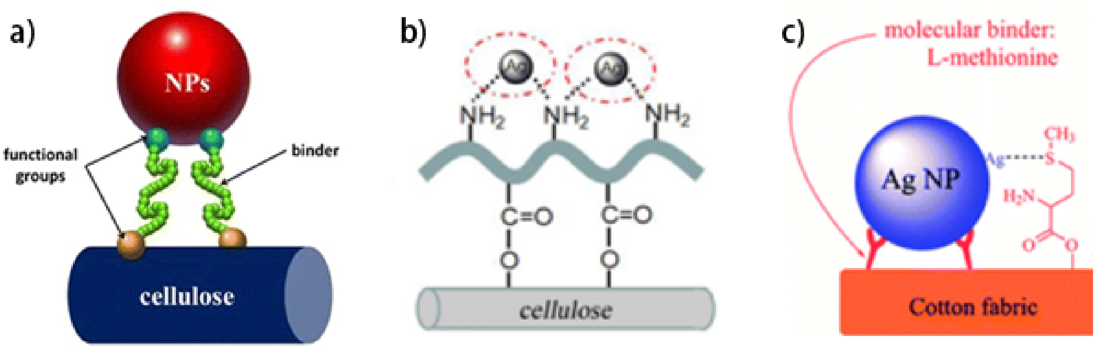

Figure 2.35 (a) Illustration of nanoparticle chemical bonding with cellulose fibres through functional groups and binders[302], (b) amine groups and carboxylic groups used for adhesion of nanoparticles and cellulose fibres[303], (c) thiol groups and carboxylic groups used for adhesion of nanoparticles and cellulose fibres[305].

2.4.4 Challenges and Outlook

This section has introduced current development of inkjet printing conductive materials on textiles, discussed the conductive inks used for inkjet printing on textiles and the methods of improving the performance of conductive inks on textile substrates. The electrical performance achieved from current development is comparable with other deposition methods for conductive electronics on flexible substrates, which demonstrates the huge potential of inkjet printing conductive textiles in academic and industrial research. However, comparing to other methods, it is necessary to confine the number of printed layers and the process of pre-treatment, and improve the durability of conductive ink on textiles without losing its intrinsic properties.

Moreover, the conductivity and washability measurement methods for e-textiles have not yet been standardised, and there are a wide range of topics to be researched. For example, the anisotropic and inhomogeneous electrical behaviour in e-textiles has been observed widely[310–314], yet requires further investigation. The standard washing method applied for common textile products may not be suitable or necessary for e-textiles [315].

All above challenges come from the complexity of the ink textile interaction, which requires more fundamental understanding of the interaction mechanisms. Therefore, the objective of this project is to the investigate the interaction of conductive inks with textiles in detail, meanwhile, seeking the opportunities to improve the performance of inkjet printed conductive textile through altering inkjet printing or textile parameters.

2.5 Conclusions

The first section of this chapter overviewed current development on wearable technology, and the potential of applying inkjet printing on textiles to improve the performance of existing wearables. The second section of this chapter introduced the structure and surface properties of textile materials, and the complicated liquid textile interaction mechanisms in fibre, yarn and fabric scaled, in terms of wetting and wicking processes. The third section of this chapter reviewed the fundamental inkjet printing techniques and illustrated the complex jetting and impacting process. At the end of this chapter, inkjet printing conductive ink on textile materials has been investigated, and as a recent scientific research topic, a range of challenges and frontier works were discussed.

In summary, the advantages of inkjet printing combined with textile materials establish the interests and prospects of this research area. The development of conductive inks and ink textile interactions show positive contribution to related wearable technology. However, the fundamentals of conductive ink deposition on fibrous substrates have not been investigated comprehensively, which is a limiting factor in this research field. The following chapters will demonstrate the approaches and results applied and studied in this project with the aim of improving the performance of inkjet printed e-textiles.

Chapter 3 Materials and Methods

3.1 Materials

A commercial silver nanoparticle ink, based on a triethylene glycol monomethyl ether solvent, was used for all the printed structures investigated in the thesis: Silverjet DGP-40LT-15C (Sigma Aldrich product code 736465, Gillingham, UK). This has a mean Ag nanoparticle (NP) size < 50 nm and the manufacturer's data are shown in Table 3.1.

Table 3.1 Key parameters of the conductive silver ink used in this project (manufacturer's data, Sigma Aldrich, Gillingham, UK).

30-35 wt.% in triethylene glycol monomethyl ether	
Surface tension	$35\text{-}40 * 10^{-3}$ N.m^{-1}
Viscosity	$10\text{-}18 * 10^{-3}$ N.s.m^{-2}
Particle Size	≤ 50 nm
Density	1.45 g.cm^{-3}
Resistivity	$1.1 * 10^{-7}$ Ω.m
Annealing Temperature	150 ºC

Textile substrates were provided by Premier Textiles (Manchester, UK), six different plain-woven 100% polyester fabrics were used in this project with the manufacturer's data presented in Table 3.2.

Table 3.2 Six types of plain-woven polyester textiles used in this project.

Fabric Abbreviation	Fabric Name	Fabric Weight (g/m^2)	Yarn Density (ends/cm) Warp	Yarn Density (ends/cm) Weft
F1	Crepe de Chine 1707	80	40	60
F2	Inherent FR 2401	145	23.6	30
F3	Phoenix 2458	240	10	11.6
F4	Portland 2442	250	14.5	18
F5	Poly Canvas 2464	290	16.5	28.5
F6	Poly Canvas 2465	450	10	25

Additionally, a polyethylene terephthalate (PET) film (5 Star Office OHP Laser Printer Film, 300 μm) was used as a control substrate of similar composition to compare with the polyester fibre properties.

A water-repellent surface treatment (Scotchgard FC-3548, from 3M, Binfield, UK) at 20 g/L on deionised water was applied to change the surface energy of the textile fibres and the control PET film. Scotchgard is a blend of fluorochemical urethane, fluorochemical acrylate and fluorochemical esters.[316] The pH of the Scotchgard solution was controlled at 4.5, through the addition of 0.2 ml/L acetic acid.

3.2 Methods

3.2.1 Fabric Surface Treatment

The textile surface water repellent treatment is applied through a pad-dry-cure process (2-Roll horizontal padder HF, Werner Mathis AG, Switzerland), as shown in Figure 3.1. 10 g Scotchgard solution was mixed with 500 mL deionised water and 0.1 ml acetic acid in a beaker and stirred for 5 minutes on top of a magnetic stirrer. The prepared padding solution was then filled between rollers with 2 bar pressure with a speed of 2 m/min for both sides of the fabric. The fabric was then dried for 2 minutes at 100 ºC and cured for 1 minute at 170 ºC (Labdryer, LTE, Werner Mathis AG, Switzerland).

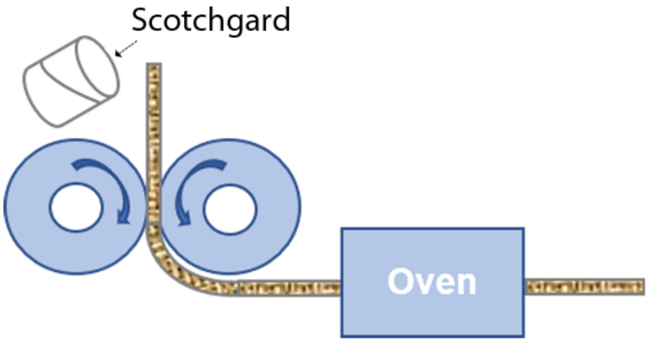

Figure 3.1 Schematic diagram showing the pad-dry-cure process for textile surface treatment.

3.2.2 Inkjet Printing

All printing experiments were carried out using a commercial, piezoelectric actuated, drop-on-demand (DOD) inkjet printer (DMP 2800, Fujifilm Dimatix, Santa Clara, CA) equipped with printhead cartridges generating a nominal drop volume 10 pl (DMC-11610, Fujifilm Dimatix), as shown in Figure 3.2.

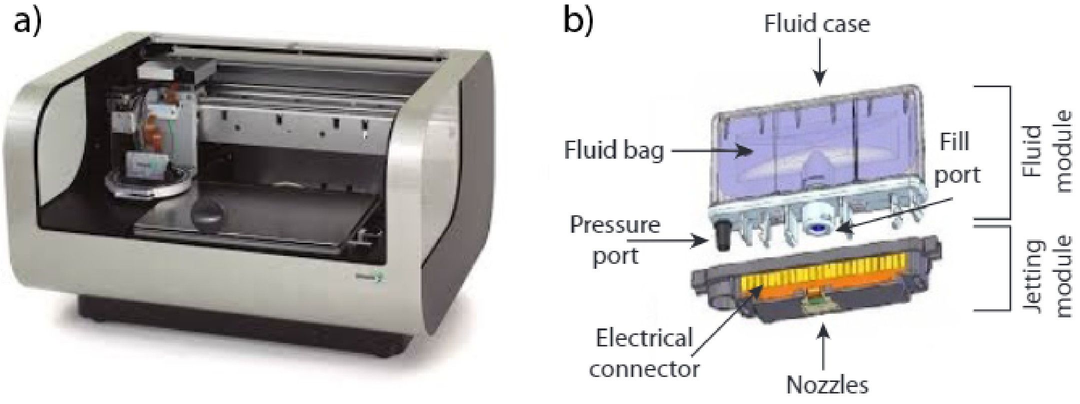

Figure 3.2 (a) Fujifilm Dimatix DOD inkjet printer and (b) the cartridges filled with silver nanoparticle ink used in this project.

The actuating waveform applied to eject the drops is shown in Figure 3.3, achieving continuous and stable droplets formation. The first stage of decreasing the actuation voltage draws the ink from the reservoir, the second stage of increasing voltage initiates the droplet at the nozzle, and the third stage of decreasing and standing by voltage breaks off the droplet from the nozzle and prepares for the next drop generation. In reality, around 70wt% (nominal drop volume 7±0.3 pl) of silver nanoparticles were retained on the fabrics (direct weight measurement) after printing and heat treatment when compared to the expected value printed (computed from drop number and volume). A diameter of 24 μm is obtained for drop in flight when we assume the droplet remains as a perfect sphere during flight with the volume of 7 pl.

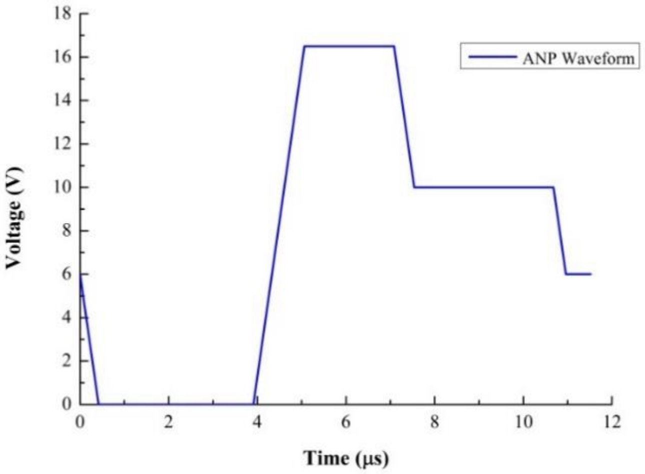

Figure 3.3 ANP Waveform used in the experiments with the 10 pL printhead.

2cm * 3cm sized fabric pieces were cut and adhered using double-side tapes on top of the glass substrate with two cardboard spacers in between. A 1.5mm gap between the fabric and the glass substrate was created preventing ink penetration through the fabric that can cause direct contact with other solid surfaces, as shown in Figure 3.4 a). Then the samples were placed on the plate of the inkjet printer and fixed using adhesive tapes, the distance between the nozzle and the substrate was set as 3300 μm in all printing procedures.

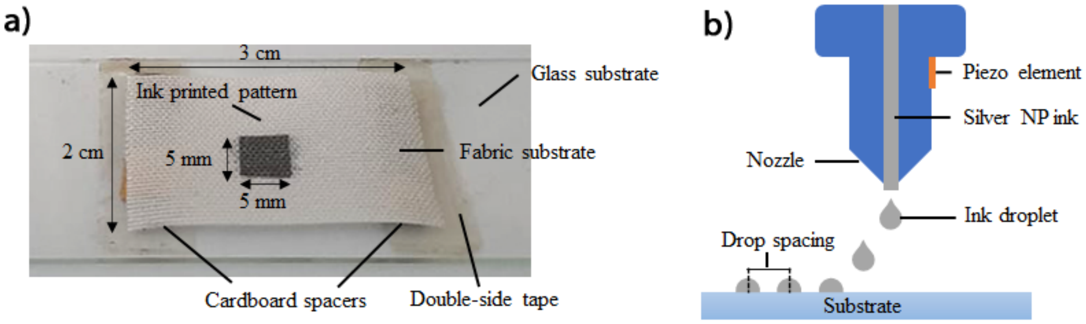

Figure 3.4 (a) Sample setup diagram for inkjet printing and (b) inkjet printing process illustration of ink ejection from nozzle onto the substrate with defined drop spacings.

Drop spacings of 200 μm, 20 μm and 10 μm was compared for a range of studies. The drop spacings were set before printing in the Dimatix Drop Manager Software Pattern Editor, resulting in the distance between the drops as shown in Figure 3.4 (b). 200μm drop spacing allows individual droplets deposition on textiles, and 20 μm and 10 μm drop spacings lead to drops coalescence to form lines of drops. 20 μm and 10 μm drop spacings were also applied correspondingly between lines to produce areas of silver pattern for conductivity measurement. In order to vary the surface concentration of the Ag ink, multiple layers (1-5, 10 and 15 layers) were inkjet printed for drop spacing of 20 μm and 10 μm samples. When multiple layers of the ink were printed, the printing of each subsequent layer was registered with reference to fiducial markers. The printed patches used for testing were approximately 5 mm × 5 mm in size and the accuracy of registration was insignificant in relation to these dimensions.

Printed fabrics were removed from the printer and heat treated in a laboratory oven temperature-controlled fan oven (Genlab general purpose laboratory oven, MINO18, Advanced Manufacturing Services Ltd, UK), to remove solvent, any polymers and surfactants present in the ink formulation and to sinter the AgNP. Two types of heat treatment conditions were involved in this project:

I) Sintering after all layers are printed (SAL): multiple layers of silver ink were continuously printed on the inkjet printer (defined in the Dimatix Drop Manager Software Pattern Editor), followed by a single heat treatment for 1 hour at 150 °C in the oven;

II) Sintering per layer (SPL): after each layer in a multilayer print run was finished, the fabric specimen was removed from the printer and sintered for 20 minutes at 150 °C before returning to the printer and realigning before a subsequent layer was printed. This process was repeated until after the final layer was printed when the completed multilayer was sintered for a further 40 minutes at 150 °C in the oven.

3.3 Characterisation

3.3.1 Fourier-transform Infrared Spectroscopy

Fourier-transform infrared spectroscopy (FTIR) was used to identify the chemical composition of six types of polyester fabrics and the PET film. The technique measures the interaction of light with samples at each wavelength through the vibrations of the molecules, which produces a molecular fingerprint (infrared spectrum of absorption or emission) of the sample.

All samples were cut into 2*2 cm^2 sized solid pieces, absorbance FTIR spectra of the fabric samples and the PET film before and after Scotchgard treatment were obtained at a mid-infrared wavelength range of 400 to 4000 cm^{-1} using a Nicolet 5700 FTIR spectrometer (Thermo Fisher Scientific Inc. MA, USA). A single reflection horizontal attenuated total reflection accessory was attached to enable the direct examination of the solid samples.

3.3.2 Thermogravimetric Analysis

Thermogravimetric analysis (TGA) was applied to measure the silver ink deposition mass on fabrics, where the polyester fabrics degrade at a lower temperature than silver metal particles, thus the weight ratio of silver metal particles to the fabrics can be calculated based on the remaining mass and the initial mass of measured samples.

Inkjet printed and sintered polyester fabrics with silver deposition were prepared through cutting along the printed patterns as 5 mm * 5 mm sized squared samples. The samples were placed in platinum pans and the temperature was increased from room temperature to 800 ℃ at an increment scanning rate of 10 ℃ per minute, and the mass degradation process was recorded continuously in TGA Q500 (TA Instruments, Netzsch, Selb, Germany).

3.3.3 Scanning Electron Microscopy

Scanning electron microscopy (SEM) can provide high resolution images of the surface morphology of the printed Ag patterns, however, SEM of textile fibres is difficult because they are non-conducting and charge easily, degrading image quality. Normally this can be overcome by coating the specimen with a thin conducting layer prior to SEM observation but because this project is studying the penetration of conducting inks, such coatings may complicate the interpretation of images. Therefore, low vacuum SEM where specimens are imaged in a low vacuum environment with a low-pressure residual gas phase present was used. A low vacuum environment leads to more gas molecules ionised by primary electrons and those reflected from the specimen can dissipate charges away from the sample [317]. In addition, due to the penetration of silver ink into textiles, back scattered electron images are preferred, where electrons are reflected from the specimen through elastic scattering, so deeper information of the specimen can be captured.

Fabric samples inkjet printed with silver nanoparticles were trimmed and adhered onto an aluminium stub using sticky carbon tabs without any further coating. The samples were scanned under 10-15 kV working energy in Quanta 200 (Thermo Fisher, Eindhoven, Netherlands) and Quanta 250 FEG (Thermo Fisher, Eindhoven, Netherlands). Low vacuum (0.2 Torr pressure) with a working distance 10 mm and a spot size 3-4 were applied in an electron back scattered imaging mode, for a better distinguish between the fibres and Ag.

3.3.4 Contact Angle Measurements

Contact angle measurements illustrates the wettability of the materials. To measure the polyester fibre contact angle, existing theories of micro droplet on mono filament, and ink yarn and fabric interaction as explained in Chapter 2 were applied:

i) Back scattered SEM images of individual ink droplets printed with 200 μm drop spacing on polyester fibres were captured following above SEM operating procedures. The images were then analysed in ImageJ, straight lines were drawn on the images along the printed droplets spreading direction, and the spreading length of the micro droplets was measured using the Analyse tool bar - Measure function (Figure 3.5). Each SEM image contains more than 10 deposited droplets, and 3 SEM images were analysed for each sample, and the average value was obtained for droplets deposited on warp and weft yarns respectively.

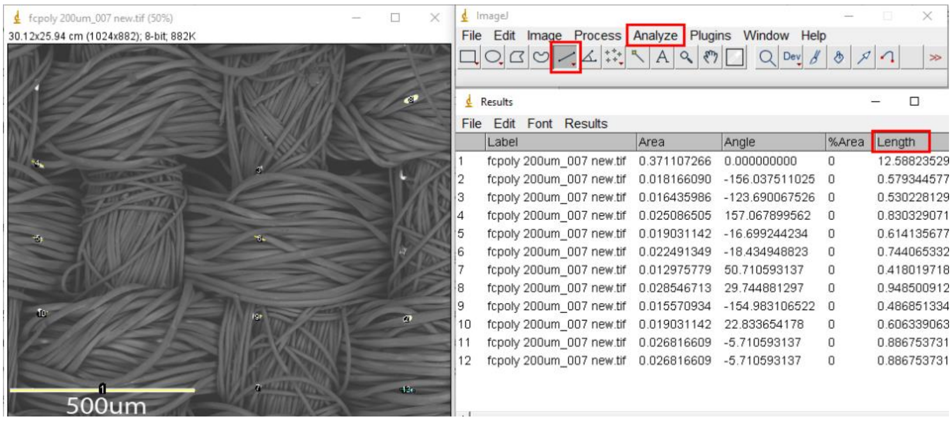

	Label	Area	Angle	%Area	Length
1	fcpoly 200um_007 new.tif	0.371107266	0.000000000	0	12.58823529
2	fcpoly 200um_007 new.tif	0.018166090	-156.037511025	0	0.579344577
3	fcpoly 200um_007 new.tif	0.016435986	-123.690067526	0	0.530228129
4	fcpoly 200um_007 new.tif	0.025086505	157.067899562	0	0.830329071
5	fcpoly 200um_007 new.tif	0.019031142	-16.699244234	0	0.614135677
6	fcpoly 200um_007 new.tif	0.022491349	-18.434948823	0	0.744065332
7	fcpoly 200um_007 new.tif	0.012975779	50.710593137	0	0.418019718
8	fcpoly 200um_007 new.tif	0.028546713	29.744881297	0	0.948500912
9	fcpoly 200um_007 new.tif	0.015570934	-154.983106522	0	0.486851334
10	fcpoly 200um_007 new.tif	0.019031142	22.833654178	0	0.606339063
11	fcpoly 200um_007 new.tif	0.026816609	-5.710593137	0	0.886753731
12	fcpoly 200um_007 new.tif	0.026816609	-5.710593137	0	0.886753731

Figure 3.5 ImageJ analysis of droplet spreading length.

ii) Ink spreading rate in yarn was measured by depositing a large volume silver ink droplet (approximately 5 μl) on individual warp and weft yarns deconstructed from the woven fabric manually and held without tension in air, as shown in Figure 3.6.

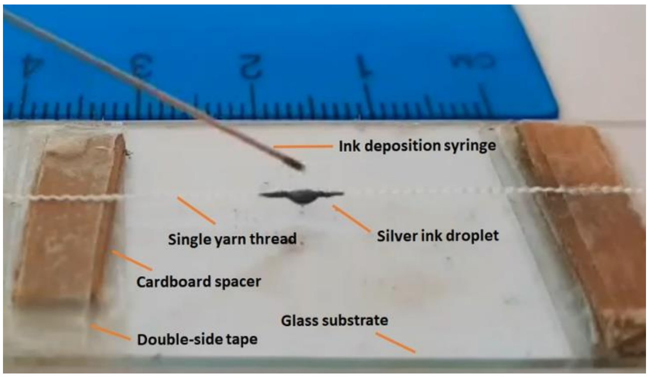

Figure 3.6 Ink yarn interaction experiment set up diagram, single yarn thread was taped on top of the glass substrate with carboard spacers in between, and a syringe with needle was used to eject a 5μl silver ink droplet on the yarn.

Video clips were taken and image frames at 0-50 seconds were captured with an increment of 5 seconds, and the spreading length of ink in yarn at each frame was analysed in ImageJ. A straight line was drawn along the ink spreading direction, and in the Analyse bar – Measure function, the spreading length was obtained by measuring the length of the straight line with the reference of the ruler in the image. Plots of ink spreading length as a function of time were gained in this method, three measurements were taken for each specimen.

iii) Additionally, a Force Tensiometer, K100 (Krüss GmbH, Hamburg, Germany) was used to record the vertical weight gain of silver ink in the fabric in both warp and weft directions as a function of time. The weight gain rates can then be converted into Washburn equation or Darcy´s law to estimate the intrinsic polyester fibre contact angle values.

Clean polyester fabrics were cut into 1 cm * 4 cm pieces along the fabric warp and weft directions respectively, clamped vertical and straight into the clamp accessory, and attached to the force tensiometer, as shown in Figure 3.7. 10 ml silver ink was prepared in an aluminium pan, and the weight gain recording started once the fabric was lowered to the ink surface. The weight gain process was recorded on the Kruss ADVANCE software (Krüss GmbH, Hamburg, Germany) for 2 minutes for each sample with a 0.04 second increment.

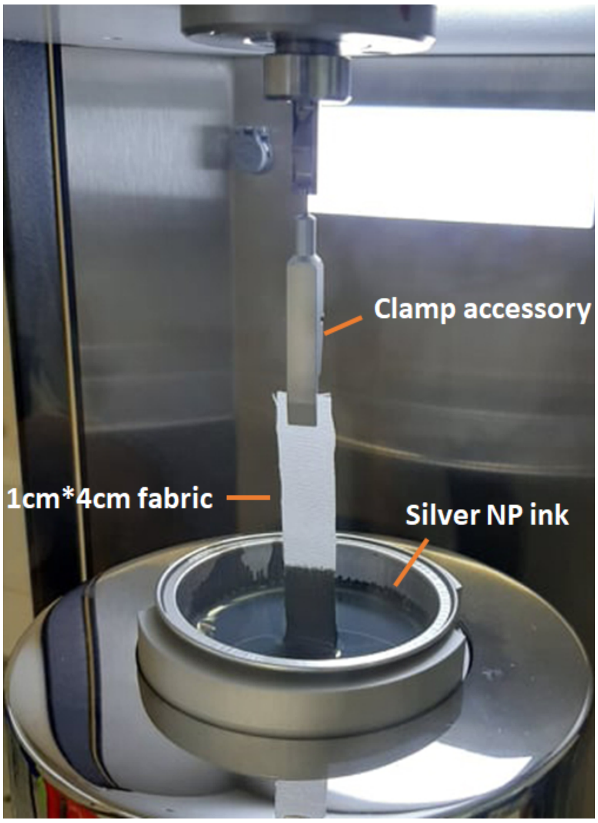

Figure 3.7 Experimental set up of the fabric weight gain of silver ink on Kruss K100.

The mechanisms of silver ink interaction with fibre, yarn and fabrics were compared to obtain the theoretical polyester fibre contact angle values from existing theories (discussed in Chapter 4), which was then compared with the direct contact angle measurement of fabrics and the PET films through a Drop Shape Analyser DSA 100 (KRÜSS GmbH, Hamburg, Germany).

All static contact angle values of as received and Scotchgard treated polyester fabrics and PET films were recorded, the samples were placed on the substrate holder and 5 μl silver ink droplets were injected on the substrate from a liquid dosing needle. All tests were conducted at 20 – 25 °C laboratory temperature and relative humidity (20 – 40%), and each sample was repeated three times with the average contact angle value taken (the accuracy of the instrument is 0.1^o). Digital images were taken by the Kruss DSA-10 digital camera, in which the images with sessile drop recorded were transferred to the drop shape analysis software. The contact angles were obtained between the modelled drop shape function (obtained by solving the Laplace equation) and the sample surface. For measuring advancing contact angle values, the distance between the needle ejection point and the substrate plate was reduced, and silver ink ejection was continuous to record the ink advancing process on the substrate, the videos were analysed in the drop shape analysis software.

3.3.5 X-ray Computed Tomography

Tomography techniques enable the reconstruction of 3D representations of a structure from sliced images. These can be obtained non-destructively with any kind of penetrating probe, such as X-rays. When X-rays pass through an object, their intensity is reduced because of their interaction with matter. This interaction is a combination of the photoelectric effect, Compton scattering, Rayleigh scattering and pair production. The total attenuation of an X-ray beam passing through a material is described by the Beer-Lambert law, with the intensity, $I(x)$, as a function of position, x, given by:

$$I(x) = I_0 e^{-\mu x} , \tag{3.1}$$

where I_0 is the initial X-ray intensity, μ is the attenuation coefficients > 0. In X-Ray Computed Tomography (XCT), 2D projections of the X-Ray intensity after it has passed through the object under study are collected from multiple angles. These are then passed through an appropriate algorithm and reconstructed to produce 3D images [318]. XCT has been previously used for evaluating fibre reinforced composites [319,320]. It is a non-destructive technique with no complicated sample preparation required. However, XCT resolution is limited to approximately a fraction of 1000-2000* of the object cross-section diameter [321]. Because to image the whole sample, the theoretical resolution to be achieved equals to the size of the sample divided by the number of pixels in the detector (2000 pixels in most detectors). So small samples are required for high resolution studies, and the source of image artefacts can be difficult to identify and eliminate. Laboratory source X-rays are of low signal intensity and it can take several hours to collect sufficient data to allow a full 3D image reconstruction.

Size 2*2 mm^2 fabric sample were mounted on an aluminium column specimen holder with double sided tape and securely located in the XCT equipment (Xradia 520 Versa, ZEISS, Oberkochen, Germany), as shown in Figure 3.8. An optimal set up was used, to avoid focus blurring and achieve an efficient pixel size during XCT scanning. 80 kV voltage, 7W source power from Tungsten transmission target, magnification *10, 10 s exposure time and pixel binning *1 is applied. Sample to detector distance was set to be 5.05 mm, sample to source distance was 23.8 mm, and the number of images taken was 3201 while the sample rotates in the vacuum chamber. The data was reconstructed using the Zeiss Scout and Scan software and the voxel size in the reconstructed data is 1.13 μm.

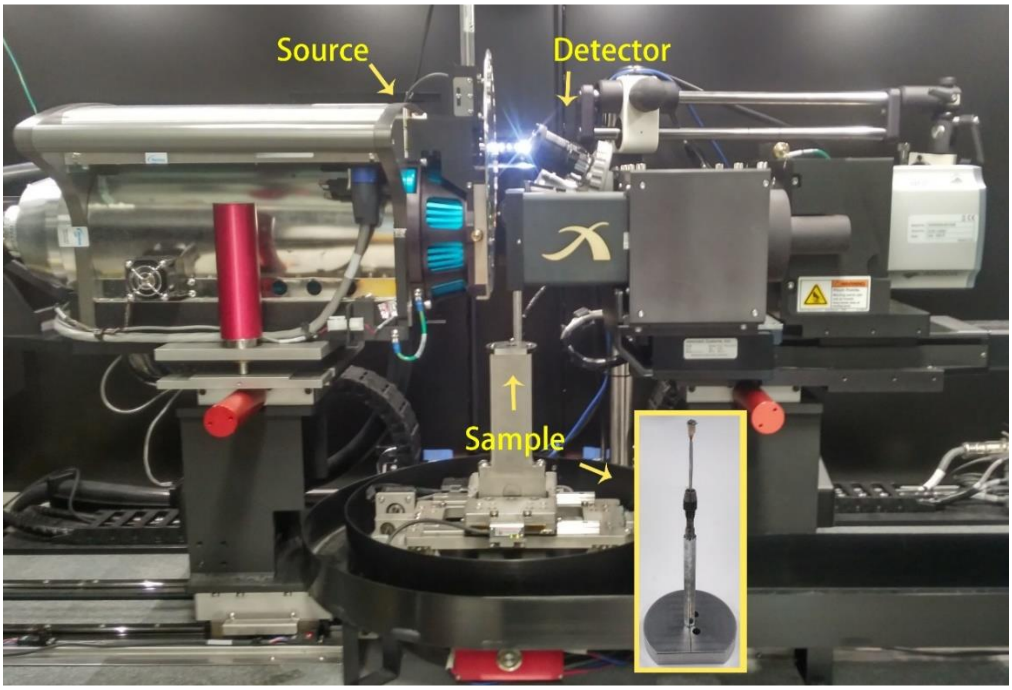

Figure 3.8 X-ray tomography system set-up diagram.

The reconstructed XCT data was further analyzed and segmented using the Avizo 9 visualization software (Amira Avizo, Thermo Fisher, Waltham, MA). Appropriate image segmentation (Figure 3.9) based on X-Ray absorption is used to separate the location of the high atomic number Ag (coloured blue-green) from the organic polyester fibre structure (coloured grey) in Figure 3.9. Tophat and global thresholding two image segmentation methods were applied and studied to reach the optimal imaging quality, and the details of the choice of thresholding will be discussed further in Chapter 5.

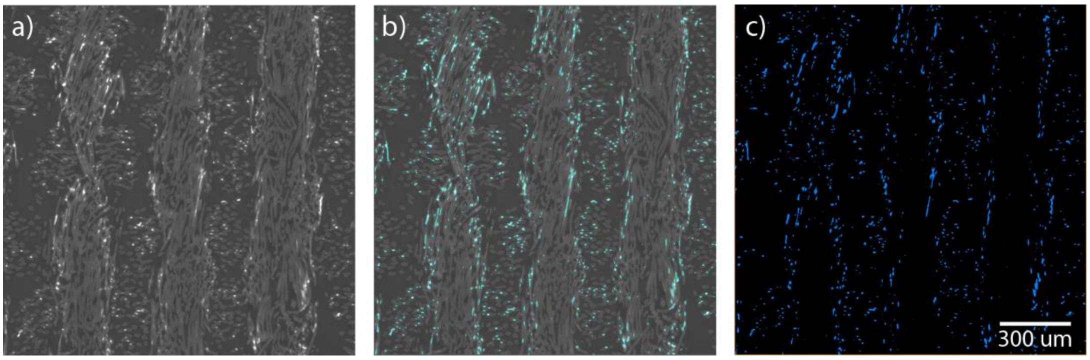

Figure 3.9 (a) 2D slice of reconstructed sample image with 1.13 um voxel size, (b) segmented silver objects and (c) generated label image representing the area of silver coverage.

3.3.6 Electrical Conductivity Measurements

Inhomogeneous and anisotropic conductive textile properties lead to uncertainties with the use of direct thin film sheet resistance measurement. In addition, because ink printed on a textile surface absorbs into the material, it is not clear whether a sheet resistance, which assumes a constant conducting film thickness across a surface, is the appropriate metric for electrical conductivity characterisation. Thus, electrical conductance along a single yarn tow, in either the warp or weft directions of the fabric, is measured using a 4-point probe station (PE4, Everbeing, Hsinchu City, Taiwan) coupled to two source measure units (SMU) (Keithley 2400, Cleveland, OH), as shown in Figure 3.10 (a).

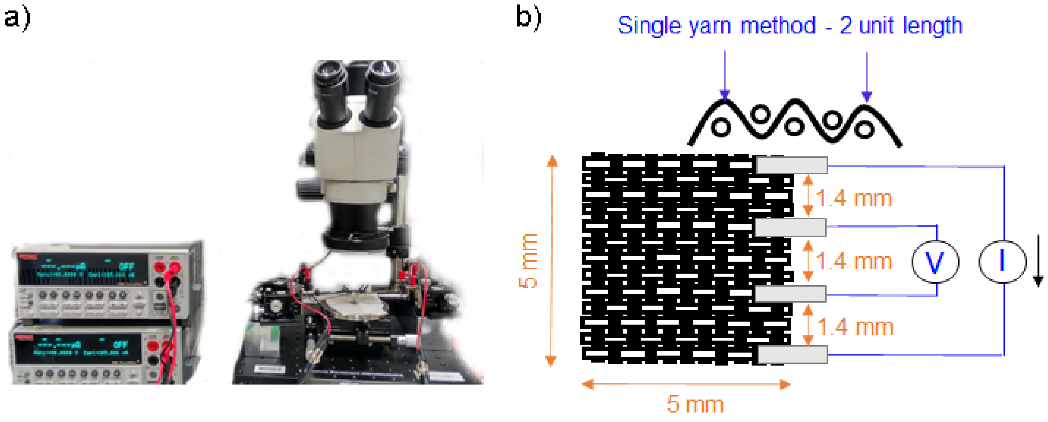

Figure 3.10 4-point probe electrical conductance measurement set-up (a) and the position of the probes (b).

Printed and heat-treated fabrics were placed and fixed on top of the probe station, the diameter of the tungsten probes (300µm, M.R.C, Holon, Israel) was modified to match the yarn diameters and the distance between the probes was set as two repeat units of the weave (1400 µm) (Figure 3.10 (b)). The position of the probes was located manually according to the observation from the microscope mounted on the probe station. Two probes were sourcing the current and two of which were measuring the voltage cross the samples. Those 4 probes were lined up in each single yarn measurement and switched together to the adjacent yarns and repeated the testing. In the connected LabTracer 2.0 SourceMeter Integration Software (Keithley Instrument, Inc. Cleveland, OH), linear sweep current (step number of 100, ranging between 0 - 1 A) was applied and adjusted according to the expected sample resistance. Measured voltage results were obtained from the software, and the resistance values were analysed and averaged among 3 measurements on each sample.

Chapter 4 Ink/Textile Interaction

4.1 Introduction

Wearable technology has attracted considerable attention from researchers and industries due to its potential applications, for example in health and environmental monitoring[6,16,17,21] and energy storage and harvesting.[82,322–324] Textile substrates provide platforms that can provide both strength and flexibility. They can be made stretchable, breathable, washable and are thus easily integrated into clothing, making them potentially more comfortable to wear than rigid alternatives[8,54,55,270]. Printing technologies show promise due to their reasonable capital cost and simple manufacturing methods. Inkjet printing is a contactless printing technique that avoids using a plate or a screen mesh, unlike lithographic or screen printing. It allows rapid design changes with a relatively low-cost machine set-up and reduced material waste.[4,204,325] Inkjet printing has been extensively used for printed and large area electronics applications on a range of flexible substrates and thus has promise as a manufacturing tool in the area of e-textiles and wearable technology[4,56,326].

Inkjet printing on textiles has been widely used in the fashion industry with coloration pigments[7,236,327,328]. However, it is well-known that there are difficulties in obtaining high printing resolution and achieving continuous, conductive patterns on textile substrates with this method[3,4,8,329]. This is believed to be a consequence of the uneven structure and high porosity of the textile surfaces, in comparison with solid polymeric films, which leads to different behaviour with the spreading, absorption and drying of the ink. These differences are also enhanced by the low viscosity and active component concentration required for inkjet delivery.

Therefore, investigating the mechanisms of ink textile interaction is of primary importance in the development of electronic textiles. Here we take textile materials to describe flexible materials fabricated from natural or synthetic fibres; the fibres can form non-woven fabrics directly or can be spun into yarns and form fabrics by weaving, knitting, or braiding[129]. The interaction of liquids with textiles has been studied extensively from different aspects, including but not limited to: single drops on filaments[138,139,141,147,330–334], capillary flow of liquid in yarns[90,91,153,154,177,335–337], and wetting and spreading of a liquid drop on a fabric surface[181,338,339]. All of which are of relevance to engineering problems in the textile or polymer composite industries[12,162]. The need to study the interaction of liquids with textiles over a range of different levels of the textile architecture is a function of the complexity of textile structures and the consequent difficulty of explaining this phenomenon through a single mechanism model. However, existing models of liquid transportation on textiles can provide some understanding of the factors that influence the structures formed after inkjet printing on textiles.

Inkjet printing produces drops in a volume range of 1 – 100 pL and these are of radius similar to that of individual textile fibres, resulting in Bond number << 1, which indicates that capillary forces dominate ink/textile interactions. The pressure difference across the fluid/air interface, as described by the Young-Laplace equation[340], and the need to maintain hydrostatic equilibrium is the fundamental principle that underlies the development of models for liquid transport mechanisms in textile substrates[340]. However, the challenge comes from that the equilibrium status of ink in textiles not only exists in the textile surface but also when ink infiltrates inside the textiles.

On the surface of textile, when a drop of liquid interacts with a single filament, the drop spreading length in relation to the fibre surface energy, fibre diameter and shape, drop size and shape can be analysed numerically or analytically, assuming equilibrium[135,137,341,342]. When a drop penetrates and interacts with many parallel fibres, governing laws introduced by Washburn and Darcy, as demonstrated in Chapter 2, can be used.

The Washburn equation
$$\frac{L^2}{t} = C\,\frac{\gamma_{lv} r_{eff} cos\theta}{2\mu} \tag{4.1}$$

Darcy’s law
$$\frac{L^2}{t} = \frac{4k\gamma_{lv} cos\theta}{\mu r_{eff}\varphi} \tag{4.2a}$$

$$k = \emptyset^2\,\frac{\varphi^3(2r_f)^2}{K(1-\varphi)^2} \tag{4.2b}$$

$$\frac{L^2}{t} = \frac{4\gamma_{lv} cos\theta\emptyset^2}{K\mu} * \frac{\varphi^3\left(2r_f\right)^2}{r_{eff}\varphi(1-\varphi)^2} = \frac{4\gamma_{lv} cos\theta\emptyset^2}{K\mu} * \frac{4\left[r_{eff}^2 + 2r_{eff}r_f\right]^2}{r_{eff}r_f^2} \approx \frac{64\gamma_{lv} cos\theta\emptyset^2}{K\mu} * r_{eff},$$

$$when\ r_f >> r_{eff} \text{ and } {r_{eff}}^2 \rightarrow 0 \tag{4.2c}$$

In the above equations θ is the contact angle, γ_{LV} is the surface tension of the liquid, r_{eff}, is the effective radius of the porosity in the fabric, r_f is the mean fibre radius, φ is the porosity and $\emptyset$ is the sphericity of the pores. Both approaches consider the transport to be driven by the Laplace pressure as from parallel cylindrical capillary tubes of radius r_{eff}, which is a reasonable simplified representation of the porous structure in the yarn. In Washburn's equation, $\frac{L^2}{t}$ is simply proportional to the effective pore radius r_{eff}, the contact angle of the ink on the polyester fibres ($cos\theta$), and a geometric constant C. In Darcy's law, the terms porosity ($\varphi = 1 - V_f$) and permeability (k) are introduced. The permeability is related to the porosity based on Kozeny and Carman's hydraulic radius theory (Equation 4.2b), where r_f is the radius of the fibres, $\emptyset$ is the sphericity of the porosity in the yarns, and K is a geometric constant K. The porosity φ can be used to estimate the effective pore radius r_{eff}, assuming ideal fibre packing geometry.

Both Washburn's and Darcy's equations show a similar relation between liquid penetration length, L, and time, t, with ($\frac{L^2}{t}$) being proportional to the fluid surface energy, cosine of the contact angle, effective pore radius and inversely proportional to the fluid viscosity (Equations 4.1 and 4.2c). These can be modified for specific geometries or fibre arrangements by adjusting the empirical constants, C and K, to predict liquid transportation in a range of different woven or knitted fabric structures[175,185,187,343,344].

The approach of Washburn and Darcy is appropriate when considering the penetration of a liquid along a single yarn or tow of fibres. However, when ink transport is considered in fabric structures, the use of the spreading length, L, to characterise the penetration of liquid as a function of time becomes inadequate, since the fabric is made of yarns intersecting at 90°, and the spreading length can only be measured along a single axis. Instead, it is normal practice to use the weight gain as a function of time expressed in the equivalent form ($\frac{m^2}{t}$). For a single yarn the weight gain can be directly related to the liquid penetration as a function of time, through the liquid density (ρ) and the cross-sectional pore area (A) in the yarn with

$$\frac{m^2}{t} = \rho^2 A^2 \frac{l^2}{t}. \tag{4.3}$$

Researchers have applied modified governing laws based on these approaches to investigate a range of fluid/textile interactions, including: liquid wicking and wetting in textiles based on infinite fluid reservoirs, spreading and penetration distances of drops on fabrics with different yarn structures[165,168,190,345,346]. However, it is well-known that these theories are generally inadequate to accurately predict fluid transport within complex textile structures.[12] In addition, we note that the small inkjet droplet size, which is comparable with the filament size within a yarn, has not yet been widely considered in published modelling work.

To our knowledge, there has not been a full characterisation of the interaction of inkjet printed conductive inks with textiles reported previously. This omission must be rectified to achieve optimal conductive performance and printing quality to allow its use with electronic textiles. This chapter will explore the fundamental mechanisms of ink textile interaction at the scale of individual fibres, yarns, and fabrics respectively and existing models will be investigated and compared with experimental results.

4.2 Experimental Methods

A plain-woven polyester fabric, Inherent FR 2401, is used as a model textile material in this chapter. Scotchgard treatment is applied to study the effect of a surface hydrophobicity modification on ink interaction with textiles. The conductive silver nanoparticle ink described in Chapter 3 (Silverjet DGP-40LT-15C) is used for all the experiments reported. The contact angle of AgNP inks on the textile fabrics and other surfaces of interest was measured using a Drop Shape Analyzer, DSA 100 (Krüss GmbH, Hamburg, Germany).

To study ink/fibre interactions at the scale of a single drop with similar dimensions to the fibres, ink drops were ejected through a piezoelectric actuated drop-on-demand (DOD) inkjet printer (DMP 2800, Fujifilm Dimatix, Santa Clara, CA), ejecting a measured drop volume of 7 pl. Drops were deposited at a spacing of 200μm allowing individual drop deposition without interaction with neighbouring drops. This was followed by heat treatment at 150 °C in air for 60 minutes using a temperature-controlled fan oven. The surface morphology of the printed Ag patterns was imaged using scanning electron microscopy (SEM) (Quanta 250 FEG, Thermo Fisher, Eindhoven, Netherlands).

To study ink interactions at the yarn length scale, a large volume silver ink droplet (approximately 5 μl) was deposited on individual warp and weft yarn threads, manually extracted from the woven fabric and held without tension in air. Video images were recorded and the ink spreading length as a function of time was analysed using image analysis (ImageJ). Finally, ink interactions at the fabric length scale were investigated using a Force Tensiometer, K100 (Krüss GmbH, Hamburg, Germany) to record the weight gain of silver ink as it infiltrated the fabric in both warp and weft directions as a function of time.

After investigating ink interactions with at the scale of textile components, inkjet printing was used to produce continuous lines and 5 mm × 5 mm patches with the Ag ink. Printing was carried out with a drop volume of 7 pl and a drop spacing of 10 or 20 μm, with the inter-line spacing set equal to the drop spacing on all fabrics. After printing, the dried ink patches were heat treated at 150 ℃ for 1 hour, as per the suppliers instructions to achieve optimal electrical conductivity. Optical images and X-ray computed tomography (XCT) (Xradia 520 Versa, ZEISS, Oberkochen, Germany) were used to study the spreading and penetration of the inkjet printed ink on the textiles.

4.3 Results and Discussion

4.3.1 Contact Angle of Textiles

The surface energy of the textile plays an important role in controlling the liquid/textile interaction. The equilibrium contact angle between the liquid and the textile surface is often used as a metric to characterise the liquid-textile interaction. In practice, it is sometimes desirable to modify the surface energy of a textile, for example to control the ingress of water, and a number of commercial treatments have been developed for this purpose. The Scotchgard (SG) treatment applies proprietary fluoropolymer coatings to the textile fibre surfaces, modifying the fibre surface energy and subsequent fluid/fibre interactions without altering important textile properties such as flexibility and breathability.[112,113] Figure 4.1 (a) shows that a single drop (0.5 μL) of the ink on the as-received polyester fabric spreads and is absorbed into the fabric with an apparent contact angle close to 0°, while after SG treatment, a drop of ink rests on the surface with an apparent contact angle of ≈ 124°, as shown in Figure 4.1 (b).

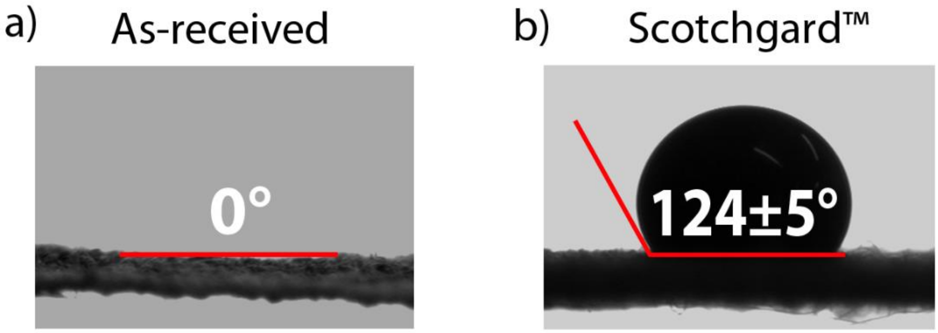

Figure 4.1 Contact angle values of silver ink on as-received polyester fabric (a) and SG-treated polyester fabric (b).

However, these above contact angle values only represent the surface properties of the substrate at a fabric scale when the liquid drop is considerably greater than the fibre diameter. As discussed in Chapter 2, Section 2.2.1.2, the roughness of the fabric surface leads to an increased apparent contact angle on a hydrophobic surface and decrease on a hydrophilic surface, based on the Wenzel and Cassie-Baxter models. Additionally, unlike conventional printed functional materials on polymeric or other non-absorbent surfaces, material printed on a textile substrate can be present both on the surface of the material and within its porous architecture to some depth below the surface. Thus, understanding the interactions between the fibres that make up the textile architecture and the ink becomes a 3-dimensional (3D) problem[128,234,235].

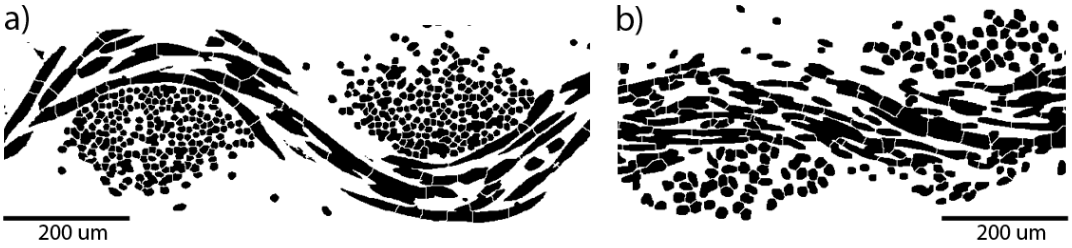

Figure 4.2 Binary images segmented by ImageJ from 2D slices of XCT reconstructions of fabric warp cross section (a) and weft cross section (b).

Considering the fabric used in this study, the warp and weft yarn tows have very different fibre architectures, even though they are both made from similar polyester fibre filaments of nominally the same composition. Figure 4.2 shows 2D slices from a XCT reconstruction analysed in ImageJ, where Figure 4.2 (a) shows a cross section of the fabric warp direction and Figure 4.2 (b) is a cross section of the fabric weft direction. It is obvious that there are a greater number of fibres in the warp yarn, with smaller fibre diameter and less yarn tortuosity (length of the yarn to the distance between its ends). The effective pore radius (r_{eff}) values, which is half of the effective pore size (a), is determined from the fibre volume fraction V_f, and mean fibre radius, r_f. as shown in the Equation (4.4-4.5) when assuming an ideal hexagonal packing of parallel fibres (Figure 4.3). The fibre volume fraction in warp yarn tows is higher than that of the weft yarn tows, which leads to smaller effective pore radius in warp yarns. Table 4.1 summarises the main yarn and fibre parameters, the detailed information and measurement methods are described in chapter 6.

$$V_f = \frac{A_f}{A_h} = \frac{\pi r_f^2}{\frac{3\sqrt{3}}{2}\left[\frac{r_{eff}+r_f}{\cos(30°)}\right]^2} \tag{4.4}$$

$$r_{eff} = \sqrt{\frac{\pi r_f^2}{2\sqrt{3}V_f}} - r_f \tag{4.5}$$

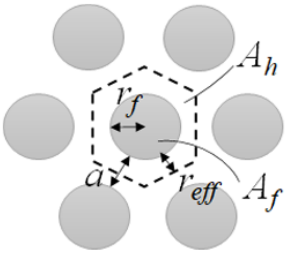

Figure 4.3 Schematic diagram showing the ideal hexagonal packing used for the effective pore spacing calculation.

Table 4.1 Key parameters of the woven fabric structures.

	Yarn longitude diameter (μm)	Fibre diameter (μm)	Mean fibres per thread	Fibre volume fraction	Effective pore radius (μm)	Tortuosity
Warp	300	10	210	0.60	1.15	1.05
Weft	300	16	50	0.50	2.75	1.19

The inkjet droplets used in this study have a volume of 7.0 pL, which is equivalent to a 24 μm diameter drop in flight. This is greater than the individual fibre diameters but of the same order of size. Thus to understand the interaction between single drops and the fibres within a yarn, the contact angle between a single droplet and a polyester fibre is of interest. Directly measuring the ink contact angle on cylindrical polyester fibres is a difficult exercise[347] and will be considered further. As a test for the validity of these methods, the advancing contact angle was measured between the silver ink and a polyester film of nominally the same composition as the fibres (Figure 4.4 (a) and (b)), with and without Scotchgard hydrophobic treatment.

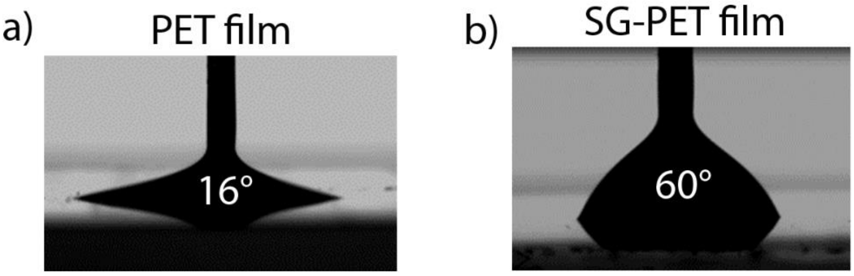

Figure 4.4 Advancing contact angle values of silver ink on polyester film (a) and Scotchgard-treated film (b).

To validate the assumption of chemical similarity between the film and fibres, IR spectra were recorded from both the Polyethylene terephthalate (PET) film and the polyester fabric (Figure 4.5(a)). The peaks at wavelengths of 718 cm^{-1}, 865 cm^{-1} and 1988 cm^{-1}, which are related to the benzene ring structure in the polymer, the ester group is present at the peak of 1090 cm^{-1} and 1241 cm^{-1} showing C-O stretching and the peak at 1710 cm^{-1} showing C=O stretching, finally the peak 2950 cm^{-1} illustrates alkane C-H stretching. The Scotchgard treatment applied by adding fluorine compound with C-F stretching at a peak range of 1000-1400 cm^{-1}is not obvious in Figure 4.5b), yet the contact angle values obtained on the PET film after applying the Scotchgard process display the effect of surface hydrophobic treatment[348–350], by increasing the contact angle from 16º to 60º (Figure 4.4).

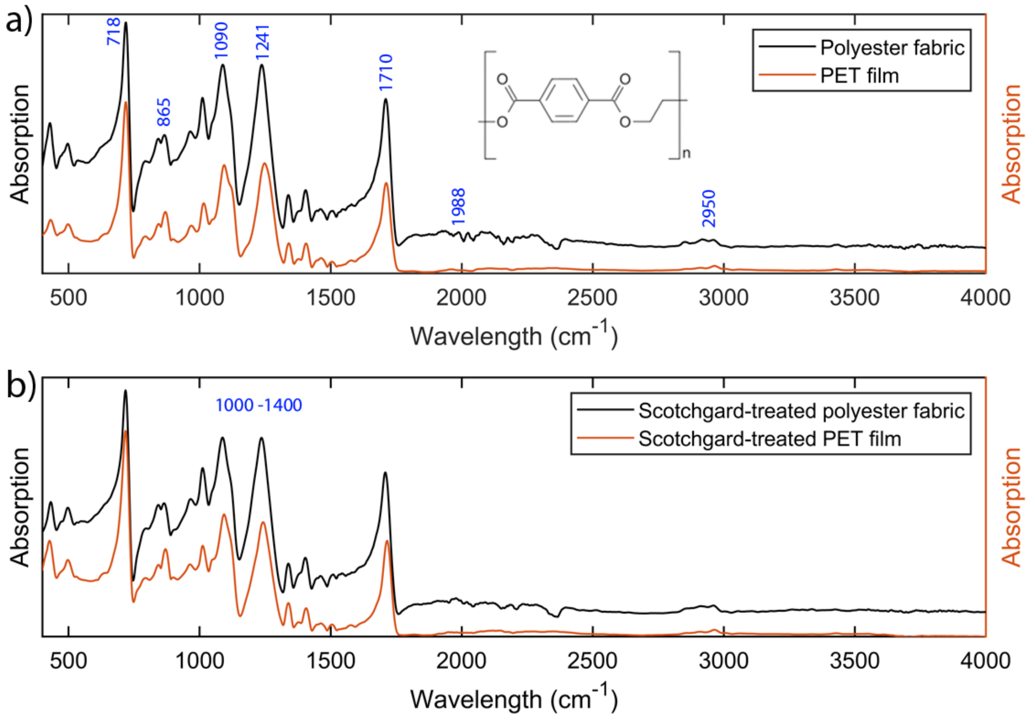

Figure 4.5 FTIR of polyester fabric and PET film (a) and Scotchgard-treated fabric and Scotchgard-treated PET film (b).

4.3.2 Ink/Fibre Interaction

The ink/fibre interaction has been studied by many researchers, with the aim of obtaining contact angle values of liquid droplets on fibres from their spreading geometries. When the scale of the drop is similar to both the fibre diameter and the spacing between fibres, three different local interaction geometries have been reported in the literature, leading to droplet morphologies termed: barrel shape, clam-shell shape and drop between fibres[138,330,334], as shown in Figure 4.6 (a). However, the warp and weft fibres in this fabric have different architectures. When ink droplets deposit on individual weft fibres, the drop diameter (24 µm) is similar to the sum of the weft fibre diameter and the weft fibre average pore spacing (23.2 µm). Thus, in most cases individual droplets interact with a single weft fibre and we expect barrel and clam-shell shaped deposition forms. This allows the drop/fibre interaction to be modelled as an equilibrium liquid-drop-shape. For the case of the warp fibres, the diameter of the droplets is two times greater than the warp fibre diameter plus its effective pore spacing (12.8 µm), hence we expect to observe drop between fibre deposition geometries.

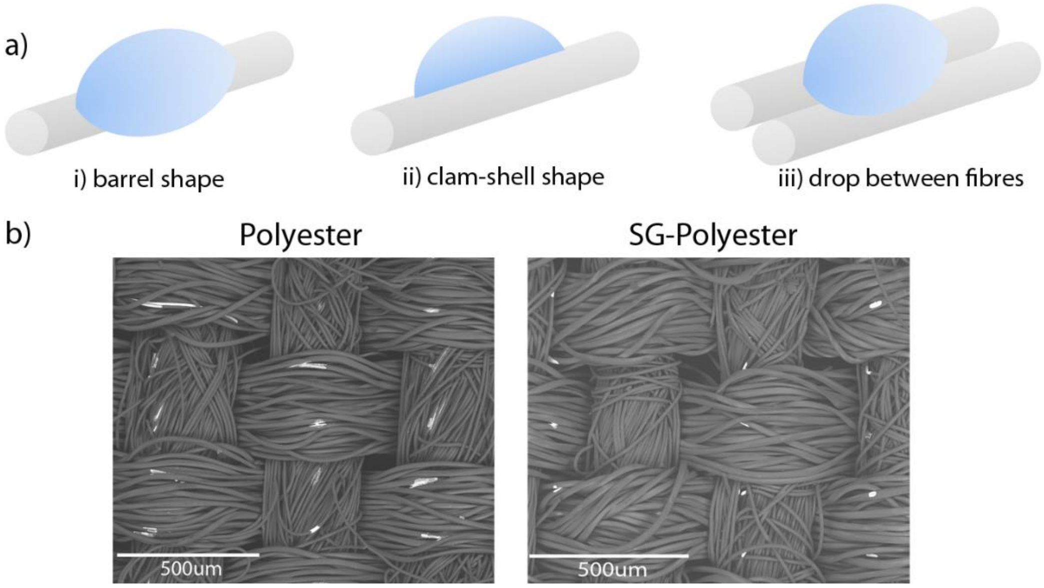

Figure 4.6 (a) 3 types of inkjet droplet interaction with fibres: barrel shape (left), clam-shell shape (middle) and drop between fibres (right); (b) SEM of single inkjet silver droplets on polyester fabrics (left) and Scotchgard-treated polyester fabrics (right).

As demonstrated in Chapter 2.2.3.1 including Yamaki and Katayama[138], Carroll and McHale[140,141], the length of fibre along which a single drop spreads can be used to estimate the contact angle between the ink and fibre surface if the volume of the drop and diameter of the fibre is known. Figure 4.6 b presents SEM images that show the extent of spreading of individual droplets of the Ag ink deposited on the as-received polyester and Scotchgard-treated fabrics after heat treatment. We assume that the ink drops are pinned and do not retract during drying and heat treatment, hence the images can be used to measure the ink spreading lengths in the warp and weft directions on each fabric sample. Considering the weft fibres, where we assume the majority of interactions are with single fibres, the silver ink droplets had a mean spreading length of 59 ± 14 μm on the as-received polyester fibres and 25 ± 8 μm on the Scotchgard treated fibres.

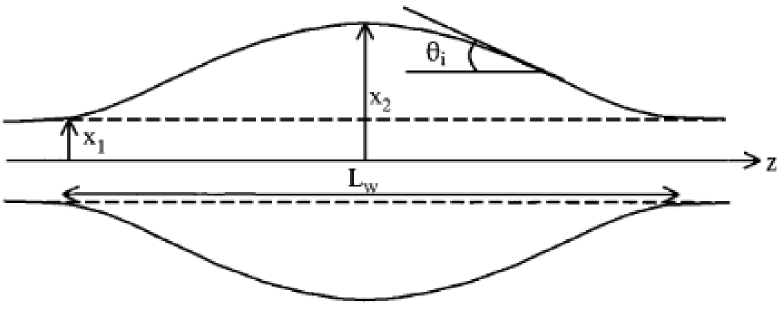

Figure 4.7 The cross section of droplet on a cylindrical geometry, in which x_1 stands for the fibre radius, x_2 represents the droplet radius, L_w is the wetted length and θ is the evaluated contact angle value.

When we apply these spreading length values into Carroll´s method[139], introducing drop on fibre system and Legendre’s standard incomplete elliptic integrals of the first and second kind. The profile of the droplet (Figure 4.7) can be solved given the wetted length (L_w) as shown in Equation 4.8. x_1 and x_2 are the two boundary conditions used to evaluate the drop profile, $\bar{L}$ is the reduced form of wetted length when x=x_1, $n = x_2/x_1$ is the reduced radius, and a, k and $\emptyset$ are defined in Equation 4.6-4.9, and the volume of the droplet (V) can be obtained as in Equation 4.10. Then the analytical expressions were derived and programmed using MATLAB (Appendix 4.1) based on the drop geometry and the equations demonstrated in Carroll’s paper.

$$\bar{L} = L_w/x_1 = 2[aF(\emptyset,k) + nE(\emptyset,k)] \tag{4.6}$$

$$a = (n\cos\theta - 1)/(n - \cos\theta) \tag{4.7}$$

$$k = \sqrt{1 - \frac{a^2}{n^2}} \tag{4.8}$$

$$sin\emptyset = \sqrt{\{(1/k^2)(1 - 1/n^2)\}} \tag{4.9}$$

$$\bar{V} = V/x_1^3 = \frac{2\pi n}{3}\left[(2a^2 + 3an + 2n^2)E(\emptyset,k) - a^2F(\emptyset,k) + \frac{1}{n}(n^2 - 1)^{\frac{1}{2}}(1 - a^2)^{\frac{1}{2}}\right] - \pi\bar{L} \tag{4.10}$$

Figure 4.8 (a) and (b) are generated and plotted in intervals of contact angle value of 5°, showing the ratio of the maximum drop height to the fibre radius (n) as a function of normalised drop volume ($\bar{V}$) and wetted length ($\bar{L}$), respectively. Through integrating the equations, the n values are highlighted when the drop volume is equal to 7pL and the wetted length equal to 59 μm (polyester fibre) and 25 μm (Scotchgard treated polyester fibre) as experimentally measured.

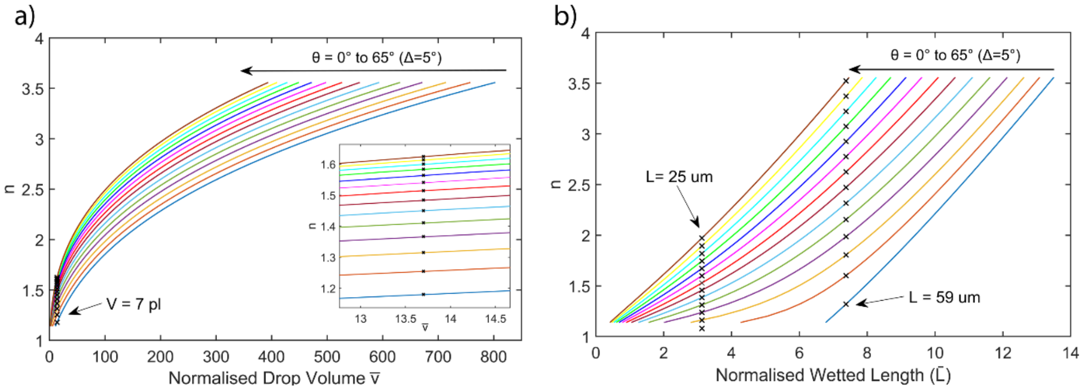

Figure 4.8 (a) Normalised drop volume ($\bar{V}$) as a function of *n* for contact angle values (θ = 0º to 65º), the corelated *n* values at when $\bar{V}$ equals to 7 pL are approximated and marked; (b) normalised wetted length as a function of *n* for contact angle values (θ = 0º to 65º), the correlated *n* values at when $\bar{L}$ equals to 25 μm and 59 μm are approximated and marked.

Accordingly, the contact angle values of the ink interaction with fibres in our experiment can be obtained at the point where the contact angle (θ) and value *n* are equal for both drop volume and wetted length. Therefore, Figure 4.9 is used to plot the contact angle values (θ) as a function of value *n*. the black lines in the figure represent the values of θ and *n* when the drop volume in 7 ± 0.3 pL, the red and yellow lines mark the region when the wetted length of drop on fibre at 59 ± 14 μm and 25 ± 8 μm respectively. Additionally the transition line from barrel to clam shell shaped deposition as demonstrated by McHale[141] is plotted in blue in the figure[143]. It is found that the drop deposition on as-received polyester fibres lies in the barrel shaped region while the drop deposition on Scotchgard treated fibres in our experiment is clearly in the clam shell shaped region. The crossing point of the red and black lines indicates a contact angle value of 5º for a silver ink droplet on the polyester fibre and a contact angle of 35º on the Scotchgard treated polyester fibre. However, since the calculation of drop volume in the Carroll's theory is based on a barrel shaped droplet, the contact angle value on the Scotchgard treated fibre is not regarded as valid.

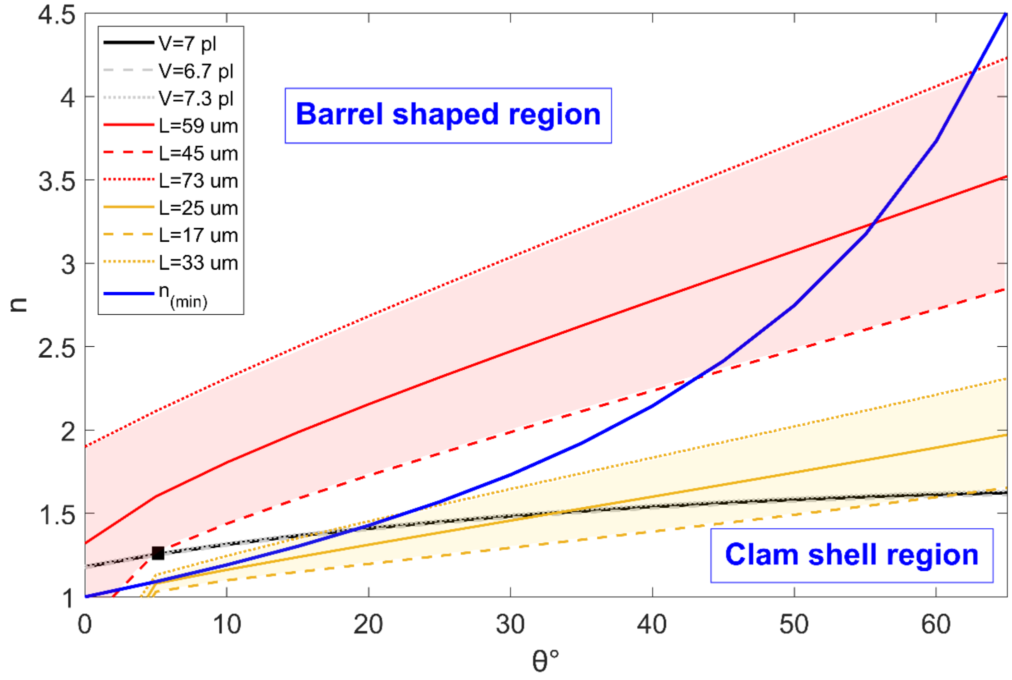

Figure 4.9 Contact angle value (*θ*) as a function of value *n* (the maximum drop height to the fibre radius), The blue line indicates the separation of the barrel shaped and clam shell shaped regions, the black line represents the values of θ and n when the drop volume in 7 ± 0.3 pL, the red and yellow areas mark when the wetted length of drop on fibre at 59 ± 14 μm and 25 ± 8 μm respectively, the black square dot shows the estimation of the contact angle value of the silver ink on the polyester fibre.

If the conditions of contact angle and drop volume are such that a liquid drop spreads to a barrel-shaped morphology on a fibre, the liquid-drop-shape interaction method can be used to extract contact angle values from measurements of the spreading length and the known drop volume. However, there is a difference between the contact angle values measured on the fibre (5°) and that measured on a PET film of similar composition (16°). This difference could be the result of the simplifying assumptions involved in modelling the fibre/fluid interactions or that the surfaces of the films have different surface energies from that of the fibres. Given the size of the difference between the two results, it is more likely that this represents a significant difference in the surface energies. The Scotchgard treatment clearly leads to a change in surface energy of the polyester film and an increase in the contact angle. We can safely assume that the contact angle also increases on treating the fibres in the textile. However, there are no analytical solutions for the equilibrium drop shape on a fibre when the surface energy and drop size leads to a clam shell or fibre bridging morphology, due to its complexity and lack of symmetry. Only numerical approaches to this problem, such as finite element computation have been reported in these cases[135,333,351,352], which is beyond the scope of this project. Nonetheless, these simple experiments show that the influence of the Scotchgard treatment on polyester fibres produces a change in contact angle that is consistent with the change seen using similar composition polymer films.

By comparing our experimental results with existing theories, the interaction of a single silver ink droplet with similar length scale as-received polyester fibres follows the behaviour consistent with a barrel-shaped equilibrium drop. However, on Scotchgard treated fibres the interaction leads to a more complex drop shape that cannot be easily analysed. It is seen from microscope images of single drops on a textile surface that drop volume, fibre surface energy and local fibre structures in the fabric all play important roles defining the ink spreading and deposition on fibres. In short, on Scotchgard-treated fibres, silver ink droplets maintain similar spreading length on both warp and weft fibres. However, on as-received, untreated polyester fibres, the silver ink droplets penetrate and form spreading columns between warp fibre gaps. On polyester weft fibres, the spreading length varies, where longer spreading length is achieved when ink droplets form barrel or clam-shell shaped deposition, yet the spreading length is reduced when ink droplets land between weft fibres where the greater fibre pore spacing favours the penetration mechanism rather than spreading along the fibre tows. Thus, although a study of single drop/single fibre interactions can be used to estimate the appropriate contact angle, a full understanding of the interaction of liquids with fibres should consider the behaviour of bundles of fibres consistent with the internal architecture of a fabric.

4.3.3 Ink/Yarn Interaction

Liquid transport at the yarn scale is expected to be different to that at the fibre scale, especially when the inter-fibre pores are filled with ink. An approach based on Washburn equation[153] and Darcy's law[154] is used to understand the ink-yarn interaction. Experiments were carried out to study and evaluate feasibility of explaining ink yarn interaction using these governing laws. A large volume ink droplet (approximately 5 μl) was deposited onto single warp and weft yarns from the woven polyester fabric as shown in Figure 4.10 (a). Ink infiltration occurred along the as-received polyester yarn as shown in Figure 4.10 (b), whereas little or no infiltration was found on the Scotchgard-treated yarn beyond spreading along the surface.

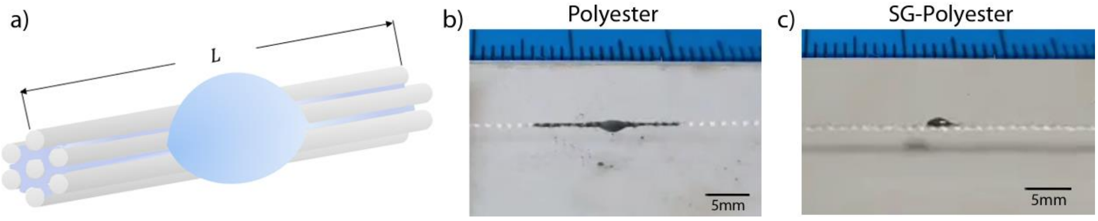

Figure 4.10 Scheme of ink/yarn interaction experiment (a) with the video snapshot of ink spreading on polyester yarn (b) and Scotchgard-treated polyester (c).

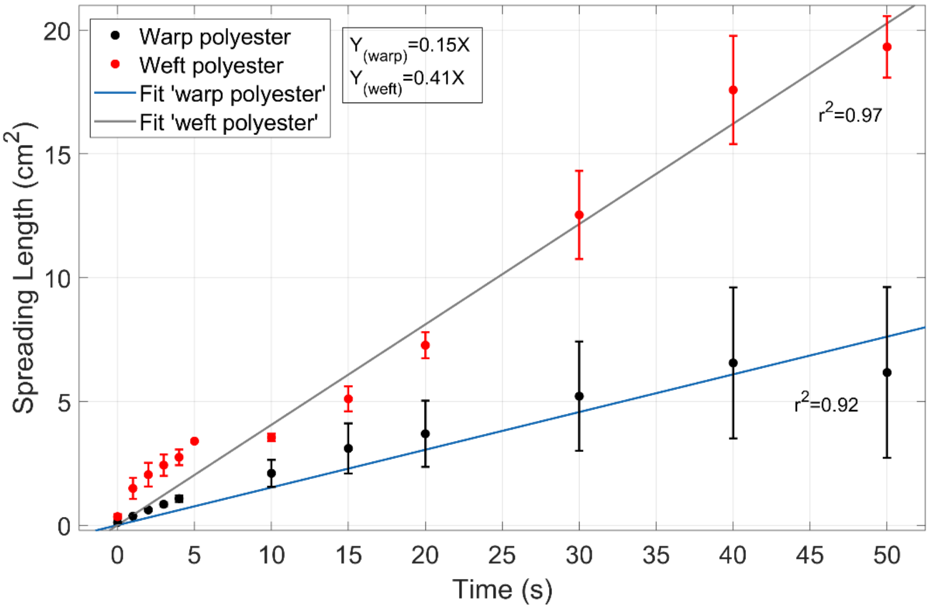

Figure 4.11 Infiltration rate of ink along as-received polyester fibre yarn tows. Spreading length squared as a function of time of ink droplet deposition on a single yarn tow, warp yarn (black dots) and weft yarn (red dots).

The infiltration data is presented as the square of the spreading length, L^2, of an ink droplet on the yarn as a function of time, t, as shown in Figure 4.11. The data shows an approximately linear relation as predicted by Equations (4.1) and (4.2). The gradient of the linear fit $(\frac{L^2}{t})$ is presented in Table 4.2, with a value 0.15 cm^2.s^{-1} measured along the warp yarn and 0.41 cm^2.s^{-1} along the weft yarn, with r^2 = 0.92 and 0.97 for the warp and weft polyester yarns, respectively. Table 4.2 also displays the values of $(\frac{L^2}{t})$ obtained using the approach of Washburn and Darcy with the experimentally determined values of fibre radius, effective pore radius and porosity as measured experimentally and given in Table 4.1. We use the manufacturer's supplied data for viscosity (μ = 14 mN.m^{-2}.s) and surface tension (γ_{LV} = 37.5 x 10^{-3} N.m^{-1}) of the ink, contact angle is as measured on the PET film (16°).

Using Washburn's equation the best agreement with experimental data occurs using an empirical constant $C = 10.9\pm0.8$, which accounts for the assumptions including the measurement of fibre pores as capillary tubes, ideal hexagonal packing format of fibres and the use of the Young-Laplace equation in a single tube condition[353,354]. Note that at these low values of contact angle the predicted infiltration rate is proportional to $\cos\theta$, which is 0.961 and 0.996 for contact angles of 16° and 5° respectively, thus the only effect of using the lower contact angle measured on the fibres will be to change the value of the constant C to 10.5.

With Darcy's law, the undefined empirical constant K introduces difficulties to evaluate the permeability of the yarn k.[167–171] The permeability also depends on fibre radius r_f (warp: 5 μm and weft: 8 μm), the porosity $\varphi=(1-V_f)$ (warp: 0.4 and weft 0.5) and the sphericity of warp and weft yarns $\emptyset$ (1.86 for 10 cm length warp and weft yarns), and apply the empirical constant $K = 86.2\pm5.4$, the permeability of warp and weft yarns results in 0.72 μm² and 5.14 μm² respectively, which leads to an estimation of the infiltration rates of ink drop on warp and weft yarns of 0.16 cm^2.s^{-1} and 0.38 cm^2.s^{-1}.

Table 4.2 Infiltration rate $\frac{L^2}{t}$ calculated through Washburn equation and Darcy's law on polyester warp and weft yarns (when estimate ink/fibre contact angle $\theta=16^o$) in comparison with experimental values.

Yarn Orientation	Experimental	Washburn ($C=10.9$)	Darcy's law ($K=86.2$)
	Infiltration rate $\frac{L^2}{t}\,(cm^2/s)$		
Warp Yarn	0.15 cm^2.s^{-1}	0.16 cm^2.s^{-1}	0.16 cm^2.s^{-1}
Weft Yarn	0.41 cm^2.s^{-1}	0.39 cm^2.s^{-1}	0.38 cm^2.s^{-1}

The Washburn's equation shows slightly better agreement with our experimental values with the effective pore radius (r_{eff}) playing the key role in the equation, where the greater pore radius in the weft yarn could lead to faster liquid transport in yarns. However, even with a close estimation through Darcy's law, the number of undefined variables in Darcy's law leads uncertainties of the prediction.

4.3.4 Ink/Fabric Interaction

Liquid/fabric interaction is often studied for textile wet finishing operations, similar models based on the approach of Washburn and Darcy can be found in the literature explaining both liquid/yarn and liquid/fabric interactions as a capillary wicking process. However, it is well-known that variation in fibre density and diameter, yarn density and thickness, and the woven structure can lead to different liquid/fabric interactions[12,171,175,337,342,355]. A silver ink wicking test[356] was conducted on the polyester fabric in both fabric warp and weft directions(Figure 4.12 (a)). A faster wicking rate and longer wicking length is observed on the fabric warp direction, which is opposite to the findings in our earlier experiments on the ink/yarn interaction. Scotchgard-treated fabric could not be analysed using this method due to of its low absorption behaviour.

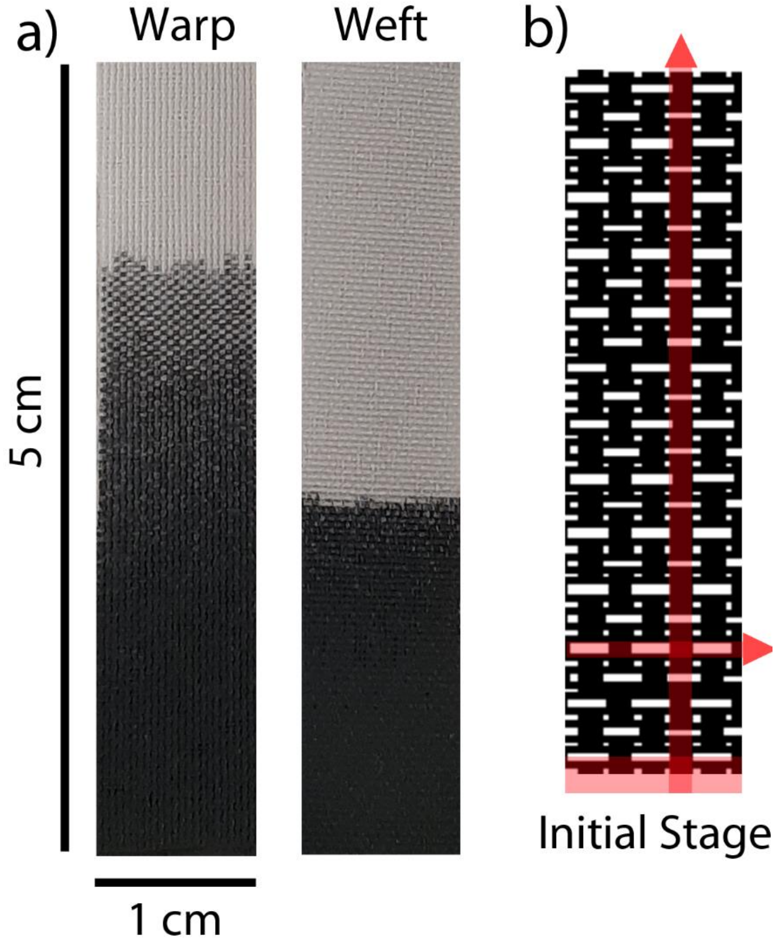

Figure 4.12 (a) ink/fabric wicking test set-up, (b) silver ink absorption on polyester fabric on warp and weft directions after 120 seconds elapsed time, (c) illustrated fabric woven structure with red marked area initiating the wicking process, and arrows pointing the potential direction of ink transportation in fabrics.

The squared weight gain (m^2) is plotted as a function of time in Figure 4.13, and the plot is divided into a linear increased initial stage where the fabric initially touches the ink reservoir as the red marked area in Figure 4.12 (b), a curved transition stage and a stabilised stage where the plot gradient is linear in the dotted orange box area (time > 20 s). The non-linear ink infiltration and wicking at the initial stage of the weight absorption test is well known [174] and its analysis is beyond the scope of this project, and we will discuss the ink/fabric interaction based only on the stabilised stage with constant L^2/t.

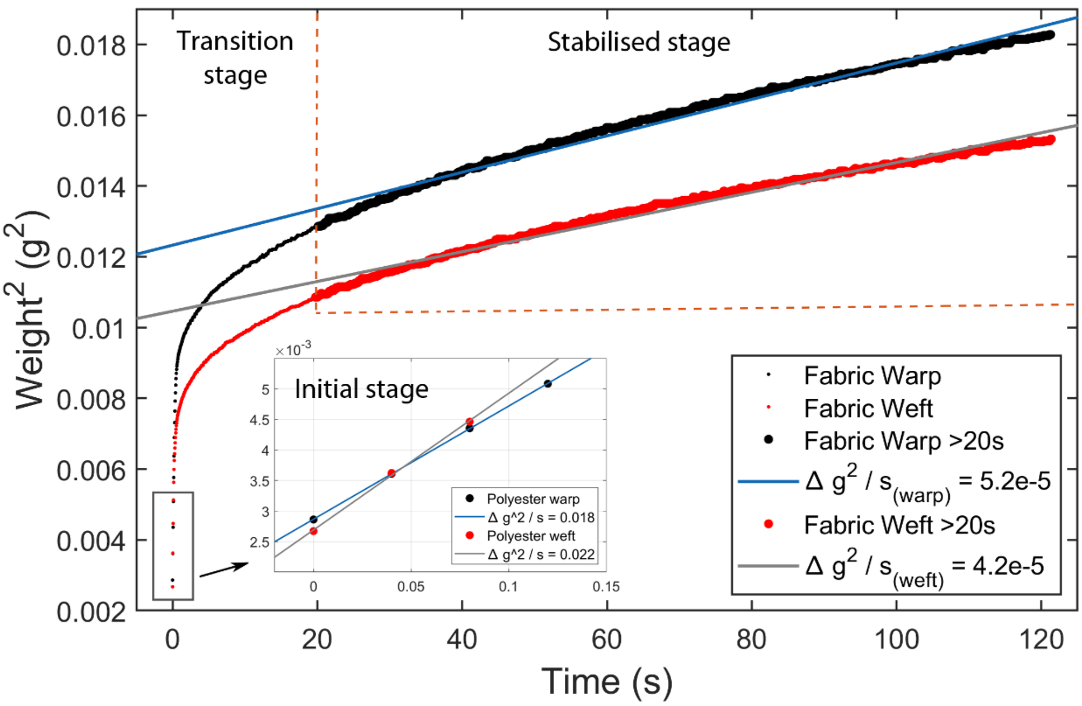

Figure 4.13 weight gain squared as a function of time as silver ink absorption on polyester warp (black dots) and weft (red dots) directions.

This wicking test method developed by Kruss GmbH. is based on Equation (4.3)[356], where the weight gain rate is measured and recorded as $\frac{m^2}{t}$, which is equal to the spreading rate $\frac{l^2}{t}$ times the squared silver ink density ρ^2 and the squared cross-section area of the pores in the fabric A^2. If we apply the silver ink density value (1.45 g/mL) from the manufactures' data and the spreading rate ($\frac{l^2}{t}$, warp: 0.15 cm^2.s^{-1} and weft: 0.41 cm^2.s^{-1}) obtained in the previous ink/yarn experiments, we can compare the estimated weight gain assuming the ink/fabric interaction follows the ink/yarn interaction.

$$A = A_{pore} * N \tag{4.11}$$

$$\rho_{fm} * fabric\ width = \rho_{y,warp} * m_{y,warp} + \rho_{y,weft} * m_{y,weft} \tag{4.12}$$

$$\frac{m_{y,warp}}{m_{y,weft}} = \frac{\rho_{fibre} * A_{y,warp} * l}{\rho_{fibre} * A_{y,weft} * l} = \frac{A_{y,warp}}{A_{y,weft}} \tag{4.13}$$

$$N = \rho_{fm}/m_y \tag{4.14}$$

The appropriate data for the fabric was either supplied by the manufacturer (Table 3.2) or measured using X-Ray tomography and was reported earlier in Table 4.1. The cross-sectional area of the pores in the fabric (A) is equal to the pore area in each yarn tow as A_{pore}, and the number of the yarns in 1 cm (N, matching the experimental fabric width), as shown in Equation (4.11). However, since ink can transport along both warp and weft yarns in the fabric, as observed in Figure 4.12 (a) and illustrated in Figure 4.12 (b), here the estimated weight gain of ink in the fabric is defined assuming the fabric is filled with only warp or weft yarns in a single direction but with the same fabric mass density (ρ_{fm}=145 g/m^2). Equation 4.12 shows that the fabric mass density is equal to the yarn linear density (ρ_y, 23.6 warp yarns.cm^{-1} and 30 weft yarns.cm^{-1}) times the individual warp and weft yarn mass (m_y). The warp and weft yarn weight ratio ($\frac{m_{y,warp}}{m_{y,weft}}$), which equals to the yarn cross-section area ratio ($\frac{A_{y,warp}}{A_{y,weft}}$), when the fibre density (ρ_{fibre}) and yarn length (l) on warp and weft directions remain identical (Equation 4.13). Through combining Equation 4.12 and 4.13, the individual warp and weft yarn mass (m_y) can be calculated, and the number of one direction yarns that can be filled parallel in the fabric reveals in Equation 4.14. Table 4.3 shows the related parameters for calculating A and the details can be found in chapter 6, and the average is taken in this section.

Table 4.3 Parameters used to calculate the cross-section pore area in a 1 cm fabric width when filled with parallel yarns.

Directions	$A_{yarn}(um^2)$	N	A_{pore} (um^2)	A (um^2)
Warp	5250π	41.8	18000	7.52E5
Weft	3200 π	68.7	12500	8.59E5

With the above information, the weight gain can be estimated from Equation 4.5. Table 4.4 compares the weight gain rate values calculated using the experimental data obtained for the ink/yarn interaction and the experimentally measured ink/fabric interaction (the gradient values in Figure 4.13).

Table 4.4 Weight gain rate comparing ideal warp and weft fabrics with that measured experimentally in the linear range in Figure 4.13.

Fabric Orientation	Multi yarns (ink/yarn based)	Fabric (experimental)
	Weight gain rate ($\frac{g^2}{s}$)	
Warp	1.8×10^{-5}	5.2×10^{-5}
Weft	6.4×10^{-5}	4.2×10^{-5}
Mean Value	4.1×10^{-5}	4.7×10^{-5}

Similar weight gain rate results were found between calculated values assuming parallel yarns in the fabrics and the experimental measured values. However, the observed greater weight gain found along the fabric warp direction than along the fabric weft direction is opposite to the results found with ink/yarn interaction experiments on single yarns, where the greater pore radius in the weft yarns leads to a faster spreading rate. There could be a number of reasons for the difference between the weight absorption rate in fabrics and yarns. One is the capillary effect of the pores between the yarns in the fabric scale – the infiltration rate is proportional to the effective pore radius so a small fraction of fabric scale pores may have a significant effect in addition to the infiltration at the fibre length scale. Additionally, the fabric weaving process makes the thicker warp yarns straight and in tension, and the thinner weft yarns result in higher tortuosity as shown in Figure 4.2 a) and b), which leads to a longer effective transportation length in the fabric weft direction. This behaviour can be seen in Figure 4.12, where ink travels faster and longer vertically on the fabric warp direction following the warp yarns, while ink travels slower and shorter on the fabric weft direction with a trend of following the horizontal warp yarns, after the 120 s experimental procedure. Moreover, the effective pore radius applied in the ink/yarn interaction could be different to that of the ink/fabric interaction, since the individual yarns deconstructed from the fabrics can vary significantly from the structure when held together in the fabric.

This section raises the difference between ink/fabric interaction and ink/yarn interaction that often ignored in other studies. It was observed that faster and greater ink was transported in the fabric warp direction with smaller effective pore radius, which is opposite to behaviours theoretically found from Washburn and Darcy's law, and experimentally. Due to sophisticated fabric structures, it is difficult to clarify the specific reason that leads to ambiguous prediction of ink/fabric interaction.

4.3.5 Inkjet Printed Silver Ink on Textiles

In order to evaluate the transport of ink delivered by inkjet printing to textile surfaces, 5 mm*5 mm silver patches were printed on polyester and Scotchgard treated polyester fabrics with 20 μm and 10 μm drop spacing, respectively. The optical images in Figure 4.14 shows that the increased surface hydrophobicity of the Scotchgard treated fabric leads to improved printing pattern quality, on the other hand the reduced drop spacing reduces the printing pattern quality, where ink feathering (blurring or unclear printed patterns) occurs with higher amount of ink deposition. Interestingly, greater ink bleeding (transport away from the desired printed area) is seen in the fabric warp direction than the weft direction in all samples, which matches the findings in the ink/fibre and ink/fabric interactions yet shows the risks of using ink/yarn interaction to predict the spreading behaviour at the fabric level.

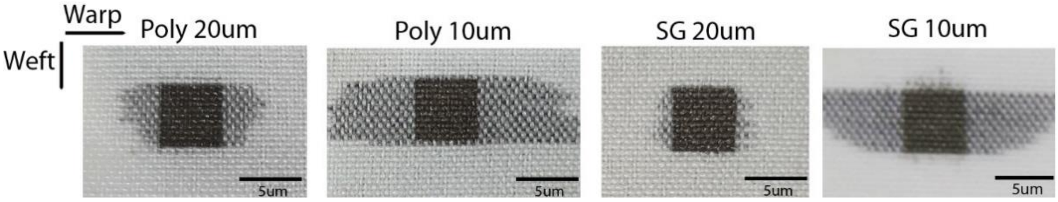

Figure 4.14 Optical images of inkjet-printed and sintered silver ink on polyester fabrics with different drop spacing (20 μm and 10 μm), hydrophobic treatment (Poly: as-received polyester fabrics, SG: Scotchgard-treated fabrics).

When ink interacts with porous textile materials, spreading is associated with penetration. To understand the cause of different spreading behaviours, Figure 4.15 displays cross sections of the fabrics in both warp and weft directions obtained by X-ray tomography, which gives a 3d view of silver ink/textile interaction (the white colour represents the silver location). It is observed that ink is only located at the surface of the warp yarns instead of penetrating to the centre of the yarns, which induces ink over-spreading and indicates a higher capillary force driving faster spreading near the yarn surface, rather than penetrating into the yarn tow interior. On the other hand, ink travels to the centre of the weft yarns suggesting that the penetration mechanism is more favoured than the spreading. This indicates that the first stage of inkjet printed ink interaction with textiles corelates with the previous studied ink/fibre interaction. After hydrophobic surface treatment, ink droplets are pinned on the surface of the fibres with increased contact angle, which leads to less spreading and higher silver deposition volume. The reduced drop spacing leads to increased silver deposition on both fabric warp and weft directions, despite worse printing quality found on the fabric warp direction where ink favours the spreading. The difference between the warp and weft directions indicates the possibility to control the printing quality by simply modifying or selecting different textile architectures.

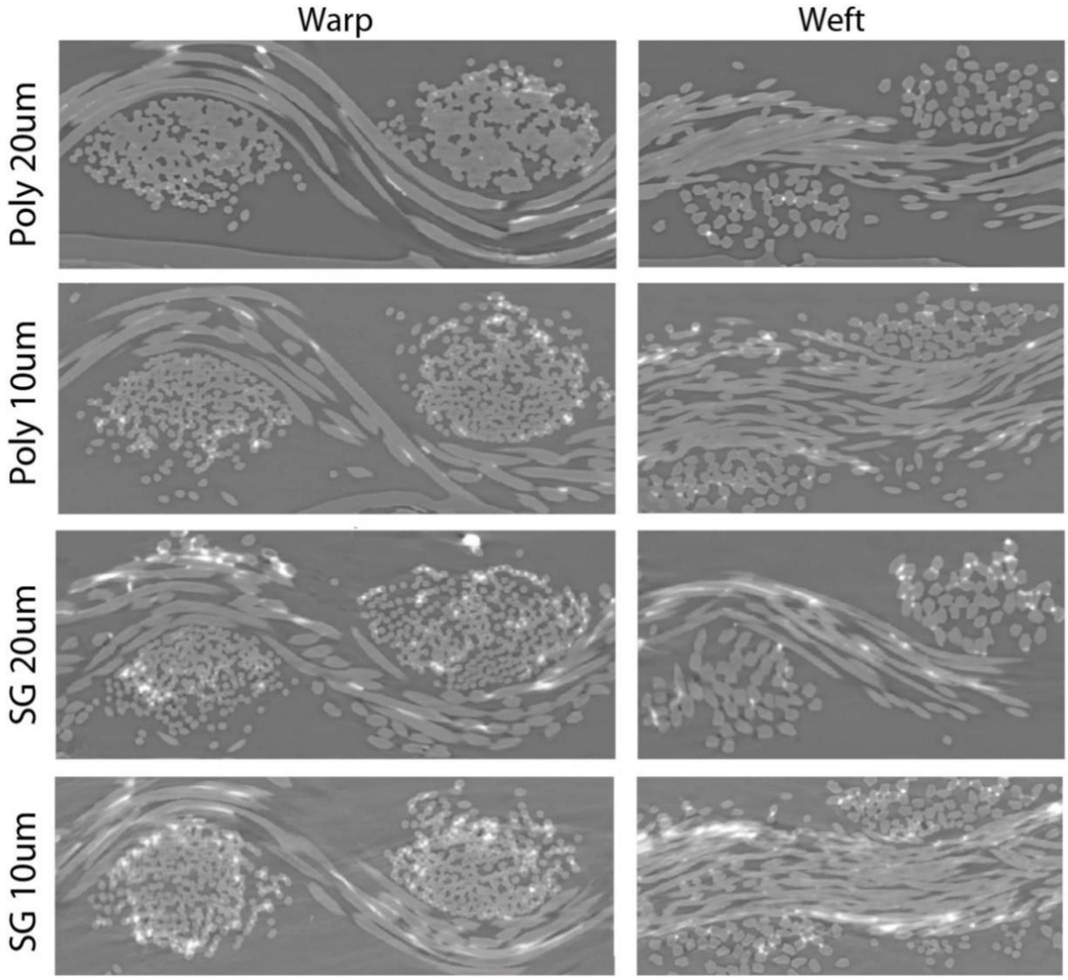

Figure 4.15 Cross-section of reconstructed X-ray tomography images of silver ink deposition on fabrics with different drop spacing (20 μm and 10 μm), hydrophobic treatment (Poly: as-received polyester fabrics, SG: Scotchgard-treated fabrics), warp stands for the cross section where warp yarns that run into the depth of the page and vice versa.

4.4 Conclusions

In conclusion, ink/textile interaction has been studied comprehensively in this chapter, where individual fibre, yarn and fabric scales were investigated by comparing experimental values and existing theories. The importance of ink/fibre contact angle and the effective pore radius between fibres was highlighted. The effective pore radius can be measured using the XCT cross section images, while the ink/fibre contact angle is difficult to be obtained. Therefore, ink/fibre interaction was initially discussed with the aim of estimating the contact angle value through the drop-on-fibre profile as reported in literatures. It was found that ink/fibre interaction corresponds with existing theories, when ink properties are constant, the low fibre surface energy leads to increased spreading on fibres, and depending on the size of the fibres and the droplets, different ink/fibre interaction shape occurs, for barrel and clam-shell shaped interactions, it is the fibre surface energy and drop and fibre geometries determines the spreading length, while pore spacing plays an important role when ink lands between fibre gaps, where smaller pore size/fibre size creates ink columns and spreading between fibres and larger pore size/ fibre size leads to ink penetration.

Subsequently, with the defined ink/fibre contact angle values, ink/yarn interaction was analysed using the approaches from Washburn and Darcy. It was found that the effective pore radius becomes the most important factor in both laws, where greater effective pore radius on weft yarns lead to faster and longer ink spreading in yarns. Meanwhile, through the experimental results of the ink penetration as a function of time and other known ink and yarn parameters, the geometric constants that used to conclude the effect of textile shape factors on ink/yarn interaction were obtained, and both laws were found to be an appropriate use of estimating the ink penetration as a function of time. Interestingly, existing theories used to explain ink/fibre and ink/yarn interactions are insufficient to explain the ink/fabric interaction. The weight gain as a function of time was used to observe the ink/fabric interaction and similar weight gain rate results were found between calculated values assuming parallel yarns in the fabrics and the experimental measured values. However, greater weight gain results on the fabric warp direction than the fabric weft direction is opposite to ink/yarn interaction findings, which indicated the need of further dynamic studies in this area due to the complexity of the textile architecture.

Chapter 5 The Conductivity of Inkjet Printed Ag on Textiles

5.1 Introduction

The application of strong and flexible textile substrates for wearable technology has shown its advantages over conventional polymer film flexible substrates[6,9,21,55,62,245,323,357]. Conducting textiles can be fabricated by incorporating conductive fibres into the fabric architecture,[358–360] or by integrating flexible structures into or onto the textile[361,362]. Conductive fibres can be attached to the textile via stitching and embroidery methods [363–365] or selective deposition of conducting material can be used to modify the fabric surface or infiltrate into the fibre architecture[53,289,366–369]. Inkjet printing has been widely studied as a promising manufacturing tool in the area of e-textiles and wearable technology[4,59,329,370,371]. However, to enable these wearable monitoring systems by the provision of power or the exchange of data, the challenge of providing continuous conductive lines and patterns on textiles must be addressed[3,4,8,15,289].

A distinct difference between printing functional materials on textile substrates and on polymeric films is the influence of substrate porosity[53,162,277,278]. The formation of inkjet printed conductive paths on solid surfaces has been shown to depend on the stability of patterns formed through the spreading and coalescence of drops on the substrate surface[194,229]. Structures printed on porous substrates, such as textiles, are controlled by two competing fluid processes after drop impact, the flow of fluid along the surface and the infiltration of the liquid into the pores via capillary interactions[91,234]. Thus, unlike conventional printed functional materials, the low viscosity inkjet ink can be present both on the surface of the material and within its porous architecture, to some depth below the surface[4,8,91]. Additionally, anisotropic behaviours on textile warp and weft directions have been reported in the literatures due to complicated textile structures, researchers have investigated on a range of electrical conductivity measurement methods in order to present the mechanism of conductive textiles appropriately[279–284].

To overcome the difficulty of printing controlled patterns on porous and rough surface of textiles, a number of different strategies to alleviate the problems associated with printing on textile surfaces have been proposed: e.g. applying thick interface and protective layers, or incorporating polymer nanoparticles into the ink[1,3,4,59,242,288,289]. However, strategies adopted to improve electrical conductivity can compromise some of the advantages associated with textiles, e.g. flexibility, breathability and wash resistance. Thus, it is essential to consider the fundamental studies of the interaction of conductive inks with fibrous substrates.

In addition to the ink/textile interaction analysis, this chapter will investigate the textile architecture and ink interaction as a 3-dimensional (3D) phenomenon that influences conductivity. This is achieved by using X-ray computed tomography (XCT), which has been widely used to provide images of 3D fibre architecture in polymer composites and its effect on their mechanical and physical properties[372–375]. It has also been used to characterize fluid flow in porous materials[376,377] and there have been a few studies have used this and similar techniques to investigate liquid transport mechanisms in textiles[378,379]. However, to the best of our knowledge, there have been no previous studies that have reported the use of XCT to investigate the interactions between conductive inks and textiles such as presented in this work[380].

In this chapter, most of the contents have been previously published[380]. A silver nanoparticle ink with high atomic number and superior electrical performance compared to polymer and carbon-based inks is used to investigate the effects of inkjet drop spacing, water repellent finishes, sintering techniques and fabric structures on the electrical performance of printed textiles. The interaction of silver nanoparticles with textile substrates after inkjet deposition and thermal treatment is investigated using X-ray computed tomography (XCT). This allows the 3D reconstructed images of the Ag distribution and an understanding of the contribution of the printed structures to conductivity. It is believed that a better understanding of the ink textile interaction process will allow the development of appropriate textile surface treatments to control ink deposition, deposit elasticity and adhesion to enable the printing of conductive tracks with retained conductivity, washability and fabric breathability.

5.2 Experimental methods

Plain woven polyester fabrics, provided by Premier Textiles (Manchester, UK), and Scotchgard-treated (FC-3548, from 3M, Binfield, UK) polyester fabrics were used as the substrates, details can be found in Chapter 3 Materials and Methods. Two drop spacings of 10 μm and 20 μm were used to study the influence of drop overlap on the substrate. 2 sets of settings (SAL and SPL) were applied to compare different sintering techniques with multiple layers of printing (DMP 2800, Fujifilm Dimatix, Santa Clara, CA, USA). The surface morphology of the printed silver patterns was imaged using scanning electron microscopy (SEM) (Quanta 250 FEG, Thermo Fisher, Eindhoven, Netherlands). In order to determine the penetration of the Ag ink into the fibre architecture of the fabric in a 3d view, Ag distribution after printing and processing was imaged using X-ray computed tomography (XCT) (Xradia 520 Versa, ZEISS, Oberkochen, Germany). An optimal set up was applied to avoid focus blurring and achieve efficient pixel size. The data was reconstructed using the Zeiss Scout and Scan software. The voxel size in the reconstructed data was 1.13 μm. The reconstructed XCT data was further analyzed and segmented using the Avizo 9 visualization software (Amira Avizo, Thermo Fisher, Waltham, MA).

Electrical conductance along a single yarn tow, in either the warp or weft directions of the fabric, was measured using a 4-point probe (Jandel Engineering, Linslade, UK) coupled to a current source and voltmeter (Keithley 2400, Cleveland, OH), as introduced in Chapter 3.3.6.

5.3 Results and Discussion

5.3.1 Distribution of AgNP Ink

5.3.1.1 The Effect of Surface Treatment and Drop Spacing

Previous work on the printing of lines and patterns on solid and porous surfaces has demonstrated the importance of both the spacing of drops printed on the surface and the fluid-substrate contact angle in determining the morphology of printed structures[91,194,229,234]. In the previous Chapter 4 it was also shown that the contact angle has a strong influence on the static equilibrium shape of a drop of ink on a single fibre and the interaction of ink with tows of fibre in yarns, although the determination of the contact angle as measured on textile surfaces was shown to have difficulties. Increased hydrophobicity on textile surfaces after treatment was found with the contact angle value of the silver ink on fabrics increasing from 0º to 124º on fabrics.

Here we used the commercial Scotchgard™ (SG) treatment to investigate the effect of contact angle. SG applies proprietary fluoropolymer coatings to the textile fibre surfaces, modifying the fibre surface energy and subsequent ink/fibre interactions without altering important textile properties such as flexibility and breathability[112–114].

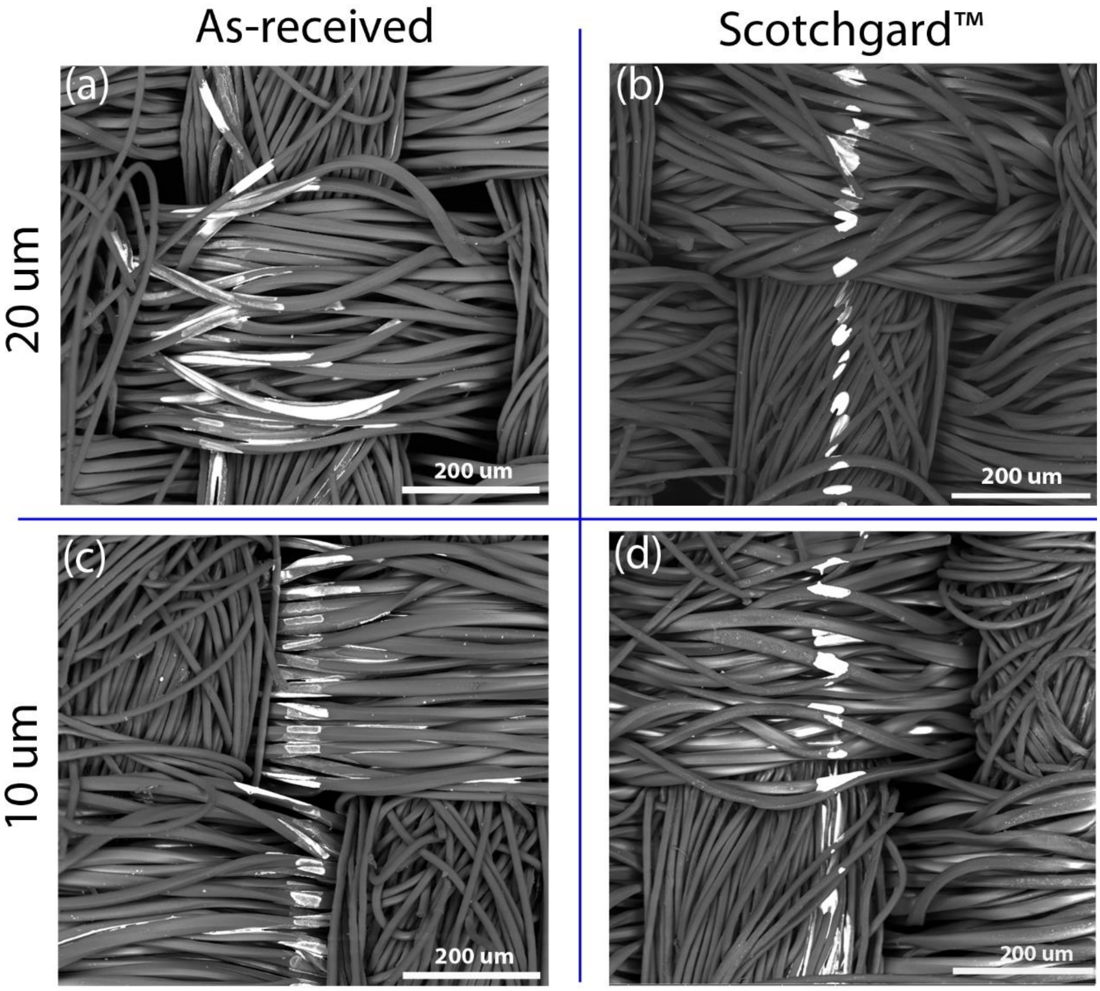

Figure 5.1 SEM images of a single Ag line on printed on the polyester fabric with 20 μm drop spacing (a) and 10 μm drop spacing (c), and on the SG-treated fabric (b) and (d).

The inkjet printer produces drops with an approximate diameter in flight of 24 μm (calculated from the measured printed drop volume). Hence we expect that at both values of printed drop spacing used in this study (10 μm and 20 μm), adjacent printed drops are expected to overlap and interact. Figures 5.1 a) and 5.1 b) show scanning electron microscope (SEM) images of a single line of ink printed with 20 μm drop spacing on the as received polyester and SG treated fabrics, respectively. The two fabrics show very different behaviour, consistent with the apparent contact angles between the ink and the fibres. The width of the Ag deposit on the surface of fabrics (Figure 5.1a and b) are approximately 60 μm and 30 μm on the as-received and SG treated fabrics respectively. The SEM image of the Ag on the as-received fabric also shows clear evidence of further ink penetration parallel to the fibres beneath the surface. This penetration and transport distance is considerably larger than the mean ejected drop diameter of 24 μm, demonstrating the strong influence of capillarity and the fibre architecture on the distribution of ink. Figures 5.1c – 1d show a similar behaviour with the prints made at a smaller drop spacing.

In order to investigate the distribution of Ag within the fibre architecture of the fabric, X-Ray Computed Tomography (XCT) reconstructed images were obtained when a single layer patch of ink is printed on the as-received and SG treated fabrics. 3D image analysis of the XCT reconstructions and appropriate image segmentation based on X-Ray absorption has been used to separate the location of the high atomic number Ag (coloured blue-green) from the organic polyester fibre structure (coloured grey) in Figure 5.2. In all of the XCT images the warp yarns are arranged vertically and the weft horizontally with respect to the page. It is clear that for both the as-received and SG treated fabrics that there is significantly more Ag associated with the warp yarns than the weft at both values of drop spacing. The effect of drop spacing is similar with both substrates and can be seen by comparing the image pairs5. 2a) and 5.2c) or 5.2b) and 5.2d), where there is more Ag evident with the 10 μm drop spaced prints than those at 20 μm. The influence of fabric treatment and contact angle is revealed by comparing the image pairs 5.2a) and 5.2b) or 5.2c) and 5.2d). From this comparison there is clearly significantly more of the Ag confined to the surface region of the SG fabric, with the as-received fabric showing a more diffuse penetration of the Ag throughout the fibre body, which results in Ag within the fabric obscured by images of the polyester fibres close to the surface. This behaviour corelates with the ink/fibre interaction findings in Chapter 4.3.2 where spreading length reduces with increased surface hydrophobicity.

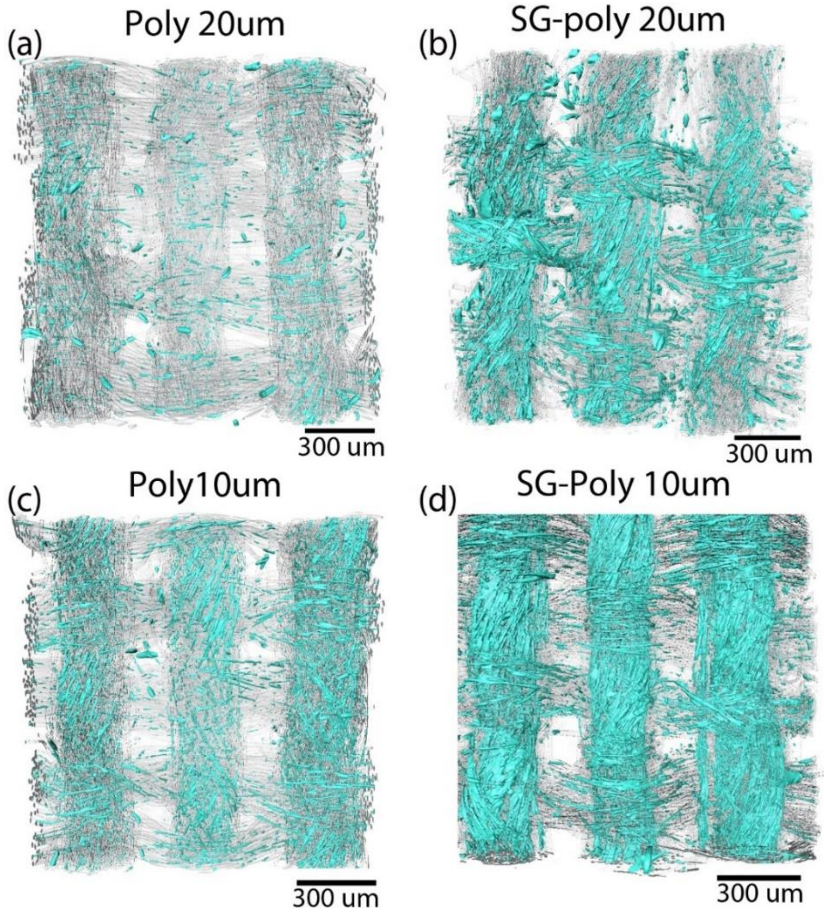

Figure 5.2 XCT reconstruction showing Ag (coloured blue-green) distribution amongst the polyester fibres (coloured grey) after printing with 20 μm drop spacing (a) and 10 μm drop spacing (b); and amongst the SG-treated polyester fibres (b) and (d).

5.3.1.2 The Effect of Number of Printing Layers and Sintering Techniques

The distribution of Ag as a function of depth beneath the surface is captured by the XCT reconstruction, this is better visualized in Figure 5.3, which shows an oblique view of the XCT reconstruction of the Ag distribution within the textile after printing and sintering 1, 5,10 and 15 layers of the ink. In this sequence of images the fibre weft direction runs along the horizontal axis and the warp fibres run vertically (or apparently into the depth of the image) from the perspective of the 2D image of the 3D reconstruction. It is clear from the figure that the total amount of Ag increases with the number of printed layers. Ink penetration into the fabric follows the direction of the fibres within the tows. This is particularly apparent after printing 10 and 15 layers, where the Ag within the weft tows passes beneath the adjacent warp tow without connecting with it. This behaviour is closely related to the observation in Chapter 4.3.2 ink/fibre interaction, where ink can land and spread on individual fibre tows, form columns and flow along fibre tows, or penetrate fibre pores, depending on the pore sizes between fibres.

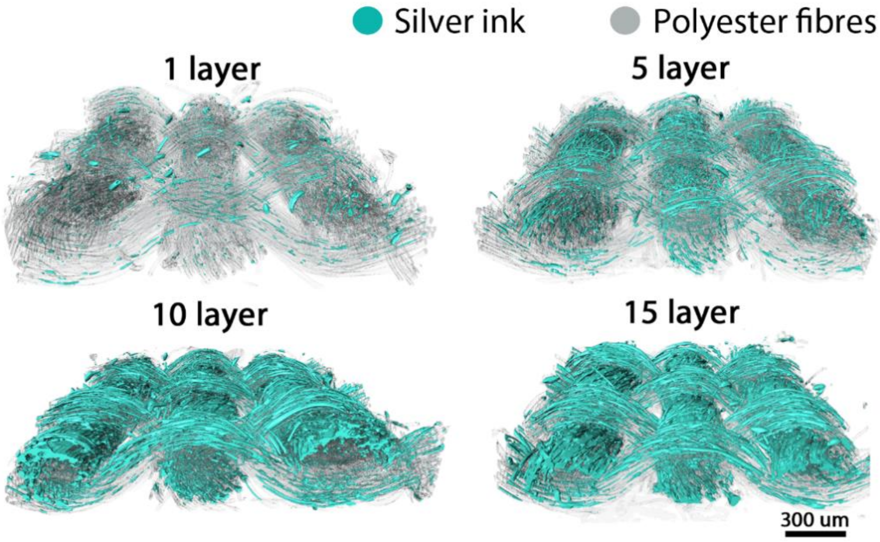

Figure 5.3 XCT 3D reconstruction images of Ag (blue-green) deposition on polyester fabrics (grey) with increasing number of printed layers after sintering. Warp fibers appear to run into the depth of the page, weft fibers undulate in the horizontal direction. The large scale macroporosity between the warp and weft yarn threads is apparent. The Ag is retained within the microporosity between the polyester fibers within the threads. Note the absence of interconnectivity across the macroporosity separating the warp and weft yarn threads.

The above studies are based on sintering the sample after printing all layers. However, this process leads to reduced definition of the edge of the printed area after overprinting because even if the previous layer dries before the overprinting, arrival of fresh solvent can transport previously printed nanoparticles in the ink by wicking beyond the initially defined pattern edge (Figure 5.4 (a) 5 layers specimens). As demonstrated in Chapter 4, increased ink volume can lead to increased spreading length during ink/fibre interaction until the equilibrium is reached, and with interconnected pore structures in textiles, if the volume of the ink exceeds the pore volumes in yarn, the spreading length increases with the increasing ink volume.

This reduction in edge definition (or pattern resolution) is prevented if the sintering process is carried out after each printing pass (Figure 5.4 (a) 5 layers spl specimens). These two processing sequences are defined as sintering after all layers printed (SAL) and sintering after each layer printed (sintering per layer or SPL). Additionally, the specimen printed at 20 μm drop spacing on SG treated fabrics shows the best edge definition, which the SEM images are shown accordingly in Figure 5.4 (b) (1 layer) (c) (5 layers) and (d) (5 layers SPL). Greater silver deposition is found with increased printing layers, and it is interesting to observe that the Ag deposits and connects between fibre pores through the sintering per layer technique. This behaviour explains the reduction of the capillary effect that induces the wicking beyond the defined pattern edge. It also corelates with the ink/yarn interaction finding in Chapter 4 on Washburn's equation and Darcy's law, where reduced pore spacing leads to decreased spreading length.

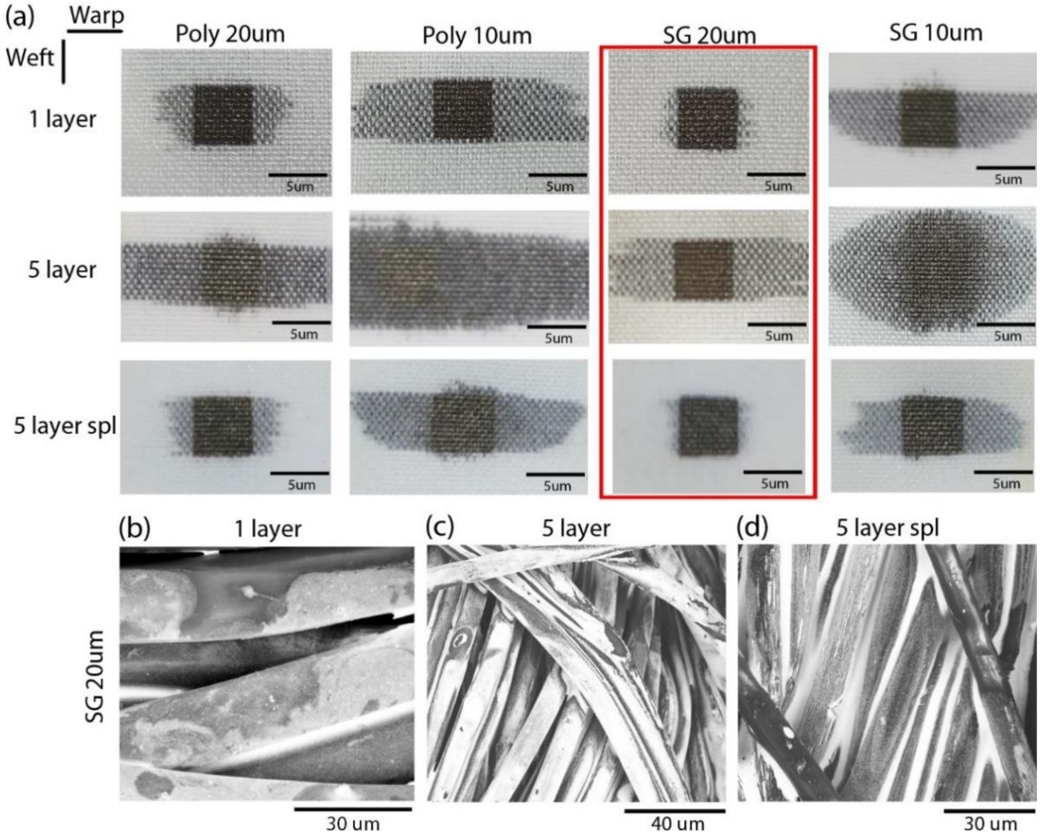

Figure 5.4 (a) Optical images of inkjet printed silver nanoparticle ink on polyester and SG-treated fabrics, with 20 μm and 10 μm drop spacings, with 1 layer of printing, and with 5 layers printing and sintering after all layers (SAL), and with 5 layers printing and sintering per layer (SPL); (b-d) SEM images of SG 20μm samples on above printing and sintering processes.

5.3.1.3 Quantified Analysis of Ag Object Size Distribution

Further image analysis and segmentation of the tomography data can be used to identify individual discrete connected Ag objects within the reconstruction (label analysis). This process is illustrated in Figure 5.5 with figure 5 (a) showing an image from a SG treated fabric, after printing 5 layers of the Ag ink at a drop spacing of 10 μm, with the Ag and polyester components identified through their different X-Ray absorption. Figure 5.5b shows the same image but with solely the Ag phase present. In Figure 5.5c further image processing is used to isolate discrete connected Ag objects, with the largest objects in the reconstruction identified and ascribed a unique identifying colour. It is remarkable that, in what appears to be a densely populated region of sintered AgNP, there are a number of discrete and therefore electrically isolated Ag objects, each of which may extend over considerable lengths within a fibre tow. For example, the centre of the leftmost warp tow in Figure 5.5c contains a large interconnected fibrous Ag object, coloured brown. This is connected to a small fraction of fibres in each weft tow and although they extend beyond the two adjacent warp tows, they do not connect with them. A similar region (coloured blue) is visible in the rightmost warp tow. Figures 5.5 (d) and 5.5 (e) show a single warp and weft tow, respectively, removed from the reconstruction, confirming that the two tows show different levels of Ag retention after printing and sintering. Colour map was assigned automatically in the Avizo software, connected objects are presented within the same colour.

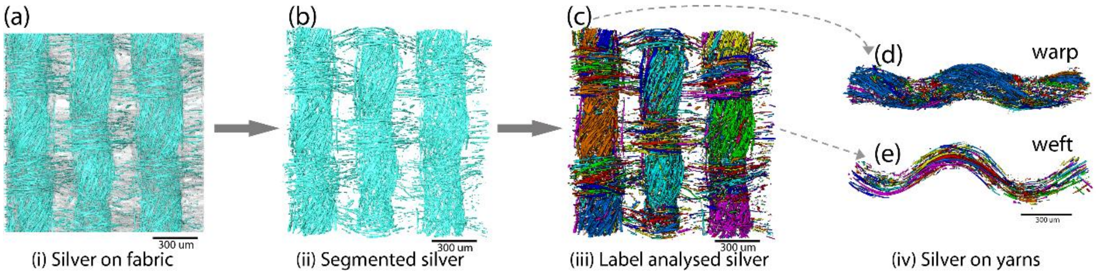

(i) Silver on fabric (ii) Segmented silver (iii) Label analysed silver (iv) Silver on yarns

Figure 5.5 (a) XCT reconstruction of 5 layers of AgNP ink deposition on Scotchgard treated polyester fabric with 10um drop spacing. (b) Segmentation of the Ag within the XCT reconstruction. (c) Label analysis of silver objects from the XCT reconstruction. Segmentation of the silver within individual yarns (d) Warp (e) Weft.

Figure 5.6 presents histograms of relative volume fraction of discrete Ag object sizes within the XCT reconstructions, obtained through label analysis. In Figure 5.6 a) we can compare the influence of both drop spacing (10 μm - black columns, 20 μm – red) and fibre surface treatment (SG – filled columns, as received – unfilled) on Ag object size after printing a single layer. Comparing the structures printed on the as-received polyester fabric the modal volume at 20 μm^3 drop spacing is about 3000 μm^3 and about 10,000 μm^3 at 10 μm spacing. In both cases when repeated on the SG treated fabric the modal size increases by an order of magnitude. Figure 5.6 (b) shows a more dramatic influence on the Ag object size through increasing the number of printed layers. With a single printed layer, the modal size of a single Ag object is 10^2 μm^3 and this represents many thousands of objects that will not necessarily span the structure. As the number of printed layers increases, the greater volume of Ag deposited leads to further coalescence of Ag particles and an increase in the fraction of larger object volumes. After 10 – 15 printed layers, the modal object size is 10^4 – 10^5 μm^3 with only a small number of large objects containing most of the Ag and providing continuous conducting paths across the specimen.

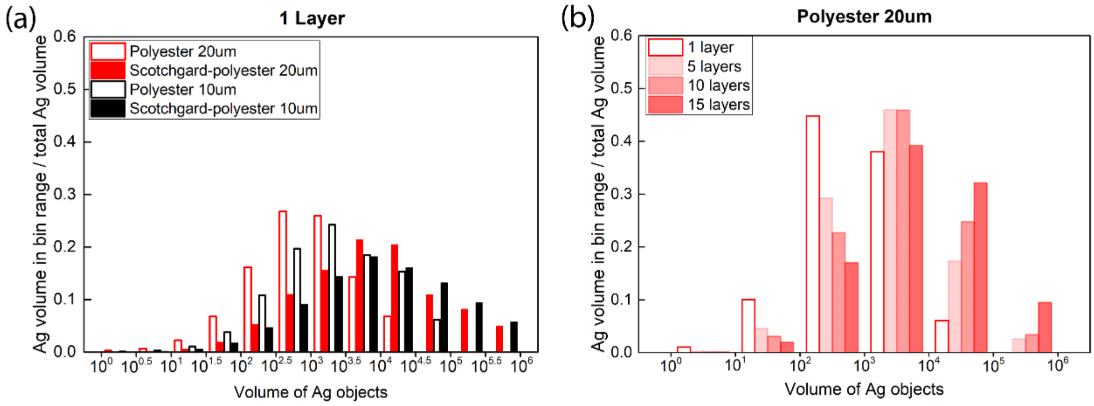

Figure 5.6 Distribution of the total volume fraction of individual connected Ag objects printed on polyester fabric after sintering: (a) Prints of 1, 5, 10, and 15 layers - 20um drop spacing. (b) Effect of surface treatment and drop spacing for a single printed layer.

The application of the sintering per layer technique is found to improve the edge definition (or pattern resolution). In which case the Ag nanoparticles sinter to form larger objects and no further transport occurs during overprinting. Sintering after each printed layer is also shown to have significant benefits for the Ag distribution after printing. This is confirmed by XCT analysis, which shows that layer sintering leads to significantly higher printed silver connectivity and larger printed object size after printing 5 layers for all surface treatments and drop spacing specimens (Figure 5.7).

The improvement through changing the sintering technique is found to be the most efficient and material saving method among others, and the time consumption can be controlled through alternative industrial inkjet printer set-ups with different sintering techniques such as ultraviolet, infrared or microwave sintering [381–383].

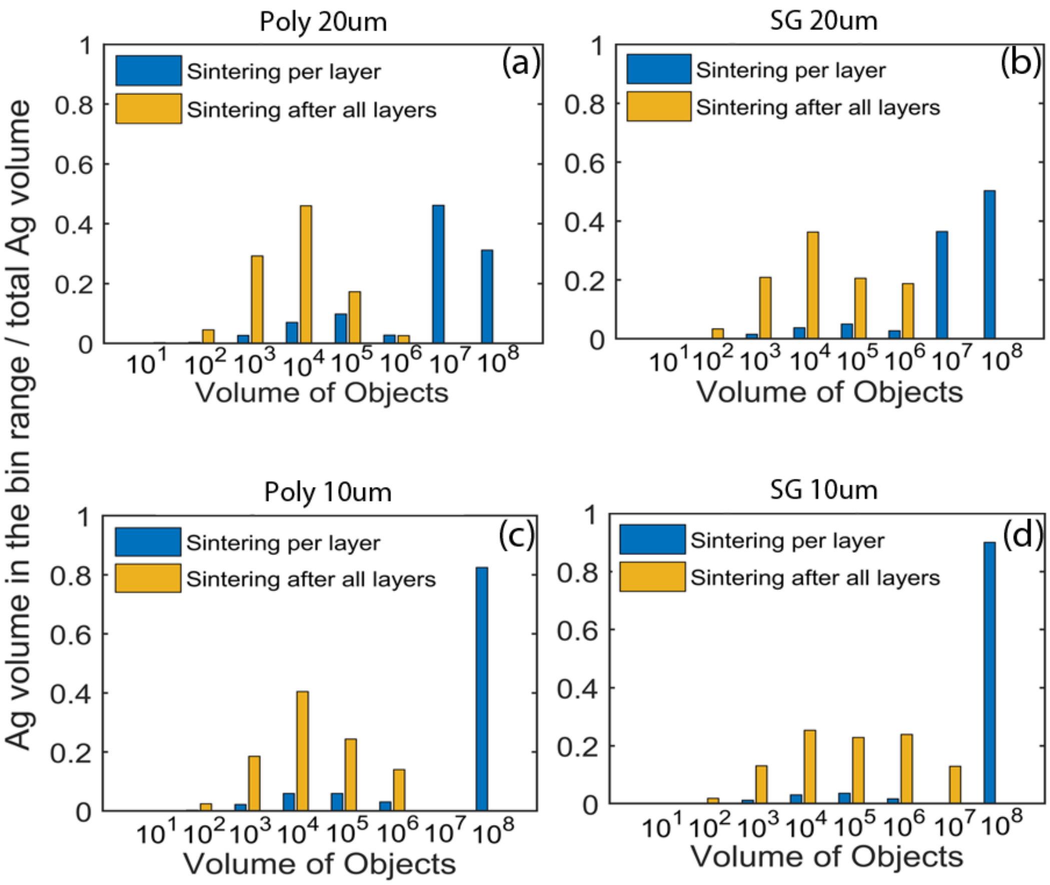

Figure 5.7 Ag object volume distribution between different sintering methods (blue bars-sintering per layer method; yellow bars-sintering after all layers method)) and processing parameters (with 20 μm (a, b) and 10 μm (c, d) drop spacings on polyester (a, c) and Scotchgard-treated polyester (b, d) fabrics).

With the obvious enhancement of Ag largest object size distribution through the sintering per layer technique, Scotchgard-treated 20 μm drop spacing specimens with the best edge definition is further analysed from printing 1 to 5 layers as shown in Figure 5.8. As the number of printed layers increases, the change of the modal object size through this sintering technique is dramatically greater than sintering after printing all layers. After 4 – 5 layers are printed, the modal object size is 10^6 – 10^7

µm3, with a greater number of large objects containing most of the Ag and providing continuous conducting paths across the specimen.

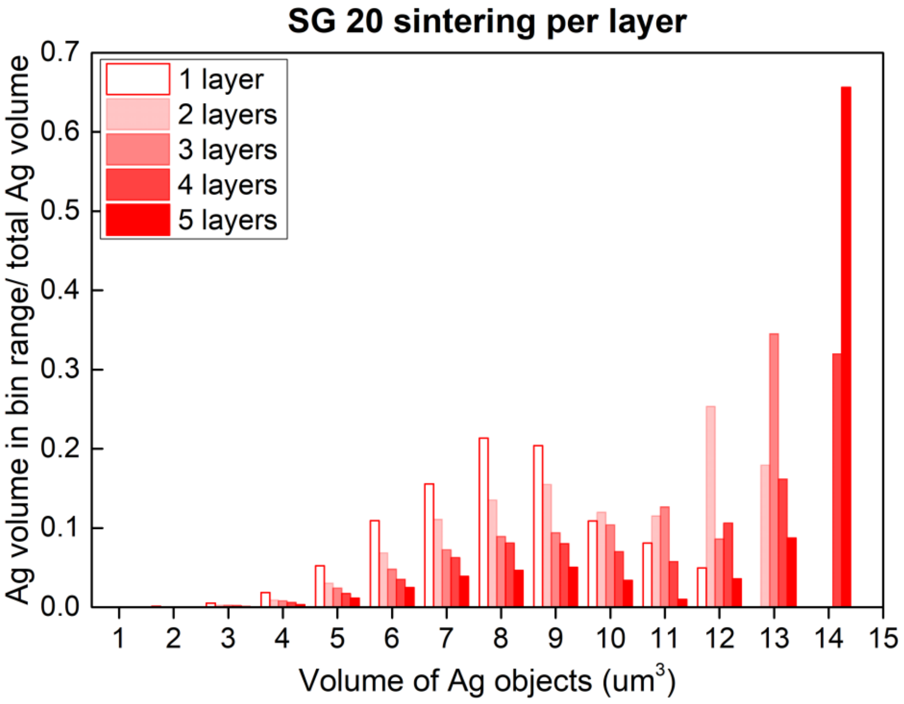

Figure 5.8 Influence of number of layers printed at 20 µm drop spacing on SG polyester fabric showing a dramatic increase in the proportion of volume in large interconnected objects as printed layer number increases.

5.3.2 Electrical Properties of Printed Ag Structures

Our visualization of silver deposition after printing on textile substrates shows that the distribution of Ag on and within the fabric is strongly controlled by the fibre architecture. Its heterogeneous nature indicates that the electrical properties are likely to be highly anisotropic, given the different levels of Ag deposition in the warp and weft yarns. The discrete nature of the Ag object distribution and the absence of a well-defined Ag conducting film also suggests that the use of a “sheet resistance” is inappropriate to characterize the electrical properties of conductors printed on textiles. Figure 5.9 (a) and (b) show the measured electrical conductance along the warp and weft yarns as a function of number of printed layers for the two surface treatments and drop spacing used with sintering after all layers technique. The difference of electrical resistance on warp and weft directions is considerable but, in both yarn directions, the conductance follows the same trend with variation in surface treatment and drop spacing. The higher electrical conductance of the warp yarns and poor connectivity of silver deposition between yarn tows shows that the warp yarns provide the dominant path for current flow.

Focusing on warp yarns, it is seen that electrical conductance increases with the number of printed layers. There is an abrupt transition in conductance as we move from printing a single layer to 5 layers. This is interpreted as indicating percolation behavior with a rapid increase in conductivity occurring as discrete Ag units become sufficiently large to span the probe length of the conductivity apparatus. However, to confirm this hypothesis needs more detailed study of conductivity at small layer numbers. Increasing the number of overprints from 5 to 10 and 15 layers shows limited further enhancement of electrical performance but also leads to reduced printing resolution, where the silver ink spreads beyond the printing area due to the capillary wicking effect. Reduced drop spacing increases the electrical conductance due to improved silver connectivity and deposition amount. The Scotchgard surface treatment gives a positive effect on electrical performance at 10 μm drop spacing samples due to an increased silver concentration (reduced wicking). However, at 20 μm drop spacing the hydrophobic surface reduces the ink wicking and spreading effect and, as a consequence, there is reduced interaction between adjacent silver drops, which leads to a reduction of electrical conductance. This has some similarities with the formation of conducting tracks on solid substrates by inkjet printing where a minimum drop spacing is required for connectivity and this value is affected by the wetting angle between ink and substrate[229].

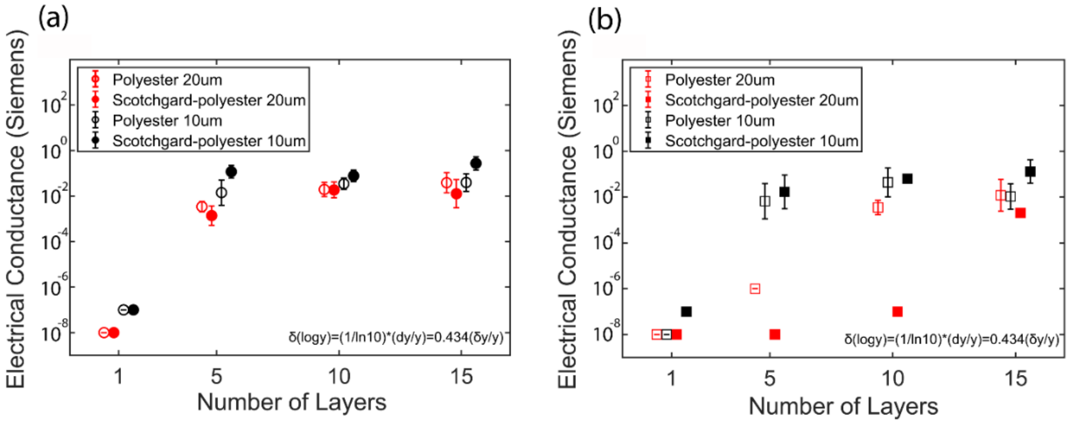

Figure 5.9 Comparison of the effects of drop spacing and surface treatment on electrical conductance of AgNP printed on polyester fabrics on warp (a) and weft (b) yarns with 1, 5, 10 and 15 layers of sintering after printing all layers.

For the case of 10 µm drop spacing (black symbols) the conductance along the warp and weft directions shows similar behaviour with the mean conductance in the warp direction being always slightly larger than that in the weft direction for both the as received and SG treated fabrics. This is ascribed to the higher density of fibres in the warp direction, give those 60 and 76 threads per inch in the warp and weft directions respectively (manufacturer's data). The electrical conductance along both directions increases by over three orders of magnitude between 1 and 5 printed layers but with further increases in number of printed layers, the conductance increase is within a single order of magnitude. There is a significantly greater difference between the conductance measured in the warp and weft directions after printing at 20 µm drop spacing (red symbols). The polyester fabric shows an order of magnitude increase in conductance once 5 layers are printed but this value is two orders of magnitude lower than seen with the corresponding 10 µm print. After 10 and 15 layers the behaviour is similar to that seen of the 10 µm prints with the weft showing slightly lower conductance than the equivalent warp yarn. Finally, the SG fabric requires 15 printed layers at 20 µm spacing before the warp and weft directions show similar conductance values.

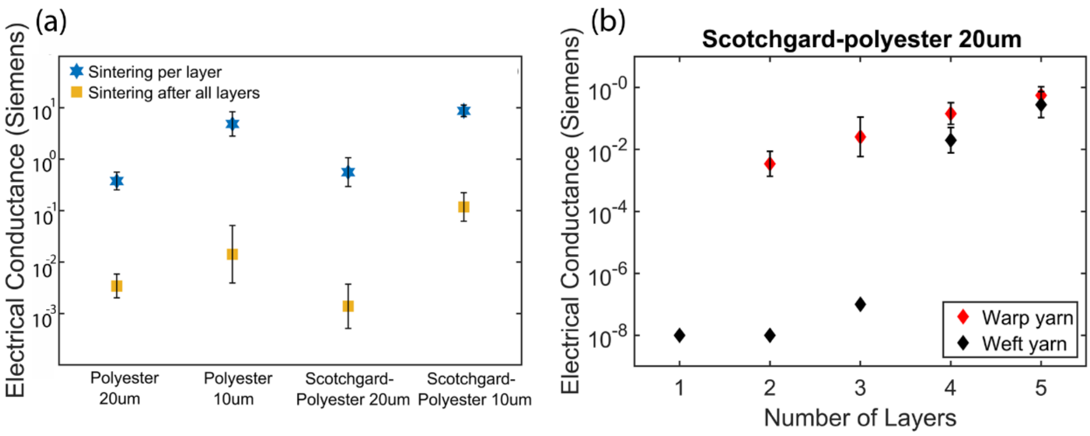

Figure 5.10 (a) Electrical conductance comparison of sintering per layer and sintering after all layers for 5 layer printing on 4 types of samples; (b) Electrical conductance measurements on warp and weft yarns as a function of number of printed layers on

Scotchgard polyester fabric with 20 μm drop spacing after sintering. Data points for both substrates coincide at 1 printed layer.

Sintering per layer s also shown to have significant benefits for the Ag distribution after printing and its electrical properties. Figure 5.10 (a) shows that layer sintering leads to significantly higher warp tow conductance values after printing and sintering 5 layers. An increasement of three orders of magnitude is found in all four types of samples with the same effect of surface treatments and drop spacing, where the reduced drop spacing and increased surface hydrophobicity lead to higher electrical conductance values.

For Scotchgard-treated 20 μm drop spacing specimens with the best edge definition as shown in Figure 5.4 (a), detailed electrical conductance measurements at small layer numbers from 1 to 5 layers are made on individual warp and weft yarn threads within the fabric (Figure 5.10 b), where the warp conductance is always greater than the weft value. The electrical conductance in both threads shows a sudden increase, greater than 2 orders of magnitude, after 2 printed layers in the warp direction and between 3 and 4 printed layers in the weft direction. Such a marked transition in behaviour, is interpreted as indicating the onset of percolation connectivity of the Ag objects.

5.3.3 Analysis: Influence of Ag Distribution on Printed Electrical Properties

A rough corelation between the printed electrical conductance and the silver object size is gradually revealed from the above studies. Comparing the XCT analysed images in Figure 5.11, it can be seen clearly that printed silver achieves better connectivity and larger printed unit size after Scotchgard treatment, reduced drop spacing and layer sintering. Therefore, the influence of Ag distribution on printed electrical properties will be studied focusing on the specimens from the layer sintering method.

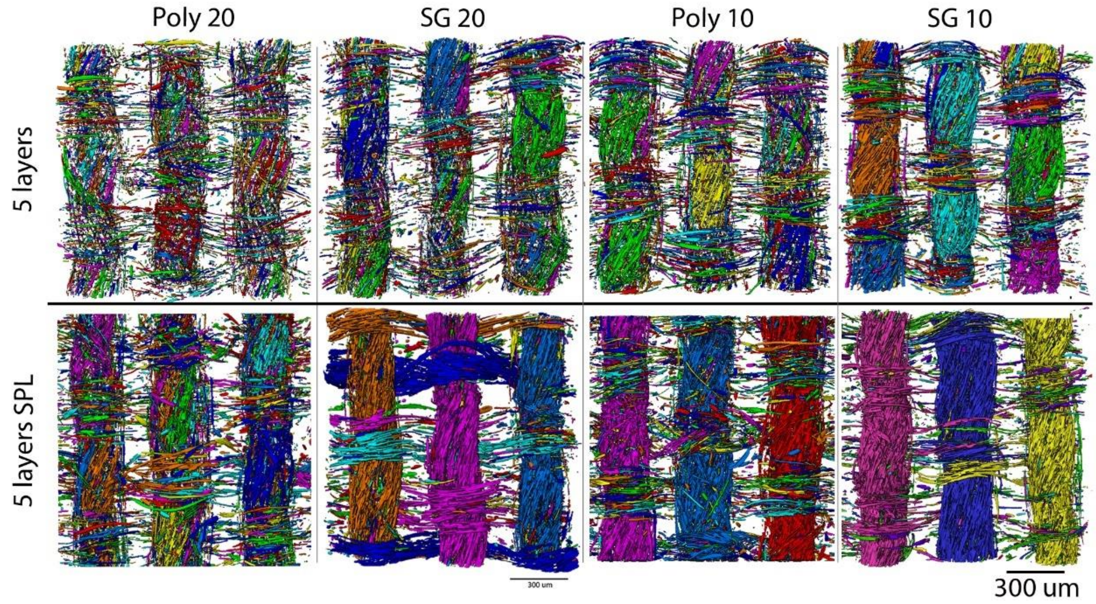

Figure 5.11 Label analysis of silver objects from the XCT reconstruction, comparing Ag distribution of between different sintering methods and processing parameters. Individual Ag objects are coloured to present their connectivity.

Our data confirms that in woven textiles, Ag distribution can be significantly different in the warp and weft directions after printing a conductive ink. The weaving process generates inherent anisotropy within a textile fabric and the two families of orthogonal yarns are not identical in structure and properties. The warp and weft yarns may be of similar or different composition, fibre density, and amount of twist per unit length. There is also only limited electrical interconnection between adjacent fibre tows in the same direction or between the warp and weft yarns at cross-over points. XCT reconstruction data in Figure 5.12 (a) shows the increase in connectivity of silver objects within one of the warp yarn tows that occurs with increasing number of printed layers. Figure 5.12 (b) compares the silver volume measured in the warp and weft yarns and their largest connected object. The proportion of the Ag ink in the warp yarns becomes larger as the number of printed layers increases. After five layers are printed, the quantity of ink in the warps is 2 times greater than in the wefts.

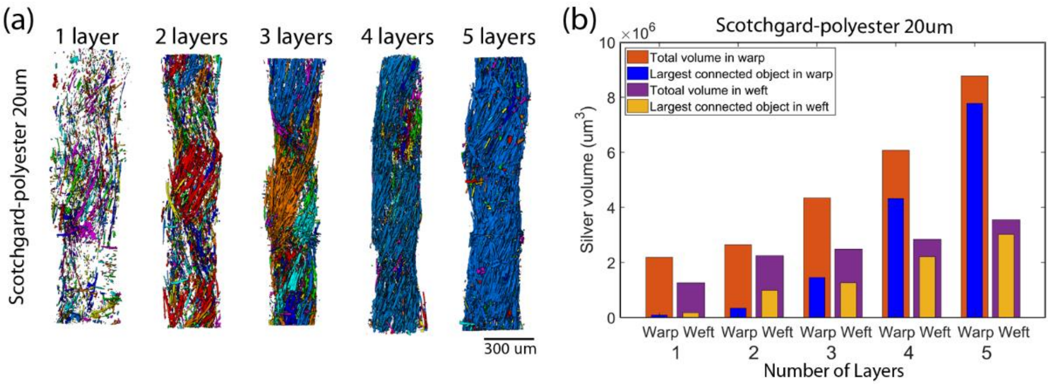

Figure 5.12 (a) Segmented silver deposition on warp yarns from printing 1 to 5 layers and (b) total printed volume and the volume of the largest silver object on the warp and weft yarns with increasing number of printed layers, on Scotchgard polyester fabric with 20 μm drop spacing after sintering.

To further understand the mechanisms for the electrical conductivity of printed Ag ink on textile surfaces we propose a simple model that relates the quantity of Ag deposited to the measured conductance. We assume that the warp and weft tows can be considered independently and that only Ag present in objects that continuously span the path between the testing probes contributes to the measured conductance. It is proposed that the conductance of a yarn can be predicted by determining the largest connected silver object in the XCT reconstruction of the yarn/silver structure and assume that this represents the conductive pathway. If the object has a volume, V_{max}, and it extends along the complete length of the fiber tow, as is necessary to provide a conductive pathway, then its length, l, is defined by the size of the reconstructed image, in this case l_{im} = 1400 μm. From inspection of the XCT reconstructions after label analysis, this assumption was always clearly valid when multiple layers of ink are printed). We further assume that the silver object can be considered as a continuous solid, in which case the cross-sectional area is defined by $A = V_{max} / l_{\mathrm{im}}$. The conductance, G, of the object along the yarn direction is then

$$G\left(l_{im}\right) = \frac{\sigma A}{l_{im}} = \frac{\sigma V_{\max}}{l_{im}^{2}} \tag{5.1}$$

where σ is the conductivity of Ag. The length l_{im} is that of the XCT reconstruction, in this case 1400 μm, the length used to measure the conductivity of the yarn is that set by the interprobe distance used in the measurement device, l_{probe} = 1400 μm. If we assume that the effective cross-sectional area, *A*, and the conductivity, σ, are both independent of measured length, then for any given length, the product of *G(l)* and *l* is constant. In which case we have for the measured probe length and image length:

$$G\left(l_{im}\right)\times l_{im}=G\left(l_{probe}\right)\times l_{probe} \tag{5.2a}$$

and hence
$$G\left(l_{probe}\right)=\frac{\sigma V_{\max}}{l_{im}l_{probe}} \tag{5.2b}$$

It is not clear whether the conductivity of bulk Ag is appropriate for objects produced by sintering AgNP given that the sintering temperature and time have been defined arbitrarily and there is likely to be significant porosity impeding conductance. To obtain the appropriate value of σ for use in equation (5.2) the effective conductivity of a Ag film printed on a polyester film using the same NP ink was measured. An estimate of the conductivity of the Ag nanoparticle ink was achieved by measuring the sheet resistance, R_s, of ink printed on a polymer sheet and subject to the identical heat treatment as used in the textile experiments. The sheet resistance was measured using a 4-point probe set up identical to that used with the textile specimens. If the layer of ink is sufficiently thin the sheet resistance is given by equation (5.3)

$$R_s=4.53\frac{V}{I} \tag{5.3}$$

And if the film is of thickness *t*, then the effective conductivity of the sintered ink is:

$$\sigma_{eff}=\frac{1}{tR_s} \tag{5.4}$$

This gives an effective conductivity of σ = 2.5 x 10^6 S.m^{-1}, which is considerably lower than the bulk value for Ag of 6.3 x 10^7 S.m^{-1}. This value was used to interpret the relationship between Ag object volume and warp tow conductivity.

The measured volume of the largest connected object (Figure 5.12 (b)) is identified by segmenting the reconstruction to accurately separate the volume of connected Ag from the rest of the material in the observed volume. Two segmentation methods were applied, the Tophat method is an operation that extracts elements that are smaller and brighter than their surroundings by subtraction from the input image, which results in better visualization fit of our samples compare to other general auto-thresholding methods[384,385]. However, there are always concerns that the image segmentation procedure used to identify the presence of Ag may incorrectly measure the total volume. Segmentation uses a critical threshold value and if this is set incorrectly it will not return a true value of the Ag content of the object. The expected volume of Ag after printing and sintering can be predicted from the volume of an individual printed drop and the number of drops printed. This can be easily computed from the area of the sample, the mean drop spacing and the number of printed layers. The total volume of ink printed, V_p, is defined:

$$V_{\mathrm{p}} = \frac{N_{\mathrm{p}}\rho_{\mathrm{ink}}F_{\mathrm{Ag}}}{\rho_{\mathrm{Ag}}} * V_{ink} \tag{5.5}$$

where N_{p} = number of droplets printed, ρ_{ink} = density of the ink, F_{Ag} = the weight fraction of Ag in the ink, ρ_{Ag} is the density of bulk solid Ag and V_{ink} represents the individual ink volume. N_{p} was calculated by measuring the area of the X-Ray image and dividing by the drop spacing in the x- and y-directions of the printer; in this case the spacing was identical in both directions. $F_{\mathrm{Ag}} = 0.30$ and $\rho_{\mathrm{ink}} = 1450$ kgm^{-3} (manufacturer's data), and $\rho_{\mathrm{Ag}} = 10500$ kgm^{-3}.

In all cases, around 70wt% of silver nanoparticles were retained on the fabrics (direct weight measurement) after printing and heat treatment compared to the expected value printed (computed from drop number and volume). This discrepancy is explained by losses due to a fraction of the ink penetrating the single fabric layer and resting on the surface beneath and other losses of poorly adherent particles from handling of the samples during transfer between printing and sintering. The quantity of Ag present after printing can also be measured using thermogravimetric analysis (TGA), in which the organic textile is removed by oxidation to gaseous product and the residue will be the printed silver (Appendix 5.1). Figure 5.13 compares the three values of Ag content:

i) the expected silver content computed from the drops printed (orange symbols);

ii) the Ag volume determined by Tophat image segmentation (blue symbols);

iii) the Ag volume determined from the residue after TGA testing (green symbols).

In all cases the actual amount of Ag determined experimentally by TGA was smaller than the expected value printed and the amount of Ag determined by image segmentation was always greater than the expected value. With decreasing drop spacing and in the presence of Scotchgard the segmentation value converges towards the expected value but the difference between the expected value and the TGA data increases. Since the TGA sample is taken from the centre of the printed samples, the textile wicking effect driven by the capillary action allows ink to flow exceeding the edges. This wicking effect as discussed above is a key factor to form conductive patterns but reduces the printing resolution and leads to reduced Ag deposition amount. Scotchgard treated polyester samples show smaller amount ink loss due to the surface hydrophobicity that can relatively prevent ink vertical penetration and reduce the wicking effect. 10 μm drop spacing samples show greater amount of ink loss due to the excessive amount of silver ink that can increase the wicking effect and possibly beyond pore volume in the fabric[338,339].

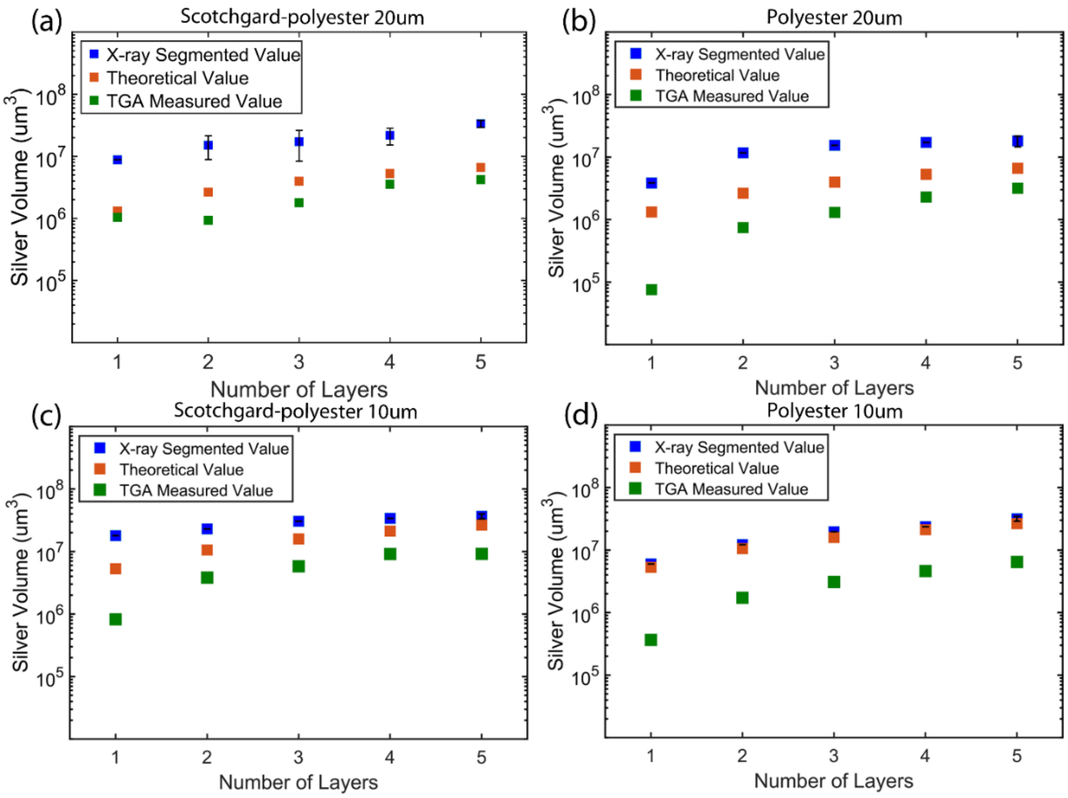

Figure 5.13 Silver volume comparison from X-ray CT, inkjet printed and TGA measured AgNP printed on polyester fabric with 20um drop spacing and that with(a) and (b) without surface treatment, and with 10um drop spacing with (c) and without (d) surface treatment.

One possible reason to explain the greater image segmentation volume through the Tophat method is the partial volume effect, which occurs when there is sufficient Ag present in the voxel to exceed the threshold, but the Ag does not completely fill the voxel. Therefore, an alternative segmentation method is to manually adjust the thresholding such that the measured volume matches the known Ag deposition volume (computed from surface drop density and efficiency of Ag deposition, Figure 5.14). This method returns poorer quality image reconstructions but suggests that the over segmentation of silver volume could lead to errors in voxel connectivity and thus predict a greater electrical conductance through the Tophat method (Figure 5.15). A fuller analysis of the two segmentation methods reveals that in all cases the Top Hat method identifies larger connected Ag volumes, and this is particularly marked with the 20 μm drop spacing samples (see Appendix 5.2 for a complete histogram of the data for the two reconstruction methods).

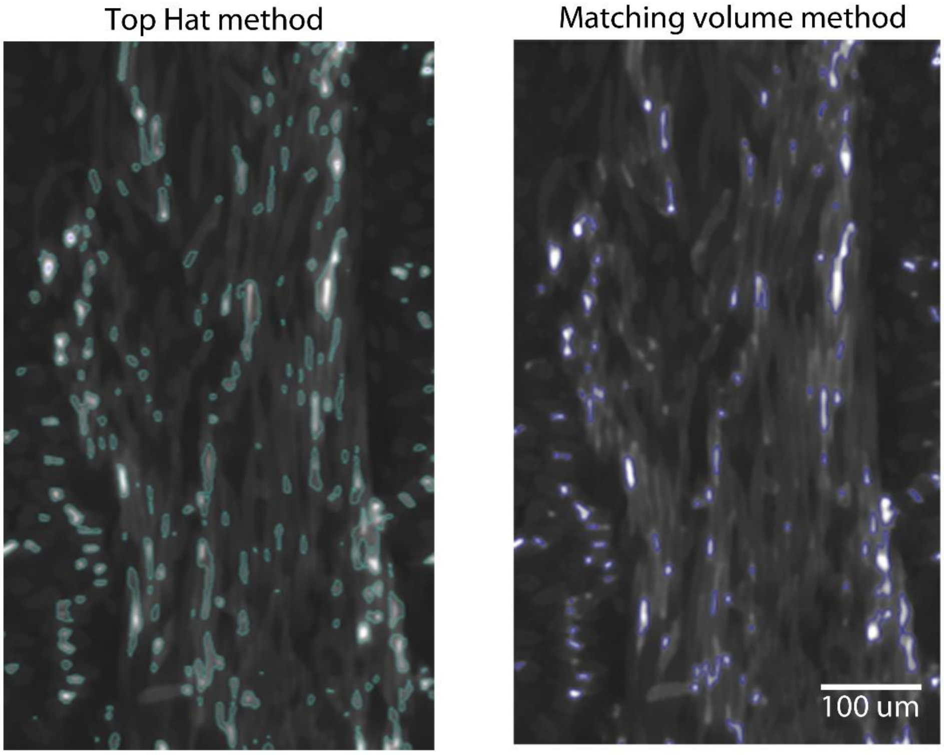

Figure 5.14 Segmentation results from Top Hat and matching printed volume.

Focusing on the warp yarns (Figure 5.15 red symbols), it is clear that electrical conductance increases with the number of printed layers at smaller number of printing layers. This is consistent with a percolation mechanism leading to an increase in conductivity as discrete Ag units become sufficiently large to span the probe length of the conductivity apparatus. This is consistent with the order of magnitude increase in the size of the modal object (Figure 5.8). Reduced drop spacing increases the electrical conductance due to improved conductor connectivity and increasing Ag volume. The Scotchgard surface treatment also gives a positive effect on electrical performance due to an increased Ag concentration (reduced wicking).

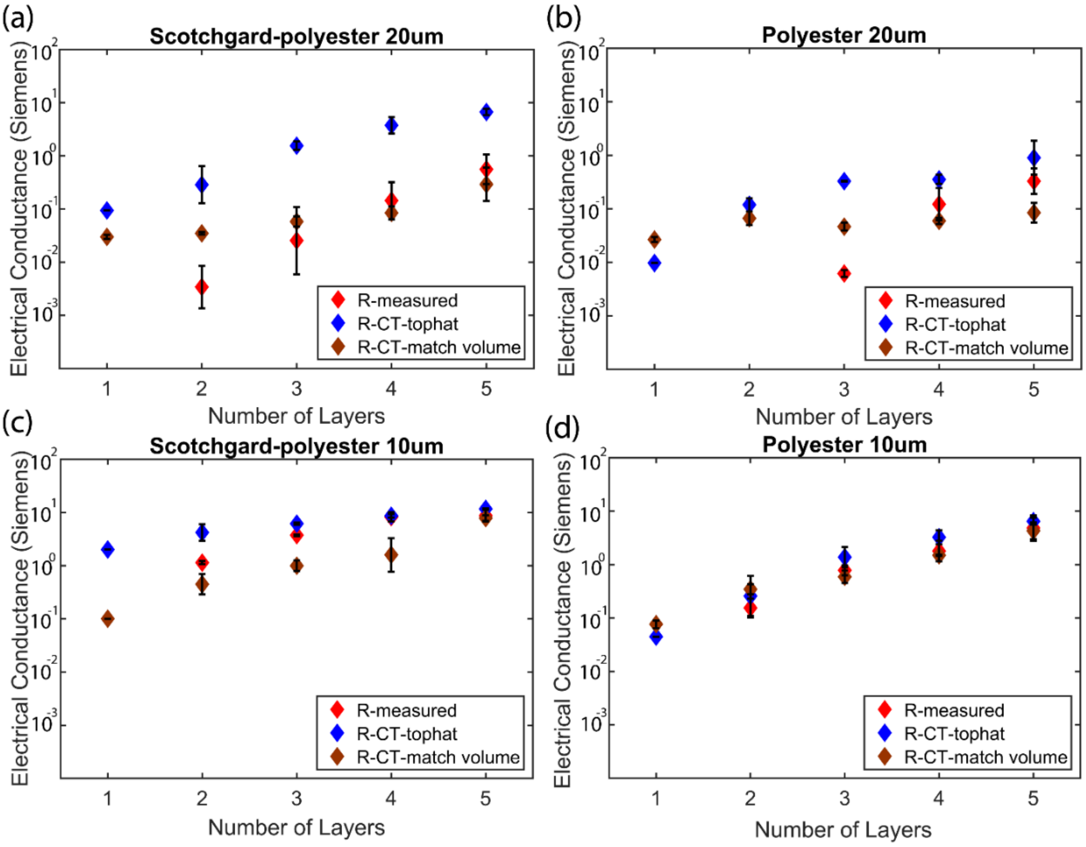

Figure 5.15. Mean electrical conductance and standard deviation measured along a single warp yarn tow after printing and sintering on a polyester fabric as a function of number of layers printed (red symbols) compared with the predicted value determined from measuring the largest single object present in the equivalent XCT reconstruction using either a Tophat algorithm (blue symbols) or total matched volume (brown symbols) to assign Ag content to a voxel. The following printing conditions are presented to allow comparison of the influence of drop spacing (figure panel columns) and fabric surface treatment (figure pane rows). (a) SG Fabric, 20 μm drop spacing, (b) as-received fabric, 20 μm drop spacing, (a) SG Fabric, 10 μm drop spacing, (d) as-received fabric, 10 μm drop spacing. Note that at 20 μm drop spacing, the conductance at 1 printed layer on the SG fabric, and at 1 and 2 printed layers with the as-received fabric, is < 10^{-7} S and thus not plotted.

The results of the predicted conductance of the fabric using the two segmentation methods are shown in Figure 5.15 with the top hat method using blue symbols and the matched volume brown. The difference in the object volumes determined by the two segmentation strategies mirrors the divergence in the predictions of conductivity. In general, the top hat segmentation method predicts larger Ag volume and this results in the predicted conductance being larger than that measured experimentally. The opposite effect is seen with the matched volume method, with the predictions now being lower than experiment. The best agreement between experimental conductance data and predictions from the Ag volume measurements occurs with the 10 μm drop spacing printed on the as-received fabric (Figure 5.15 (d)) where both segmentation methods converge to a good agreement with experiment. The greatest divergence occurs at larger drop spacings and fewer printed layers, where the electrical conductivity is highly sensitive to the percolation of conductive pathways and the limited voxel resolution of the XCT data leads to greatest uncertainty.

The limitations to quantitative data analysis from tomographic reconstructions are well known and have been discussed in the literature. The complete process used in this study involves X-ray generation, interaction with the scanned object, detection and image processing. The segmentation of the image to isolate Ag volume is based on a threshold value that can illustrate the image intensity change[318,386]. Ideally, the reconstruction process would be capable of reforming raw image sinogram and applying filters to apply correct value of linear attenuation coefficient to each voxel. However, this process is difficult to achieve in our case with inhomogeneous materials and polychromatic X-ray, not to mention the possible loss of geometric and quantum efficiency during the detection process[318]. Finally, we note that XCT studies of Ag distribution within printed fabrics is not limited to simple interpretations of local conductivity. Future studies could investigate the influence of fibre orientation and weave architecture on ink flow and with the use of high flux sources such as synchrotrons, dynamic aspects of ink transport could be tracked.

5.4 Conclusions

X-ray computed tomography is a powerful tool for monitoring the distribution of a Ag conductive ink in textile substrates after inkjet printing. Reduced drop spacing and increased surface ink phobicity lead to localized Ag concentration post-deposition and improved connectivity after sintering leading to increased electrical conductivity. Sintering after each layer is printed shows advantages in terms of electrical performance and printing resolution but will reduce production rate compared to a single heat treatment after multilayer printing. Local fibre architecture is found to be important with Ag transport occurring preferentially along the direction of the fibre tows in the fabric. The warp and weft yarns present different silver concentrations after printing due to their different fibre architectures, with the warp direction dominating both the Ag content and conductivity due to its greater thread density than the weft direction. This and other heterogeneities in the textile architecture demonstrates that the use of a “sheet resistance” is inappropriate for describing the electrical performance of conductive materials deposited on textile substrates.

Detailed study of XCT reconstructions after printing and segmentation of the Ag distribution in the warp and weft yarns show that the majority of the conductive paths develop along each yarn direction and that there is poor electrical connectivity between individual yarn tows even when they overlap in the weave. The electrical conductivity within a yarn increases rapidly with increasing number of printed layers. The conductivity is shown to be strongly dependent on the effective volume of Ag in continuous conductive objects spanning the specimen volume which is consistent with a percolation threshold network model for yarn conductance. A simple model has been developed using segmented Ag volume data from XCT reconstructions to predict the conductance of the specimens through ohm’s law. This model is consistent with the trends in electrical properties measured as a function of fabric properties and printed drop spacing, although precise agreement with the results is strongly influenced by the segmentation method used to identify the presence of Ag in the reconstructions.

Chapter 6 The Effect of Fabric Structures on Inkjet Printed Electronic Textiles

6.1 Introduction

Potential applications of electronic textiles (E-textiles) for use in wearable technology have been previously demonstrated by a number of researchers and industries [8,56,245,387–389]. E-textiles that contain electrically conductive tracks can be embedded or layered with other electronic components to enable systems for a range of purposes including sensing, computing, communication, and actuation[390–393]. Depending on the fabric's purpose, the conductive tracks can be used as interconnects, antennae or for electrodes in energy storage devices to exploit its flexible and stretchable nature[55,59,329,394].

Previous reports on the conductive properties of E-textiles achieved through inkjet printing have shown promising results, however they indicate that the textiles' flexibility, wearability, breathability, and washability may be compromised[1–3]. Additionally, there have been reports of unwanted migration of the conductive material on and within textile substrates. This ink bleeding phenomenon leads to a waste of expensive functional inks and reduces the electrical performance[15,124,188]. A variety of methods have been introduced to improve the printing quality on fabrics, such as modifying the textile surface energy or the sintering process[13,190]. However, to achieve outstanding printing quality and produce conductive E-textiles, without affecting the intrinsic textile properties, remains a great challenge.

In the previous results chapters, the interaction of a functional Ag nanoparticle ink with polyester fibres, yarns and a woven fabric have been reported. This has demonstrated that the ink fibre surface interaction and associated capillarity forces drive the flow across and within the fibrous structure of the fabric. The importance of the effective pore radius in driving the ink transportation speed in the yarn was revealed. Meanwhile a conflict in the transport behaviour between experiments on ink/yarn and ink/fabric interaction illustrated the important effect of fabric woven structures on ink transportation. Additionally, the effect of the fibre and yarn architecture was demonstrated by the distinct difference in electrical properties measured in the warp and weft directions of the standard fabric used after printing and sintering the Ag ink. This influence of the internal fibre structure is as important as the effects of surface treatment, drop spacing or sintering methods on the printing quality and electrical performance of the textile.

These studies have revealed the fundamental mechanisms of ink textile interaction and the electrically conductive mechanism in e-textiles. Individual printed ink droplets can form connected conductive paths among the pores in yarns. Increased effective pore radius led to increased ink infiltration rate in the yarn, while other geometric factors such as an increase in the volume fraction of fabric scale pores (pores between crossing yarns) and reduced tortuosity of the yarns, could result in reduced ink infiltration rate in fabrics. A greater infiltration rate at the fabric scale could lead to better connectivity of ink objects in a yarn and improved electrical performance. These observations raise the possibility of simply altering the textile's structure to achieve improved printing quality and conductive performance of e-textiles[380], which to our knowledge, has not been previously discussed in the prior literature. In order to explore the effect of the fabric structure further, six examples of polyester woven fabrics with nominally the same fibre composition but with different fabric structures are investigated. These observations will be compared with their expected interaction behaviours will be evaluated through combining models of fluid infiltration used earlier, and any findings will be used to determine the influence of fabric structure on printing quality and subsequent electrical conductivity.

6.2 Research Methods

Six types of plain-woven polyester fabrics, provided by Premier Textiles (Manchester, UK), have been used as substrates and listed in Table 6.1. Note that fabric F2 is the same fabric as used in chapters 4 and 5 and is identified by bold letters in the table. Since it was found that the reducing the drop spacing improves the electrical properties, the silver ink was inkjet printed using 10 μm drop spacing with a DMP 2800 printer (Fujifilm Dimatix, Santa Clara, CA) and printheads of nominal drop volume 10 pl (DMC-11610, Fujifilm Dimatix) to produce lines and 5 mm × 5 mm patches with the inter-line spacing set equal to the drop spacing. No surface treatment was applied to the fabric prior to printing. Heat treatment method (SPL) was applied with 5 layers of ink printed, with each layer sintered for 20 mins at 150 ℃ immediately after printing and drying before overprinting any subsequent layer, once the final printed layer was dried the multilayer was sintered for a further 40 mins at 150 ℃.

FTIR was used to examine the chemical composition of the polyester fabrics. Electrical conductance along a single yarn tow was measured using a 4-point probe (PE4, Everbeing, Hsinchu City, Taiwan) coupled to a current source and voltmeter (Keithley 2400, Cleveland, OH). The radius of the probes was modified to 150 μm and the distance between the probes was one repeat units of the weave. Optical images and X-ray tomography were used to observe the spreading of silver ink on the fabrics and the connectivity of silver deposition on textiles.

6.3 Results and Discussions

6.3.1 Fabric Characterisation

Figure 6.1 shows FTIR spectra obtained for each of the 6 different fibre samples used in this study. The spectra show little difference from each other, which is consistent with the assumption that all the polyester fibres used in the supplied fabrics have a similar composition. The strong peaks at wave numbers 718 cm^{-1}, 865 cm^{-1} and 1988 cm^{-1} are related to the benzene ring structure of polyterephthalate, while the peaks at 1090 cm^{-1} and 1241 cm^{-1} represent the C-O stretching, and the peak at 1710 cm^{-1} indicates C=O stretching in the ester linkages, finally the peak at 2950 cm^{-1} illustrates alkane C-H stretching. There is no significant new peak or intensity change comparing fabric F2 as studied in previous chapters with the other fabrics. We believe that the similar nature of the spectra indicates a similar surface energy for the fibres in the fabric. Therefore, we assume that the ink/fibre contact angle will be constant for the six fabrics studied and that any differences in their behaviour will be predominantly caused by differences in the textile architecture.

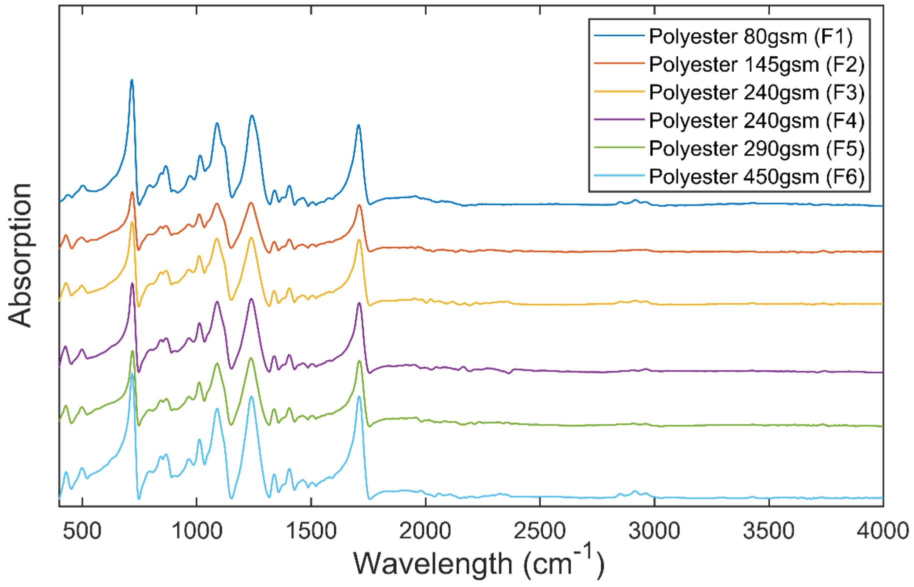

Figure 6.1 FTIR spectrum of the fabric samples F1 to F6.

Key parameters for the textile architecture of each fabric were measured and are summarised in Table 6.1. All the measurements for each of the 6 fabrics studied was obtained from cross-sections of the fabrics obtained from XCT reconstructions and analysed using ImageJ (Figure 6.2), each measurement is a mean and standard deviation from 5 samples.

Table 6.1 Fibre, yarn and fabric parameters of six types of plain-woven polyester textiles used in this project. Fabric weight and yarn density data given by the supplier; all other measurements are derived from analysis of XCT reconstructions. Each measurement was averaged among three samples, and the standard deviation was calculated.

Fabric Name		F1	**F2**	F3	F4	F5	F6
Fabric Weight (g/m^2)		80	**145**	240	250	290	450
Total Fibre Volume per area in Fabric (µm^3/ µm^2)		60.4	**110**	176	181	192	302
Yarn Density (ends/cm)	warp	40	**23.6**	10	14.5	16.5	10
	weft	60	**30**	11.6	18	28.5	25
No. Fibres in Yarn	warp	70±3	**210±4**	650±7	500±5	350±5	520±7
	weft	45±2	**50±2**	210±4	330±3	350±5	500±7
Fibre Diameter (µm)	warp	10±0.7	**10±0.6**	10±0.5	10±0.3	10±0.6	10±0.4
	weft	10±0.5	**16±0.8**	18±0.9	10±0.5	10±0.3	10±0.5
Yarn Longitude Diameter (µm)	warp	140±9.4	**300±8.5**	650±16	400±4.5	350±22	500±21
	weft	150±3.9	**300±15**	820±40	550±8.9	480±20	600±6.1
Yarn Latitude Diameter (µm)	warp	80±6.8	**200±17**	200±5.7	270±8.9	180±18	300±27
	weft	70±2.1	**100±6.2**	250±3.5	150±2.5	160±8.2	280±18
Tortuosity	warp	1.03±0.01	**1.05±0.01**	1.05±0.01	1.05±0.01	1.07±0.01	1.03±0.01
	weft	1.18±0.01	**1.19±0.01**	1.08±0.01	1.1±0.01	1.15±0.01	1.25±0.01
Fibre Volume Fraction in Yarn	warp	0.60±0.02	**0.60±0.01**	0.65±0.01	0.71±0.01	0.70±0.01	0.70±0.02
	weft	0.50±0.03	**0.50±0.02**	0.55±0.01	0.68±0.03	0.68±0.02	0.60±0.02
Effective Fibre Pore Size (mean fibre separation) (µm)	warp	2.3±0.08	**2.3±0.04**	1.8±0.03	1.3±0.01	1.4±0.02	1.4±0.04
	weft	3.5±0.21	**5.5±0.22**	5.1±0.09	1.5±0.06	1.5±0.04	2.3±0.07
Cross-section Pore Area in a Single Yarn (µm^2)	warp	4000±260	**18000±1900**	38500±1300	23500±110	16200±1700	36000±4100
	weft	5000±310	**12500±390**	67500±5800	16000±520	17600±1200	52000±3300
Pore Volume Density in yarn in fabric (µm^3/ µm^2)		51.8±3.3	**89.2±6.1**	125±8.6	67.5±1.2	86.3±6.9	200±15

The total fibre volume per area in fabric is defined as the fibre volume in the fabric captured using XCT divided by the area of the image, which represents similar results as the fabric weight data provided by the manufacturer. The number of fibres in the yarn was counted using the ImageJ 'multipoint' tool (Figure 6.2). The fibre diameter, yarn diameter and tortuosity (ratio of the curved length to the distance between its ends), and yarn area were measured by drawing straight or freehand lines across appropriate areas in the image and measured using the 'Analyse-Measure' function. The yarn area was measured using the same method while drawing an elliptical shape to define the yarn perimeter. Because of the consistent spinning process from fibres to yarns, the number of fibres and the fibre diameters were stable without any large deviations from the mean values. The yarn diameters show greater variation as in woven fabrics the fibres on the surface can be loose as shown in Figure 6.2, while the tortuosity of the yarns remains consistent.

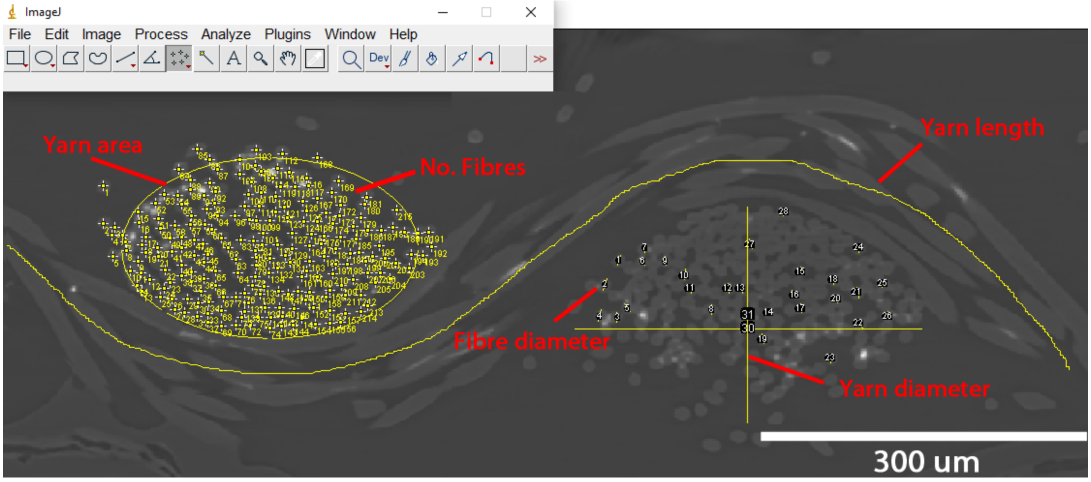

Figure 6.2 Example of analysis of number of fibres, fibre diameter, yarn diameter and yarn tortuosity measurements using ImageJ.

The fibre volume fraction in the yarn, V_f, was measured using the area fraction of fibres in the cross-sectional images. As shown in Figure 6.3, through selecting the image thresholding, the area of fibres was segmented out from the pore area, and by drawing the elliptical shape around the yarn area and applying 'Analyse-Measure' function, the area fraction of fibres in yarn can be obtained in ImageJ, and the cross-section pore area in the yarn equals the yarn area multiplied by (1- V_f).

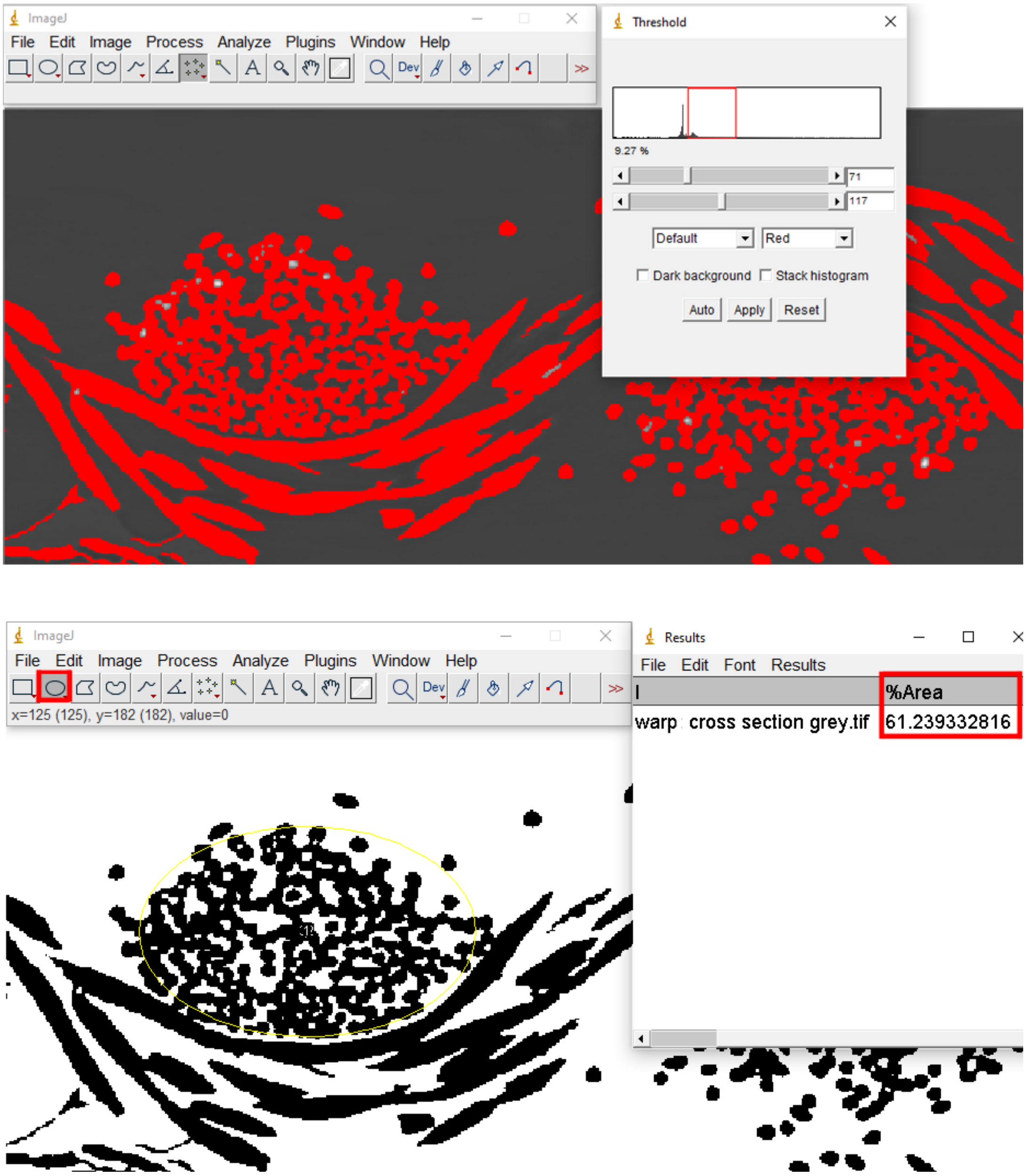

9.27 %

71

117

Default Red

☐ Dark background ☐ Stack histogram

x=125 (125), y=182 (182), value=0

l	%Area
warp cross section grey.tif	61.239332816

Figure 6.3 Example of the method used to obtain fibre volume fraction in yarn through the cross-section image from XCT and ImageJ.

The effective pore size is calculated assuming an ideal hexagonal packing of parallel fibres (Figure 6.4). The effective pore size, a, is defined as two times the effective pore radius, r_{eff}, and is determined from the fibre volume fraction V_f, and mean fibre radius, r_f. as follows:

$$V_f = \frac{A_f}{A_h} = \frac{\pi r_f^2}{\frac{3\sqrt{3}}{2}\left[\frac{r_{eff}+r_f}{\cos(30^\circ)}\right]^2} \qquad (6.1)$$

$$a = 2r_{eff} = 2 * (\sqrt{\frac{\pi r_f^2}{2\sqrt{3}V_f}} - r_f) \quad (6.2)$$

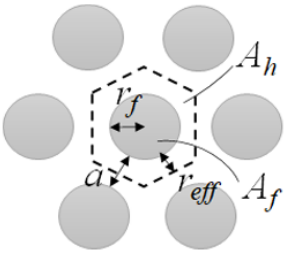

Figure 6.4 Schematic diagram showing the ideal hexagonal packing used for the effective pore size calculation.

The cross-section pore area (A_{py}) of a single yarn can be obtained from XCT cross section images as shown in Figure 6.3 through ImageJ analysis, which is the pore area in the drawing elliptical shape around the yarn area. The volume density of pores in yarns in fabric (V_{pf}) can be calculated through Equation 6.3, where A_{py} refers to the area of pores in individual yarns, and A_{pf} includes both warp and weft direction yarns. It is noteworthy that the pore volume in the yarns within the fabrics does not proportionally relate to the effective pore size.

$$\begin{aligned} V_{pf} &= (A_{py} * yarn\ length * number\ of\ yarns)_{warp+weft} / fabric\ area \\ &= (A_{py} * yarn\ density * yarn\ toruosity)_{warp+weft} \end{aligned} \quad (6.3)$$

Comparing with fabric F2, as used in the previous chapters, F1 is a thinner fabric, composed of thinner yarns with a smaller number of fibres in each yarn, yet has a similar fibre volume fraction and effective fibre pore size as F2. In contrast, fabrics F3 to F6 are thicker fabrics compared to F2; they have thicker yarns comprising a larger number of fibres with higher fibre volume fraction and a smaller effective fibre pore size. Additionally, thicker yarns can limit the yarn density in the fabric.

6.3.2 Inkjet Printing Quality and Conductivity of Electronic Textiles

The optical images in Figure 6.5 (a) shows a dramatic change in printing quality with different textile structures. Figure 6.5 (b) quantifies the ink spreading length in each fabric, the normalised spreading length represents the spreading length of ink on fabrics divided by the originally printed pattern length. It is shown that fabrics F1 and F2 show a large amount of ink bleeding, where the ink bleeds for over 2 times the distance of the originally printed length. Fabrics F3 to F6 show improved printing quality with little ink bleeding occurred. The most anisotropic printing quality is found in fabric F2, where the ink spreading difference between warp and weft yarns is the greatest due to the difference in the yarn structures.

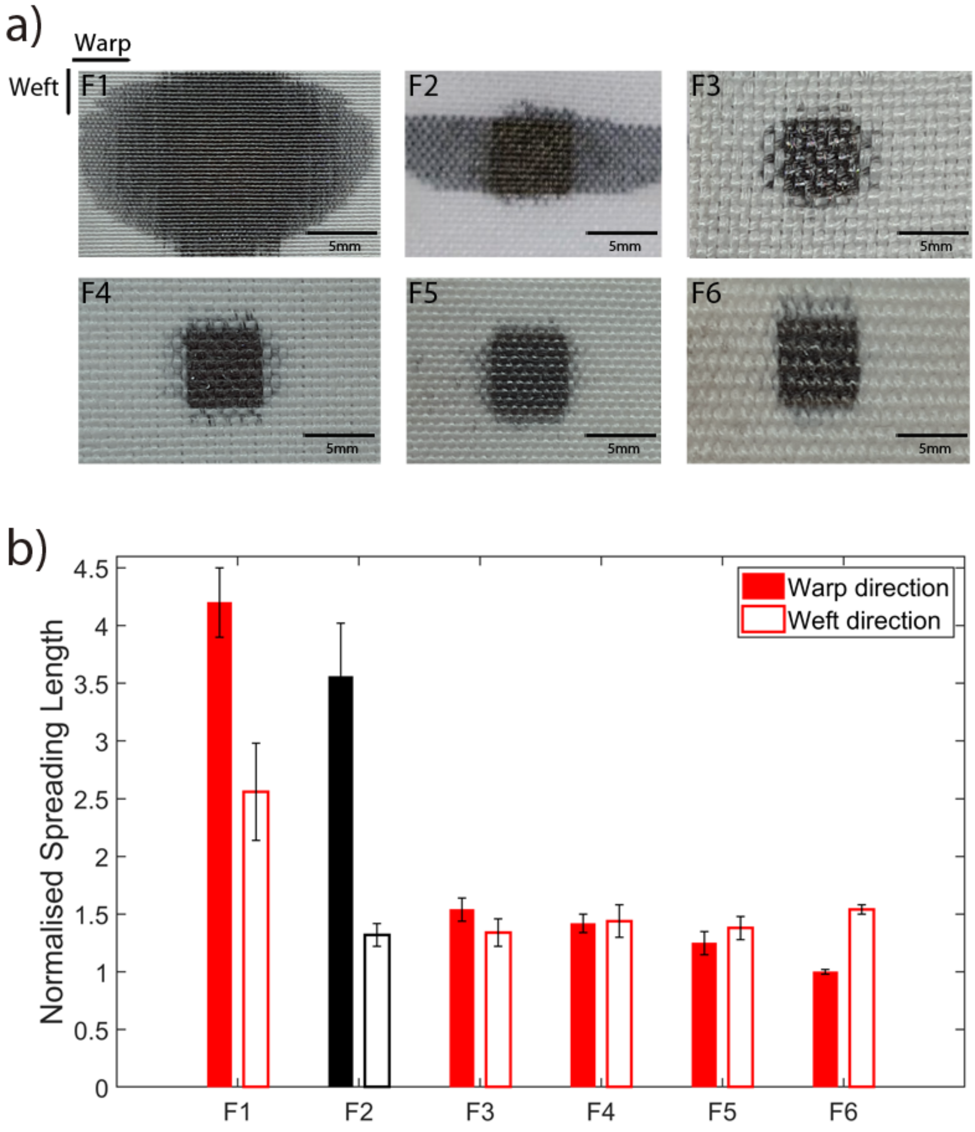

Figure 6.5 (a) Optical images of Ag deposition on six fabric structures from F1 to F6 with 5 layers sintering per layer and 10μm drop spacing, same warp and weft directions apply on all six fabrics as indicated on the top left of the figure. (b) Spreading length of the ink, normalised by the printed patch length, on six types of fabrics in warp and weft directions, based on three specimens for each measurement.

Apart from improving the ink printing quality on textiles, the electrical conductivity of e-textiles requires enhancement. The measured conductance values for 5 layers of silver ink printed on six types of fabrics with 10 μm drop spacing were measured, as shown in Table 6.2. The conductance is reported only along the warp direction because low conductive performance was observed along all fabric weft directions. The length used to measure the conductance of the yarn is that set by the interprobe distance used in the measurement device, which depends on the fabric woven structure, individual l_{probe} applied for fabric F1 to F6 are shown in Table 6.2. To compare the conductance values without the effect of the probe measuring length, the values were normalised based on the measurement conductance times with the probe length applied on measurement, and the results are plotted as shown in Figure 6.6. It is found that fabrics F1 to F3 show better conductance results compared to fabrics F4 to F6.

Table 6.2 Measured conductance results with their corelated probe lengths, and the total silver volume captured in XCT imaged area.

Fabrics	F1	F2	F3	F4	F5	F6
Measured conductance (Siemens)	3.6±2.3 $*10^{-2}$	2.5±2.0 $*10^{-2}$	4.4±3.8 $*10^{-2}$	9.6±9.0 $*10^{-4}$	6.1±5.9 $*10^{-3}$	1.6±0.8 $*10^{-4}$
Probe length (μm)	280	1400	1750	1090	750	850
Yarn conductance (Siemens·μm)	10.0± 6.4	34.9± 28.6	77.5± 66.9	1.05± 0.98	4.56± 4.43	0.14± 0.07
Total Ag volume in imaged area (μm^3) (1350um*1350um)	1.4±0.2 $*10^7$	3.2±0.2 $*10^7$	4.2±0.7 $*10^7$	3.3±0.5 $*10^7$	3.7±0.5 $*10^7$	4.1±0.7 $*10^7$
Total inkjet printed Ag volume (μm^3)	2.64* 10^7	2.64* 10^7	2.64* 10^7	2.64* 10^7	2.64* 10^7	2.64* 10^7
Ag volume density fraction	0.53	1.21	1.59	1.25	1.40	1.55

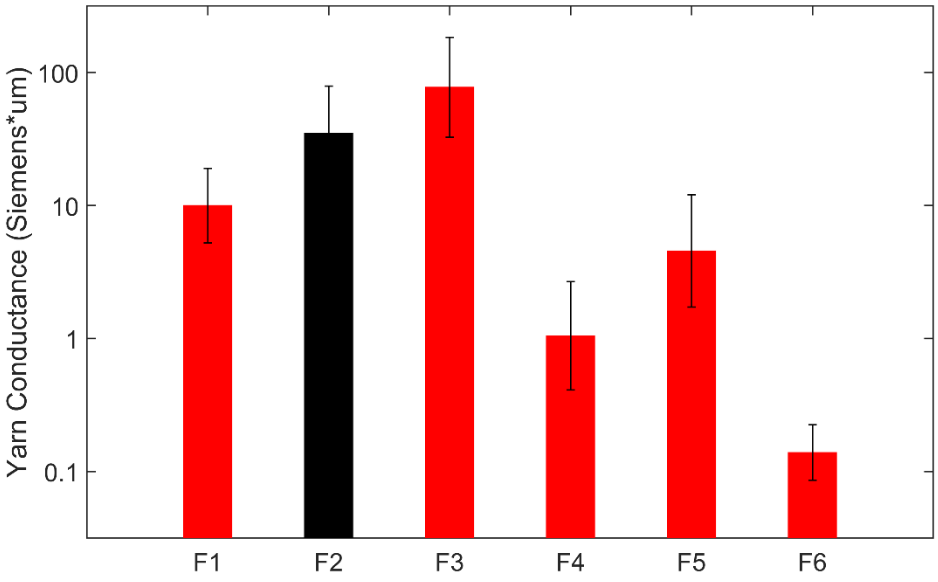

Figure 6.6 Normalised electrical conductance values of 5 layers silver ink printed on the six types of fabrics with10 μm drop spacing.

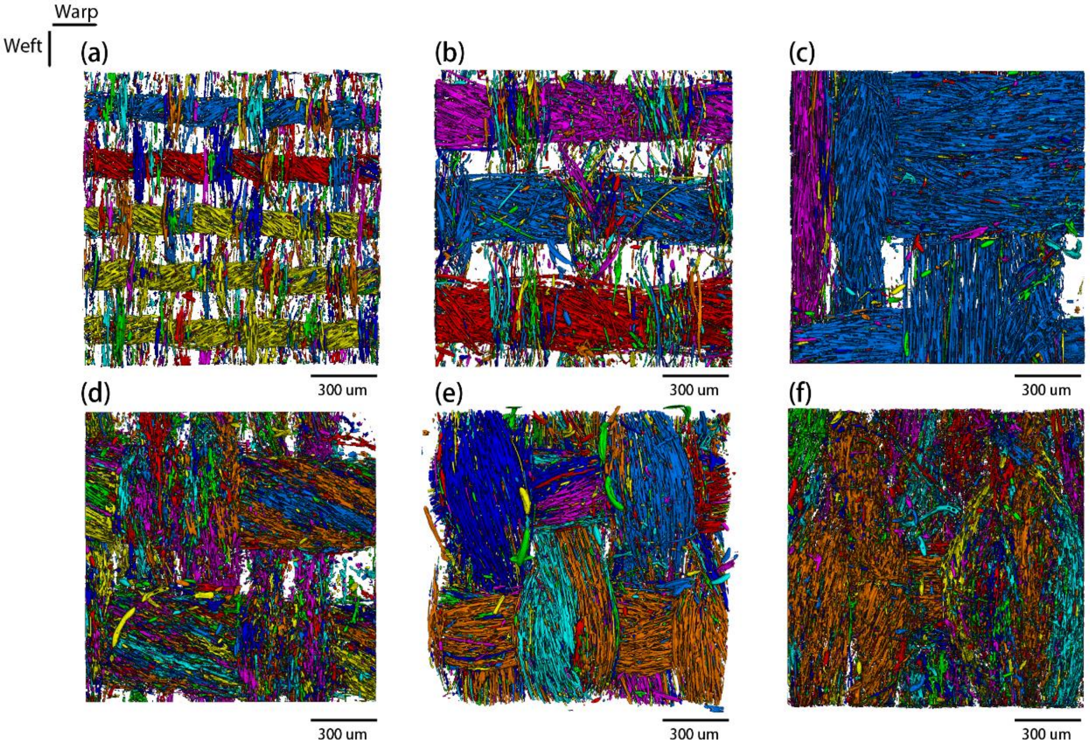

Figure 6.7. Segmented X-ray images of Ag deposition on six fabric structures of (a)-F1, (b)-F2, (c)-F3, (d)-F4, (e)-F5 and (f)-F6 with 5 layers sintering per layer and 10um drop spacing, same warp and weft directions apply on all six fabrics as indicated on the top left of the figure.

Table 6.2 also presents the Ag volume values obtained from XCT images, where higher total silver volume in imaged area was obtained in fabrics F2 to F6 comparing to F1. Note that the total Ag volume measured from the XCT data is different from the total volume of Ag printed as determined from the number of drops printed (2.64 x 10^7 μm^3, this will be discussed with the other XCT results.

To further understand the effect of textile structures on e-textiles, segmented X-ray tomography images of silver deposition on the six fabric structures is shown in Figure 6.7. Constant colour regions in the warp yarns shows the extensive silver connectivity in fabric F1 to F3, and discontinuous silver objects are observed in fabric F4 to F6. Additionally, the silver objects can be separated when multiple threads are involved in single yarn tows in fabrics F4 to F6, where different colour regimes were detected in weft yarns in fabric F3 to F6 as shown in Figure 6.7 (c-f). The silver volume density can then be obtained through the Ag volume measured in the imaged area divided by the area captured (shown in Table 6.2), and the fraction of the silver volume density captured in the XCT image to the originally inkjet printed silver volume density is shown as Ag volume density fraction in Table 6.2. Since the sintered silver volume captured in XCT is greater than the actual deposited silver volume due to the segmentation method applied as discussed in chapter 5, the silver volume density results in values greater than one in all fabrics except fabric F1.

Interestingly, it is observed that the electrical performance of the six types of fabrics is in contrast with their printing quality (resistance to bleeding). Lower printing quality was observed in fabrics F1 to F3 and these showed the highest electrical conductance values. It is noticeable in Figure 6.7 that the silver object connectivity reduces with increased printing pattern quality when the spreading mechanism is limited in fabric F4 to F6.

6.3.3 The Effect of Fabric Structures on the Printing Quality of Inkjet Printed Electronic Textiles

Figure 6.5b presented the ink spreading length on the six types of fabrics. This data can be compared with the predictions of the models of Washburn and Darcy. If we assume a constant contact angle (16°), yarn sphericity ($\varnothing$ =1.86), ink viscosity (μ = 14 mN.m^{-2}.s) and surface tension (γ_{LV} = 37.5 x 10^{-3} N.m^{-1}) for ink transport in all six fabrics, Table 6.3 summarises the predicted infiltration rate ($\frac{L^2}{t}$) through applying Washburn (geometric constant $C=10.9$) and Darcy's law (geometric constant $K=86.2$) as measured in chapter 4 using fabric F2.

Table 6.3 Ink infiltration rate, L^2/t, in the warp and weft fabric directions, as predicted using the approach of Washburn and Darcy, comparing with spreading length measured. for the 6 fabrics. (Averaged L-measured values are presented, see Appendix 6.1 for detailed measurement values)

Fabrics	Orientation	F1	F2	F3	F4	F5	F6
L^2/t (cm^2/s) (Washburn)	Warp	0.16	0.16	0.13	0.09	0.10	0.11
L^2/t (cm^2/s) (Washburn)	Weft	0.25	0.39	0.36	0.11	0.16	0.16
L^2/t (cm^2/s) (Darcy)	Warp	0.16	0.16	0.14	0.11	0.11	0.11
L^2/t (cm^2/s) (Darcy)	Weft	0.23	0.38	0.35	0.12	0.12	0.16
L-measured (cm)	Warp	2.10	1.78	0.77	0.71	0.63	0.50
L-measured (cm)	Weft	1.28	0.66	0.67	0.72	0.69	0.77
L-measured^2/(L^2/t) (s) (Washburn)	Warp	*13.1*	*11.1*	*5.92*	*7.88*	*6.30*	*4.54*
L-measured^2/(L^2/t) (s) (Washburn)	Weft	*5.12*	*1.69*	*1.86*	*6.54*	*4.31*	*4.81*
L-measured^2/(L^2/t) (s) (Darcy)	Warp	*13.1*	*11.1*	*5.50*	*6.45*	*5.72*	*4.54*
L-measured^2/(L^2/t) (s) (Darcy)	Weft	*5.56*	*1.74*	*1.9*	*6.00*	*5.75*	*4.81*

In Table 6.3, L-measured values represent the ink spreading length observed on optical images, and L-measured^2/(L^2/t) shows the time (t) that requires in theory for ink spreading to the measured length. We assume that the total time available for spreading is constant in each case because the ink and printing conditions are identical. Thus, we use the metric of the measured ink transport length raised to the power 2 (L^2) divided by the infiltration rate predicted by the Washburn and Darcy's models (L^2/t) as a comparator between model and experiment (in italics, Table 6.3).

First, we consider fabrics F4, F5 and F6, all of which showed relatively little ink bleeding along either the warp or weft directions. For these three fabrics the Washburn and Darcy models predict similar infiltration rates along warp and weft, which is consistent with experiment as seen by the $(L^2)/(L^2/t)$ values. However, fabrics F1, F2 and F3 show considerable differences from the models' predictions. In all three cases fluid is transported considerably greater lengths along the weft direction than the warp direction. This contradicts the predictions of the infiltration models, which predict greater infiltration along the warp direction and this is confirmed by the considerable difference in the $(L^2)/(L^2/t)$ values for the warp and weft directions, in contrast with the similar values seen for fabrics F4 – F6. This phenomenon was observed and discussed in chapter 4, where the investigated fabric F2 showed different ink/yarn and ink/fabric interaction and requires more in-depth study. Therefore, we will focus on the difference among six types of the fabrics rather than the warp and weft directions in single fabrics in this section.

In terms of ink printing quality on fabrics, the small pore volume density in yarn in fabric (V_{pf}) F1 was considered to be one of the reasons that leads to its excessive spreading behaviour. The pore volume density in yarn in fabric (V_{pf}) is calculated from the pore volume in the fabric divided by the area of the fabric. This can be compared with the printed ink volume density before heat treatment to realise the possibility of printed ink volume excessing the pore volume in fabric. The printed ink volume density (ρV_{ink}) can be calculated as shown in Equation 6.5, through the 10 μm drop spacing and the droplet volume (V_{drop}) 7 pL, and ρV_{ink} = 70 μm is calculated from Equation 6.5. The number is greater than the pore volume density in yarn in fabric (V_{pf}) in F1, but similar or higher than other values from F2 to F6.

$$\rho V_{ink} = N_{drop} * V_{drop}/printed\ area = \left(\frac{V_{drop}}{drop\ spacing}\right)^2 \qquad (6.5)$$

When silver ink is sintered after each layer of printing, it is found that the volume of pores in F1 is smaller than the volume of each ink layer printed in theory, which means that there is not enough volume to hold the amount of ink printed on fabric F1. On the other hand, from fabric F2 to F6, all the volumes of pores in fabric are similar or higher than the amount of ink deposited.

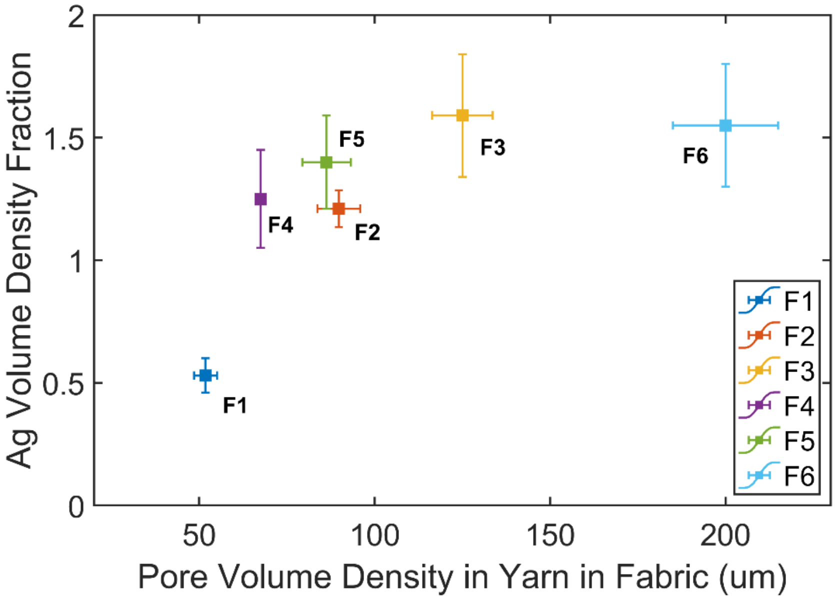

Figure 6.8 Total Ag volume in fabric of 5 layers inkjet printed with 10 μm drop spacing and sintered per layer as a function of total pore volume in yarns of six types of fabrics.

It is found that Ag volume density increases with increasing pore volume density, more than twice the average amount of Ag was measured in fabrics F2 to F6 compared to fabric F1. Nevertheless, the effect of the pore volume in yarn only takes place after assuming that the ink can penetrate to the centre of the yarn and fill all the pores in yarn, and it cannot represent the total pore volume in a fabric scale. Apart from the effect of the pore volume in yarn on ink bleeding of fabric F1, the fact that the greater pore volume density in yarns in fabric F2 than ρV_{ink} leads to ink bleeding in fabric F2, on the contrary, fabric F4 with smaller pore volume in yarns in F4 presents less ink bleeding compared to F2, clearly indicates that the spreading mechanism is influenced by more than just the pore volume in the yarn.

The other main parameter dominating the ink spreading was considered to be the capillary forces as considered in existing models such as Washburn and Darcy. When there is sufficient pore volume in the yarns such as in fabrics F2 and F4, the lower fibre volume fraction and higher effective pore size in fabric F2 compared to F4, leads to increased capillary pressure at the yarn scale and more ink bleeding in the fabrics. Additionally, there are other common features displayed by fabrics F3 to F6 but not in fabrics F1 and F2, such as the increased fabric weight, total fibre volume in the fabrics, the number of fibres in the yarn, and the yarn diameters (see Table 6.2) that are associated with the overall capillary pressure in the fabric scale, which could prohibit the ink spreading behaviour.

In addition, the weft direction of fabric F6 shows different spreading behaviour to F2 with the same pore size, yet the increased tortuosity could be a factor that limits the spreading of ink in F6 weft direction. However, for the lower tortuosity value of fabric F6 in the warp direction, similar printing quality is reached in the fabric weft direction as the pore size plays an important role for the spreading behaviours. Therefore, a combination of effects are found to influence the ink spreading on textiles. Overall, through comparing these six types of fabric structures in this study, it is found that the key parameters that can improve the printing quality on textiles, are sufficient pore volume in yarns in fabrics, the reduced capillary pressure in both the yarn and the fabric scales. This overall capillary pressure reduces with reduced effective pore size (increased fibre volume fraction) in yarns, and thicker and tighter packed yarns (the increased fabric weight, total fibre volume in fabrics, the number of fibres in yarn, and the yarn diameters).

6.3.4 The Effect of Fabric Structures on the Conductivity of Inkjet Printed Electronic Textiles

As well as the effect of textile structures on ink spreading and printed image quality, their effect on the ink connectivity and the conductivity of e-textiles needs to be determined. Interestingly, improved printing quality with fabrics F4 to F6 leads to reduced ink connectivity within the fabric and reduced conductivity of the ink in these fabrics. Figure 6.9 shows the total silver volume measured by XCT in the warp yarn threads and also the volume of the largest individual Ag object in each of the 6 fabrics. From chapter 4 we identified that the electrical conductance correlates strongly with the largest Ag object rather than the total Ag in the fabric and this is true for the fabrics studied here as is clearly demonstrated in figure 6.10. Fabrics F4 - F6 showed reduced connectivity in the fabric (Figure 6.7) and smaller values of the largest connected Ag volume, consistent with their low conductance. Fabrics F2 and F3 show better electrical conductance results and have larger connected silver objects. Interestingly, fabric F1 with smaller largest Ag volume in the warp yarn compared to fabrics F4 and F5 still shows better yarn conductance values. However, in Figure 6.7 this fabric shows better long-range connectivity, which confirms the importance of achieving the percolation threshold in textile structures to reach optimal electrical performance.

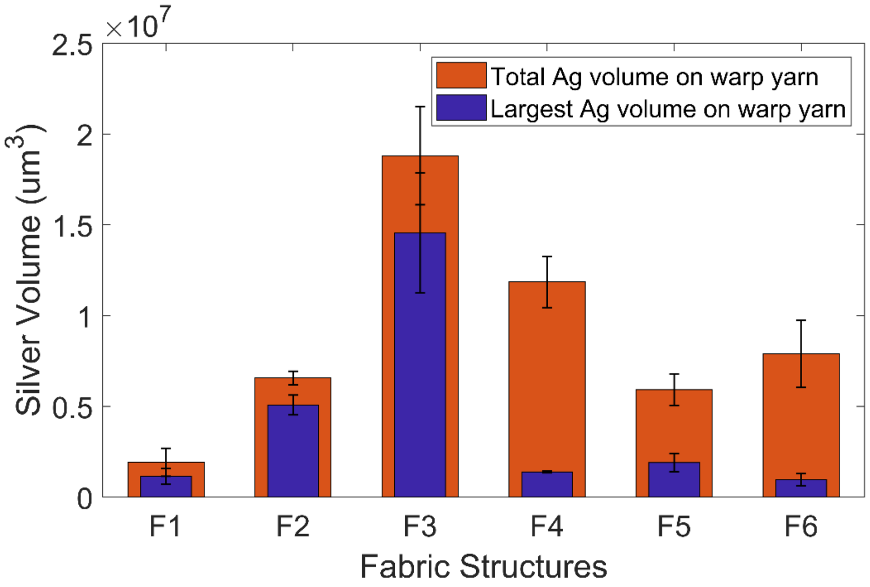

Figure 6.9 Largest connected silver object volume (blue bars) and total silver volume (orange bars) on warp yarns.

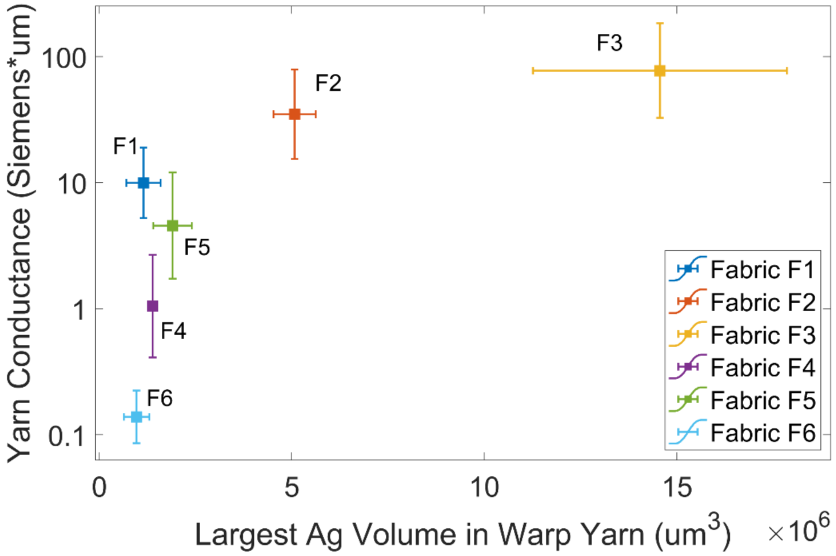

Figure 6.10 electrical conductance as a function of largest Ag volume to the total Ag volume in warp yarn ratio.

Reduced capillarity in the fabric could be the main reason for reduced silver object connectivity, where there is not external force to promote the transport of the ink along the fibre tows. It was proposed that the capillary pressure reduces with reduced effective pore size (increased fibre volume fraction) in yarns, and thicker and tighter packed yarns (the increased fabric weight, total fibre volume in fabrics, the number of fibres in yarn, and the yarn diameters). Figure 6.11 a) shows that effective fibre pore size in the range 1.8 μm to 2.4 μm of fabrics F1, F2 and F3 delivers higher yarn electrical conductance values than effective fibre pore size smaller than 1.6 μm. Figure 6.11 b) shows that increased total fibre volume in fabric that leads to improved printed quality in fabrics reduce the electrical conductance values. A compromise is achieved in fabric F3 where the middle ranged effective pore radius and total volume in fabric guarantees the ink connectivity (electrical performance) and the printing quality at the same time.

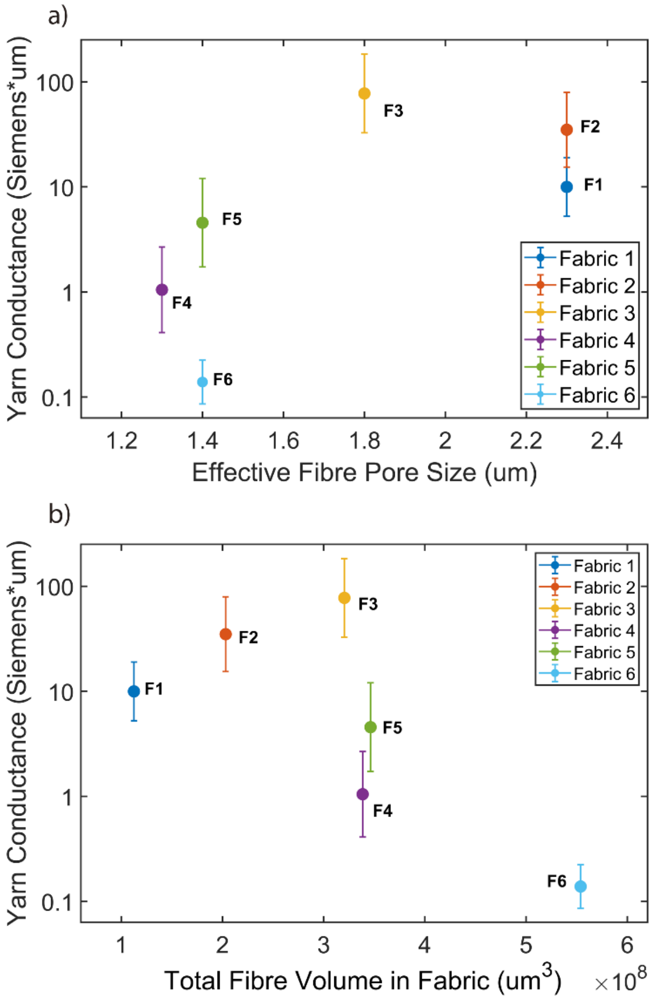

Figure 6.11 Electrical conductance values as a function of effective fibre pore size (a) and total fibre volume in fabric (b) in six fabric structures.

In Chapter 4, the theories of ink/fibre interaction indicates that large fibre pore size in yarn (5.1 μm) promotes ink penetration instead of spreading, however in this chapter we found that a pore size smaller than 1.6 μm could also limit the spreading mechanism since the capillary force in the yarn is reduced. This phenomenon correlates with the ink/yarn interaction theory where both Washburn's equation and Darcy's law state that reduced pore size confines the spreading rate. Additionally, it is observed that apart from the effect of pore size on the ink spreading mechanism, increasing total fibre volume in the fabric constrains the ink spreading in the fabric due to an overall decreased capillary force in the fabric, which is the key for enhanced printing quality of e-textiles. Moreover, the relation between the printing quality and the electrical property emphasises the importance of ink connectivity as mentioned in the previous chapter 5, which needs to be considered during the selection of textile structures.

6.4 Conclusions

In conclusion, it is found that the altering the fabric structure can control inkjet printing image quality and conductivity of electronic textiles, which is a promising approach to improve the performance of e-textiles without compromising the intrinsic advantages of textiles. Sufficient pore volume in yarn is essential to avoid ink bleeding occurred on fabric F1. Additionally, decreased effective fibre pore size, and thicker and tighter packed fabrics (fabrics F4 to F6) are found important to reduce the capillarity in the textile structure, which increased the volume of ink deposition density and improved the printed image quality. However, the electrical conductance on six types of fabric structures is found related to the silver ink connectivity (the largest connected silver object volume) instead of the total silver ink deposition volume, as suggested in chapter 5 (where fabric F1 with less Ag deposition shows better electrical performance than fabrics F4-F5). Higher electrical performance is achieved when ink transport freely in yarns with greater capillary force such as fabric F1 and F2, however, the printing quality is reduced as the spreading mechanism is favoured. The complexity of textile structures is illustrated and the parameters in fibre, yarn and fabric scales need to be considered collectively to control the ink deposition. Therefore, carefully selecting the textile structure for inkjet printing such as fabric F3, which the pore size allows easy ink transportation and the total fibre volume in fabric controls the optimal capillary force for improved printing quality, is essential to achieve both improved printing quality and conductivity of e-textiles.

Chapter 7 Conclusions and Future Work

7.1 Conclusions

This project has analysed the fundamental interactions between a Ag nanoparticle ink and textiles after inkjet printing and studied how this affects the electrical conductivity of the patterns after heat treatment. It has assessed the 3D distribution of ink in fabric structures through X-ray tomography imaging; and investigated the effects of printing drop spacing and number of layers, sintering techniques, textile surface properties and textile structures on inkjet printing quality and electrical conductance of the subsequent electronic textiles.

The ink/textile interaction, at the level of a single fibre, yarn and textiles have been compared with existing models where appropriate. The importance of ink/fibre contact angle and the effective pore radius between fibres has been identified. Ink/fibre interactions were initially studied with the aim of estimating the contact angle value through the drop-on-fibre profile as reported in literatures. It was found that ink/fibre interaction corresponds with existing theories, the contact angle value can be obtained with known fibre surface energy and drop and fibre geometries at low values of contact angle but were not practical when the contact angle was increased through the Scotchgard process. Using these measured ink/fibre contact angle values, ink/yarn interaction was analysed using the approaches from Washburn and Darcy, and both laws were found to be appropriate to model the ink penetration as a function of time along a single tow of fibre. It was found that the effective pore radius was the most important factor in both laws, where greater effective pore radius on weft yarns lead to faster and longer ink spreading. Interestingly, existing theories used to explain ink/fibre and ink/yarn interactions along a single isolated yarn were found to be insufficient to explain the ink/fabric interaction when the same yarns were used to make fabric structures. In experiments of fabrics, greater ink transport was measure along the warp direction than the fabric weft direction is opposite to ink/yarn interaction findings and the predictions of the Washburn and Darcy models of transport. This inconsistency was also found with a number (but not all) of different fabrics. This inconsistent behaviour of small volume droplets interaction within textile architectures has not been addressed in previous literature reports.

3D images of the Ag ink textile interaction were produced using X-ray computed tomography, which, to our knowledge, have never been reported previously in studying e-textiles. The 3D structures clearly show the deposition and transport of the conductive silver ink within woven textiles. After inkjet printing, ink transport occurs preferentially along the direction of the fibre tows in the fabric. Reduced drop spacing, increased number of printing layers and textile hydrophobicity increase the volume and connectivity of inkjet printed silver ink after deposition. In the meantime, the sintering per layer technique further increases the volume and connectivity of inkjet printed silver ink on textiles through an enhanced ink penetration mechanism perpendicular to the fibre tows. X-ray CT images also illustrated the importance of the connectivity and effective volume of printed silver structures on the electrical performance of conductive textiles, which is consistent with a percolation threshold network model. A simple model has been developed to predict the conductance of the specimens through X-ray CT measurements of the effective volume of Ag in continuous conductive objects. It was also found that the majority of the conductive paths develop along each yarn direction and that there is poor electrical connectivity between individual yarn tows even when they overlap in the weave. In addition, due to different yarn structures on fabric warp and weft directions, anisotropic electrical conductance behaviour was found with conductive materials deposited on a range of textile substrates.

After understanding the parameters that could influence the ink deposition and the conductive mechanism, six types of polyester woven structures were studied with the aim of improving the inkjet printing quality and conductive performance on textiles simply through altering the textile structures. It was found that decreased effective pore size, and thicker and tighter packed fabrics improve the printed image quality. However, the prohibited ink spreading reduces the silver objects connectivity and the electrical performance of e-textiles. Therefore, carefully selecting the textile structure with appropriate fibre pore size for ink transportation while controlling the total capillarity in fabric is essential to achieve both improved printing quality and conductivity of e-textiles.

7.2 Outlook and Future Work

The work presented in this thesis provides a fundamental analysis of inkjet printed conductive ink deposition on textiles and explores a range of parameters that could enhance the printing quality and electrical performance of e-textiles. However, further investigation are needed to confirm and consolidate the findings. In chapter 4, the polyester fibre contact angle with the silver ink might be measured with a higher precision force tensiometer to obtain a more accurate comparison of experimental values and existing theories. This might also allow a direct measurement of the change in contact angle after hydrophobic surface treatment such as the Scotchgard process.

Future studies could investigate the influence of fibre orientation and weave architecture on ink flow and with the use of high flux sources such as synchrotrons, dynamic aspects of ink transport could be tracked[378,395]. This might also help identify why the Washburn and Darcy models give a good representation of ink flow in an isolated yarn but not when incorporated in some, but not all, fabric structures.

In chapter 5, there is room for improvement for quantified data analysis from tomography images with higher resolution images. Even with longer scanning time. the intrinsic inhomogeneous composition of materials still limits the reconstruction process to apply accurate values to each voxel. Further quantified analysis might be applied using Avizo software to study not only the silver objects volume distribution but also the density and location of the silver objects. In addition, the number of printed layers applied for sintering per layer technique could be increased further to improve the electrical conductance results. In chapter 6, more woven fabric structures could be involved to refine the selection of fibre pore spacing and fibre volume in fabric to provide more specific guidance in terms of the optimal textile structure to improve both inkjet printing quality and electrical performance.

The last but not the least, it is essential to investigate the durability and washability of inkjet printed conductive textiles for the commercialisation, even though the washing standard applied for e-textiles needs a common agreement. For conductive tracks that serve the function as interconnectors in the wearable design, encapsulation can help protect the durability of printed tracks even if it reduces the breathability of certain areas of the textile substrate. Nevertheless, for large areas that require conductive tracks providing electrical performance on the surface, it is fundamental to apply binders between the textile substrate and the ink without affecting the textile breathability and the ink conductive network. Moreover, the development of stretchable ink could potentially increase the durability of the conductive performance of e-textiles.

Overall, the advantages from inkjet printing and textile substrates deliver promise in the area of e-textiles and wearable technology. This work contributes a fundamental understanding and enhancement on the performance of the products in this research topic. Remaining challenges will need to be tackled done to achieve commercialisation of inkjet printed e-textiles, and the work in this thesis provides a guidance.

References

1. Karim, N. *et al.* All Inkjet-printed Graphene-based conductive pattern for wearable e-textiles application. *J. Mater. Chem. C* **5**, 11640–11648 (2017).

2. Kim, I., Shahariar, H., Ingram, W. F., Zhou, Y. & Jur, J. S. Inkjet process for conductive patterning on textiles: Maintaining inherent stretchability and breathability in knit structures. *Adv. Funct. Mater.* **29**, 1–12 (2019).

3. Carey, T. *et al.* Fully inkjet-printed two-dimensional material field-effect heterojunctions for wearable and textile electronics. *Nat. Commun.* **8**, (2017).

4. Gao, M., Li, L. & Song, Y. Inkjet printing wearable electronic devices. *J. Mater. Chem. C* **5**, 2971–2993 (2017).

5. Yan, K., Li, J., Pan, L. & Shi, Y. Inkjet printing for flexible and wearable electronics. *APL Mater.* **8**, 120705 (2020).

6. Stoppa, M. & Chiolerio, A. Wearable electronics and smart textiles: A critical review. *Sensors (Switzerland)* **14**, 11957–11992 (2014).

7. Z FU, R. and H. C. Pigmented ink formulation. in *Digital printing of Textiles* 218–232 (2006).

8. Tao, X. *Handbook of smart textiles*. *Handbook of Smart Textiles* (2015). doi:10.1007/978-981-4451-45-1

9. Ghahremani Honarvar, M. & Latifi, M. Overview of wearable electronics and smart textiles. *J. Text. Inst.* **108**, 631–652 (2017).

10. Azeem, M., Boughattas, A., Wiener, J. & Havelka, A. Mechanism of liquid water transport in fabrics; A review. *Vlakna a Text.* **24**, 58–65 (2017).

11. Patnaik, A., Rengasamy, R. S., Kothari, V. K. & Ghosh, A. Wetting and wicking in fibrous materials. *Text. Prog.* **5167**, (2017).

12. Pan, N. & Zhong, W. Fluid transport phenomena in fibrous materials. *Text. Prog.* **38**, 1–93 (2006).

13. Whittow, W. G. *et al.* Inkjet-printed microstrip patch antennas realized on textile for wearable applications. *IEEE Antennas Wirel. Propag. Lett.* **13**, 71–

74 (2014).

14. Kastner, J. *et al.* Silver-based reactive ink for inkjet-printing of conductive lines on textiles. *Microelectron. Eng.* **176**, 84–88 (2017).

15. Nechyporchuk, O., Yu, J., Nierstrasz, V. A. & Bordes, R. Cellulose nanofibril-based coatings of woven cotton fabrics for improved inkjet printing with a potential in e-textile manufacturing. *ACS Sustain. Chem. Eng.* **5**, 4793–4801 (2017).

16. Liu, Y., Pharr, M. & Salvatore, G. A. Lab-on-Skin: A review of flexible and stretchable electronics for wearable health monitoring. *ACS Nano* **11**, 9614–9635 (2017).

17. Wang, X., Liu, Z. & Zhang, T. Flexible sensing electronics for wearable/attachable health monitoring. *Small* **13**, 1–19 (2017).

18. Sorayani Bafqi, M. S., Bagherzadeh, R. & Latifi, M. Nanofiber alignment tuning: An engineering design tool in fabricating wearable power harvesting devices. *J. Ind. Text.* **47**, 535–550 (2017).

19. Park, S., Chung, K. & Jayaraman, S. Chapter 1.1 – Wearables: Fundamentals, advancements, and a roadmap for the future. in *Wearable Sensors* 1–23 (2014). doi:10.1016/B978-0-12-418662-0.00001-5

20. An, B. W. *et al.* Smart sensor systems for wearable electronic devices. *Polymers (Basel).* **9**, 303 (2017).

21. Majumder, S., Mondal, T. & Deen, M. Wearable sensors for remote health monitoring. *Sensors* **17**, 130 (2017).

22. Mann, S. Smart ctothing: The wearable computer and WearCam. *Pers. Ubiquitous Comput.* **1**, 21–27 (1997).

23. Wilson, S. & Laing, R. *Wearable technology: Present and future*. (2018).

24. Want, R., Hopper, A., Falcao, V. & Gibbons, J. The active badge system. *ACM Trans. Inf. Syst.* **10**, 91–102 (1992).

25. Ometov, A. *et al.* A survey on wearable technology: History, state-of-the-art and current challenges. *Comput. Networks* **193**, 108074 (2021).

26. Mehdi, M. & Alharby, A. Purpose, scope, and technical considerations of wearable technologies. *Wearable Technol. Concepts, Methodol. Tools, Appl.* 1–20 (2018). doi:10.4018/978-1-5225-5484-4.ch001

27. Van Krevelen, R. *Augmented reality: Technologies, applications, and limitations*. (2007). doi:10.13140/RG.2.1.1874.7929

28. Mann, S. Smart clothing: The wearable computer and wearcam. *Pers. Technol.* **1**, 21–27 (2005).

29. Want, R., Hopper, A., Falcão, V. & Gibbons, J. The active badge location system. *ACM Trans. Inf. Syst.* **10**, 91–102 (1992).

30. Park, S. *et al.* Flexible molecular-scale electronic devices. *Nat. Nanotechnol.* **7**, 438–442 (2012).

31. Kim, D.-H. *et al.* Epidermal electronics. *Science (80-.).* **333**, 838–843 (2011).

32. Amanda Myers, Allison Bowles, Hasan Shahariar, R. B. and J. S. J. Wearable electronics. *Textile World* (2017).

33. Baran, D., Corzo, D. & Blazquez, G. Flexible electronics: Status, challenges and opportunities. *Front. Electron.* **1**, 2 (2020).

34. Heo, J. S., Hossain, M. F. & Kim, I. Challenges in design and fabrication of flexible/stretchable carbon- and textile-based wearable sensors for health monitoring: A Critical Review. *Sensors (Basel).* **20**, 3927 (2020).

35. Yang, C. Y. *et al.* Phase-driven magneto-electrical characteristics of single-layer MoS2. *Nanoscale* **8**, 5627–5633 (2016).

36. Chmiola, J., Largeot, C., Taberna, P.-L., Simon, P. & Gogotsi, Y. Monolithic Carbide-derived carbon films for micro-supercapacitors. *Science (80-.).* **328**, 480–483 (2010).

37. Wang, Y. F. *et al.* Fully Printed PEDOT:PSS-based temperature sensor with high humidity stability for wireless healthcare monitoring. *Sci. Rep.* **10**, 1–8 (2020).

38. Sowade, E., Polomoshnov, M., Willert, A. & Baumann, R. R. Toward 3D-printed electronics: Inkjet-printed vertical metal wire interconnects and

screen-printed batteries. *Adv. Eng. Mater.* **21**, 1900568 (2019).

39. Nag, A., Mukhopadhyay, S. C. & Kosel, J. Wearable flexible sensors: A review. *IEEE Sens. J.* **17**, 3949–3960 (2017).

40. Dong, C. *et al.* High-efficiency super-elastic liquid metal based triboelectric fibers and textiles. *Nat. Commun.* **11**, 3537 (2020).

41. Shuai, L. *et al.* Stretchable, self-healing, conductive hydrogel fibers for strain sensing and triboelectric energy-harvesting smart textiles. *Nano Energy* **78**, 105389 (2020).

42. Wang, L. *et al.* Customizable textile sensors based on helical core–spun yarns for seamless smart garments. *Langmuir* **37**, 3122–3129 (2021).

43. Ma, Y. *et al.* Flexible all-textile dual tactile-tension sensors for monitoring athletic motion during taekwondo. *Nano Energy* **85**, 105941 (2021).

44. Hu, X. *et al.* Conductive graphene-based E-textile for highly sensitive, breathable, and water-resistant multimodal gesture-distinguishable sensors. *J. Mater. Chem. A* **8**, 14778–14787 (2020).

45. Gozutok, Z., Agırbas, O., Bahtiyari, M. I. & Ozdemir, A. T. Low-voltage textile-based wearable heater systems fabricated by printing reactive silver inks. *Sensors Actuators A Phys.* **322**, 112610 (2021).

46. Hong, H., Jiyong, H., Moon, K.-S., Yan, X. & Wong, C. Rheological properties and screen printability of UV curable conductive ink for flexible and washable E-textiles. *J. Mater. Sci. Technol.* **67**, 145–155 (2021).

47. Kim, T. *et al.* Supersonically sprayed washable, wearable, stretchable, hydrophobic, and antibacterial rGO/AgNW fabric for multifunctional sensors and supercapacitors. *ACS Appl. Mater. Interfaces* **13**, 10013–10025 (2021).

48. Keum, K. *et al.* Fully-integrated wearable pressure sensor array enabled by highly sensitive textile-based capacitive ionotronic devices. *Nano Energy* **79**, 105479 (2021).

49. Satharasinghe, A., Hughes-Riley, T. & Dias, T. A review of solar energy harvesting electronic textiles. *Sensors* **20**, (2020).

50. Yin, L. *et al.* A self-sustainable wearable multi-modular E-textile bioenergy microgrid system. *Nat. Commun.* **12**, 1542 (2021).

51. Shi, J. *et al.* Smart Textile-integrated microelectronic systems for wearable applications. *Adv. Mater.* **32**, 1–37 (2020).

52. Sridhar, A. *et al.* Inkjet-printing- and electroless-plating- based fabrication of RF circuit structures on high-frequency substrates. *J. Micromechanics Microengineering* **19**, (2009).

53. Lacerda Silva, N., Gonçalves, L. M. & Carvalho, H. Deposition of conductive materials on textile and polymeric flexible substrates. *J. Mater. Sci. Mater. Electron.* **24**, 635–643 (2013).

54. Malik, S. K., Kadian, S. & Kumar, S. Advances in ink-jet printing technology of textiles. *Indian J. Fibre Text. Res.* **30**, 99–113 (2005).

55. Castano, L. M. & Flatau, A. B. Smart fabric sensors and e-textile technologies: A review. *Smart Mater. Struct.* **23**, (2014).

56. Torrisi, F. *et al.* Inkjet-printed graphene electronics. *ACS Nano* **6**, 2992–3006 (2012).

57. Bidoki, S. M. *et al.* Inkjet printing of conductive patterns on textile fabrics. *AATCC Rev.* **5**, 11–14 (2005).

58. Walker, S. B. & Lewis, J. A. Reactive silver inks for patterning high-conductivity features at mild temperatures. *J. Am. Chem. Soc.* **134**, 1419–1421 (2012).

59. Li, Y., Torah, R., Beeby, S. & Tudor, J. An all-inkjet printed flexible capacitor on a textile using a new poly(4-vinylphenol) dielectric ink for wearable applications. *Proc. IEEE Sensors* 5–8 (2012). doi:10.1109/ICSENS.2012.6411117

60. Nawab, Y. *et al. Textile Engineering: An introduction*. (De Gruyter, 2016).

61. Yilmaz, K. B., Sabuncuoglu, B., Yildirim, B. & Silberschmidt, V. V. A brief review on the mechanical behavior of nonwoven fabrics. *J. Eng. Fiber. Fabr.* **15**, 1558925020970197 (2020).

62. Kuroda, T., Takahashi, H. & Masuda, A. Chapter 3.2 – Woven electronic textiles. in *Wearable Sensors* 175–198 (2014). doi:10.1016/B978-0-12-418662-0.00021-0

63. Majumdar, A. *Principles of woven fabric manufacturing*. (2016). doi:10.1201/9781315367729

64. Gries, T., Raina, M., Quadflieg, T. & Stolyarov, O. 1 - Manufacturing of textiles for civil engineering applications. in (ed. Triantafillou, T. B. T.-T. F. C. in C. E.) 3–24 (Woodhead Publishing, 2016). doi:https://doi.org/10.1016/B978-1-78242-446-8.00002-1

65. Ayranci, C. & Carey, J. 2D braided composites: A review for stiffness critical applications. *Compos. Struct.* **85**, 43–58 (2008).

66. Gries, T., Stüve, J., Grundmann, T., St, J. & Grundmann, T. Textile reinforcement structures. *Ceram. Matrix Compos.* 21–47 (2008). doi:https://doi.org/10.1002/9783527622412.ch2

67. Gong, H. & Ozgen, B. 5 - Fabric structures: Woven, knitted, or nonwoven. in *The Textile Institute Book Series* (eds. Miao, M. & Xin, J. H. B. T.-E. of H.-P. T.) 107–131 (Woodhead Publishing, 2018). doi:https://doi.org/10.1016/B978-0-08-101273-4.00007-X

68. Kumar, B. & Hu, J. 6 - Woven fabric structures and properties. in *The Textile Institute Book Series* (eds. Miao, M. & Xin, J. H. B. T.-E. of H.-P. T.) 133–151 (Woodhead Publishing, 2018). doi:https://doi.org/10.1016/B978-0-08-101273-4.00004-4

69. Shaker, K., Umair, M., Ashraf, W. & Nawab, Y. Fabric manufacturing. *Phys. Sci. Rev.* **1**, (2016).

70. Kumar, R. S. *Textiles for industrial applications*. (CRC Press, 2016).

71. Alagirusamy, R. & Das, A. Chapter 8 - Conversion of fibre to yarn: An overview. in *Woodhead Publishing Series in Textiles* (ed. Sinclair, R. B. T.-T. and F.) 159–189 (Woodhead Publishing, 2015). doi:https://doi.org/10.1016/B978-1-84569-931-4.00008-8

72. Jost, K., Dion, G. & Gogotsi, Y. Textile energy storage in perspective. *J.*

Mater. Chem. A **2**, 10776–10787 (2014).

73. Tyagi, G. K. 5 - Yarn structure and properties from different spinning techniques. in *Woodhead Publishing Series in Textiles* (ed. Lawrence, C. A. B. T.-A. in Y. S. T.) 119–154 (Woodhead Publishing, 2010). doi:https://doi.org/10.1533/9780857090218.1.119

74. Saini, A., Rauert, C., Simpson, M. J., Harrad, S. & Diamond, M. L. Characterizing the sorption of polybrominated diphenyl ethers (PBDEs) to cotton and polyester fabrics under controlled conditions. *Sci. Total Environ.* **563**–**564**, 99–107 (2016).

75. Grishanov, S. 2 - Structure and properties of textile materials. in *Woodhead Publishing Series in Textiles* (ed. Clark, M. B. T.-H. of T. and I. D.) **1**, 28–63 (Woodhead Publishing, 2011).

76. Shinzawa, H., Awa, K. & Ozaki, Y. Compressino-induced morphological and molecular structura changes of cellulose tablets probed with near infrared imaging. *J. Near Infrared Spectrosc.* **19**, 15–22 (2011).

77. Jarvis, K., Evans, P. & Triani, G. Influence of the polymeric substrate on the water permeation of alumina barrier films deposited by atomic layer deposition. *Surf. Coatings Technol.* **337**, (2017).

78. Yu, C. Chapter 2 - Natural textile fibres: Vegetable fibres. in *Woodhead Publishing Series in Textiles* (ed. Sinclair, R. B. T.-T. and F.) 29–56 (Woodhead Publishing, 2015). doi:https://doi.org/10.1016/B978-1-84569-931-4.00002-7

79. Deopura, B. L. & Padaki, N. V. Chapter 5 - Synthetic textile fibres: polyamide, polyester and aramid Fibres. in *Woodhead Publishing Series in Textiles* (ed. Sinclair, R. B. T.-T. and F.) 97–114 (Woodhead Publishing, 2015). doi:https://doi.org/10.1016/B978-1-84569-931-4.00005-2

80. Ismar, E., Kurşun Bahadir, S., Kalaoglu, F. & Koncar, V. Futuristic clothes: electronic textiles and wearable technologies. *Glob. Challenges* **4**, 1900092 (2020).

81. Paul, G., Torah, R., Beeby, S. & Tudor, J. The development of screen printed

conductive networks on textiles for biopotential monitoring applications. *Sensors Actuators A Phys.* **206**, 35–41 (2014).

82. Lee, Y.-H. H. *et al.* Wearable textile battery rechargeable by solar energy. *Nano Lett.* **13**, 5753–5761 (2013).

83. Gaikwad, A. M. *et al.* Highly stretchable alkaline batteries based on an embedded conductive fabric. *Adv. Mater.* **24**, 5071–5076 (2012).

84. Wang, J. *et al.* A humidity-resistant, stretchable and wearable textile-based triboelectric nanogenerator for mechanical energy harvesting and multifunctional self-powered haptic sensing. *Chem. Eng. J.* **423**, 130200 (2021).

85. Wang, L., He, D., Li, J., He, B. & Qian, L. Conductive cotton fabrics with ultrahigh washability by electroless silver plating after silane modification. *Cellulose* **28**, 5881–5893 (2021).

86. Fangueiro, R., Filgueiras, A., Soutinho, F. & Meidi, X. Wicking behavior and drying capability of functional knitted fabrics. *Text. Res. J.* **80**, 1522–1530 (2010).

87. Wang, L. The use of spacer fabrics for absorbent medical applications. *J. Fiber Bioeng. Informatics* **4**, 321–329 (2008).

88. Kan, C. W. & Yuen, C. W. M. Digital ink-jet printing on textiles. *Res. J. Text. Appar.* **16**, 1–24 (2012).

89. Pierce, R. S. & Falzon, B. G. Simulating resin infusion through textile reinforcement materials for the manufacture of complex composite structures. *Engineering* **3**, 596–607 (2017).

90. Denesuk, M., Zelinski, B. J. J., Kreidl, N. J. & Uhlmann, D. R. Dynamics of incomplete wetting on porous materials. *Journal of Colloid And Interface Science* **168**, 142–151 (1994).

91. Holman, R. K., Cima, M. J., Uhland, S. A. & Sachs, E. Spreading and infiltration of inkjet-printed polymer solution droplets on a porous substrate. *J. Colloid Interface Sci.* **249**, 432–440 (2002).

92. Wallace, K. & Yoshida, K. Determination of dynamic spread factor of water droplets impacting on water-sensitive paper surfaces. *J. Colloid Interface Sci.* **63**, 164–165 (1978).

93. Sun, C. & Berg, J. C. A review of the different techniques for solid surface acid – base characterization. *Adv. Colloid Interface Sci.* **105**, 151–175 (2003).

94. Alleborn, N. & Raszillier, H. Spreading and sorption of a droplet on a porous substrate. *Chem. Eng. Sci.* **59**, 2071–2088 (2004).

95. Jung, S. Y., Lim, S. & Lee, S. J. Investigation of water seepage through porous media using X-ray imaging technique. *J. Hydrol.* **452–453**, 83–89 (2012).

96. Milczarek, J. J., Czachor, A., El-Ghany El Abd, A. & Wiśniewski, Z. Dynamic neutron radiography observations of water migration in porous media. *Nucl. Instruments Methods Phys. Res. Sect. A Accel. Spectrometers, Detect. Assoc. Equip.* **542**, 232–236 (2005).

97. Reis, N. C., Griffiths, R. F., Mantle, M. D. & Gladden, L. F. Investigation of the evaporation of embedded liquid droplets from porous surfaces using magnetic resonance imaging. *Int. J. Heat Mass Transf.* **46**, 1279–1292 (2003).

98. Reis, N. C., Griffiths, R. F. & Santos, J. M. Numerical simulation of the impact of liquid droplets on porous surfaces. *J. Comput. Phys.* **198**, 747–770 (2004).

99. Jung, S., Hwang, H. J. & Hong, S. H. Drops on substrates. *Fundam. Inkjet Print.* **1**, 199–218 (2016).

100. Young, T. III. An essay on the cohesion of fluids. *Philos. Trans. R. Soc. London* **95**, 65–87 (1805).

101. de Gennes, P. G. Wetting: statics and dynamics. *Rev. Mod. Phys.* **57**, 827–863 (1985).

102. Hubbe, M. A., Gardner, D. J. & Shen, W. Contact angles and wettability of cellulosic surfaces: A review of proposed mechanisms and test strategies. *bioresources* **10**, 8657–8749 (2015).

103. Wenzel, R. N. Resistance of solid surfaces to wetting by water. *Ind. Eng. Chem.* **28**, 988–994 (1936).

104. Cassie, A. B. D. & Baxter, S. Wettability of porous surfaces,. 546–551 (1944).

105. Kim, J. & Choi, S. O. *Superhydrophobicity*. *Waterproof and water repellent textiles andcClothing* (2017). doi:10.1016/B978-0-08-101212-3.00010-1

106. Sun, D. & Stylios, G. K. Fabric surface properties affected by low temperature plasma treatment. *J. Mater. Process. Technol.* **173**, 172–177 (2006).

107. Gu, Y. *et al.* Research progress of biomimetic superhydrophobic surface characteristics, fabrication, and application. *Adv. Mech. Eng.* **9**, 1–13 (2017).

108. PACKHAM, D. E. Chapter 7 - Surface roughness and adhesion. in *Adhesion Science and Engineering* (eds. Dillard, D. A., Pocius, A. V & Chaudhury, M. B. T.-A. S. and E.) 317–349 (Elsevier Science B.V., 2002). doi:https://doi.org/10.1016/B978-044451140-9/50007-X

109. Loghin, C., Ciobanu, L., Ionesi, D., Loghin, E. & Cristian, I. Introduction to waterproof and water repellent textiles. *Waterproof Water Repel. Text. Cloth.* 3–24 (2017). doi:10.1016/B978-0-08-101212-3.00001-0

110. Zaman, M., Liu, H., Xiao, H., Chibante, F. & Ni, Y. Hydrophilic modification of polyester fabric by applying nanocrystalline cellulose containing surface finish. *Carbohydr. Polym.* **91**, 560–567 (2013).

111. Özek, H. Z. *Development of waterproof breathable coatings and laminates*. *Waterproof and Water Repellent Textiles and Clothing* (2017). doi:10.1016/B978-0-08-101212-3.00002-2

112. Sivaramakrishnan, C. N. *The use of surfactants in the finishing of technical textiles*. *Advances in the Dyeing and Finishing of Technical Textiles* (2013). doi:10.1533/9780857097613.2.199

113. Sayed, U. & Dabhi, P. *Finishing of textiles with fluorocarbons*. *Waterproof and Water Repellent Textiles and Clothing* (Elsevier Ltd., 2017). doi:10.1016/B978-0-08-101212-3.00006-X

114. Audenaert, F., Lens, H., Rolly, D. & Vander Elst, P. Fluorochemical textile

repellents—synthesis and applications: A 3M perspective. *J. Text. Inst.* **90**, 76–94 (1999).

115. X, L., G, Y. & L, V. Effects of fluorine atoms amount and fluorinated acrylic chain length chemically attached to hydroxyl groups on the hydrophobic Properties of Cotton Fabrics. *Mod. Chem. Appl.* **05**, 1–4 (2017).

116. Gulrajani, M. L. Nano finishes. *Indian J. Fibre Text. Res.* **31**, 187–201 (2006).

117. Prusty, A., Gogoi, N., Jassal, M. & Agrawal, A. K. Synthesis and characterization of non-fluorinated copolymer emulsions for hydrophobic finishing of cotton textiles. *Indian J. Fibre Text. Res.* **35**, 264–271 (2010).

118. Shim, M. H., Kim, J. & Park, C. H. The effects of surface energy and roughness on the hydrophobicity of woven fabrics. *Text. Res. J.* **84**, 1268–1278 (2014).

119. East, A. J. 3 - Polyester fibres. in *Woodhead Publishing Series in Textiles* (ed. McIntyre, J. E. B. T.-S. F.) 95–166 (Woodhead Publishing, 2005). doi:https://doi.org/10.1533/9781845690427.95

120. Kbra, H. & Babaarsl, O. Polyester microfilament woven fabrics. *Woven Fabr.* (2012). doi:10.5772/38483

121. Kapsali, V. *Biomimetic principles for design of water repellent surfaces*. *Waterproof and Water Repellent Textiles and Clothing* (Elsevier Ltd., 2017). doi:10.1016/B978-0-08-101212-3.00005-8

122. Mao, N. & Du, M. *Sol-gel-based treatments of textiles for water repellence*. *Waterproof and Water Repellent Textiles and Clothing* (Elsevier Ltd., 2017). doi:10.1016/B978-0-08-101212-3.00009-5

123. Edward, N. W. M. & Goswami, P. *Plasma-based treatments of textiles for water repellency*. *Waterproof and Water Repellent Textiles and Clothing* (Elsevier Ltd., 2018). doi:10.1016/B978-0-08-101212-3.00008-3

124. Wang, C. C. C. & Wang, C. C. C. Surface pretreatment of polyester fabric for ink jet printing with radio frequency O2 plasma. *Fibers Polym.* **11**, 223–228 (2010).

125. Pransilp, P., Pruettiphap, M., Bhanthumnavin, W., Paosawatyanyong, B. & Kiatkamjornwong, S. Surface modification of cotton fabrics by gas plasmas for color strength and adhesion by inkjet ink printing. *Appl. Surf. Sci.* **364**, 208–220 (2016).

126. de Laplace, P. S. *Traité de mécanique céleste*. (Typ. Crapelet, 1805).

127. Cottet, J. & Renaud, P. Chapter 1 - Introduction to microfluidics. in *Developments in Biomedical Engineering and Bioelectronics* (ed. Chappel, E. B. T.-D. D. D. and T. S.) 3–17 (Academic Press, 2021). doi:https://doi.org/10.1016/B978-0-12-819838-4.00014-6

128. Vallett, R. *et al.* Digital fabrication of textiles: an analysis of electrical networks in 3D knitted functional fabrics. **1019406**, 1019406 (2017).

129. Rebenfeld, L. Chapter VI - Fibers and fibrous materials. in *Absorbent Technology* (eds. Chatterjee, P. K. & Gupta, B. S. B. T.-T. S. and T.) **13**, 199–232 (Elsevier Masson SAS, 2002).

130. J..Matteson, M. *Filtration: Principles and Practices*. (Chemical Industries, 1987).

131. Tang, K. P. M. M., Chau, K. H., Kan, C. W. & Fan, J. T. Characterizing the transplanar and in-plane water transport properties of fabrics under different sweat rate: Forced Flow Water Transport Tester. *Sci. Rep.* **5**, 17012 (2015).

132. Kissa, E. Wetting Wicking. *Text. Res. J.* **66**, 660–668 (1996).

133. Liu, T., Choi, K. & Li, Y. Wicking in twisted yarns. *J. Colloid Interface Sci.* **318**, 134–139 (2008).

134. Brochard, F. Spreading of liquid drops on thin cylinders: The ‘manchon/droplet’ transition. *J. Chem. Phys.* **84**, 4664–4672 (1986).

135. McHale, G. & Newton, M. I. Global geometry and the equilibrium shapes of liquid drops on fibers. *Colloids Surfaces A Physicochem. Eng. Asp.* **206**, 79–86 (2002).

136. McHale, G., Newton, M. I. & Carroll, B. J. The shape and stability of small liquid drops on fibers. *Oil Gas Sci. Technol.* **56**, 47–54 (2001).

137. Bedarkar, A., Wu, X. F. & Vaynberg, A. Wetting of liquid droplets on two parallel filaments. *Appl. Surf. Sci.* **256**, 7260–7264 (2010).

138. Yamaki, J. -I I. & Katayama, Y. New method of determining contact angle between monofilament and liquid. *J. Appl. Polym. Sci.* **19**, 2897–2909 (1975).

139. Carroll, B. J. The accurate measurement of contact angle, phase contact areas, drop volume, and Laplace excess pressure in drop-on-fiber systems. *J. Colloid Interface Sci.* **57**, 488–495 (1976).

140. Carroll, B. J. Equilibrium conformations of liquid drops on thin cylinders under forces of capillarity. A theory for the roll-up process. *Langmuir* **2**, 248–250 (1986).

141. McHale, G., Käb, N. A., Newton, M. I. & Rowan, S. M. Wetting of a high-energy fiber surface. *J. Colloid Interface Sci.* **186**, 453–461 (1997).

142. Lorenceau, É. & Quéré, D. Drops on a conical wire. *J. Fluid Mech.* **510**, 29–45 (2004).

143. De Ruiter, R. *et al.* Stability limits of capillary bridges: How contact angle hysteresis affects morphology transitions of liquid microstructures. *Phys. Rev. Lett.* **114**, (2015).

144. Princen, H. . Capillary phenomena in assemblies of parallel cylinders. III. Liquid Columns between Horizontal Parallel Cylinders. *J. Colloid Interface Sci.* **34**, 171–184 (1970).

145. Princen, H. M. Capillary phenomena in assemblies of parallel cylinders. I. Capillary rise between two cylinders. *J. Colloid Interface Sci.* **30**, 69–75 (1969).

146. Princen, H. M. Capillary phenomena in assemblies of parallel cylinders: II. Capillary rise in systems with more than two cylinders. *J. Colloid Interface Sci.* **30**, 359–371 (1969).

147. Duprat, C., Protière, S., Beebe, A. Y. & Stone, H. A. Wetting of flexible fibre arrays. *Nature* **482**, 510–513 (2012).

148. Protiere, S., Duprat, C. & Stone, H. A. Wetting on two parallel fibers: Drop to

column transitions. *Soft Matter* **9**, 271–276 (2013).

149. Wu, X.-F., Bedarkar, A. & Vaynberg, K. A. Droplets wetting on filament rails: Surface energy and morphology transition. *J. Colloid Interface Sci.* **341**, 326–332 (2010).

150. Qiu, S., Fuentes, C. A., Zhang, D., Van Vuure, A. W. & Seveno, D. Wettability of a single carbon fiber. *ICCM Int. Conf. Compos. Mater.* **2017-Augus**, 20–25 (2017).

151. Ge, W. K., Lu, G., Xu, X. & Wang, X. D. Droplet spreading and permeating on the hybrid-wettability porous substrates: A lattice Boltzmann method study. *Open Phys.* **14**, 483–491 (2016).

152. Frank, X. & Perré, P. Droplet spreading on a porous surface: A lattice Boltzmann study. *Phys. Fluids* **24**, (2012).

153. Washburn, E. W. The dynamics of capillary flow. *Phys. Rev.* **17**, 273–283 (1921).

154. Whitaker, S. Flow in porous media I: A theoretical derivation of Darcy's law. *Transp. Porous Media* **1**, 3–25 (1986).

155. Chen, X., Kornev, K. G., Kamath, Y. K. & Neimark, A. V. The wicking kinetics of liquid droplets into yarns. *Text. Res. J.* **71**, 862–869 (2001).

156. Reviews, A., Leonard, J. & Poiseuille, M. the History of Poiseuille ' S. *Annu. Rev. Fluid Mech.* 1–19 (1953).

157. Reza Masoodi, Hua Tan, K. M. P. Darcy's Law–based numerical simulation for modeling 3D liquid absorption into porous wicks. *Am. Inst. Chem. Eng.* **57**, 1132–1143 (2011).

158. Vo, H. N. *et al.* Capillary wicking in bio-based reinforcements undergoing swelling – Dual scale consideration of porous medium. *Compos. Part A Appl. Sci. Manuf.* **134**, 105893 (2020).

159. Pillai, K. M. & Advani, S. G. Wicking across a fiber-bank. *J. Colloid Interface Sci.* **183**, 100–110 (1996).

160. Pillai, R. M. and K. M. Darcy's law-based models for liquid absorption in

polymer wicks. *Am. Inst. Chem. Eng.* **53**, 2769–2782 (2007).

161. Pilla, R. M. and K. M. Darcy's law-based model for wicking in paper-like swelling porous media. *Am. Inst. Chem. Eng.* **56**, 2257–2267 (2010).

162. Gambaryan-Roisman, T. Liquids on porous layers: Wetting, imbibition and transport processes. *Curr. Opin. Colloid Interface Sci.* **19**, 320–335 (2014).

163. Mao, N. & Russell, S. J. Anisotropic liquid absorption in homogeneous two-dimensional nonwoven structures. *J. Appl. Phys.* **94**, 4135–4138 (2003).

164. Lekakou, C., Johari, M. A. K. B. & Bader, M. G. Compressibility and flow permeability of two-dimensional woven reinforcements in the processing of composites. *Polym. Compos.* **17**, 666–672 (1996).

165. Amico, S. & Lekakou, C. Mathematical modelling of capillary micro-flow through woven fabrics. *Compos. Part A Appl. Sci. Manuf.* **31**, 1331–1344 (2000).

166. Amico, S. & Lekakou, C. An experimental study of the permeability and capillary pressure in resin-transfer moulding. *Compos. Sci. Technol.* **61**, 1945–1959 (2001).

167. Ozgumus, T., Mobedi, M. & Ozkol, U. Determination of kozeny constant based on porosity and pore to throat size ratio in porous medium with rectangular rods. *Eng. Appl. Comput. Fluid Mech.* **8**, 308–318 (2014).

168. Yu, B. & Lee, L. J. Simplified in-plane permeability model for textile fabrics. *Polym. Compos.* **21**, 660–685 (2000).

169. Gebart, B. R. Permeability of Unidirectional Reinforcements for RTM. *J. Compos. Mater.* **26**, 1100–1133 (1992).

170. A. Nakayama, F. Kuwahara, and Y. S. Concept of equivalent diameter for heat and fluid flow in porous media. *AIChE J.* (2007). doi:10.1002/aic

171. Zarandi, M. A. F., Arroyo, S. & Pillai, K. M. Longitudinal and transverse flows in fiber tows: Evaluation of theoretical permeability models through numerical predictions and experimental measurements. *Compos. Part A Appl. Sci. Manuf.* **119**, 73–87 (2019).

172. Nguyen, V. H., Lagardère, M., Park, C. H. & Panier, S. Permeability of natural fiber reinforcement for liquid composite molding processes. *J. Mater. Sci.* **49**, 6449–6458 (2014).

173. Markicevic, B. *et al.* Infiltration time and imprint shape of a sessile droplet imbibing porous medium. *J. Colloid Interface Sci.* **336**, 698–706 (2009).

174. Zhang, Y., Wang, H., Zhang, C. & Chen, Y. Modeling of capillary flow in shaped polymer fiber bundles. *J. Mater. Sci.* **42**, 8035–8039 (2007).

175. Wiener, J. & Dejlová, P. Wicking and wetting in textiles. *Autex Res. J.* **3**, 64–71 (2003).

176. Rajagopalan, D., Aneja, A. P. & Marchal, J. M. Modeling capillary flow in complex geometries. *Text. Res. J.* **71**, 813–821 (2001).

177. Hollies, N. R. S., Kaessinger, M. M., Watson, B. S. & Bogaty, H. Water transport mechanisms in textile materials Part II: Capillary-type penetration in yarns and fabrics. *Text. Res. J.* **27**, 8–13 (1957).

178. Das, B., Das, A., Kothari, V. K., Fanguiero, R. & De Araújo, M. Effect of fibre diameter and cross-sectional shape on moisture transmission through fabrics. *Fibers Polym.* **9**, 225–231 (2008).

179. Tahir, M. W. *Dual scale porosity and interlaminar properties of composite Materials*. *KTH School of Engineering Sciences* (2014).

180. Sharabaty, T., Biguenet, F., Dupuis, D. & Viallier, P. Investigation on moisture transport through polyester/cotton fabrics. *Indian J. Fibre Text. Res.* **33**, 419–425 (2008).

181. Gillespie, T. The spreading of low vapor pressure liquids in paper. *J. Colloid Sci.* **13**, 32–50 (1958).

182. Xu, P. & Yu, B. Developing a new form of permeability and Kozeny-Carman constant for homogeneous porous media by means of fractal geometry. *Adv. Water Resour.* **31**, 74–81 (2008).

183. Yu, B., James Lee, L. & Cao, H. A fractal in-plane permeability model for fabrics. *Polym. Compos.* **23**, 201–221 (2002).

184. Yu, B., Lee, L. J. & Cao, H. Fractal characters of pore microstructures of textile fabrics. *Fractals* **09**, 155–163 (2001).

185. Benltoufa, S., Fayala, F. & BenNasrallah, S. Capillary rise in macro and micro pores of jersey knitting structure. *J. Eng. Fiber. Fabr.* **3**, 155892500800300 (2008).

186. Lu, Y., Wang, Y. & Gao, W. Wicking behaviors of ring and compact-siro ring spun yarns with different twists. *Autex Res. J.* **19**, 68–73 (2019).

187. Hsieh, Y. lo. Liquid transport in fabric structures. *Text. Res. J.* **65**, 299–307 (1995).

188. Mhetre, S. Effect of fabric structure on liquid transport, Ink jet drop spreading and printing quality. (Georgia Institute of Technology, 2009).

189. Lei, M. *et al.* Effect of weaving structures on the water wicking-Evaporating behavior of woven fabrics. *Polymers (Basel).* **12**, (2020).

190. Park, H., Carr, W. W., ok, H. & Park, S. Image quality of inkjet printing on polyester fabrics. *Text. Res. J.* **76**, 720–728 (2006).

191. Mhetre, S., Carr, W. & Radhakrishnaiah, P. On the relationship between ink-jet printing quality of pigment ink and the spreading behavior of ink drops. *J. Text. Inst.* **101**, 423–430 (2010).

192. Sampath, M. B., Mani, S. & Nalankilli, G. Effect of filament fineness on comfort characteristics of moisture management finished polyester knitted fabrics. *J. Ind. Text.* **41**, 160–173 (2011).

193. Nyoni, A. B. & Brook, D. Wicking mechanisms in yarns-the key to fabric wicking performance. *J. Text. Inst.* **97**, 119–128 (2006).

194. Derby, B. Inkjet printing of functional and structural materials: Fluid property requirements, feature stability, and resolution. *Annu. Rev. Mater. Res.* **40**, 395–414 (2010).

195. Hutchings, I. M., Martin, G. D. & Hoath, S. D. Introductory remarks. *Fundam. Inkjet Print.* 1–12 (2016). doi:https://doi.org/10.1002/9783527684724.ch1

196. Seerden, K. A. M. *et al.* Ink-jet printing of wax-based alumina suspensions. *J. Am. Ceram. Soc.* **84**, 2514–2520 (2001).

197. Boehm, R. D., Miller, P. R., Daniels, J., Stafslien, S. & Narayan, R. J. Inkjet printing for pharmaceutical applications. *Mater. Today* **17**, 247–252 (2014).

198. Kipphan, H. *Handbook of print media: Technologies and production methods*. (Springer, 2001).

199. Rosa, P., Câmara, A. & Gouveia, C. The potential of printed electronics and personal fabrication in driving the internet of things. *Open J. Internet Things* **1**, 16–36 (2015).

200. Thomson, W. On signalling through submarine cables. *Math. Phys. Pap.* 168–172 (1884).

201. Rayleigh, Lord. On the instability of jets. *Proc. London Math. Soc.* **s1-10**, 4–13 (1878).

202. Williams, C. Ink-jet printers go beyond paper. *Phys. World* **19**, 24–29 (2006).

203. Tang, H. K., Kuek, W. H., Gozali, R. & Liew, R. Ink jet printer pioneers and competitors. *Proc. 2000 IEEE Int. Conf. Manag. Innov. Technol.* **1**, 94–98 (2000).

204. Martin, G. D., Hoath, S. D. & Hutchings, I. M. Inkjet printing - The physics of manipulating liquid jets and drops. *J. Phys. Conf. Ser.* **105**, 0–14 (2008).

205. Reis, N., Ainsley, C. & Derby, B. Ink-jet delivery of particle suspensions by piezoelectric droplet ejectors. *J. Appl. Phys.* **97**, 8–14 (2005).

206. Derby, B. Additive manufacture of ceramics components by inkjet printing. *engineering* **1**, 113–123 (2015).

207. Driessen, T. & Jeurissen, R. Drop formation in inkjet printing. *Fundam. Inkjet Print.* 93–115 (2016).

208. Reynolds, O. An Experimental Investigation of the circumstances which determine whether the motion of water shall be direct or sinuous, and of the law of resistance in parallel channels. *R. Soc.* **174**, 935–982 (2009).

209. Bergeron, V., Bonn, D., Martin, J. Y. & Vovelle, L. Controlling droplet

deposition with polymer additives. *Nature* **405**, 772–775 (2000).

210. McKinley, G. H. & Renardy, M. Wolfgang von Ohnesorge. *Phys. Fluids* **23**, (2011).

211. Duineveld, P. C. *et al.* Ink-jet printing of polymer light-emitting devices. 59 (2002). doi:10.1117/12.457460

212. Fromm, J. E. Numerical calculation of the fluid dynamics of drop-on-demand jets. *IBM J. Res. Dev.* **28**, 322–333 (1984).

213. Bhola, R. & Chandra, S. Parameters controlling solidification of molten wax droplets falling on a solid surface. *J. Mater. Sci.* **34**, 4883–4894 (1999).

214. Haskal, E. I. *et al.* Ink Jet printing of passive-matrix polymer light emitting displays. *SID Symp. Dig. Tech. Pap.* **33**, 776–779 (2002).

215. Xu, D. *et al.* Inkjet printing of polymer solutions and the role of chain entanglement. *J. Mater. Chem.* **17**, 4902–4907 (2007).

216. Maleki, H. & Bertola, V. Recent advances and prospects of inkjet printing in heterogeneous catalysis. *Catal. Sci. Technol.* **10**, 3140–3159 (2020).

217. Schiaffino, S. & Sonin, A. A. Molten droplet deposition and solidification at low Weber numbers. *Phys. Fluids* **9**, 3172–3187 (1997).

218. Bonn, D., Eggers, J., Indekeu, J., Meunier, J. & Daniel Bonn, Jens Eggers, Joseph Indekeu, Jacques Meunier, E. R. Wetting and spreading. *Rev. Mod. Phys.* **81**, 739–805 (2009).

219. Rioboo, R., Marengo, M. & Tropea, C. Time evolution of liquid drop impact onto solid, dry surfaces. *Exp. Fluids* **33**, 112–124 (2002).

220. W.Extrand, C. Spontaneous spreading of viscous liquid drops. *Colloid Interface Sci.* **157**, 72–76 (1993).

221. Ravi, V., Jog, M. A. & Manglik, R. M. Effects of interfacial and viscous properties of liquids on drop spread dynamics. *ILASS Am.* **22**, (2010).

222. Antonini, C., Amirfazli, A. & Marengo, M. Drop impact and wettability: From hydrophilic to superhydrophobic surfaces. *Phys. Fluids* **24**, (2012).

223. Šikalo, Š., Marengo, M., Tropea, C. & Ganić, E. N. Analysis of impact of droplets on horizontal surfaces. *Exp. Therm. Fluid Sci.* **25**, 503–510 (2002).

224. Soltman, D. & Subramanian, V. Inkjet-printed line morphologies and temperature control of the coffee ring effect. *Langmuir* **24**, 2224–2231 (2008).

225. DUINEVELD, P. C. The stability of ink-jet printed lines of liquid with zero receding contact angle on a homogeneous substrate. *J. Fluid Mech.* **477**, 175–200 (2003).

226. Davis, S. H. Moving contact lines and rivulet instabilities. Part 1. The static rivulet. *J. Fluid Mech.* **98**, 225–242 (1980).

227. SCHIAFFINO, S. & SONIN, A. I. N. A. Formation and stability of liquid and molten beads on a solid surface. *J. Fluid Mech.* **343**, 95–110 (1997).

228. Smith, P. J., Shin, D.-Y., Stringer, J. E., Derby, B. & Reis, N. Direct ink-jet printing and low temperature conversion of conductive silver patterns. *J. Mater. Sci.* **41**, 4153–4158 (2006).

229. Stringer, J. & Derby, B. Formation and stability of lines produced by inkjet printing. *Langmuir* **26**, 10365–10372 (2010).

230. Stringer, J. & Derby, B. Limits to feature size and resolution in ink jet printing. *J. Eur. Ceram. Soc.* **29**, 913–918 (2009).

231. Deegan, R. D. *et al.* Capillary flow as the cause of ring strins from dried liquid drops. *Nat.* **389**, 827–829 (1997).

232. De Gans, B. J. & Schubert, U. S. Inkjet printing of well-defined polymer dots and arrays. *Langmuir* **20**, 7789–7793 (2004).

233. Hu, G. *et al.* Functional inks and printing of two-dimensional materials. *Chem. Soc. Rev.* **47**, 3265–3300 (2018).

234. Dou, R. & Derby, B. Formation of coffee stains on porous surfaces. *Langmuir* **28**, 5331–5338 (2012).

235. Pack, M., Hu, H., Kim, D. O., Yang, X. & Sun, Y. Colloidal drop deposition on porous substrates: Competition among particle motion, evaporation, and infiltration. *Langmuir* **31**, 7953–7961 (2015).

236. Marie, M. M., El-Hamaky, Y. H., Maamoun, D., Ibrahim, D. F. & and S.M. Abbas. Pigment ink formulation for inkjet printing of different textile materials. *Int. J. Innov. Appl. Stud.* **4**, 239–247 (2013).

237. Fang, K., Wang, S., Wang, C. & Tian, A. Inkjet printing effects of pigment inks on silk fabrics surface-modified with O_2 plasma. *J. Appl. Polym. Sci.* **107**, 2949–2955 (2008).

238. Hoath, S. D. *Fundamentals of inkjet printing: The science of inkjet and droplets*. (Wiley-VCH, 2015). doi:10.1002/9783527684724

239. Whittow, W. G. *et al.* Inkjet printed microstrip patch antennas realised on textile for wearable applications. *IEEE Antennas Wirel. Propag. Lett.* **13**, 71–74 (2014).

240. Li, L., Guo, Y., Zhang, X. & Song, Y. Inkjet-printed highly conductive transparent patterns with water based Ag-doped graphene. *J. Mater. Chem. A* **2**, 19095–19101 (2014).

241. Krykpayev, B., Farooqui, M. F., Bilal, R. M., Vaseem, M. & Shamim, A. A wearable tracking device inkjet-printed on textile. *Microelectronics J.* **65**, 40–48 (2017).

242. Stempien, Z., Rybicki, E., Rybicki, T. & Lesnikowski, J. Inkjet-printing deposition of silver electro-conductive layers on textile substrates at low sintering temperature by using an aqueous silver ions-containing ink for textronic applications. *Sensors Actuators, B Chem.* **224**, 714–725 (2015).

243. Guo, Y. *et al.* PEDOT:PSS ‘wires’ printed on textile for wearable electronics. *ACS Appl. Mater. Interfaces* **8**, 26998–27005 (2016).

244. Stempien, Z., Rybicki, E., Patykowska, A., Rybicki, T. & Szynkowska, M. I. Shape-programmed inkjet-printed silver electro-conductive layers on textile surfaces. *J. Ind. Text.* 1528083717690610 (2017). doi:10.1177/1528083717690610

245. Kaushik, V. *et al.* Textile-based electronic components for energy applications: Principles, problems, and perspective. *Nanomaterials* **5**, 1493–1531 (2015).

246. Atabaki, F., Yousefi, M. H., Abdolmaleki, A. & Kalvandi, M. Poly(3,4-ethylenedioxythiophene):Poly(styrenesulfonic Acid) (PEDOT:PSS) conductivity enhancement through addition of imidazolium-ionic liquid derivatives. *Polym. - Plast. Technol. Eng.* **54**, 1009–1016 (2015).

247. Li, J. *et al.* Efficient inkjet printing of graphene. *Adv. Mater.* **25**, 3985–3992 (2013).

248. Li, W. *et al.* Flexible circuits and soft actuators by printing assembly of graphene. *ACS Appl. Mater. Interfaces* **8**, 12369–12376 (2016).

249. Yun, Y. J., Hong, W. G., Kim, W. J., Jun, Y. & Kim, B. H. A novel method for applying reduced graphene oxide directly to electronic textiles from yarns to fabrics. *Adv. Mater.* **25**, 5701–5705 (2013).

250. Abdelkader, A. M. *et al.* Ultraflexible and robust graphene supercapacitors printed on textiles for wearable electronics applications. *2D Mater.* **4**, (2017).

251. Su, H. *et al.* Preparation water dispersible reduced graphene oxide as ink materials for the flexible and wearable energy storage devices. *2016 17th Int. Conf. Electron. Packag. Technol. ICEPT 2016* 218–221 (2016). doi:10.1109/ICEPT.2016.7583123

252. Mengal, N. *et al.* Fabrication of a flexible and conductive lyocell fabric decorated with graphene nanosheets as a stable electrode material. *Carbohydr. Polym.* **152**, 19–25 (2016).

253. Chen, Y., Li, Y., Xu, D. & Zhai, W. Fabrication of stretchable, flexible conductive thermoplastic polyurethane/graphene composites via foaming. *RSC Adv.* **5**, 82034–82041 (2015).

254. Kim, K., Ahn, S. Il & Choi, K. C. Simultaneous synthesis and patterning of graphene electrodes by reactive inkjet printing. *Carbon N. Y.* **66**, 172–177 (2014).

255. Stempien, Z. *et al.* In-situ deposition of reduced graphene oxide layers on textile surfaces by the reactive inkjet printing technique and their use in supercapacitor applications. *Synth. Met.* **256**, 116144 (2019).

256. Bhore, S. S. Formulation and evaluation of resistive inks for applications in

printed electronics. 1–94 (2013). doi:10.1002/adma.201101328

257. Perelaer, J., Klokkenburg, M., Hendriks, C. E. & Schubert, U. S. Microwave flash sintering of inkjet-printed silver tracks on polymer substrates. *Adv. Mater.* **21**, 4830–4834 (2009).

258. Reinhold, I. *et al.* Argon plasma sintering of inkjet printed silver tracks on polymer substrates. *J. Mater. Chem.* **19**, 3384 (2009).

259. Abulikemu, M. *et al.* Insitu synthesis of self-assembled gold nanoparticles on glass or silicon substrates through reactive inkjet printing. *Angew. Chemie - Int. Ed.* **53**, 420–423 (2014).

260. Stempien, Z., Pawlak, R. & Korzeniewska, E. Thin conductive structures on coated textiles. *2016 Sel. Issues Electr. Eng. Electron. WZEE 2016* 8–13 (2016). doi:10.1109/WZEE.2016.7800248

261. Wang, Z., Wang, W., Jiang, Z. & Yu, D. Low temperature sintering nano-silver conductive ink printed on cotton fabric as printed electronics. *Prog. Org. Coatings* **101**, 604–611 (2016).

262. Wang, Z., Wang, W., Jiang, Z. & Yu, D. A novel and simple method of printing flexible conductive circuits on PET fabrics. *Appl. Surf. Sci.* **396**, 208–213 (2017).

263. Schoner, C. *et al.* Concepts of metal-organic decomposition (MOD) silver inks for structured metallization by inkjet printing. *Mater. Res. Soc. Symp. Proc.* **1285**, 13–18 (2011).

264. Dearden, A. L. *et al.* A low curing temperature silver ink for use in ink-jet printing and subsequent production of conductive tracks. *Macromol. Rapid Commun.* **26**, 315–318 (2005).

265. Olson, L. P., Whitcomb, D. R., Rajeswaran, M., Blanton, T. N. & Stwertka, B. J. The simple yet elusive crystal structure of silver acetate and the role of the Ag - Ag bond in the formation of silver nanoparticles during the thermally induced reduction of silver carboxylates. *Chem. Mater.* **18**, 1667–1674 (2006).

266. Chen, S. P., Kao, Z. K., Lin, J. L. & Liao, Y. C. Silver conductive features on

flexible substrates from a thermally accelerated chain reaction at low sintering temperatures. *ACS Appl. Mater. Interfaces* **4**, 7064–7068 (2012).

267. Liu, H. *et al.* A novel two-step method for fabricating silver plating cotton fabrics. *J. Nanomater.* **2016**, (2016).

268. Montazer, M. & Allahyarzadeh, V. Electroless plating of silver nanoparticles/nanolayer on polyester fabric using AgNO3/NaOH and ammonia. *Ind. Eng. Chem. Res.* **52**, 8436–8444 (2013).

269. Calvert, P., Duggal, D., Patra, P., Agrawal, A. & Sawhney, A. Conducting polymer and conducting composite strain sensors on textiles. *Mol. Cryst. Liq. Cryst.* **484**, (2008).

270. Calvert, P. *et al.* Piezoresistive sensors for smart textiles. *Electroact. Polym. Actuators Devices* **6524**, 65241I-65241I–8 (2007).

271. Sawhney, A. *et al.* Soft structured sensors and connectors by inkjet printing. *AATCC Rev.* **7**, 42–51 (2007).

272. Walker SB, Ahn BY, L. J. Reactive silver inks for high-performance printed electronics. *Sigma Aldrich Tech. Doc.* (2015).

273. Tada, Y., Inoue, M. & Tokumaru, T. An evaluation of the characteristics of a stretchable ink wire suitable for the measurement of biological signals. *J. Text. Inst.* **105**, 692–700 (2014).

274. Matsuhisa, N. *et al.* Printable elastic conductors with a high conductivity for electronic textile applications. *Nat. Commun.* **6**, 7461 (2015).

275. Jeerapan, I., Sempionatto, J. R., Pavinatto, A., You, J.-M. & Wang, J. Stretchable biofuel cells as wearable textile-based self-powered sensors. *J. Mater. Chem. A* **4**, 18342–18353 (2016).

276. Lee, S. *et al.* Ag nanowire reinforced highly stretchable conductive fibers for wearable electronics. *Adv. Funct. Mater.* **25**, 3114–3121 (2015).

277. Perelaer, J., Hendriks, C. E., De Laat, A. W. M. & Schubert, U. S. One-step inkjet printing of conductive silver tracks on polymer substrates. *Nanotechnology* **20**, (2009).

278. Cie, C. & Cie, C. 2 – The development of ink jet printing on textiles. in *Ink Jet Textile Printing* 15–27 (2015). doi:10.1016/B978-0-85709-230-4.00002-9

279. Muthukumar, N. & Thilagavathi, G. Development and characterization of electrically conductive polyaniline coated fabrics. **19**, 434–441 (2012).

280. Santos, C. A. M., Campos, A. De, Luz, M. S., White, B. D. & Neumeier, J. J. Montgomery method procedure for measuring electrical resistivity of anisotropic materials : A revision of the Montgomery method. **083703**, (2017).

281. Kazani, I. *et al.* About the collinear four-point probes inability to measure the technique resistivity of anisotropic electroconductive fabrics. (2013). doi:10.1177/0040517512452951

282. Decaens, J. & Vermeersch, O. Specific testing for smart textiles. (2018).

283. Zie, M. T. M. F. J. Electrical properties of flat textile material as inhomegeneous and anisotropic structure. 5061–5068 (2013). doi:10.1007/s10854-013-1524-4

284. Banaszczyk, J., Schwarz, A., Mey, G. De & Langenhove, L. Van. The Van der Pauw method for sheet resistance measurements of polypyrrole-coated para-aramide woven fabrics. (2010). doi:10.1002/app

285. Irurzun, U. B., Dutschk, V., Calvimontes, A. & Akkerman, R. Generation of micro-sized conductive lines on glass fibre fabrics by inkjet printing. *Autex Res. J.* **12**, 55–61 (2012).

286. Calvert, P. Inkjet printing for materials and devices. *Chem. Mater.* **13**, 3299–3305 (2001).

287. Suh, M., Carroll, K. E., Grant, E. & Oxenham, W. Effect of fabric substrate and coating material on the quality of conductive printing. *J. Text. Inst.* **104**, 213–222 (2013).

288. Roshni, S. B., Jayakrishnan, M. P., Mohanan, P. & Surendran, K. P. Design and fabrication of an E-shaped wearable textile antenna on PVB-coated hydrophobic polyester fabric. *Smart Mater. Struct.* **26**, (2017).

289. Yang, K., Torah, R., Wei, Y., Beeby, S. & Tudor, J. Waterproof and durable

screen printed silver conductive tracks on textiles. *Text. Res. J.* **83**, 2023–2031 (2013).

290. Aspland, J. R. Pigments as textile colorants. Chapter 14: Pigmenting or pigmentation. *Text. Chem. Color.* **25**, 31–37 (1993).

291. Khan, M. R. Pigment ink formulation , tests and test methods for pigmented textile inks. **8**, 78–86 (2016).

292. Mimaki Global. For textile and apparel, Direct-on-textile inkjet printer 'Tx300P-1800' and 'Tx300P-1800B' hybrid inkjet printer announcement. (2017).

293. Rehnby, W., Gustafsson, M. & Skrifvars, M. Coating of textile fabrics with conductive polymers for smart textile applications. *Welcome to Ambience'08* 100–103 (2008).

294. Govaert, F. & Vanneste, M. Preparation and application of conductive textile coatings filled with honeycomb structured carbon nanotubes. *J. Nanomater.* **2014**, (2014).

295. Eren, M., Akbulut, G., Senler, S. & Kayaoğlu, B. K. Synthesis of core–shell-type styrene acrylic latexes with low NMA content and their application in pigment printing pastes. *J. Coatings Technol. Res.* 1–9 (2017). doi:10.1007/s11998-017-9955-0

296. Åkerfeldt, M., Lund, A. & Walkenström, P. Textile sensing glove with piezoelectric PVDF fibers and printed electrodes of PEDOT:PSS. *Text. Res. J.* **85**, 1789–1799 (2015).

297. Topp, K., Haase, H., Degen, C., Illing, G. & Mahltig, B. Coatings with metallic effect pigments for antimicrobial and conductive coating of textiles with electromagnetic shielding properties. *J. Coatings Technol. Res.* **11**, 943–957 (2014).

298. Cao, Q. An Investigation into the development of environmentally friendly pigment colouration. (2013).

299. Chapter 1 - Introduction and adhesion theories. in *Adhesive Technology Handbook* (ed. Ebnesajjad, S. B. T.-A. T. H. (Second E.) 1–19 (William

Andrew Publishing, 2009). doi:https://doi.org/10.1016/B978-0-8155-1533-3.50004-9

300. Karimi, M. A. A flexible inkjet printed inverted-F antenna on textile. in *Creative materials* (2016). doi:10.1109/MECAP.2016.7790101

301. Zhao, C., Wang, C., Chen, K. & Yin, Y. Improvement of ink-jet printing performances using β-cyclodextrin forming inclusion complex on cotton fabric. *Fibers Polym.* **18**, 619–624 (2017).

302. Zhang, Y., Xu, Q., Fu, F. & Liu, X. Durable antimicrobial cotton textiles modified with inorganic nanoparticles. *Cellulose* **23**, 2791–2808 (2016).

303. Xu, Q. B., Wu, Y. H., Zhang, Y. Y., Fu, F. Y. & Liu, X. D. Durable antibacterial cotton modified by silver nanoparticles and chitosan derivative binder. *Fibers Polym.* **17**, 1782–1789 (2016).

304. Xu, Q. *et al.* One-pot fabrication of durable antibacterial cotton fabric coated with silver nanoparticles via carboxymethyl chitosan as a binder and stabilizer. *Carbohydr. Polym.* **204**, 42–49 (2019).

305. Zhou, J. *et al.* Excellent binding effect of l-methionine for immobilizing silver nanoparticles onto cotton fabrics to improve the antibacterial durability against washing. *RSC Adv.* **8**, 24458–24463 (2018).

306. Xu, Q. *et al.* Enhancing the surface affinity with silver nano-particles for antibacterial cotton fabric by coating carboxymethyl chitosan and l-cysteine. *Appl. Surf. Sci.* **497**, 143673 (2019).

307. Xu, Q. B. *et al.* Silver-based, single-sided antibacterial cotton fabrics with improved durability via an l-cysteine binding effect. *Cellulose* **25**, 2129–2141 (2018).

308. Xu, Q., Ke, X., Zhang, Y., Fu, F. & Liu, X. Facile fabrication of durable antibacterial cotton fabric realized by thioglycolic acid and silver nanoparticles. *Fibers Polym.* **19**, 2307–2316 (2018).

309. Zhu, S. *et al.* Multi-functional and highly conductive textiles with ultra-high durability through ‘green’ fabrication process. *Chem. Eng. J.* **406**, 127140 (2021).

310. Tokarska, M. & Orpel, M. Study of anisotropic electrical resistance of knitted fabrics. *Text. Res. J.* **89**, 1073–1083 (2018).

311. Chen, S., Song, Y., Ding, D., Ling, Z. & Xu, F. Flexible and anisotropic strain sensor based on carbonized crepe paper with aligned cellulose fibers. *Adv. Funct. Mater.* **28**, 1–9 (2018).

312. Tyurin, I. N., Getmantseva, V. V. & Andreeva, E. G. Van der Pauw method for measuring the electrical conductivity of smart textiles. *Fibre Chem.* **51**, 139–146 (2019).

313. Li, B. M. *et al.* Iron-on carbon nanotube (CNT) thin films for biosensing E-Textile applications. *Carbon N. Y.* **168**, 673–683 (2020).

314. Zheng, S. *et al.* Multifunctional and highly sensitive piezoresistive sensing textile based on a hierarchical architecture. *Compos. Sci. Technol.* **197**, 108255 (2020).

315. Zaman, S. U., Tao, X., Cochrane, C. & Koncar, V. E-textile systems reliability assessment—A miniaturized accelerometer used to investigate damage during their washing. *Sensors* **21**, (2021).

316. Roy Choudhury, A. K. 7 - Repellent finishes. in *Woodhead Publishing Series in Textiles* (ed. Roy Choudhury, A. K. B. T.-P. of T. F.) 149–194 (Woodhead Publishing, 2017). doi:https://doi.org/10.1016/B978-0-08-100646-7.00007-2

317. Thiel, B. L. & Toth, M. Secondary electron contrast in low-vacuumenvironmental scanning electron microscopy of dielectrics. *J. Appl. Phys.* **97**, (2005).

318. Leach, R., Carmignato, S. & Dewulf, W. *Industrial X-ray computed tomography*. *Materials Evaluation* (2018). doi:10.1007/978-3-319-59573-3

319. Yoshimura, A., Hosoya, R., Koyanagi, J. & Ogasawara, T. X-ray computed tomography used to measure fiber orientation in CFRP laminates. *Adv. Compos. Mater.* **25**, 19–30 (2016).

320. Huang, S.-Y. *et al.* Three-dimensional graphene foam and carbon fibers reinforced epoxy resin composites with enhanced thermal conductivity. *2016 China Semicond. Technol. Int. Conf.* 1–3 (2016).

doi:10.1109/CSTIC.2016.7463947

321. du Plessis, A., Broeckhoven, C., Guelpa, A. & le Roux, S. G. Laboratory x-ray micro-computed tomography: a user guideline for biological samples. *Gigascience* **6**, 1–11 (2017).

322. Jeong, E. G., Jeon, Y., Cho, S. H. & Choi, K. C. Textile-based washable polymer solar cells for optoelectronic modules: Toward self-powered smart clothing. *Energy Environ. Sci.* **12**, 1878–1889 (2019).

323. Sala de Medeiros, M., Chanci, D., Moreno, C., Goswami, D. & Martinez, R. V. Waterproof, breathable, and antibacterial self-powered e-textiles based on omniphobic triboelectric nanogenerators. *Adv. Funct. Mater.* **29**, (2019).

324. Wen, Z. *et al.* Self-powered textile for wearable electronics by hybridizing fiber-shaped nanogenerators, solar cells, and supercapacitors. *Sci. Adv.* **2**, (2016).

325. Derby, B. Inkjet printing ceramics: From drops to solid. *J. Eur. Ceram. Soc.* **31**, 2543–2550 (2011).

326. Lee, H. H., Chou, K. Sen & Huang, K. C. Inkjet printing of nanosized silver colloids. *Nanotechnology* **16**, 2436–2441 (2005).

327. Cie, C. 7 – Inks for digital printing. in *Ink Jet Textile Printing* 85–97 (2015). doi:10.1016/B978-0-85709-230-4.00007-8

328. TetraPak. *Fundamentals and practices in colouration of textiles, Second Edition*. (2014).

329. Li, Y., Torah, R., Beeby, S. P. & Tudor, J. Inkjet printed flexible antenna on textile for wearable applications. *2012 Text. Inst. World Conf.* (2012).

330. Carroll, B. J. Deposition of liquid drops on a long cylindrical fiber. *Text. Res. J.* **58**, 495–500 (1988).

331. Wagner, H. D. Spreading of liquid droplets on cylindrical surfaces: Accurate determination of contact angle. *J. Appl. Phys.* **67**, 1352–1355 (1990).

332. Wu, X. F. & Dzenis, Y. A. Droplet on a fiber: Geometrical shape and contact angle. *Acta Mech.* **185**, 215–225 (2006).

333. Wu, X. F., Bedarkar, A. & Vaynberg, K. A. Droplets wetting on filament rails: Surface energy and morphology transition. *J. Colloid Interface Sci.* **341**, 326–332 (2010).

334. Princen, H. M. Capillary phenomena in assemblies of parallel cylinders. I. Liquid Columns between Horizontal Parallel Cylinders. *J. Colloid Interface Sci.* **34**, 171–184 (1970).

335. Lucas, R. Ueber das Zeitgesetz des kapillaren Aufstiegs von Flüssigkeiten. *Kolloid-Zeitschrift* **23**, 15–22 (1918).

336. Neuman, S. Theoretical derivation of Darcy's Law. *Acta Mech.* **25**, 153–170 (1977).

337. Schwartz, A. M. & Minor, F. W. A simplified thermodynamic approach to capillarity. *J. Colloid Sci.* **14**, 584–597 (1959).

338. Kissa, E. Capillary sorption in fibrous assemblies. *J. Colloid Interface Sci.* **83**, 265–272 (1981).

339. Kawase, T., Sekoguchi, S., Fujii, T. & Minagawa, M. Capillary spreading of liquids. *Text. Res. J.* **56**, 409–414 (1986).

340. Daniel Bonn, Jens Eggers, Joseph Indekeu, Jacques Meunier, E. R. *Wetting and spreading*. *Surfaces, Interfaces, and Colloids* doi:10.1002/0471234990.ch17

341. Glen Mchale; Michael Ian Newton. The Shape and stability of small liquid drops on fibers. **63**, 9–19 (2001).

342. Chou, T. H., Hong, S. J., Liang, Y. E., Tsao, H. K. & Sheng, Y. J. Equilibrium phase diagram of drop-on-fiber: Coexistent states and gravity effect. *Langmuir* **27**, 3685–3692 (2011).

343. Das, B., Das, A., Kothari, V. K. & Fangueiro, R. Development of mathematical model to predict vertical wicking behaviour.part I: flow through yarn. *J. Text. Inst.* **102**, 957–970 (2011).

344. Almoughni, H. & Gong, H. Capillary flow of liquid water through yarns: A theoretical model. *Text. Res. J.* **85**, 722–732 (2015).

345. Calvimontes, A., Hasan, M. M. B. & Dutschk, V. Effects of topographic structure on wettability of woven fabrics. *Woven Fabr. Eng.* 71–92 (2010).

346. Paul, C. & Poonam, C. Mathematical modeling of transport of inkjet-printed suspensions into textiles. *Res. J. Text. Appar.* **13**, 46–52 (2009).

347. Yuehua Yuan, T. R. L. *Contact angle and wetting properties*. *Surface Science Techniques* **51**, (2013).

348. Negi, A. *et al.* The role of electronic energy loss in PET polymer. *Radiat. Eff. Defects Solids* **166**, 621–627 (2011).

349. Sigma-Aldrich. IR Spectrum Table & Chart.

350. Burkinshaw, S. M. Physico-chemical aspects of textile coloration. *Physico-Chemical Asp. Text. Color.* 1–622 (2015). doi:10.1002/9781118725658

351. Lu, Z., Ng, T. W. & Yu, Y. Fast modeling of clam-shell drop morphologies on cylindrical surfaces. *Int. J. Heat Mass Transf.* **93**, 1132–1136 (2016).

352. Berim, G. O. & Ruckenstein, E. Cylindrical droplet on nanofibers: A step toward the clam-shell drop description. *J. Phys. Chem. B* **109**, 12515–12524 (2005).

353. Cai, J. *et al.* Lucas–Washburn equation-based modeling of capillary-driven flow in porous systems. *Langmuir* **37**, (2021).

354. Marmoret, L., Beji, H., Lewandowski, M. & Perwuelz, A. Using capillarity and permeability experimental data to study the flow phenomena inside a fibrous medium. in *Focus on Porous Media Research* 335–358 (2013).

355. Rader, C. A. & Schwartz, A. M. The migration of liquids in textile assemblies. *Text. Res. J.* **32**, 140–153 (1962).

356. Rulison, C. Wettability studies for porous solids including powders and fibrous materials. *Tech. note, Krus. Lab.* **302**, 1–14 (1996).

357. Wang, C. *et al.* Intrinsically stretchable and conductive textile by a scalable process for elastic wearable electronics. *ACS Appl. Mater. Interfaces* **9**, 13331–13338 (2017).

358. Zhang, H., Tao, X., Yu, T. & Wang, S. Conductive knitted fabric as large-

strain gauge under high temperature. *Sensors Actuators A Phys.* **126**, 129–140 (2006).

359. Cho, G., Jeong, K., Paik, M., Kwun, Y. & Sung, M. Performance evaluation of textile-based electrodes and motion sensors for smart clothing. *IEEE Sensors J. - IEEE SENS J* **11**, 3183–3193 (2011).

360. Lee, J. *et al.* Conductive fiber-based ultrasensitive textile pressure sensor for wearable electronics. *Adv. Mater.* **27**, 2433–2439 (2015).

361. Kinkeldei, T., Zysset, C., Cherenack, K. & Troster, G. A textile integrated sensor system for monitoring humidity and temperature. *2011 16th Int. Solid-State Sensors, Actuators Microsystems Conf. TRANSDUCERS'11* 1156–1159 (2011). doi:10.1109/TRANSDUCERS.2011.5969238

362. Jinno, H. *et al.* Stretchable and waterproof elastomer-coated organic photovoltaics for washable electronic textile applications. *Nat. Energy* **2**, (2017).

363. Guo, L., Berglin, L. & Mattila, H. Improvement of electro-mechanical properties of strain sensors made of elastic-conductive hybrid yarns. *Text. Res. J.* **82**, 1937–1947 (2012).

364. Post, E., Orth, M., Russo, P. R. & Gershenfeld, N. E-broidery: Design and fabrication of textile-based computing. *IBM Syst. J.* **39**, 840–860 (2000).

365. Gimpel, S., Möhring, U., Mueller, H., Neudeck, A. & Scheibner, W. Textile-based electronic substrate technology. *J. Ind. Text. - J IND TEXT* **33**, 179–189 (2004).

366. Khirotdin, R. K. Printing of conductive ink tracks on textiles using silkscreen printing. *Eng. Appl. Sci.* **11**, 6619–6624 (2016).

367. Ahmed, Z., Torah, R., Yang, K., Beeby, S. & Tudor, J. Investigation and improvement of the dispenser printing of electrical interconnections for smart fabric applications. *Smart Mater. Struct.* **25**, (2016).

368. Yang, K., Freeman, C., Torah, R., Beeby, S. & Tudor, J. Screen printed fabric electrode array for wearable functional electrical stimulation. *Sensors Actuators, A Phys.* **213**, 108–115 (2014).

369. Wills, K. A. *et al.* Additive process for patterned metallized conductive tracks on cotton with applications in smart textiles. *J. Text. Inst.* **5000**, 1–10 (2017).

370. Romaguera, V. S., Madec, M. B. & Yeates, S. G. Inkjet printing of conductive polymers for smart textiles and flexible electronics. in *Materials Research Society Symposium Proceedings* **1192**, 26–31 (2009).

371. Sawhney, A., Agrawal, A., Patra, P. & Calvert, P. Piezoresistive Sensors on Textiles by Inkjet Printing and Electroless Plating. *Mater. Res. Soc. Symp. Proc.* **920**, 103 (2006).

372. Zhang, G., Parwani, R., Stone, C. A., Barber, A. H. & Botto, L. X-ray imaging of transplanar liquid transport mechanisms in single layer textiles. *Langmuir* **33**, 12072–12079 (2017).

373. Garcea, S. C., Sinclair, I. & Spearing, S. M. In situ synchrotron tomographic evaluation of the effect of toughening strategies on fatigue micromechanisms in carbon fibre reinforced polymers. *Compos. Sci. Technol.* **109**, 32–39 (2015).

374. Garcea, S. C., Wang, Y. & Withers, P. J. X-ray computed tomography of polymer composites. *Compos. Sci. Technol.* **156**, 305–319 (2018).

375. Jespersen, K. M., Zangenberg, J., Lowe, T., Withers, P. J. & Mikkelsen, L. P. Fatigue damage assessment of uni-directional non-crimp fabric reinforced polyester composite using X-ray computed tomography. *Compos. Sci. Technol.* **136**, 94–103 (2016).

376. Pak, T., Archilha, N. L., Mantovani, I. F., Moreira, A. C. & Butler, I. B. An X-ray computed micro-tomography dataset for oil removal from carbonate porous media. *Sci. Data* **6**, 1–9 (2019).

377. Shah, S. M., Gray, F., Crawshaw, J. P. & Boek, E. S. Micro-computed tomography pore-scale study of flow in porous media: Effect of voxel resolution. *Adv. Water Resour.* **95**, 276–287 (2016).

378. Yoiti Ito Parada, M., Matthias Schlepütz, C., Michel Rossi, R., Derome, D. & Carmeliet, J. Two-stage wicking of yarns at the fiber scale investigated by synchrotron X-ray phase-contrast fast tomography. *Text. Res. J.* (2019).

doi:10.1177/0040517519843461

379. Parada, M., Derome, D., Rossi, R. M. & Carmeliet, J. A review on advanced imaging technologies for the quantification of wicking in textiles. *Text. Res. J.* **87**, 110–132 (2017).

380. Wang, Z., Lowe, T. & Derby, B. Fluid/Fiber Interactions and the conductivity of inkjet printed Ag on textile substrates. *ACS Appl. Mater. Interfaces* **12**, 45516–45524 (2020).

381. Gaspar, C., Passoja, S., Olkkonen, J. & Smolander, M. IR-sintering efficiency on inkjet-printed conductive structures on paper substrates. *Microelectron. Eng.* **149**, 135–140 (2016).

382. Perelaer, J. *et al.* Roll-to-roll compatible sintering of inkjet printed features by photonic and microwave exposure: From non-conductive ink to 40% bulk silver conductivity in less than 15 seconds. *Adv. Mater.* **24**, 2620–2625 (2012).

383. Lai, C. Y. *et al.* Synthesis and characterization of silver nanoparticles and silver inks: Review on the past and recent technology roadmaps. *J. Mater. Eng. Perform.* **23**, 3541–3550 (2014).

384. Haralick, R. M., Sternberg, S. R. & Zhuang, X. Image analysis using mathematical morphology. *IEEE Trans. Pattern Anal. Mach. Intell.* PAMI-9, 532–550 (1987).

385. Serra, J. *Image analysis and mathematical morphology*. (Academic Press, Inc., 1983).

386. Maire, E. & Withers, P. J. Quantitative X-ray tomography. *Int. Mater. Rev.* **59**, 1–43 (2013).

387. Han, S.-T. *et al.* An overview of the development of flexible sensors. *Adv. Mater.* **1700375**, 1700375 (2017).

388. Ma, L. *et al.* All-in-one fibrous capacitive humidity sensor for human breath monitoring. *Text. Res. J.* **91**, 398–405 (2020).

389. Zhang, J., Zhang, Y., Li, Y. & Wang, P. Textile-based flexible pressure

sensors: A Review. *Polym. Rev.* 1–31 (2021). doi:10.1080/15583724.2021.1901737

390. Tseghai, G. B., Malengier, B., Fante, K. A., Nigusse, A. B. & Van Langenhove, L. Integration of conductive materials with textile structures, an overview. *Sensors* **20**, (2020).

391. Sanchez, V., Walsh, C. J. & Wood, R. J. Textile technology for soft robotic and autonomous garments. *Adv. Funct. Mater.* **31**, 2008278 (2021).

392. Wilson, P. & Teverovsky, J. 9 - New product development for e-textiles: experiences from the forefront of a new industry. in *Woodhead Publishing Series in Textiles* (ed. Horne, L. B. T.-N. P. D. in T.) 156–174 (Woodhead Publishing, 2012). doi:https://doi.org/10.1533/9780857095190.2.156

393. Yang, T., Xie, D., Li, Z. & Zhu, H. Recent advances in wearable tactile sensors: Materials, sensing mechanisms, and device performance. *Mater. Sci. Eng. R Reports* **115**, 1–37 (2017).

394. Liu, S., Wang, H., He, T., Dong, S. & Lee, C. Switchable textile-triboelectric nanogenerators (S-TENGs) for continuous profile sensing application without environmental interferences. *Nano Energy* **69**, 104462 (2020).

395. Zhang, G., Quetzeri-Santiago, M. A., Stone, C. A., Botto, L. & Castrejón-Pita, J. R. Droplet impact dynamics on textiles. *Soft Matter* **14**, 8182–8190 (2018).

Appendices

Appendix 4.1 Matlab code used to compare experimental results with Carroll’s theoretical values of ink drop spreading on single fibres.

```
/////////////////////////////////% Drop on Fibre - Carroll Model%//////////////////////////////

% n = max drop ratio at centre of drop.
%40 incrementing values between the two limits
n=(1.14:0.062:3.558);
% theta is contact angle 14 incremented values
theta=(0:5:65);
% Defining variable array sizes,
% row represents n value
% column is theta value
% a is variable a in carroll
a=zeros(40,14);
% k is variable k for elliptic integral
k= ones(40,14);
% phi is variable for elliptic inegral
phi=zeros(40,14);
% aphi is intermediate variable to compute phi
aphi=zeros(40,14);
%EF1 is result of elliptic integral (incomplete first kind)
EF1=zeros(40,14);
%EC2 is result of elliptic integral (incomplete second kind)
EC2=zeros(40,14);
% L is normalised droplet length on fibre
L=zeros(40,14);
% V is normalised droplet volume
V=zeros(40,14);
% v1 and v2 are intermediate variables to compute V
v1=zeros(40,14);
v2=zeros(40,14);
%mt and mn are dummy variables to call appropriate array elements
for the
%calculations
% mt calls for theta
for mt=1:14
    % mn calls for n
    for mn = 1:40
        % a calculated from carroll equation 11 with n=x2/x1
        a(mn,mt)=(n(mn)*cosd(theta(mt))-1)/(n(mn)-cosd(theta(mt)));
        % Carroll equation 13
        k(mn,mt)=sqrt((1-(a(mn,mt)/n(mn))^2));
        % Carroll equation 13
        phi(mn,mt)=asin(sqrt((n(mn)^2-1)/(n(mn)^2-a(mn,mt)^2)));
        % Elliptical Integrals using MATLAB
        % Elliptical integral of first kind
        EF1(mn,mt)=ellipticF(phi(mn,mt),k(mn,mt));
        % Elliptocal integral of second kind
        EC2(mn,mt)=ellipticE(phi(mn,mt),k(mn,mt));
        % Carroll Equation 16
        L(mn,mt)=2*(a(mn,mt)*EF1(mn,mt)+n(mn)*EC2(mn,mt));
        %Carroll equation 24

v1(mn,mt)=(2*a(mn,mt)^2+3*a(mn,mt)*n(mn)+2*n(mn)^2)*EF1(mn,mt)-
a(mn,mt)^2*EC2(mn,mt);
```

```
        v2(mn,mt)=n(mn)^-1(n(mn)^2-1)^0.5*(1-a(mn,mt)^2)^0.5;
        V(mn,mt)=(2*pi*n(mn)/3)*(v1(mn,mt)+v2(mn,mt))-pi*L(mn,mt);
    end
end

% Array L has the wetted length of the fibre for n (x2/x1)and theta
within the ranges specified
% Array V has the drop volume normalised by x1^3 (drop radius cubed)
% Find n and theta for 7 pL and n and theta for measured wetted
length
% Correct theta is when theta and n are the same for both measured
length and known volume
```

Appendix 5.1 TGA graphs of AgNP printed on polyester fabric with 20um drop spacing and that with(a) and (b) without surface treatment, and with 10um drop spacing with (c) and without (d) surface treatment.

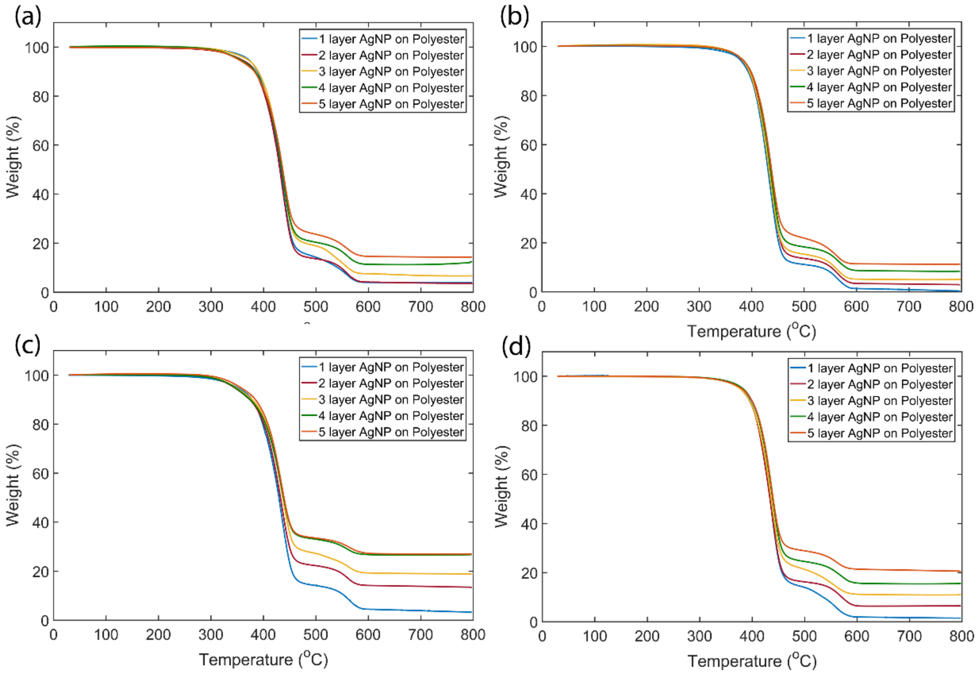

Appendix 5.2 Comparison of the Ag object volume distribution determined using the two segmentation methods for 5 layers AgNP printed on polyester fabric with 20um drop spacing (a) with and (b) without surface treatment, and with 10um drop spacing (c) with and (d) without surface treatment.

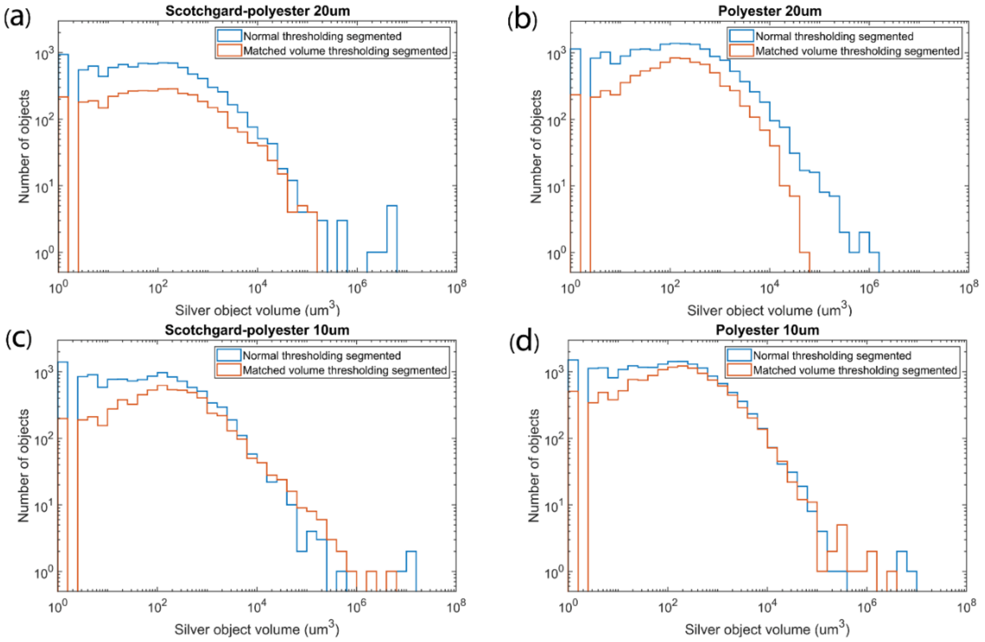

Appendix 6.1 Spreading length of ink on six types of fabrics through optical images of three specimens each.

Fabric type	Warp ink spreading length (mm)	Weft ink spreading length (mm)
F1	21.0 ± 1.5	12.8 ± 2.1
F2	17.8 ± 2.3	6.6 ± 0.5
F3	7.7 ± 0.5	6.7 ± 0.6
F4	7.1 ± 0.4	7.2 ± 0.7
F5	6.3 ± 0.5	6.9 ± 0.5
F6	5.0 ± 0.1	7.7 ± 0.2